Investigating Nonlinear Integrable Optics with a Paul Trap

Jake Flowerdew
St. Cross College, Oxford

Thesis submitted in fulfilment of the requirements for the degree of Doctor of Philosophy at the University of Oxford

Trinity Term, 2023

Acknowledgements

I want to start off by thanking my supervisors, Armin and Suzie for their guidance and mentorship throughout my PhD. Suzie, thank you for giving me this opportunity and for encouragement when I needed it the most. Armin, I am grateful for the many thought-provoking conversations we had throughout my PhD. These discussions were invaluable to developing my understanding of accelerator concepts.

I want to thank Hiromi and the Hiroshima group for their insights into testing beam dynamics in Paul traps and for their valuable comments and feedback on my research. Their expertise was instrumental in shaping the trajectory of my work.

I am deeply indebted to Stas for his support and for such insightful meetings throughout my PhD, where I gained most of my understanding of Nonlinear Integrable Optics. His continued belief in my project was a driving force behind my research.

Thank you to everyone in the Intense Beams group, Shinji, David, JB, and Chris, for their continuous support and guidance throughout my PhD. Shinji and David, your feedback on my results throughout my PhD, as well as your patient explanations of accelerator concepts, were invaluable. I would also like to thank Emi from the ISIS diagnostics team for all her help with the MCP detector. I am so grateful for everyone's support.

I am immensely thankful to the STFC engineers, Ross, Galen, and Dave, for their meticulous attention to detail in the design and manufacturing of the IBEX trap. Without their expertise and dedication, these experiments would not have been possible. I also extend my gratitude to Sam for creating the remarkable 3D printed IBEX model.

Thank you to Adam for his exceptional work in designing and manufacturing the new HV amplifiers for the IBEX trap. Thank you for working so closely with me throughout the design process to ensure that the amplifiers were the best they could be. You taught me so much about electronics along the way, a subject I had been terrified of before.

I express my gratitude to Dan Faircloth for his help getting me up and running with VSim on the SCARF cluster, as well as to the STFC SCARF support team. I also extend my thanks to the Tech-X VSim support team for helping me tackle some problems whilst learning this code for the first time. My appreciation also goes to Pete for his LabView support and to Lucy for getting me up and running with IBEX.

I would like to thank Max and Carl for their coffee break discussions that got me through the final year of my PhD. Thank you for all the troubleshooting, your helpful

ideas and for listening to me complain for months on end about how I couldn't synchronise the AWGs. Your company and support were instrumental in overcoming challenges and keeping me motivated.

I am grateful to my friends and family for their unwavering support and encouragement throughout my PhD journey. Your belief in me was a constant source of motivation.

And finally I want to thank Sabrina. Thank you not only for proofreading this entire thesis, but for your support and the kindness you showed throughout this entire degree.

Abstract

Designing high-intensity accelerators has traditionally relied on using computer simulations to study the beam dynamics. As intense beams are comprised of large numbers of particles, all interacting via Coulomb forces, such simulations require significant computational power in order to numerically predict these interactions. The Intense Beams Experiment (IBEX) is a linear Paul trap that can replicate the transverse beam dynamics in accelerators by trapping low-energy ions using RF electric fields that emulate the magnetic focusing elements of particle accelerators. IBEX's flexibility allows different lattice designs and beam intensities to be tested with ease, which means that it can be used to test novel lattice configurations for high-intensity accelerators. Examples of such lattices arise from the theory of Nonlinear Integrable Optics, and, as discussed in this thesis, the related theory of Quasi-Integrable Optics (QIO). These theories suggest techniques for introducing nonlinear elements such as octupoles into an accelerator lattice, while keeping the system integrable and hence maintaining stable particle motion.

In this work, an upgrade to the original IBEX trap was designed, manufactured, and commissioned with the aim of experimentally testing the principles of QIO. Simulations were used to test the ability of a quasi-integrable lattice to damp a space-charge-driven coherent resonance without exciting the 4th order incoherent resonance in the vicinity. This lattice was then compared to a lattice which broke the integrability conditions, which was shown to excite the 4th order resonance. Using the newly-commissioned IBEX-2 trap, we were then able to test the quasi-integrable lattice experimentally and verify the results from simulations. This thesis demonstrates the first ions successfully trapped in a quasi-integrable lattice in a Paul trap, and discusses the benefits of introducing octupole elements according to the method prescribed by the theory of QIO. The experimental results presented here show the potential value of QIO to research on high-intensity beams in accelerators.

Contents

List of Figures

List of Tables

Chapter 1

High-intensity hadron accelerators

In this chapter I explore the motivations for constructing high-intensity particle accelerators and discuss some of the problems that arise when designing and operating them. I then address several potential solutions to these problems, including possible routes to increasing beam intensity in the future, which is required for a range of applications. Specifically, I introduce Nonlinear Integrable Optics as one possible solution to damping resonances in accelerators, which will be the main focus of this thesis.

1.1 Introduction to high-intensity hadron accelerators

Recent developments in accelerator technology and the wide range of potential applications of this technology have created the need to further investigate the dynamics of high-intensity particle beams. An intense beam is achieved when a large number of particles are successfully confined within a small area. A high-intensity accelerator is a machine that can accelerate, focus and steer these intense beams to a desired target or collision point. The intensity of an accelerator is measured by its beam current, defined as the rate of flow of charged particles past a given plane. This is distinct from beam power, which is defined as the average beam current multiplied by the beam energy (in eV). Once the high intensity beams are confined within a small area, the charge density increases and the repulsive force between charged particles becomes non-negligible compared with the external confinement force. This creates a defocusing term which can

lead to resonant behaviour and beam loss.

The Large Hadron Collider (LHC), located at CERN, is well-known as the highest energy hadron accelerator in the world. It currently collides particle bunches together with a center of mass energy of 13.6 TeV. It is scheduled to have a long shut down (LS3) to boost the performance of the machine in 2026 [1, 2]. A main focus of this upgrade is to increase the luminosity. The luminosity is a parameter of a collider proportional to the number of collisions that occur in a given amount of time. The more collisions that occur in a certain time frame, the more data is collected by the experiment, which makes it more likely to observe rare processes. This upgrade will see the number of particles per bunch increase from 1.15×10^{11} to 2.2×10^{11}, increasing the current to 1.09 A [3]. This requires a detailed understanding of the machine optics and beam instabilities to ensure successful operation.

Not only do intense beams offer the possibility of probing fundamental physics, they are also used across multiple industries for purposes as diverse as bio-science [4,5], nuclear energy [6], and even research on ancient artifacts [7]. The advancements of high-intensity accelerators such as ISIS [8], J-PARC [9] and SNS [10] have allowed for rich scientific programs since their development. The ISIS synchrotron at the Rutherford Appleton Laboratory, UK has a proton beam current of 225 µA and beam energy of 800 MeV. Neutrons are created by bombarding a tungsten target with these protons. This causes the ejection of neutrons from excited nuclei, a process called spallation. The neutrons are slowed (moderated) to speeds useful for research and are then directed to a variety of different experiments [11]. One use of these neutron beams is for neutron diffraction, an imaging technique that can determine the atomic structure of molecules or materials. This can be used in a variety of different fields from developing drug-delivery systems in medicine to creating more efficient solar cells [12, 13]. A unique property of neutrons is that they have a neutral charge as well as carrying a spin. This allows us to use neutrons to probe the microscopic magnetic structure of materials which is not possible using x-ray diffraction.

In addition to scientific research, the development of high-intensity accelerators will also benefit Accelerator-Driven Systems (ADS) [14]. One use of an ADS is to use spallation neutrons created by a proton beam to transmute long-lived radioisotopes (mostly actinides) in spent nuclear fuel into shorter-lived fission products. This would reduce the radiotoxicity of high-level nuclear waste and facilitate the storage and disposal of the waste from nuclear reactors. There is also interest in using ADS to run sub-critical reactors fuelled by thorium, referred to as an Accelerator-Driven Sub-critical Reactor (ADSR) [15]. An ADSR can be 'turned off' by stopping the incident proton beam, and thus eliminating the neutron flux needed to sustain nuclear fission. This removes the need to lower control rods into the reactor in order to absorb neutrons and stop the fission reaction which is considered to be a safer alternative to conventional nuclear reactors.

In order to design and build accelerators that push the intensity frontier and enable both innovative high-energy physics research and a wide range of industrial applications, it is necessary to have a good understanding of the particle dynamics of these beams. Understanding the mechanisms behind particle losses at high intensities allows us to work on solutions to overcome these losses and build more practical and efficient high-intensity machines.

1.2 Limitations when designing high-intensity accelerators

The most common accelerator for high-energy hadron beams (> 500 MeV) is the synchrotoron. Current synchrotrons utilize a system of alternating focusing and defocusing quadrupole magnets to confine a beam of charged particles. Dipole magnets are used to bend the beam of charged particles around a circular machine. Dipole and quadrupole magnets are referred to as 'linear' due to their magnetic field strength varying linearly across the transverse axis of the magnet. The use of linear magnets leads to a Hamiltonian of the system that can be made time-independent and separated to obtain two

invariants (the horizontal and vertical Hamiltonian). In general, an integrable system means that there are N invariants of motion for the N-degrees of freedom in the system. Therefore, a linear lattice (the arrangement of magnets in an accelerator) is said to be integrable in 2D.

In accelerators, imperfections in the magnetic fields and magnet alignment introduce small errors into the focusing system that make these accelerators vulnerable to the excitation of resonances. In circular storage rings, these resonances appear naturally due to the periodic interaction of particles with the focusing elements, which produce perturbations from the design orbit. Particles can be driven into resonant oscillations by small perturbations that can lead to beam instabilities and particle loss. The loss of particles from a beam can damage the components of the accelerator and can activate parts of the machine to levels which make them inaccessible for maintenance by human operators. Typically, unplanned beam loss should be kept below an average of $1\,\mathrm{Wm}^{-1}$ for > 1 MeV machines, which is becoming increasingly problematic as beams become more intense [16]. As an example, for an accelerator with a circumference of 100 m, the average beam loss would need to be kept below 100 W. For a 1 MW machine, this would require limiting beam loss to below 0.01 %. Therefore, in the case of high-intensity beams, where space-charge effects are present, it is especially important to avoid the excitation of resonances.

1.2.1 Resonances

As a particle travels along a circular path in an accelerator, referred to as the design orbit, it makes oscillations around this orbit. These oscillations are referred to as 'betatron oscillations'. The number of betatron oscillations per revolution around a circular accelerator is defined as the 'tune'. The non-integer part of the tune is called the 'fractional tune'. A particle beam will often make many revolutions[1] around a circular accelerator and therefore resonant behaviour becomes important. A resonance is the amplification

[1] In the LHC particles make 11,245 revolutions per second and are often circulated for hours at a time.

of oscillations in a system when the driving frequency matches an integer multiple of the natural frequency. The natural frequency of a particle in an accelerator is its betatron frequency. As there are oscillations in both the horizontal and vertical planes, when we introduce linear coupling resonances (driven by skew quadrupole components) the full resonant condition becomes

$$kQ_x + lQ_y = n, \tag{1.1}$$

where k, l and n are integers. The harmonic of the resonance is given by n and the order of the resonance is given by $k + l = m$. Q_x and Q_y are the horizontal and vertical tunes respectively. If this resonance condition is met, particle oscillations will be driven to larger amplitudes until they hit the physical aperture of the machine's beam pipe. In reality, the resonance condition in Eq. 1.1 does not have to be exact as most resonances will have a finite width, referred to as the stopband.

Therefore, in order to avoid resonances around the ring, integer fractions of the tune are avoided (i.e. $Q = 1$, 1/2, 1/3, 1/4 etc.). This is because the particle will return to the same place in the accelerator after an integer number of turns, making it susceptible to a kick from imperfections in the machine, driving a resonance. To ensure that these resonances are avoided, the tune spread (the extent to which the particle tunes are distributed around the nominal tune) must be kept sufficiently low.

Figure 1.1 shows an illustration of a tune diagram for an accelerator. The grey lines show resonances up to 4th order and the black circle indicates the nominal fractional tune in this example. It has been chosen to avoid the resonance lines and to have a low tune spread. The blue diamond shows an example of a space-charge tune spread (see Section 1.2.2).

From Fig. 1.1, it is clear that minimising the tune spread is one approach to avoid resonant behaviour and particle loss. In order to achieve low tune spreads, higher-order magnets such as sextupoles can be introduced into the lattice to correct for the spread in particle momenta, known as the chromaticity [17]. When this correction is applied, the lattice is no longer linear and the particle tune becomes dependent on the particle's

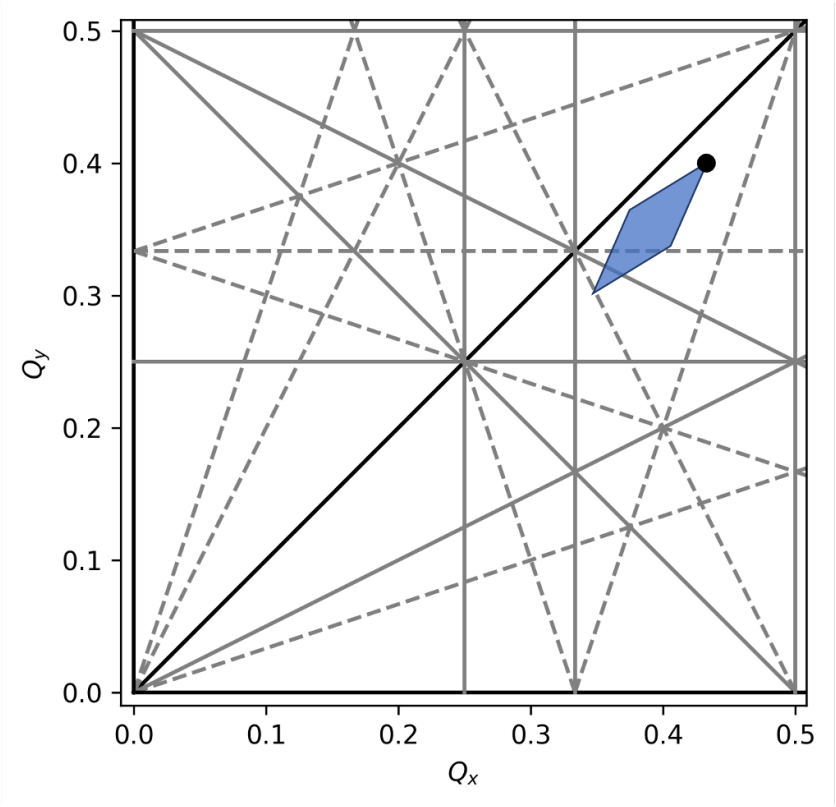

Figure 1.1: Tune diagram showing resonances up to 4th order. Normal resonances are shown with solid lines and dashed lines represent skew resonances. A black circle marks the particle tune without space charge. A blue diamond shows the tune spread of a particle beam with space charge (tune footprint).

deviation from the design momentum. The lattice will no longer be integrable and hence the Hamiltonian of the system is not conserved, meaning that the sextupole magnets also drive their own set of resonances in the system. This limits the available phase space in which the particle motion is stable. The largest trajectory in phase space where the particle motion is stable is known as the dynamic aperture. While the introduction of sextupoles is effective for lower-intensity beams, it poses a challenge to the design of accelerators for beams of higher intensities. This is due to the Coulomb interaction between charged particles (space-charge forces) which create a tune spread that cannot be avoided. The blue diamond in Fig. 1.1 (often referred to as a 'neck-tie' or 'tune footprint') gives an example of what the tune spread from space charge looks like in theory. The space-charge tune spread can be seen to move some particles in the beam onto resonances.

1.2.2 Space charge

There are two competing space-charge forces in a particle beam. The first is the electrostatic Coulomb repulsion of the charged particles. The second force comes from the fact that the charged particles, travelling with some velocity v, act like current carrying wires which attract each other. Assuming a uniform beam with a cylindrical cross-section and a charge density ρ, the transverse electromagnetic forces acting on a test particle in polar coordinates (r, ϕ) are given by [18]

$$\vec{E}_r = \frac{\rho}{2\epsilon_0}\vec{r} \quad \text{and} \quad \vec{B}_\phi = \frac{\rho v}{2\epsilon_0 c^2}\vec{r}, \tag{1.2}$$

where ϵ_0 is the electric constant and c is the speed of light. Using the Lorentz force, the total force on the test particle with charge q is

$$\vec{F} = q(\vec{E} + \vec{v} \times \vec{B}) = \frac{q\rho}{2\epsilon_0}\left(1 - \frac{v^2}{c^2}\right)\vec{r} = \frac{q\rho\vec{r}}{2\epsilon_0\gamma^2}, \tag{1.3}$$

where $\gamma = \frac{1}{\sqrt{1-\beta^2}}$ is the relativistic factor and $\beta = v/c$. From Eq. 1.3 we can see that as the speed of the particle approaches the speed of light, $v \to c$, the space-charge force vanishes. Therefore, space-charge forces are a more significant problem at lower energies in the acceleration cycle. The total force is repulsive and hence introduces a defocusing force to the accelerator lattice.

1.2.2.1 Incoherent and Coherent resonances

When space charge is non negligible, the accelerator elements can not only excite single-particle resonances in the beam, but can also excite collective effects, driving the beam core to oscillate at larger amplitudes. A distinction should be made between incoherent motion — the oscillations of a single particle in a distribution, and coherent motion — the oscillations of the distribution as a whole. Therefore, single-particle resonances are referred to as incoherent and collective resonances are referred to as coherent.

The 2D incoherent resonant condition was introduced in Eq. 1.1. In one dimension this simply becomes

$$Q_0 = n/m, \tag{1.4}$$

where Q_0 represents the bare tune of the particle, excluding any space-charge tune shift and n and m represent the harmonic and order of the resonance respectively. Space-charge forces will modify where these resonances occur. Including the tune shift due to incoherent space-charge forces, ΔQ, known as the incoherent space-charge tune shift, Eq. 1.1 becomes.

$$Q_0 + \Delta Q = n/m, \tag{1.5}$$

In order to arrive at an equation to describe the coherent resonance, the beam envelope equations must be solved along the beams trajectory s, (introduced more formally in Chapter 2). For a quadrupole ($m = 2$) coherent oscillation and horizontal and vertical RMS beam size σ_x and σ_y, the envelope equations are,

$$\frac{d^2\sigma_x}{ds^2} + K_x(s)\sigma_x - \frac{\epsilon_x^2}{\sigma_x^3} - \frac{K_{sc}}{2(\sigma_x + \sigma_y)} = 0, \tag{1.6}$$

$$\frac{d^2\sigma_y}{ds^2} + K_y(s)\sigma_y - \frac{\epsilon_y^2}{\sigma_y^3} - \frac{K_{sc}}{2(\sigma_x + \sigma_y)} = 0, \tag{1.7}$$

where ϵ_x and ϵ_y are the transverse emittances and $K(s)$ is the quadrupole focusing strength. The emittance describes the area the beam occupies in position and momentum phase space (see Section 2.1.5). The space-charge defocusing strength K_{sc} is given by

$$K_{sc} = \frac{Nq^2}{2\pi\epsilon_0 m\gamma^3 v^2}, \tag{1.8}$$

where N is the number of particles per unit length (beam line density), q the particle charge, m the particle rest mass, γ is the relativistic Lorentz factor, and v is the longitudinal beam velocity. Applying the smooth approximation[2], and solving the envelope equations, the 2nd order coherent resonance condition is found to be

$$Q_0 + C_2\Delta Q_{rms} = n/m, \tag{1.9}$$

where ΔQ_{rms} is the RMS incoherent tune shift of the beam. When the horizontal and vertical tunes are equal, there are two possible modes of oscillation of the beam core.

[2]The smooth approximation averages out the time-dependent focusing of the quadrupoles into a constant restoring force. This assumes a constant, average beta function which can be found by $\langle\beta\rangle = L/\phi$, where ϕ is the phase advance over a length L of periodic beamline.

The symmetric, "breathing" mode has a value of $C_2 = 1/2$ and the anti-symmetric mode has a value of $C_2 = 3/4$ [19]. Anti-symmetric modes are more commonly excited by quadrupoles and so we will consider only anti-symmetric modes in this thesis.

The condition can be generalised to higher order eigenmodes, m, by solving the linearised Vlasov-Poisson equation [20] where we arrive at

$$Q_0 + C_m \Delta Q_{rms} = n/m. \tag{1.10}$$

For the case of 2D round beams with equal transverse tunes, the theoretical C_m factors up to 4th order are summarised in Table 1.1. The eigenmode solutions from the Vlasov-Poisson equation are the coherent oscillations of the beam profile and are shown in Fig. 1.2. The C_m factor lies between $0 \leq C_m < 1$ and is independent of the driving term of the resonance.

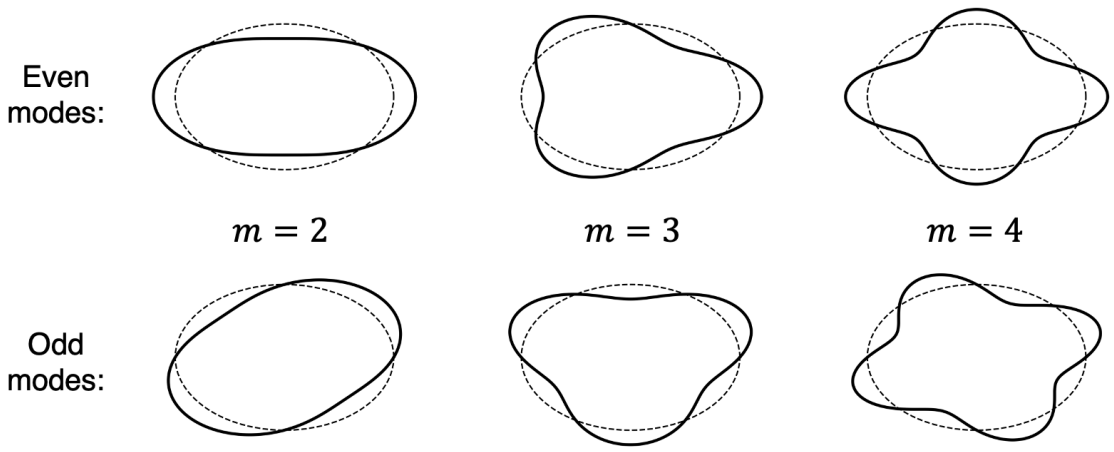

Figure 1.2: Transverse beam cross sections, in real space, of even and odd coherent modes up to 4th order [21].

1.2.3 Space-charge mitigation with octupoles

1.2.3.1 Decoherence

Instead of creating particle beams with a small tune spread to avoid resonances in a machine, another technique is to intentionally create a large tune spread which can

Table 1.1: Analytically calculated C_m values for the symmetric and anti-symmetric modes for a 2D round beam [22]

Order of coherent resonance (m)	1	2	3	4
Symmetric C_m	0	$\frac{1}{2}$	$\frac{3}{4}$	$\frac{13}{16}$
Anti-symmetric C_m	0	$\frac{3}{4}$	$\frac{11}{12}$	$\frac{31}{32}$

damp instabilities through decoherence [23]. Figure 1.3 plots five sine waves, analogous to five particle betatron tunes with a spread in frequencies. The sum of these amplitudes represents the centroid of the particle beam and is plotted in black. If the coherent mode frequency of the centroid matches a resonant frequency then the coherent motion will excite particles to larger particle amplitudes, leading to particle loss. In Fig. 1.3 the centroid is seen to be damped by the spread in betatron frequencies (tune spread) and therefore coherent instabilities can be suppressed. The strength of decoherence only depends on the lattice parameters and not on the beam distribution.

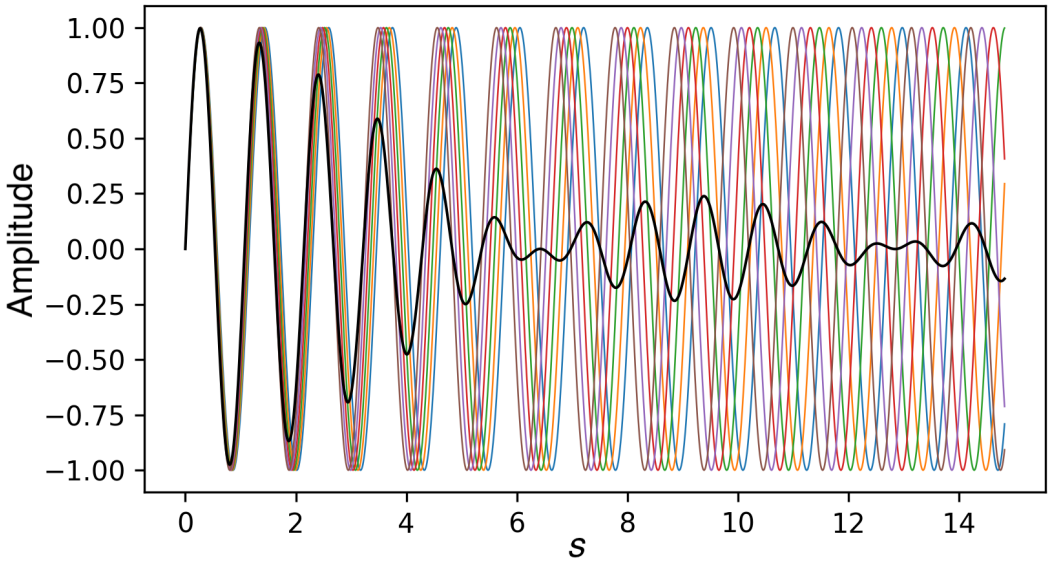

Figure 1.3: Illustration of decoherence where five sine waves have a small spread in frequencies. The sum of the amplitudes (normalised) is plotted in black.

1.2.3.2 Landau damping

Landau damping is defined as the damping of a collective mode of oscillations in a collision-less plasma. The collective or coherent oscillations are damped by the beam energy being transferred from the coherent oscillations to the incoherent (single particle) motion and thus the coherent instability never fully forms. Landau damping is a difficult concept to understand intuitively, and it often gets mistaken for decoherence [24]. As described in [25], there are three conditions to be satisfied for Landau damping to occur. First, the beam must have an incoherent frequency (tune) spread. The second condition is that the coherent mode and the tune spread must have spectral overlap. The final condition is that the coherent mode ω_c must lie on the downwards slope of the betatron frequency distribution function (see Fig. 1.4). Unlike decoherence, Landau damping is, however, dependent on the betatron frequency distribution as it requires a larger density of particles in the center of the distribution.

In the schematic Fig. 1.4, particles with a betatron frequency lower than the coherent frequency ($v_x < \omega_c$) will gain in amplitude to match the coherent frequency [20]. The particles with a frequency higher than the coherent frequency ($v_x > \omega_c$) will do the reverse, losing energy to match the coherent mode. If there is a larger population of particles with a frequency less than the coherent mode, as in Fig. 1.4, energy is transferred from the coherent oscillation of the beam core to the incoherent oscillation of individual particles. The result of this is that the coherent oscillation is damped.

1.2.3.3 Octupole tune spread

Octupoles are often added to lattices to create an amplitude-dependent tune shift which can damp coherent beam instabilities through decoherence and Landau damping [26–28]. A derivation of the amplitude-dependent tune spread can be found in Section 2.2.2. As the amplitude-dependent tune shift increases with amplitude, and there is often not a large density of particles in the tails of the distribution (high-amplitude particles), large octupole strengths are often required to create the desired tune spread. As was the

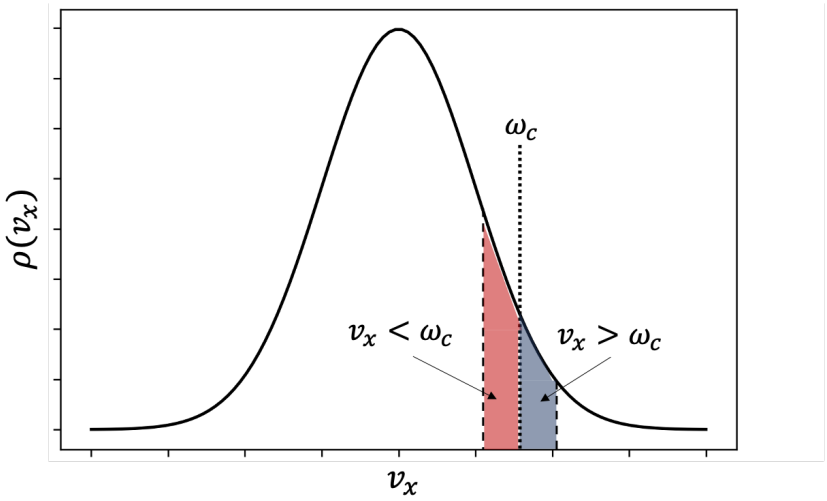

Figure 1.4: Schematic of a betatron frequency distribution of a particle beam with tune spread. The red region highlights particles that will gain energy to match the coherent frequency, ω_c and the blue region highlights the particles that will lose energy. Figure recreated from [20].

case for sextupoles, nonlinear magnets lead to a non-integrable lattice which results in a reduction in the dynamic aperture as the nonlinear elements will drive their own set of resonances. To address this problem, it is desirable to introduce nonlinear magnets into the system that are effective for creating beams with a large tune spread but which do not further excite resonances. These lattices would conserve the Hamiltonian of the system and are referred to as nonlinear integrable lattices. These lattices are the main object of study for Nonlinear Integrable Optics (NIO) and will be the main focus of this thesis. NIO is outlined briefly below but is described in more detail in Chapter 3.

1.3 Proposed solutions for realising high-intensity accelerators

The theory of Nonlinear Integrable Optics (NIO) seeks to circulate particles around an accelerator with nonlinear elements, without exciting resonances associated with those nonlinear elements. Thus the benefits of the nonlinear element are obtained whilst still maintaining a large dynamic aperture. In a nonlinear integrable lattice, as described by the theory of NIO [29], the trajectory of the particle beam would both occupy large

stable regions in phase space and maintain a large tune spread. This would open up the possibility of accelerating beams with larger tune spreads, allowing for the suppression of instabilities, and thus of achieving higher-intensity beams.

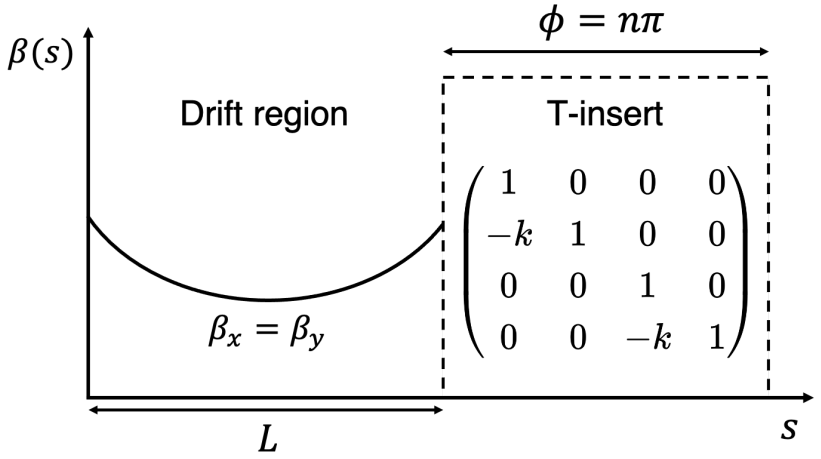

Figure 1.5: Schematic of T-insert and drift region for a nonlinear insert.

The theory of NIO was laid out in 2010 by Danilov and Nagaitsev [29] in which they proposed an integrable, nonlinear lattice consisting of a linear 'T-insert' made from focusing and defocusing quadrupoles and a drift region for a nonlinear magnet insert. A schematic of a T-insert and drift region is shown in Fig. 1.5. The T-insert lattice requires an $n\pi$ (where n is an integer) phase advance[3] to provide quasi-periodic motion through the drift region. Quasi-periodic motion ensures that any given particle will return to the same position in phase space (or 180° out of phase in the case that n is odd) each time it passes through the T-insert lattice. This essentially makes the T-insert 'invisible' to a single particle. More formally, the T-insert is defined as having the transfer matrix of a thin axially symmetric lens (see Fig. 1.5). The T-insert must also provide equal beta functions in the drift region for the nonlinear insert ($\beta_x = \beta_y$). The nonlinear magnet potential must then scale with the beta function in the drift region in order to keep the Hamiltonian time independent and hence integrable. Since the Hamiltonian is designed to be time independent, then, according to KAM theory [30], the system will

[3]The phase advance is equal to $2\pi \times$ tune (see Section 2.1.4).

always be close to an integrable solution, even when small perturbations such as magnet misalignment and space charge are included.

NIO offers a compelling opportunity to effectively achieve higher-intensity beams, but the construction and operation of test accelerators to study this approach is a costly and energy-intensive process. Furthermore, once they are built, test accelerators do not generally allow the flexibility to adjust lattice structures and beam intensities to explore large parameter spaces. While simulations can be a productive substitute in some situations, in the case of higher-intensity beams they become computationally expensive when reproducing the space-charge forces that are present in these beams over long timescales. This makes relying solely on simulations impractical for the study of NIO and higher-intensity beam dynamics.

1.3.1 Using a Paul trap to study accelerator physics

The difficulties in carrying out beam loss studies in accelerators and the computationally exhaustive simulations required to compute space-charge effects over long timescales has led to the development of Paul traps for research in accelerator physics. Most notably, Paul trap experiments have been developed at Hiroshima University [31, 32], Princeton University [33], and, most recently, the Rutherford Appleton Laboratories (RAL), in collaboration with the University of Oxford [34]. These traps are used to study the dynamics necessary to understand how to realise future high-intensity accelerators. One of those potential future methods is NIO which is planned to be tested with the Intense Beams Experiment (IBEX).

The IBEX experiment at RAL is a table-top sized linear Paul trap that can replicate the transverse motion of particles in an alternating-gradient accelerator without dispersion or chromaticity. This trap can be used to effectively study the dynamics of high-intensity beams because the transverse Hamiltonians of ions in a Paul trap and of particles in an accelerator are equivalent (Section 2.2). IBEX is not only a less expensive alternative to building an accelerator to study beam dynamics, but it is also relatively

safe and simple to operate. IBEX confines ions at low energy (< 1 eV) so there is no risk of the equipment being damaged or activated by particle loss. Different lattices can be tested in IBEX by adjusting the amplitude and frequency of the voltage waveforms applied to the electrodes. The intensity can be adjusted by increasing the ionisation time or gas pressure and hence number of ions stored in the trap. This makes it a very attractive tool for testing various new types of lattices for high-intensity beams.

This thesis presents the design and commissioning of an upgrade to IBEX to allow for higher-order multipoles to be created in order to test NIO experimentally. To enable the exploration of non-linear accelerator lattices, the upgrade will allow for the creation of the octupole fields and the linear T-insert lattice that are needed for the study of NIO. However, it should be noted that the fully integrable nonlinear lattice requires a complex elliptical potential in the non-linear drift region. This lattice is being tested at the Integrable Optics Test Accelerator (IOTA) at Fermilab in Chicago [35]. This elliptical potential is challenging to create experimentally (both in Paul traps and accelerators), so IBEX will first be used to test a quasi-integrable case which only requires a linear lattice and a scaling octupole potential. This thesis will discuss the use of the IBEX Paul trap to test quasi-integrable optics with the ultimate aim of expanding these studies to the exploration of high-intensity accelerator physics.

1.4 Thesis outline

The structure of this thesis is as follows. Chapter 2 introduces Paul traps as tools for accelerator physics, and the experimental setup of the IBEX Paul trap is outlined. A section is also dedicated to informing the reader of previous accelerator physics studies that have been performed with Paul traps in the past. Chapter 3 describes the theory of Nonlinear Integrable Optics and the design of the T-insert lattice to be tested in IBEX.

Chapter 4 details the design of the nonlinear upgrade to the IBEX experiment and describes the operation of the new trap. It includes the design of the amplifiers needed

to generate the high voltages applied to the trap electrodes. It also outlines the commissioning of the high-voltage amplifiers along with the rest of the trap and detectors.

In Chapter 5, an investigation into testing Quasi-Integrable Optics (QIO) in a Paul trap is carried out through simulation. Chapter 6 presents the first results of an experimental investigation of QIO in a Paul trap. These results show the first demonstration of a Quasi-Integrable lattice storing ions in a Paul trap. Conclusions and ideas for further exploration are given in Chapter 7.

Chapter 2

Beam dynamics, Linear Paul trap dynamics, and IBEX

Wolfgang Paul was awarded the Nobel Prize in Physics in 1989 for "the development of the ion trap technique." In his Nobel lecture he emphasised the similarity between electromagnetic particle traps and the focusing devices used in nuclear and particle physics to confine particles [36]. Paul discussed techniques for trapping particles using both time-varying and static electric fields, as well as using the combination of magnetic and electric fields. This thesis will concentrate on the ion trap which uses electric fields only, and was later given the name 'Paul trap'. In this chapter I will derive the Hamiltonian of an accelerator and introduce the relevant beam dynamics that will be used throughout this thesis. Detailed derivations of the concepts in this chapter can be found in [37, 38]. I will then compare the transverse Hamiltonian of an accelerator to the Hamiltonian of a Paul trap to show their equivalence. Previous work using Paul traps to study accelerator physics is discussed and I also provide an outline of the IBEX Paul trap experiment. A detailed overview of the IBEX experiment and commissioning is given in [39].

2.1 Transverse beam dynamics

2.1.1 Hamiltonian of a particle in an accelerator

An accelerator is designed to give energy to particles by passing the particles through RF cavities with high electric fields. In the case of circular accelerators, particles can make multiple passes through these RF cavities to gain energy. Dipole magnets are used to steer particles around the machine, allowing multiple passes through RF cavities in circular rings. Quadrupole magnets provide transverse focusing forces, confining particles along their orbit. Thus, the charged particles in an accelerator are controlled by electromagnetic forces described by the Lorentz force

$$\frac{d\vec{p}}{dt} = \vec{F} = q(\vec{E} + \vec{v} \times \vec{B}), \tag{2.1}$$

where $\vec{p} = \gamma m\vec{v}$ is the relativistic momentum ($\gamma = 1/\sqrt{1 - v^2/c^2}$) of the particle with mass m. $\vec{F}$ is the force experienced by a particle with charge q, travelling through an electric field $\vec{E}$ and magnetic field $\vec{B}$ with velocity $\vec{v}$. The electric and magnetic fields can be written in terms of the vector potential $\vec{A}$ and the scalar potential Φ as,

$$\vec{E} = -\nabla\Phi - \frac{\partial\vec{A}}{\partial t} \quad \text{and} \quad \vec{B} = \nabla \times \vec{A}. \tag{2.2}$$

Using the vector and scalar potentials, the Lagrangian of the system can be described by,

$$L = -mc^2\sqrt{1 - v^2/c^2} - q\Phi + q\vec{v} \cdot \vec{A}. \tag{2.3}$$

Using the canonical momentum, $\vec{P} = \frac{\partial L}{\partial \vec{v}} = \vec{p} + e\vec{A}$, and Lagrangian of the system, we can express the Hamiltonian, $H = \vec{P} \cdot \vec{v} - L$, of a charged particle in an electromagnetic field as,

$$H = q\Phi + \sqrt{c^2(\vec{P} - q\vec{A})^2 + m^2c^4}, \tag{2.4}$$

where the Hamiltonian, H is also equivalent to the sum of the kinetic and potential energy. In Cartesian coordinates, the equations of motion for the particle in the transverse plane can then be found using Hamilton's equations given by

$$\frac{dx}{dt} = \frac{\partial H}{\partial P_x}, \qquad \frac{dP_x}{dt} = -\frac{\partial H}{\partial x}, \qquad \frac{dy}{dt} = \frac{\partial H}{\partial P_y}, \qquad \frac{dP_y}{dt} = -\frac{\partial H}{\partial y}. \tag{2.5}$$

The equations of motion in the $z-$direction are omitted as this is the direction in which the acceleration of the particle is applied. In this work we assume non-accelerating beams and are thus only concerned with the motion in the transverse plane. Before applying Hamilton's equations to Eq. 2.4, it is useful to first transform from Cartesian coordinates to a coordinate system more natural to that of a particle in an accelerator.

2.1.2 Frenet-Serret coordinates

It is often convenient to describe the particle motion with a co-moving coordinate system that follows the ideal orbit of a particle in a circular accelerator. The ideal orbit traced out by a particle in a circular accelerator is referred to as the reference orbit. A particle is usually confined to within small deviations from this reference orbit.

The Frenet-Serret coordinate system is shown in Fig. 2.1. In this coordinate system $(\hat{x}, \hat{y}, \hat{s})$, s is the path length measured along the reference orbit, $\vec{r_0}(s)$, from an arbitrary initial point. The unit vector $\hat{s}$ is tangent to the reference orbit at any given point and is referred to as the longitudinal direction. The transverse coordinates are described by, $\hat{x}$ which is perpendicular to the tangent vector $\hat{s}$ and lies on the tangential plane, and $\hat{y}$, which is perpendicular to both $\hat{s}$ and $\hat{x}$. The unit vectors are defined as

$$\hat{x}(s) = -\rho(s)\frac{d\hat{s}(s)}{ds}, \qquad \hat{y}(s) = \hat{x}(s) \times \hat{s}(s), \qquad \hat{s}(s) = \frac{d\vec{r_0}(s)}{ds}, \tag{2.6}$$

where $\rho(s)$ is the radius of curvature of the reference orbit. The particle position is then given by $\vec{r}(s) = \vec{r_0}(s) + x\hat{x}(s) + y\hat{y}(s)$.

In the Frenet-Serret coordinate system, the Hamiltonian can be found through a canonical transformation, changing the independent variable from time, t to position, s [37]. The new momenta (p_x, p_y) are defined in Frenet-Serret coordinates as $p_x = \vec{P} \cdot \hat{x}$ and $p_y = \vec{P} \cdot \hat{y}$, where $\vec{P}$ is the canonical momentum in Cartesian coordinates. Expanded to second-order in the momenta, p_x and p_y, for an orbit with a radius of curvature ρ, the Hamiltonian in Eq. 2.4 becomes

$$H \approx -p(1 + \frac{x}{\rho}) + \frac{(1 + x/\rho)}{2p}[(p_x - qA_x)^2 + (p_y - qA_y)^2] - qA_s, \tag{2.7}$$

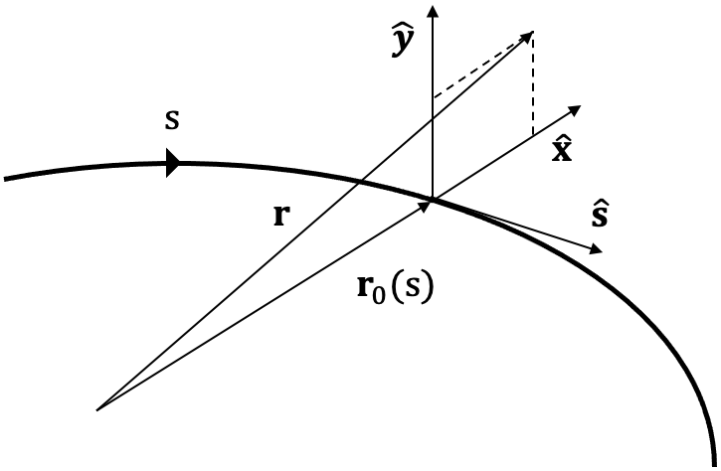

Figure 2.1: The Frenet-Serret coordinate system.

where p is the total momentum, $p = \sqrt{\frac{E^2}{c^2} - m^2c^2}$. The kinetic energy of a particle in general is given by $E = H - q\Phi$. We have assumed no accelerating field, and no space charge, therefore the electrical potential in the above Hamiltonian has been set to zero, $\Phi = 0$. In the case of an accelerator with only transverse focusing and defocusing magnets ($A_x = A_y = 0$), the Hamiltonian can be written as

$$H \approx -p(1 + \frac{x}{\rho}) + \frac{(1 + x/\rho)}{2p}(p_x^2 + p_y^2) - qA_s. \tag{2.8}$$

For accelerators with a large circumference we can use the straight-line approximation, $\rho = \infty$ [1]. Applying this approximation and using the following substitution,

$$\tilde{p}_x = \frac{p_x}{p}, \qquad \tilde{p}_y = \frac{p_y}{p}, \qquad \tilde{H} = \frac{H}{p}, \tag{2.9}$$

the scaled Hamiltonian can be written as

$$\tilde{H} = \frac{1}{2}(\tilde{p}_x^2 + \tilde{p}_y^2) - \frac{q}{p}A_s. \tag{2.10}$$

2.1.3 Multipole-field expansion

In Eq. 2.10, we derived a Hamiltonian in terms of the scaled particle momentum and the magnetic-field component, A_s. Before we use this Hamiltonian to solve Hamilton's

[1] When it comes to dealing with the dynamics of a Paul trap, the assumption of $\rho = \infty$ holds true as the trapping potential acts like a straight line of quadrupoles.

equations, we will first describe the magnetic-field component in terms of the magnetic elements of an accelerator. There are two orientations for accelerator magnets in a beam line, namely 'normal' and 'skew'. An example of both a normal quadrupole and a skew quadrupole configuration is shown in Fig. 2.2, where the skew quadrupole has been rotated (or rolled) by 45° around the magnet's geometrical central axis when compared to the normal quadrupole. In general, the skew magnet is obtained by rotating the normal magnet by $180°/2n$ where n is the order of the magnet. The multipole expansion of the vector potential, $\vec{A}$, for a magnet with $2n$ poles can be expressed in Cartesian coordinates as [18]

$$\vec{A} = \sum_n A_n f_n(x,y) \qquad \text{where,} \quad f_n = (x+iy)^n, \tag{2.11}$$

and A_n are the multipole coefficients. Using the assumption of long magnets where we can ignore the end fields and assuming that the vector potential is parallel to the magnets geometrical central axis (paraxial approximation) then $\vec{A} = (0,0,A_s)$. The real terms of Eq. 2.11 give the normal magnetic components and the imaginary terms represent the skew components. Equation 2.11 is expanded out for normal and skew magnets in Table 2.1. From this table we can see that normal dipoles and quadrupoles keep the transverse motion (x,y) decoupled, however, skew quadrupoles, and higher order magnets will couple the transverse motion (i.e. they contain xy terms). In this thesis we will be concerned with only normal magnets as synchrotrons are almost always constructed using normal dipoles and quadrupoles. However, it should be noted that rotational (roll) misalignment of magnets in accelerators will introduce skew components.

In terms of the magnetic field,

$$\begin{aligned} B_y(y=0) &= -\frac{\partial A_s}{\partial x} = -\sum_{n=1}^{\infty} n A_n x^{n-1} \\ &= -\sum_{n=1}^{\infty} \frac{x^{n-1}}{(n-1)!} \left(\frac{d^{n-1} B_y}{dx^{n-1}} \right)_{x=0;y=0}. \end{aligned} \tag{2.12}$$

Equating Eq. 2.11 and Eq. 2.12 we get the magnetic multipole coefficients,

$$A_n = \frac{1}{n!} \left(\frac{d^{n-1} B_y}{dx^{n-1}} \right)_{x=0;y=0}. \tag{2.13}$$

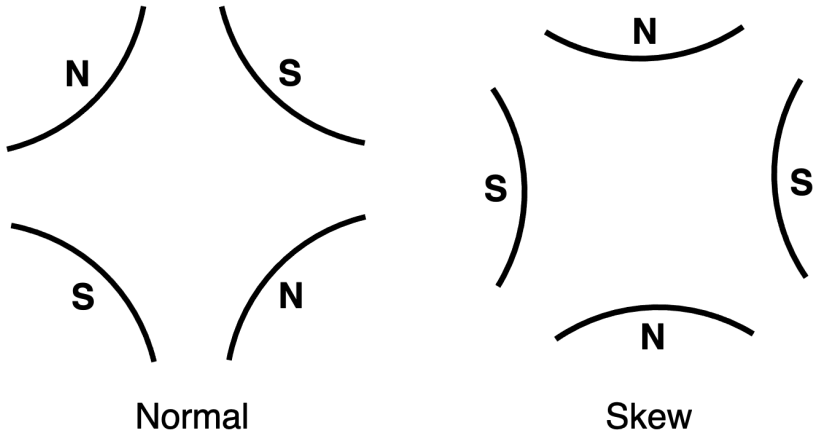

Figure 2.2: Example of the magnetic poles orientation for a Normal quadrupole (Left) and Skew quadrupole (Right).

Table 2.1: Cartesian expansion of the magnetic vector potential, f_n for elements up to 4th order [18].

Multipole	n	Normal f_n	Skew f_n
Dipole	1	x	y
Quadrupole	2	$x^2 - y^2$	$2xy$
Sextupole	3	$x^3 - 3xy^2$	$3x^2y - y^3$
Octupole	4	$x^4 - 6x^2y^2 + y^4$	$4x^3y - 4xy^3$

2.1.4 Hills equation

The Hamiltonian for a straight lattice ($\rho = \infty$), without acceleration and space-charge forces, was obtained in Eq. 2.10. The magnetic multipoles can now be substituted into this Hamiltonian and Hamilton's equations can be solved to give us the equations of motion for a particle. Starting from a lattice with only normal quadrupoles ($n = 2$), the vector potential can be expressed using Eq. 2.13 as

$$\vec{A} = \begin{pmatrix} 0 \\ 0 \\ \frac{1}{2}\left(\frac{\partial B_y}{\partial x}\right)_0 (x^2 - y^2) \end{pmatrix}, \tag{2.14}$$

where the assumption that the quadrupole field is in ideal alignment with the reference orbit is used and hence $A_x = A_y = 0$. The subscript 0 has been used to denote the values of $x = y = 0$, at which the derivative is evaluated. The Hamiltonian for a particle

moving through a single quadrupole is then given by

$$\begin{aligned}\tilde{H} &= \frac{1}{2}\left(\tilde{p}_x^2 + \tilde{p}_y^2\right) - \frac{1}{2}\frac{q}{p}\left(\frac{\partial B_y}{\partial x}\right)_0 \left(x^2 - y^2\right) \\ &= \frac{1}{2}\left(\tilde{p}_x^2 + \tilde{p}_y^2\right) + \frac{K}{2}\left(x^2 - y^2\right),\end{aligned} \tag{2.15}$$

where $K = -\frac{q}{p}\left(\frac{\partial B_y}{\partial x}\right)_0$ is the strength of the quadrupole. In a synchrotron, particles are confined using alternating-gradient focusing which requires a sequence of quadrupoles with alternating polarity. A quadrupole magnet can only focus in one transverse plane, while defocusing in the other plane. The Hamiltonian for an accelerator lattice consisting of an array of quadrupoles is thus described by

$$\tilde{H} = \frac{1}{2}\left(\tilde{p}_x^2 + \tilde{p}_y^2\right) + \frac{K(s)}{2}\left(x^2 - y^2\right), \tag{2.16}$$

where the $K(s)$ is now dependent on the positions, s of quadrupoles around the ring. For particles with no momentum spread ($\Delta p/p_0 = 0$), Hill's equations [40] are found to be

$$\begin{aligned}x'' + K_x(s)x &= 0 \\ y'' + K_y(s)y &= 0.\end{aligned} \tag{2.17}$$

The prime notation (x'') denotes the 2nd derivative with respect to s, and $K_x(s)$ and $K_y(s)$ represent the focusing strength in the horizontal and vertical directions respectively. The simplest arrangement of quadrupoles is referred to as a FODO lattice. In a FODO, the 'F' denotes a focusing quadrupole, the 'O' a drift and the 'D' a defocusing quadrupole. In this case, $K_y(s) = -K_x(s)$.

Imposing periodicity on the focusing over a period of length L, $K(s + L) = K(s)$, the solution to Hill's equations take the form of harmonic oscillations,

$$\begin{aligned}x &= \sqrt{2\beta_x(s)J_x}\cos\left(\phi_x(s) - \phi_0\right) \\ y &= \sqrt{2\beta_y(s)J_y}\cos\left(\phi_y(s) - \phi_0\right).\end{aligned} \tag{2.18}$$

These oscillations around the reference orbit are referred to as betatron oscillations where $\beta(s)$ is the beta function defining the envelope of the oscillations and $\phi(s)$ is the phase advance. The beta function and phase advance are both dependent on the accelerator

lattice and can be related by the following equation,

$$\phi(s) = \int \frac{ds}{\beta(s)}. \tag{2.19}$$

This relation is obtained by substituting the solutions in Eq. 2.18 back into Hill's equations. The action, J, and initial phase, ϕ_0, are determined from the initial conditions of the particle. Transforming from phase space coordinates (z, p_z), to action-angle coordinates (J_z, ϕ_z) can be achieved with the generating function

$$F_1(x, \phi_z) = -\frac{z^2}{2\beta_z}\left(\tan\phi_z - \frac{\beta_z'}{2}\right), \tag{2.20}$$

where $\beta_z' = d\beta_z/ds$ and $z \in x, y$. The action, J_z is a measure of the single-particle amplitude (related to the single-particle emittance in Section 2.1.5) and the phase advance, ϕ_z describes the angle rotated about the origin in phase space.

The tune of the accelerator is defined as the number of betatron oscillations per revolution around a circular accelerator and can be written in terms of the phase advance as $Q = \frac{1}{2\pi}\phi$. Figure 2.3 shows a schematic of the particle motion in one plane, through a series of focusing and defocusing quadrupoles. The beam envelope is marked with the black dashed line and the coloured lines represent the motion of single particles, i.e. betatron motion. Particles that pass straight through the center of a quadrupole have their trajectory unchanged.

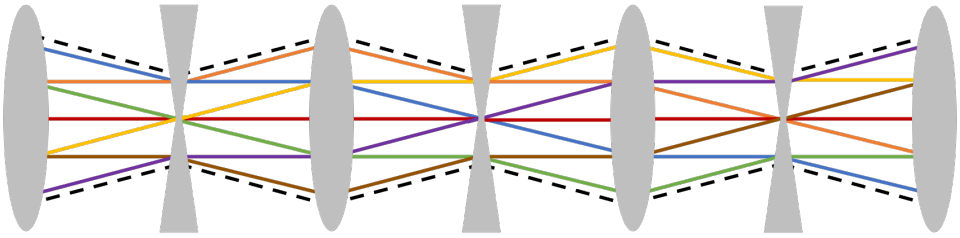

Figure 2.3: Schematic of betatron motion in one plane, through a lattice. The grey 'lenses' represent focusing and defocusing quadrupoles and the black dashed line describes the beam envelope. The solid coloured lines show the single-particle motion of 7 different particles through the lattice.

2.1.5 Courant-Snyder representation

The Courant-Snyder invariant of a single particle can be described by the following equation [41]

$$\beta_z z'^2 + 2\alpha_z z z' + \gamma_z^2 z^2 = \epsilon_z, \tag{2.21}$$

for $z \in x, y$, and where α, β, and γ are referred to as the Twiss parameters and are defined in terms of the beta function, β, as follows:

$$\alpha_z(s) = -\frac{1}{2}\beta_z'(s), \quad \gamma_z(s) = \frac{1 + \alpha_z(s)^2}{\beta_z(s)}. \tag{2.22}$$

Again, the prime notation denotes the derivative with respect to s. Equation 2.21 and the Twiss parameters in Eq. 2.22 are used to match a beam's orientation in phase space to the accelerator lattice. The Courant-Snyder invariant, ϵ, is also known as the single-particle emittance and is related to the action from before by $\epsilon_z = 2J_z$. Figure 2.4 shows a phase space ellipse traced out by a particle with an enclosing area of $\pi\epsilon$. Liouville's theorem states that under conservative forces the area of this phase space ellipse, and hence the particle emittance, is conserved.

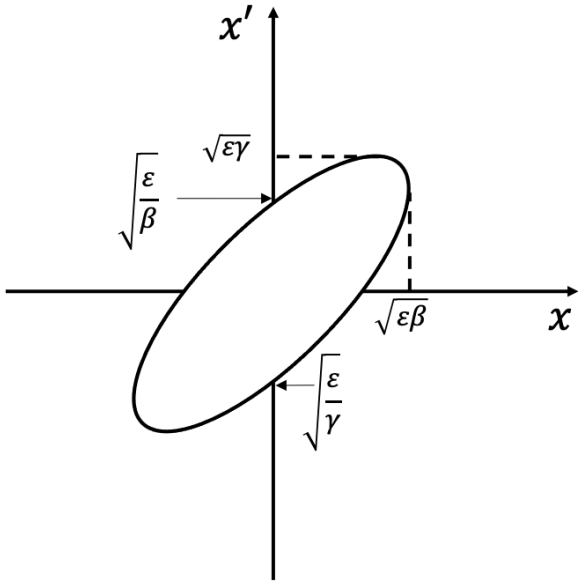

Figure 2.4: Phase space ellipse showing the relation of x and x' to the Twiss parameters.

For particle beams it is often more useful to use a statistical measure of the emittance. There are various definitions of the statistical emittance which describe different fractions

of the beam contained within the phase space ellipse. The main definition that will be used in this thesis is the RMS emittance, as this is the most useful definition for Gaussian beams, which are assumed throughout this work. The RMS emittance is defined as

$$\begin{aligned} \epsilon_{rms} &= \sqrt{\langle z^2 \rangle \langle z'^2 \rangle - \langle z^2 z'^2 \rangle} \\ \langle z^2 \rangle = \beta \epsilon_z, \qquad \langle z'^2 \rangle &= \gamma \epsilon_z, \qquad \langle z^2 z'^2 \rangle = -\alpha \epsilon_z, \end{aligned} \tag{2.23}$$

for $z \in x, y$. The RMS beam size can thus be defined as $\sigma(s)_{rms} = \sqrt{\epsilon_{rms}\beta(s)}$.

2.1.6 Transfer matrices

The solution to Hill's equations can also be written in matrix form where the matrices represent the transformation of the particle's phase space variables from one point in the ring, s_1 to another point s_2,

$$\begin{pmatrix} z(s_2) \\ z'(s_2) \end{pmatrix} = M_{12} \begin{pmatrix} z(s_1) \\ z'(s_1) \end{pmatrix} \tag{2.24}$$

where the general 2×2 linear transfer matrix, M_{12} is given by

$$M_{12} = \begin{pmatrix} \sqrt{\frac{\beta_2}{\beta_1}} \left(\cos\phi_z - \alpha_1 \sin\phi_z\right) & \sqrt{\beta_2 \beta_1} \sin\phi_z \\ \frac{(\alpha_1 - \alpha_2)\cos\phi_x - (\alpha_2\alpha_1 + 1)\sin\phi_z}{\sqrt{\beta_2\beta_1}} & \sqrt{\frac{\beta_1}{\beta_2}} \left(\cos\phi_z + \alpha_2 \sin\phi_z\right) \end{pmatrix}. \tag{2.25}$$

The matrix M_{12} describes a rotation in phase space by an angle ϕ_z, which is the phase advance between the two points in the lattice. The parameters $\alpha_{1,2}$ and $\beta_{1,2}$ denote the Twiss parameters at points 1 and 2 in the lattice, where the z notation has been dropped for clarity. Considering a periodic system, the transfer matrix between two points in a lattice where $\beta_1 = \beta_2 = \beta$ and $\alpha_1 = \alpha_2 = \alpha$, simplifies to

$$M = \begin{pmatrix} \cos\phi_z + \alpha \sin\phi_z & \beta \sin\phi_z \\ -\gamma \sin\phi_z & \cos\phi_z - \alpha \sin\phi_z \end{pmatrix}. \tag{2.26}$$

As accelerators often consist of periodic cells, the simplified matrix form in Eq. 2.26 is useful for particle tracking code. Transfer matrices can be found for individual elements in an accelerator lattice and the total transfer matrix of these elements can be found by multiplying these matrices together. A drift region in a lattice is defined as the space

between magnets where no external forces act upon the beam. The transfer matrix for a drift with length l is found to be

$$M_{drift} = \begin{pmatrix} 1 & l \\ 0 & 1 \end{pmatrix}. \tag{2.27}$$

The transfer matrices for focusing ($K > 0$) and defocusing ($K < 0$) quadrupoles are presented below,

$$\begin{aligned} M_F &= \begin{pmatrix} \cos\sqrt{|K|}l & \frac{1}{\sqrt{|K|}}\sin\sqrt{|K|}l \\ -\sqrt{|K|}\sin\sqrt{|K|}l & \cos\sqrt{|K|}l \end{pmatrix} \\ M_D &= \begin{pmatrix} \cosh\sqrt{|K|}l & \frac{1}{\sqrt{|K|}}\sinh\sqrt{|K|}l \\ \sqrt{|K|}\sinh\sqrt{|K|}l & \cosh\sqrt{|K|}l \end{pmatrix}. \end{aligned} \tag{2.28}$$

In the case of thin quadrupoles, the small angle approximation can be applied to the matrices in Eq. 2.28 to give a thin lens approximation which, for a focusing quadrupole, becomes

$$M_F = \begin{pmatrix} 1 & 0 \\ -Kl & 1 \end{pmatrix}, \tag{2.29}$$

where $Kl = 1/f$, gives the focal length of the quadrupole, f.

2.2 Analogy between accelerators and Paul traps

2.2.1 Transverse dynamics in a Paul trap

Earnshaw's theorem states that a collection of charged particles cannot be confined in all three spatial directions using a static configuration of electric fields [42]. However, a quadrupole ion trap can confine charged particles in a pseudo-potential[2] using a combination of DC (time-independent) and RF (time-dependent) electric fields. The trapping electric potential has the general form in 3D,

$$\begin{aligned} \Phi_{\text{Trap}}(x,y,z;t) =& U\frac{1}{2}\left(ax^2 + by^2 + cz^2\right) \\ &+ V\cos\left(\omega_{\text{rf}}t\right)\frac{1}{2}\left(\lambda x^2 + \sigma y^2 + \gamma z^2\right) \end{aligned} \tag{2.30}$$

[2] A pseudo-potential is an average confining force created by time-varying electric fields.

where U and V are the voltage amplitudes for the DC and radio-frequency (RF) potentials respectively. The x and y coordinates define the transverse plane and the z coordinate defines the longitudinal direction. A schematic of a quadrupole ion trap is shown in Fig. 2.5. The RF frequency is given by ω_{rf} and a, b, c, λ, σ and γ are geometrical factors. In order for Eq. 2.30 to be a realisable potential, it must satisfy the Laplace equation, $\nabla^2 \Phi_{\mathrm{Trap}} = 0$. This leads to the following conditions for the geometrical factors

$$\begin{aligned} a + b + c &= 0, \\ \lambda + \sigma + \gamma &= 0. \end{aligned} \tag{2.31}$$

One choice for the geometrical factors is $a = b = c = 0$ and $\lambda + \sigma = -\gamma$. From the potential in Eq. 2.30 we can see that the first term would be zero and the potential would require trapping using entirely RF voltages [43].

A second solution is $-(a + b) = c > 0$ and $\lambda = -\sigma$, where $\gamma = 0$. This requires RF confinement in the x-y plane, and a static potential well in the z direction which confines ions longitudinally. This trapping technique is referred to as a linear Paul trap and is the trapping configuration which is used in this work.

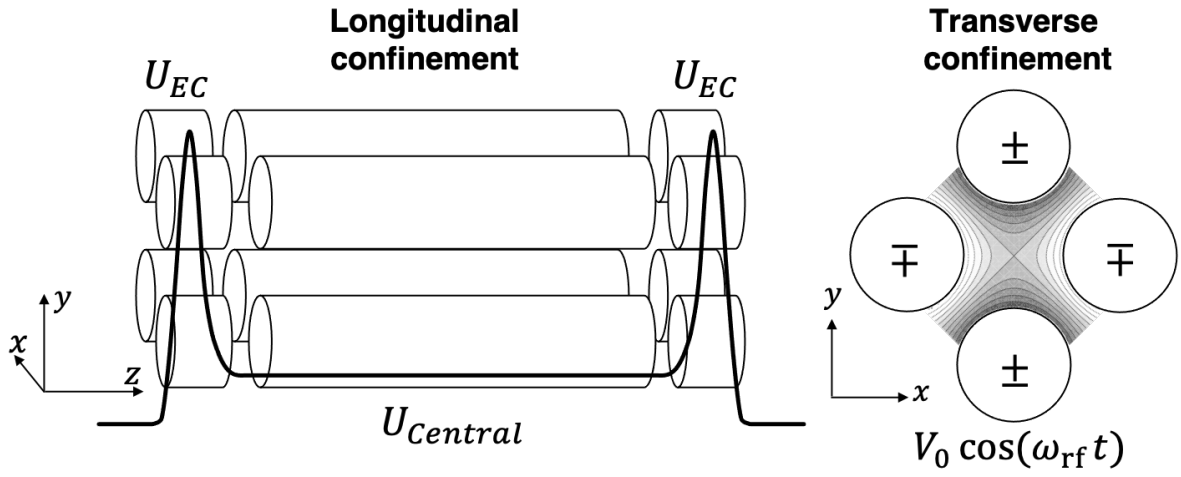

Figure 2.5: Schematic diagram of a Linear Paul trap. (Left) DC voltages create a potential well to longitudinally confine ions. (Right) RF voltages create a pseudo-potential to confine ions transversely.

Ignoring the longitudinal direction, z, for a linear Paul trap consisting of four electrodes (see Fig. 2.5), with an electrode inscribed radius of r_0, the transverse potential

becomes

$$\Phi_{\text{Trap}}\left(x, y; t\right) = \frac{V_0 \cos\left(\omega_{\text{rf}} t\right)}{r_0^2}\left(x^2 - y^2\right). \tag{2.32}$$

This pseudo-potential used for transverse confinement of ions in a Paul trap is analogous to the alternating-gradient focusing of quadrupoles, as derived in Eq. 2.16, used to confine particles in an accelerator. In the next section we will see the equivalence between the Hamiltonian of a particle in an accelerator and that of a particle in a Paul trap.

2.2.1.1 Hamiltonian of a Paul trap

The Hamiltonian of a charged particle in an electromagnetic field was derived in Eq. 2.4. For a non-relativistic particle in the presence of electromagnetic fields, this can be simplified to

$$H = q\Phi + \frac{(\vec{P} - q\vec{A})^2}{2m}. \tag{2.33}$$

As the Paul trap uses only electric fields, the magnetic vector potential can be set to zero ($\vec{A} = 0$). Substituting in the transverse electric field potential in Eq. 2.32, the Hamiltonian for a particle of charge q and mass m in a Paul trap can be expressed as

$$H_{\text{Paul}} = \frac{(p_x^2 + p_y^2)}{2m} + qV_Q(t)\frac{(x^2 - y^2)}{r_0^2} + q\phi_{\text{sc}}, \tag{2.34}$$

where $V_Q(t)$ is the time-varying amplitude of the quadrupole potential and ϕ_{sc} is the potential due to space-charge forces created by other particles.

Applying the following transformations,

$$\frac{H_{\text{Paul}}}{mc^2} \rightarrow \hat{H}_{\text{Paul}}, \quad \frac{p_x}{mc} \rightarrow \hat{p}_x, \quad \frac{p_y}{mc} \rightarrow \hat{p}_y, \tag{2.35}$$

where the Hamiltonian and canonical momenta are made dimensionless, and also changing the independent variable from time t, to length $\tau = ct$, the Hamiltonian becomes

$$\hat{H}_{\text{Paul}} = \frac{(\hat{p}_x^2 + \hat{p}_y^2)}{2} + \frac{1}{2}K_p(\tau)\left(x^2 - y^2\right) + \frac{q}{mc^2}\phi_{\text{sc}}. \tag{2.36}$$

The quadrupole focusing strength is defined as

$$K_p(\tau) = \frac{2qV_Q(\tau)}{mc^2 r_0^2}, \tag{2.37}$$

which can be equated to the quadrupole focusing strength of an accelerator in the following way

$$K = \frac{q}{p}\left(\frac{\partial B_y}{\partial x}\right)_0 = \frac{2qV_Q(\tau)}{mc^2 r_0^2}. \tag{2.38}$$

A Paul trap can thus act as an analog simulation of the transverse focusing in particle accelerators. The quadrupole strength can be calculated using Eq. 2.38 and the voltage waveform applied to the trap electrodes defines the structure of the accelerator lattice. The coordinate transformation from time t to a distance $\tau = ct$ is analogous to a change in reference frame to that of the particle bunch. Throughout this thesis the velocity of this bunch is assumed to be the speed of light, c. Due to this transformation, traditional accelerator software such as MAD-X [44] can be used to design lattices to confine particles in Paul traps.

2.2.2 Amplitude-dependent tune shift in a Paul trap

As octupoles are an important part of this work, in this section we will derive the amplitude-dependent tune shift caused by an octupole potential. The Hamiltonian of a single particle in a Paul trap can be extended to include an octupole potential,

$$\hat{H}_{\text{Paul}} = \frac{1}{2}(\hat{p}_x^2 + \hat{p}_y^2) + \frac{1}{2}K_2(\tau)\left(x^2 - y^2\right) + \frac{1}{4}K_4(\tau)\left(x^4 - 6x^2y^2 + y^4\right), \tag{2.39}$$

where we are neglecting space-charge forces for the time being and have defined the quadrupole focusing strength as $K_2(\tau)$ and the octupole strength as $K_4(\tau)$. Although this derivation is using the Hamiltonian of a particle in a Paul trap, it also holds true for an accelerator where $K_2(s)$ and $K_4(s)$ would be used as the $s-$dependent focusing terms of the quadrupole and octupole magnets respectively.

Canonical perturbation theory can be used to study the effects of introducing the nonlinear octupole potential [38], where we treat the Hamiltonian as $\hat{H}_0 + \hat{H}_p$ where $\hat{H}_p$ is a perturbation to the linear Hamiltonian. The part of the Hamiltonian which arises from the introduction of the octupole field is the following

$$\hat{H}_4 = \frac{K_4(\tau)}{4}\left(x^4 - 6x^2y^2 + y^4\right), \tag{2.40}$$

which we will treat as a perturbation to the linear Hamiltonian. Following the derivation of the amplitude-dependent tune shift in the presence of an octupolar field in [45], the tune shift can be obtained by averaging the perturbation Hamiltonian over all phase space variables and computing the integrals,

$$\Delta Q_{x,y} = \frac{1}{2\pi} \oint \frac{\partial}{\partial J_{x,y}} \left\langle \hat{H}_p \right\rangle d\tau, \tag{2.41}$$

where $J_{x,y}$ is the particle's horizontal and vertical action. Substituting action-angle coordinates, $x(\tau) = \sqrt{2J_x\beta_x(\tau)}\cos\phi_x$ and $y(\tau) = \sqrt{2J_y\beta_y(\tau)}\cos\phi_y$ into Eq. 2.40 we can describe the perturbation Hamiltonian in terms of action as,

$$\hat{H}_4 = \frac{K_4(\tau)}{4}\left(4J_x^2\beta_x^2(\tau)\cos^4\phi_x - 24J_xJ_y\beta_x(\tau)\beta_y(\tau)\cos^2\phi_x\cos^2\phi_y + 4J_y^2\beta_y^2(\tau)\cos^4\phi_y\right). \tag{2.42}$$

Averaging Eq. 2.42 over all phase space variables and using $\langle\cos^2\phi\rangle = \int_0^{2\pi}\cos^2\phi\, d\phi = 1/2$ and $\langle\cos^4\phi\rangle = \int_0^{2\pi}\cos^4\phi\, d\phi = 3/8$ we obtain,

$$\langle\hat{H}_4\rangle = \frac{K_4(\tau)}{4}\left(\frac{3}{2}J_x^2\beta_x^2(\tau) - 6J_xJ_y\beta_x(\tau)\beta_y(\tau) + \frac{3}{2}J_y^2\beta_y^2(\tau)\right). \tag{2.43}$$

Taking the partial derivative of Eq. 2.43 with respect to J_x,

$$\frac{\partial}{\partial J_x}\left\langle\hat{H}_4\right\rangle = \frac{K_4(\tau)}{4}(3J_x\beta_x^2(\tau) - 6J_y\beta_x(\tau)\beta_y(\tau)), \tag{2.44}$$

and substituting Eq. 2.44 into Eq. 2.41, the horizontal tune shift is found to be

$$\Delta Q_x = \frac{3}{8\pi}\oint K_4(\tau)(\beta_x^2(\tau)J_x - 2\beta_x(\tau)\beta_y(\tau)J_y)d\tau. \tag{2.45}$$

Assuming the beta function and octupole strength are constant over the time for which the octupole potential is applied[3], the tune shift can be simplified to

$$\Delta Q_x = \frac{3k_4}{8\pi}(\beta_x^2J_x - 2\beta_x\beta_yJ_y), \tag{2.46}$$

$$\Delta Q_y = \frac{3k_4}{8\pi}(\beta_y^2J_y - 2\beta_y\beta_xJ_x), \tag{2.47}$$

[3]Note that this is not the case for a long octupole insert in QIO as both the beta function and octupole strength vary.

where k_4 is the integrated octupole strength. From Eq. 2.46 and Eq. 2.47 it is clear that the tune shift is proportional to the action, J of the particle and hence there is an amplitude-dependent tune shift in the presence of an octupole field. As there are a range of particle amplitudes in any realistic particle distribution, the introduction of an octupole field will therefore introduce a tune spread equal to ΔQ_{max}, where ΔQ_{max} is the tune shift achieved by the particle with the largest amplitude.

2.3 Paul traps for accelerator physics: previous work

A Paul trap can replicate the transverse confinement of ions in particle accelerators using electric fields, resulting in low energy ($<$ 1eV) confined ions. This means that, unlike in high-energy accelerators, losing particles in a Paul trap will not damage or activate components. Also, due to the low energy of the ions, from Eq. 1.3, space-charge forces will be much larger than for accelerators with high-velocity particles. This makes a Paul trap a useful tool for beam loss and resonance studies, particularly for high space charge beams. In addition, Paul traps have the potential to study space-charge mitigation techniques such as nonlinear integrable optics.

Changing the intensity of beams in accelerators and varying the lattice design are often difficult. However, in a Paul trap, different accelerator lattices can be tested, without modifications of the hardware, by simply varying the amplitude and time structure of the applied electrode voltage $V_Q(\tau)$. Space-charge effects can also be studied by varying the number of ions stored in the trap. The number of ions stored can be varied from $\sim 10^3$ – 10^7, replicating space-charge tune depressions of $Q/Q_0 = 1 \rightarrow 0.85$.

Simulation tools are a vital part of the design process for accelerators but replicating the beam dynamics of intense beams with high space charge is computationally intensive and cannot fully replace experimental verification. Thus, Paul traps offer a way to simulate the transverse dynamics in accelerators in a fraction of the time compared to computer modelling and without the granularity of time steps, macro-particles or grid sizes. For example, a FODO lattice can be created with a 1 MHz RF sine wave in a

Paul trap, meaning it can simulate 1,000,000 FODO cells in $\sim 1\,\mathrm{s}$. Depending on the simulation code, number of particles tracked, and inclusion of space-charge forces, this could take anywhere between a few seconds to multiple days for a computer simulation. Paul traps also offer more flexibility with respect to lattice design and intensity and can be built and operated for significantly less cost than accelerators. For example, the Integrable Optics Test Accelerator (IOTA) at Fermilab is a compact ring and has an estimated project cost of \$20 M [46]. In comparison, the original IBEX Paul trap cost around £100 k to build.

As with all models, Paul traps have their limitations when replicating the particle dynamics in accelerators. Due to the Paul trap using electric fields instead of magnetic fields to confine particles, the focusing is independent of momentum. Therefore, the trap cannot be used to simulate momentum-dependent effects such as dispersion and chromaticity. However, this can also be seen as a benefit as it can simplify experimental beam-dynamics studies and isolate the transverse effects. The benefits of using Paul traps to study accelerator physics have led to a number of traps being built for this purpose which are discussed in more detail below.

2.3.1 The Paul Trap Simulator Experiment (PTSX)

The Paul Trap Simulator Experiment (PTSX) [47–49] was constructed at the Princeton plasma physics laboratory in 2001, with the goal of studying beam mismatch, envelope instabilities, mechanisms for emittance growth and the production of halo particles [47]. A 2 m long trap was created with four cylinder-segment electrodes at an inscribed radius of 0.1 m. This required a peak applied voltage of $V_0 = 235\,\mathrm{V}$ at an RF frequency of $\omega_{\mathrm{rf}} = 75\,\mathrm{kHz}$ in order to trap Cs^+ ions [48].

PTSX has been used to study random noise-induced beam degradation in high-intensity accelerators caused by machine imperfections in the quadrupole focusing system [50]. In this article, the small errors in quadrupole focusing were emulated by adding small random noise on the voltage waveform applied to the electrodes. These studies are

useful because they help us understand the effects of current fluctuations in quadrupole magnets. It was found that the transverse emittance increased almost linearly with the duration of the noise and produced a non-thermal tail of trapped ions. This work was also extended to study halo-particle production and adiabatic transverse bunch compression [51].

PTSX has also successfully excited dipole and quadrupole collective modes using perturbations applied to electrodes to study the effect of magnet errors on collective processes in intense beams [52]. In 2013, Chung also proposed that PTSX could be used to experimentally study continuously rotating quadrupole focusing channels [53].

2.3.2 Simulator for Particle Orbit Dynamics (S-POD)

Okamoto of Hiroshima University and Tanaka of Kyoto University proposed in 1999 to use either an RF quadrupole trap or solenoidal magnetic confinement trap to study halo formation in charged-particle beams [31]. A design for an RF quadrupole trap was explored in further detail in 2002 [32] before settling upon a much smaller trap design compared to PTSX [54]. A smaller trap requires lower voltages and higher frequency RF in order to trap particles of the same charge-to-mass ratio. As there is a limit to the length of time that ions can survive in a Paul trap, higher frequencies can be advantageous as they can replicate longer accelerator lattices in a given amount of time [55]. However, the benefit of larger traps is that they are able to confine more ions, leading to the need for less sensitive detectors.

The linear Paul trap that was eventually built at Hiroshima University, the Simulator for Particle Orbit Dynamics (S-POD), consists of four cylindrical rod electrodes with radius $\rho_0 = 5.75\,\mathrm{mm}$ and an inscribed radius $r_0 = 5\,\mathrm{mm}$. These dimensions were chosen to minimise unwanted nonlinearities in the quadrupole field [32] and required voltages of $< 150\,\mathrm{V}$ applied at RF frequencies of $\omega_{\mathrm{rf}} \sim 1\,\mathrm{MHz}$. The length of the central rod electrodes was 50 mm.

S-POD was initially designed to store Ca^+ ions as they can be laser cooled using semiconductor lasers in the visible spectrum [54]. Cooling the ions allows for the possibility of larger space-charge forces by decreasing the emittance. In 2010, Ca^+ ions were trapped in S-POD and laser cooled to temperatures close to absolute zero ($\sim 0.54\,\mathrm{mK}$) to create a Coulomb crystal [56]. The Coulomb crystal was imaged using the fluorescence of the ions. The Hiroshima group later optimised their setup to trap larger densities of Ca^+ ions for ultrahigh-density beam dynamics experiments [57].

Due to $^{40}Ca^+$ and $^{40}Ar^+$ ions having the same mass-to-charge ratio ($m_{Ca}/m_{Ar} = 40.078/39.948$), S-POD can also trap argon ions without changing the trapping setup. S-POD has been used to study the effects of quadrupole focusing field fluctuations on the stability of intense hadron beams [58] as well as to study resonance crossings in the Fixed-Field Accelerator (FFA), EMMA [59,60]. This work formed a collaboration between the Hiroshima group and the Intense Beams group at the Rutherford Appleton Laboratories. Lucy Martin, a PhD student from the Intense beams group, visited Hiroshima University to study coherent and incoherent resonances with S-POD [61]. Her work scanned over lattice tunes between 0.1 - 0.4, at eight different intensities. The resonances were studied at various space-charge tune shifts and the C_m coherent factors (see Section 1.2.2.1) were measured and found to differ from theoretical values.

Four S-POD traps have now been constructed by the Hiroshima group. The most recent trap (S-POD IV) is a compact ion trap that is designed to study the space-charge effects in drift-tube linear accelerators [62]. This trap has the same electrode dimensions and inscribed radius as previous S-POD traps, however the central rod electrode length is just 8.9 mm. This allows for short bunches where the synchrotron tune (the number of oscillations particles make in the longitudinal direction) is comparable to the betatron tune to be studied. Most recently S-POD IV was used to study various betatron and synchro-betatron resonance stop bands in high-intensity short hadron bunches [63].

2.3.3 The Intense Beams Experiment (IBEX)

The Intense Beams Experiment (IBEX) was designed and assembled at RAL in 2016 [64], with the first ions trapped in 2017 [34]. A similar design to the S-POD trap was chosen with the main difference being the central trapping rods in IBEX were chosen to be 50 % longer. This came with the advantage of being able to store more ions in the trap, requiring less sensitive detectors. Although a longer trap design comes at the cost of replicating smaller space-charge tune shifts for a given number of stored particles.

The IBEX trap was commissioned by PhD student Lucy Martin and was used to study the 1/4 integer resonance at both equal and unequal transverse tunes [39]. A future goal of IBEX was an upgrade to study Quasi-Integrable Optics (QIO) [65]. Ions were successfully trapped in a linear T-insert lattice in 2019 and it was shown that a QI lattice could be created with realistic trap voltages [39].

During my PhD I have taken on the task of upgrading the IBEX trap to allow for the creation of octupole fields to test QIO [66, 67]. The design and commissioning of the new IBEX trap is detailed in Chapter 4. I will first give an overview of the original IBEX trap in Section 2.4.

2.4 Original IBEX experimental setup

The original IBEX Paul trap (IBEX-1) consisted of four stainless steel cylindrical rods which had a time-varying electric potential $V(\tau)$ applied to them to create transverse confinement of ions. The peak-to-peak voltage applied to the rods was on the order of $60 - 180\,\mathrm{V}$ to store $^{40}Ar^{+}$. The trap also had four smaller cylinders on either side of the central rods, which are referred to as the end caps, which were used to confine ions longitudinally.

Figure 2.6 shows a schematic of the linear IBEX Paul trap. The trap electrodes had a radius of $\rho_0 = 5.75\,\mathrm{mm}$ and an inscribed radius $r_0 = 5\,\mathrm{mm}$, the same as the S-POD trap [32]. The trap electrodes were machined to within a tolerance of 10 µm and aligned within tolerances of 50 µm [39]. Opposite electrodes had the same polarity, whereas

adjacent electrodes had opposite polarities. A DC voltage bias of 25 V was applied to the end cap electrodes to provide longitudinal confinement of ions. The central rods also had a DC bias of around 10 V to aid the extraction of ions. Ions were stored in the trap for the desired amount of time, at which point one of the end cap voltages was dropped to 0 V and the ions were extracted onto either a Faraday cup or Micro-Channel Plate (MCP) detector. Figure 2.7 shows a CAD model of the linear IBEX trap with labelled components and Fig. 2.8 shows the assembled trap.

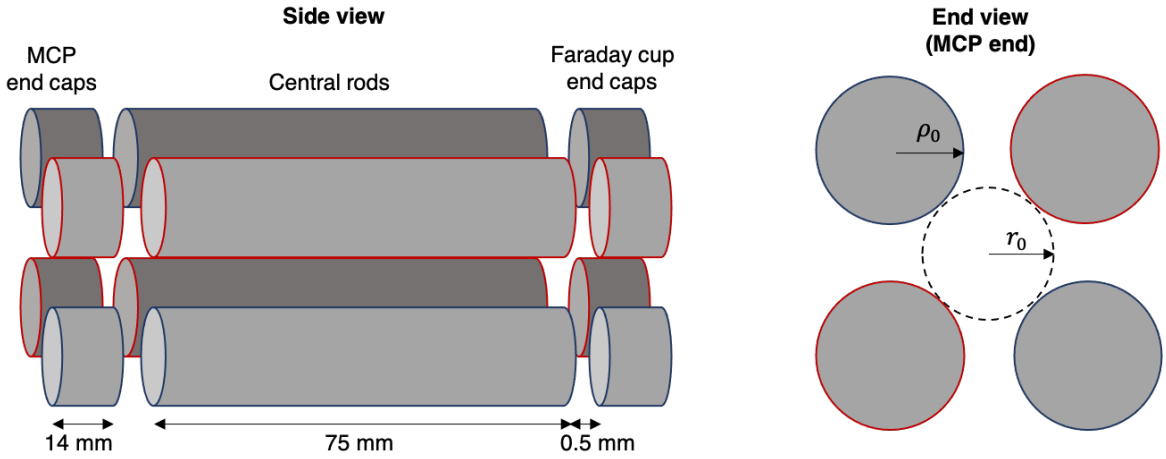

Figure 2.6: Schematic of the original IBEX Paul trap. Red outlined electrodes have a voltage of $+V$ at $t = 0$, whereas blue outlined electrodes have a voltage of $-V$ at $t = 0$.

Ionisation: The IBEX trap is situated in a custom-built, multi-port, vacuum vessel under ultra-high vacuum on the order of 1×10^{-10} mbar. To achieve this level of vacuum an Edwards nXDS10i scroll pump and an Oerlikon Leybold Turbovac 450iX turbopump are used. While the trap is pumping down, to achieve ultra-high vacuum, the vessel is baked out at $\sim$ 130°C for 2-3 days to outgas components. It is important to reach an ultra-high vacuum to avoid the trapped ions colliding with residual gasses within the vacuum vessel.

Argon gas is introduced into the vessel using a VAT Series 59 variable leak valve to pressures within the range of 4.0×10^{-9} mbar to 3.0×10^{-7} mbar. This range in argon gas pressure corresponds to an ion mean-free-path between $\sim$ 20 km and 250 m. Before the argon gas is leaked into the vessel, the gas line is purged using a second Edwards nXDS10i

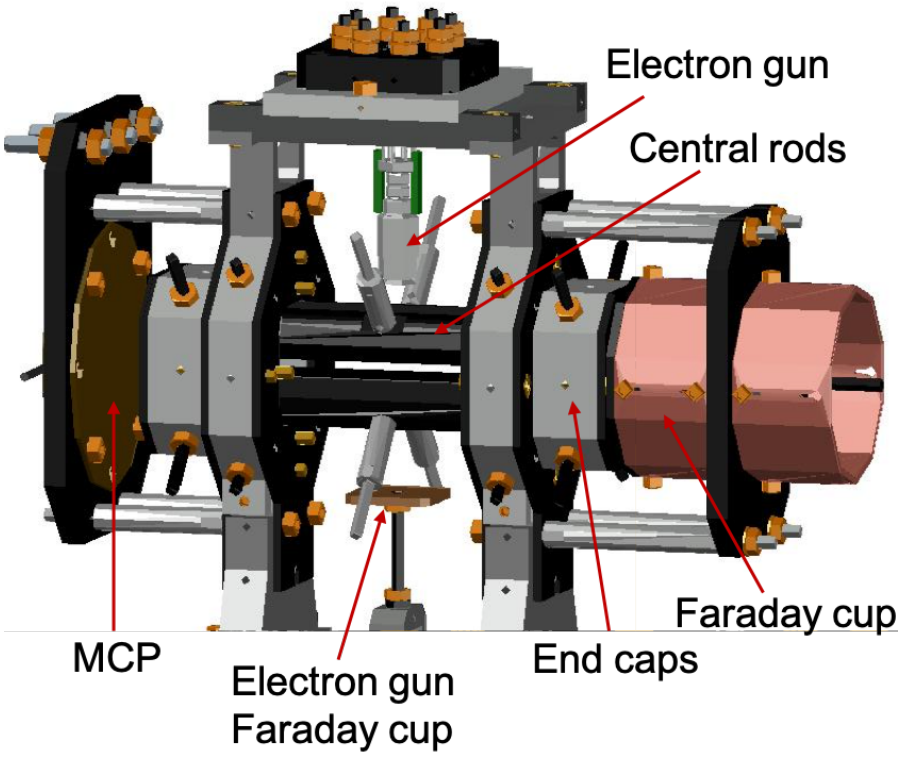

Figure 2.7: CAD model of the original linear IBEX trap.

scroll pump to ensure a high purity of argon gas. An electron gun is used to singly ionise the argon gas while the RF voltage is applied to the electrodes, trapping $^{40}Ar^{+}$. Note that a small fraction will be doubly ionised but due to their larger charge-to-mass ratio, they will not be confined in the trap. The electron gun can produce a 400 eV electron beam with currents between 10 µA and 100 µA depending on the applied filament current and grid voltages. Typically the electron-gun filament current is $\sim$ 14 mA and produces an electron beam with an expected beam diameter between 3 mm and 5 mm depending again on grid voltages. The electron gun beam energy and filament current were kept constant throughout this work, although in the future they could be exploited to help vary the number of ions created in the trap.

Trapping: The voltage waveform applied to the electrodes was supplied using a four-channel WW1074 Tabor Electronics Arbitrary Waveform Generator (AWG) which outputs up to $\pm$5 V. Waveforms were supplied to the AWG from Python-generated .csv files and loaded using a LabView control system. The output voltage from the AWG was

then amplified ×50 using high-voltage (HV) high-slew-rate amplifiers. On the inside of the vessel, voltages were carried to the electrodes using kapton-coated, ultra-high vacuum wire. For one set of end caps, two Falco Systems WMA-300 amplifiers were used, where the other end caps had a fixed DC voltage applied using a low-voltage power-supply. The voltage applied to the central rods was amplified using two custom-built HV amplifiers which used a PA98 APEX operational amplifier [39, 68]. Voltages were monitored after amplification using 10:1 passive Teledyne LeCroy scope probes connected to a Teledyne LeCroy HDO4024A oscilloscope.

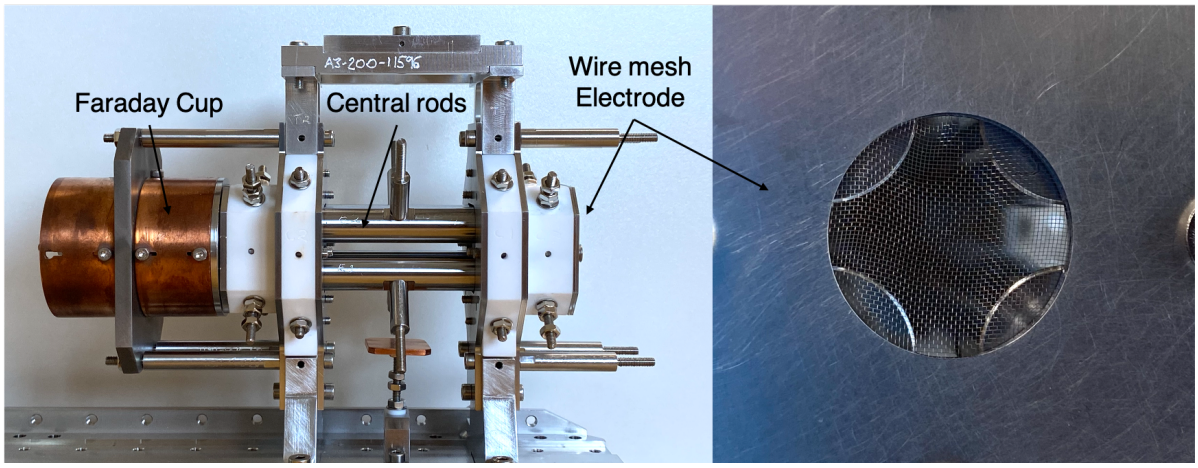

Figure 2.8: (Left) Original IBEX assembly. (Right) Wire mesh electrode.

Detection: To detect ions, the DC voltage on one set of end caps was dropped to 0 V and ions were detected destructively on one of two detectors. The positive DC of 10 V, applied to the central rods, aids extraction onto the detector. This acceleration voltage was kept constant throughout this thesis. A grounded, fine-wire mesh electrode was located between the end caps and MCP detector for electrostatic shielding as well as for focusing ions onto the detector. The mesh electrode, pictured in Fig. 2.8, shielded the electrodes from the large bias voltages applied to the MCP. The fine mesh was woven from 0.0254 mm tungsten wire and had open-area ratio of 0.8. From this ratio of open area to wire mesh, it is therefore estimated that around 80 % of ions released from the trap made it to the detector.

An additional copper Faraday-cup plate sat under the central electrodes, below the electron gun. This Faraday-cup plate allowed for measurements of the electron-gun current for diagnostic purposes.

The Faraday-cup detector was essentially a copper plate, which neutralised incident ions that collided with it, gaining a small net charge as a result. The current resulting from this charge was then amplified by a transimpedance amplifier through a resistance of $2.80 \times 10^6\ \Omega$ and the detector was sensitive to roughly $>1 \times 10^6$ ions.

The second detector was a Micro-Channel Plate (MCP) detector (see Fig. 2.9). This was made of multiple micrometer-thick glass capillaries (channels) that were tilted off axis, embedded into a plate made from Inconel (a nickel-chromium-based alloy). When an incident ion collided with the channel wall, it created a cascade of electrons which were accelerated down the channel with a voltage, $V = U_{\mathrm{OUT}} - U_{\mathrm{IN}}$. This amplified the signal of ions, depending on the voltage bias across the plate. IBEX had a two-stage Hamamatsu P43 phosphor MCP [69] with a GLASSMAN high-voltage supply connected to one plate and a Trek model 677B high-voltage supply connected to the other plate. These two power supplies were used to create the potential difference across the MCP. A phosphor screen sat behind the MCP and could be used to convert the output signal of the MCP into a visible image. A CCD camera was aligned with the phosphor screen, outside the vacuum vessel, behind a glass port. This camera could be used to image the ion distribution from capturing the light from the fluorescing phosphor screen.

The phosphor screen could also be used in a similar manner to a Faraday-cup plate where the amplified electron signal could be read out and converted to an ion number through calibration with the Faraday cup. This was achievable due to an aluminium film or an indium-tin oxide (ITO) transparent conductive film layer applied to the phosphor screen [69]. The signal from the phosphor screen was further amplified with a gain of 5.74×10^6 [39].

Timings and control: IBEX was controlled using a LabView controls system created by Peter Griffin-Hicks [70]. A National Instruments BNC-2121 timings card was

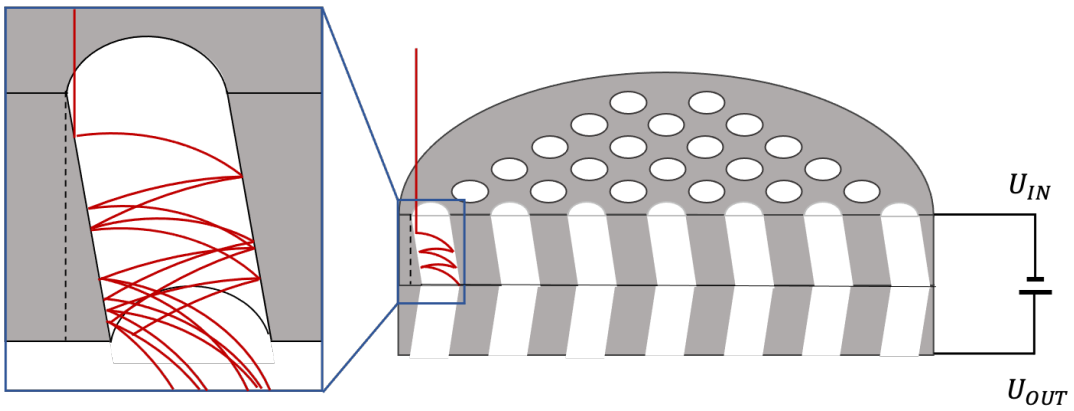

Figure 2.9: Schematic of Micro-Channel Plate (MCP) detector.

used to create the TTL signals used to switch the electron gun on and off, changing the applied waveform to the trap electrodes and switch on the HV supply to the MCP before ion extraction. The timings for a typical experiment are shown in Fig. 2.10. The MCP could not be turned on continuously as the power supplies were connected through the capacitance of the MCP. If both power supplies were on continuously for long periods of time, the wrong voltage bias could be applied across the MCP [39]. The MCP HV had to be turned on 50 ms before the extraction to allow for the voltage to stabilise.

	Ionisation (300 ms)	Stabilisation (50 ms)	Ramp of tune/ Matching (0.1 ms)	Storage (50 ms)	Extraction (2 ms)	Reset (700 ms)
Electron gun	ON	OFF	OFF	OFF	OFF	OFF
Central rods	ON	ON	Change of applied waveform	ON	ON	OFF
MCP end caps	ON	ON	Change of applied waveform	ON	ON (DC offset removed)	OFF
FC end caps	ON	ON	ON	ON	ON	ON
MCP HV	OFF	OFF	OFF	ON	ON	OFF

0 300 350 350.1 400.1 402.1 1102.1

Time (ms)

Figure 2.10: Timings chart of a typical IBEX experiment in the original trap. Recreated from [39].

2.5 Chapter summary

In this chapter the Hamiltonian of a particle in an accelerator was derived and Hamilton's equations were solved to give the equations of motion. The relevant transverse beam

dynamics theory and concepts which are used throughout the rest of this thesis were also laid out. The transverse Hamiltonian of a particle in an accelerator and particle in a Paul trap were shown to be equivalent and the relation between quadrupole strength and voltage was derived. Due to the equivalence of Hamiltonians, Paul traps can be used to model the transverse dynamics in alternating-gradient accelerators.

Other Paul traps such as PTSX and S-POD, also designed to study accelerator physics, were briefly discussed before giving an overview of the original IBEX experimental setup of IBEX-1. IBEX allows for rapid and automated experiments to be run which can model space-charge-dominated beams in a fraction of the time it would take computer simulations.

In the next chapter the theory of nonlinear integrable optics is presented along with the lattice design work to test this concept experimentally in IBEX. The desire to upgrade the IBEX linear Paul trap to a multipole trap, in order to test integrable optics, has been an over-arching goal of the Intense Beams group at RAL since its inception [64, 71].

Chapter 3

Nonlinear Integrable Optics

Accelerators are designed with the underpinning assumption of a linear lattice. A linear lattice consists of elements such as dipoles (order $n = 1$) and quadrupoles (order $n = 2$) which have a transverse force proportional to the particle displacement, x and y. In general, the transverse force of the magnet is proportional to $x^{(n-1)}$ and so for higher order magnets ($n > 2$), the transverse force is not linear over the particle displacement. Assuming perfect magnet alignment and no field errors, the Hamiltonian of a single particle through a linear lattice can be separated into two invariants of motion (the horizontal and vertical Hamiltonian). As stated by the Liouville-Arnold theorem, if a system has as many invariants of motion as degrees of freedom, it is integrable [72]. Therefore, a linear lattice is integrable in 2D, meaning particles exhibit uncoupled, non-chaotic motion and have an infinite dynamic aperture. In reality, the elements of a linear lattice will not be aligned perfectly and the individual magnets will also have some field errors and nonlinearities. As more particles are introduced into the system, space-charge forces also introduce nonlinearities. These nonlinearities can drive resonances in realistic linear lattices, which leads to unstable motion and emittance growth.

Nonlinear elements such as sextupoles and octupoles can be added to lattices to try and correct for these nonlinearities. A quadrupole magnet's focusing strength is dependent on the particle momentum. Therefore, a particle beam with a momentum deviation ($\Delta p/p_0$) will lead to particles with a higher momentum ($p > p_0$) having a longer focal length, analogous to chromatic aberrations in optical lenses. This effect is

referred to as chromaticity in accelerators and can be corrected using sextupoles which have a transverse force proportional to x^2. This nonlinear dependence of the focusing strength on the particle amplitude results in a focusing compensation for off-momentum particles, thus correcting their betatron frequencies.

Octupoles have a transverse force proportional to x^3 which creates an amplitude-dependent tune shift (see Section 2.2.2). Octupole magnets are also included in high-intensity machines to damp collective instabilities such as coherent resonances through Landau damping [26–28]. However, nonlinear elements can also drive resonances and lead to a reduction in dynamic aperture. In these cases, nonlinear magnet strengths are often kept to a minimum in an attempt to stay close to an integrable, linear system [73].

The theory however, does not dictate that only linear lattices can be integrable. The desire to keep accelerator lattices close to linear historically comes from a place of simplicity and familiarity [73]. Thus, the idea of Nonlinear Integrable Optics (NIO) aims to find a way of incorporating nonlinear elements into a lattice, whilst maintaining integrability. Therefore, a nonlinear integrable lattice would have the benefits of the nonlinear element (i.e. chromaticity correction or Landau damping), without driving the resonances associated with that element and thus maintaining a large dynamic aperture.

In this chapter I outline the theory of NIO laid out by Danilov and Nagaitsev in 2010 [29]. I then detail the design work of the T-insert lattice and octupole insert strength to allow for the investigation of Quasi-Integrable optics in the IBEX Paul trap. I also give an overview of work being done in the field of NIO to contextualise my own work on this subject.

3.1 Theory of Nonlinear Integrable Optics

3.1.1 Hamiltonian of a linear lattice

For a system of N degrees of freedom, N invariants of motion are required for the system to be integrable. In terms of accelerators, an integrable system means that particles exhibit bounded, non-chaotic motion. For an ideal accelerator lattice built from linear

components such as dipoles and quadrupoles, this is indeed the case. The Hamiltonian for a single particle through a lattice with equal focusing quadrupoles in the transverse planes is given by

$$H = \frac{1}{2}\left(p_x^2 + p_y^2\right) + \frac{1}{2}\left(K_x(s)x^2 + K_y(s)y^2\right), \tag{3.1}$$

where $K_x(s)$ and $K_y(s)$ are the focusing strengths of the quadrupoles and it is assumed that $K_x(s) = -K_y(s)$. Introducing the following normalised phase-space coordinate transformation as in [29],

$$x_N = \frac{x}{\sqrt{\beta_x(s)}}, \quad p_{x_N} = p_x\sqrt{\beta_x(s)} - \frac{\beta_x'(s)x}{2\sqrt{\beta_x(s)}}, \tag{3.2}$$

$$y_N = \frac{y}{\sqrt{\beta_y(s)}}, \quad p_{y_N} = p_y\sqrt{\beta_y(s)} - \frac{\beta_y'(s)y}{2\sqrt{\beta_y(s)}}, \tag{3.3}$$

these can be substituted into Eq. 3.1 to give a Hamiltonian in normalised coordinates,

$$H_N = \frac{1}{2}\left(p_{x_N}^2 + p_{y_N}^2\right) + \frac{1}{2}\left(x_N^2 + y_N^2\right), \tag{3.4}$$

where we have the following equation for β,

$$(\sqrt{\beta})'' + K(s)\sqrt{\beta} = \frac{1}{\sqrt{\beta^3}}, \tag{3.5}$$

where the prime denotes the derivative with respect to s.

The Hamiltonian in Eq. 3.4, expressed in normalised coordinates, is now s-independent and hence it is an invariant quantity of the system. As we can transform from time, t to the displacement around the ring, s via $s = ct$, 's-independent' is often referred to as 'time-independent' in the literature and these terms will be used interchangeably in this thesis. We now have a conserved, uncoupled Hamiltonian for both transverse planes, $H_{x_N} = \frac{1}{2}\left(p_{x_N}^2 + x_N^2\right)$ and $H_{y_N} = \frac{1}{2}\left(p_{y_N}^2 + y_N^2\right)$. This means two invariants of motion for the 2D system, and thus this system is described as integrable. Therefore, a single particle in an accelerator built with ideal quadrupoles will exhibit bounded, non-chaotic motion.

3.1.2 Hamiltonian of a nonlinear lattice

Starting with the linear Hamiltonian in Eq. 3.1 and adding an arbitrary non-linear, time-dependent potential $V(x, y, s)$, we arrive at a general Hamiltonian of a nonlinear lattice,

$$H = \frac{1}{2}\left(p_x^2 + p_y^2\right) + \frac{1}{2}\left(K_x(s)x^2 + K_y(s)y^2\right) + V(x, y, s). \tag{3.6}$$

In general, the Hamiltonian in Eq. 3.6 is time-dependent for conventional, nonlinear elements. The Hamiltonian is thus not an invariant and the system is said to be non-integrable. This means the nonlinear element can drive resonances, leading to a reduced dynamic aperture. However, with the correct nonlinear potential scaling and careful placement of the nonlinear element, the Hamiltonian in Eq. 3.6 can be made time-independent and hence integrable.

Following the derivation of the time-dependent nonlinear Hamiltonian in [29, 73], a number of assumptions have been made about the linear optics in to which the nonlinear element is introduced. The linear optics is described in more detail in Section 3.1.3 but for now the assumptions made about the optics are stated explicitly below:

- The optics is symmetric, i.e. $\beta_x = \beta_y$ and $K_x = K_y$,
- The particle has no momentum deviation ($\Delta p/p_0 = 0$),
- There is no dispersion, $\eta = 0$, and zero chromaticity, $\xi = 0$,
- The particle orbit is straight, $1/\rho = 0$.

Applying the coordinate substitutions in Eq. 3.2 and 3.3 to Eq. 3.6 and introducing the new 'time' which is now the phase advance (where $\phi = \int 1/\beta(s)ds$), we obtain the new Hamiltonian in normalised coordinates,

$$H_N = \frac{p_{xN}^2 + p_{yN}^2}{2} + \frac{x_N^2 + y_N^2}{2} + \beta(\phi)V\left(x_N\sqrt{\beta(\phi)}, y_N\sqrt{\beta(\phi)}, s(\phi)\right), \tag{3.7}$$

where $\beta_x = \beta_y = \beta$. If the potential, V, can be created in such a way that it cancels out the beta dependence $\beta(\phi)$, then $U(x_N, y_N) = \beta(\phi)V\left(x_N\sqrt{\beta(\phi)}, y_N\sqrt{\beta(\phi)}, s(\phi)\right)$ is

time-independent and the Hamiltonian in Eq. 3.7 also becomes time-independent. This means that the system has at least one invariant of motion, the Hamiltonian itself, which can be expressed in the more compact form,

$$H_N = \frac{p_{xN}^2 + p_{yN}^2}{2} + \frac{x_N^2 + y_N^2}{2} + U(x_N, y_N). \tag{3.8}$$

The challenge is to find a time-dependent potential $U(x_N, y_N)$ which also satisfies Laplace's equation and can be realised in an accelerator beam line. Two solutions, proposed by Danilov and Nagaitsev, are the Quasi-Integrable solution with just one invariant of motion and the fully integrable solution with two invariants. These solutions are discussed below.

3.1.2.1 Quasi-Integrable solution

One such time-independent potential is that of an octupole occupying the entire drift region, L (see Fig. 1.5), with a strength that is inversely proportional to β^3,

$$V(x, y, s) = \frac{k}{\beta^3(s)} \left(\frac{x^4}{4} + \frac{y^4}{4} - \frac{3x^2y^2}{2} \right). \tag{3.9}$$

Here, k is an arbitrary constant, determining the relative strength of the octupole. Applying the coordinate transformation in Eq. 3.2 and 3.3, and using $U(x_N, y_N) = \beta(\phi)V\left(x_N\sqrt{\beta}, y_N\sqrt{\beta}, s\right)$, the octupole potential in normalised coordinates becomes

$$U(x_N, y_N) = k \left(\frac{x_N^4}{4} + \frac{y_N^4}{4} - \frac{3x_N^2y_N^2}{2} \right), \tag{3.10}$$

which is time-independent. This leads to the nonlinear, time-independent Hamiltonian,

$$H_N = \frac{p_{xN}^2 + p_{yN}^2}{2} + \frac{x_N^2 + y_N^2}{2} + k \left(\frac{x_N^4}{4} + \frac{y_N^4}{4} - \frac{3x_N^2y_N^2}{2} \right). \tag{3.11}$$

The Hamiltonian is thus an invariant of the system. However, due to the coupled motion introduced by the octupole potential, the Hamiltonian can no longer be separated into two invariants of motion, as in the linear case. This results in just one invariant, in a system with two degrees of freedom, and so the system is referred to as Quasi-Integrable (QI). Although not fully integrable, nonlinear potentials that conserve the Hamiltonian

have stable motion around the closed orbit and have well-defined boundaries in phase-space [29]. Also, when perturbations from field errors and space charge are reintroduced, the system will still stay close to an integrable system [30]. The QI solution is also referred to as the Hénon-Heiles octupole as it is similar to the Hénon-Heiles map, first applied to planetary motion [74]. In the literature it is also known as 'single-invariant optics', however it will be referred to as Quasi-Integrable optics throughout this thesis.

The region of stable motion for the quasi-integrable octupole potential is limited by the four hyperbolic fixed points at $(x_N, y_N) = (\pm\sqrt{\frac{1}{2k}}, \pm\sqrt{\frac{1}{2k}})$, where k is the octupole strength [75]. A Hamiltonian contour map in Fig. 3.1(Left) shows these fixed points for an octupole strength parameter of $k = 1/2$.

Octupole magnets can be used to create an amplitude-dependent tune spread. This spread in the betatron frequencies leads to decoherence which can damp coherent instabilities through Landau damping, suppressing resonant losses and halo formation [75,76]. Thus, implementing a scaling octupole prescribed by NIO would allow for large tune spreads to be created in the beam, without the excitation of octupole (4th order) resonances.

It is important to note that this octupole potential is not the only time-independent potential that will lead to an invariant Hamiltonian. In fact, for an element of order n (i.e. $n = 3$ for sextupole, $n = 4$ for octupole etc.), the required scaling condition is $\beta^{-\frac{n}{2}-1}$ [73]. However, in this thesis we will only be concerned with the octupole potential as using octupoles is an important strategy for the suppression of coherent resonances in intense beams.

It is also important to draw attention to the fact that the octupole strength will need to continually vary as $1/\beta^3(s)$ across the drift region. In accelerators, this would have to be approximated with multiple, independently powered octupole magnets that have their strength scaled according to $1/\beta^3(s)$. In the Integrable Optics Test Accelerator (IOTA), where this octupole channel was studied, a series of 18 equally spaced octupoles (17 in Run 2) were chosen to approximate the scaling octupole potential [77]. In the IBEX Paul

trap, a continuously scaling octupole potential can be created with a voltage waveform applied to the electrodes and therefore no approximation of the field is needed. This is an advantage of testing QIO in IBEX.

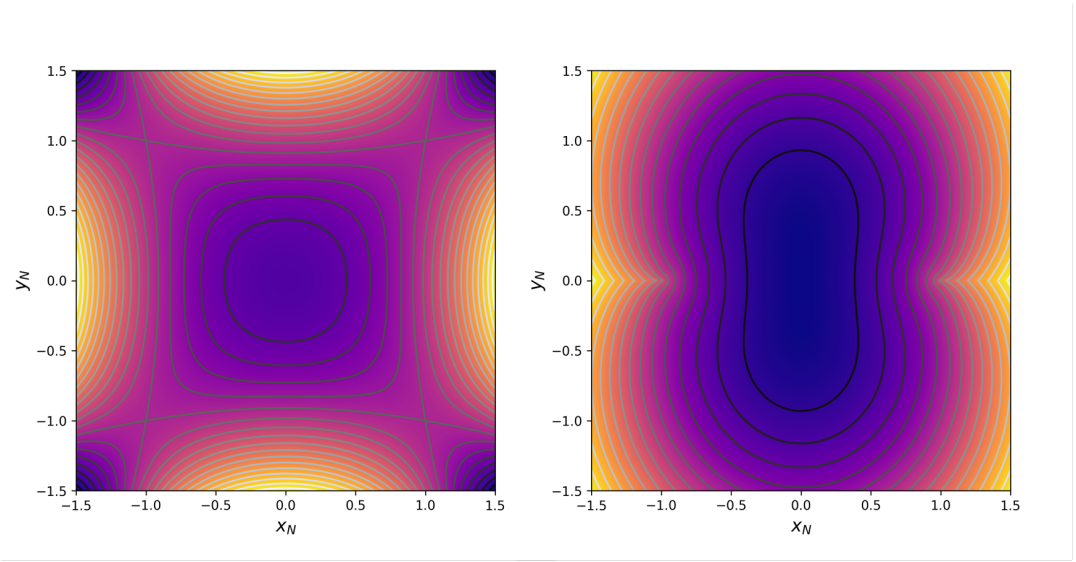

Figure 3.1: Hamiltonian contour lines. (Left) Quasi-Integrable octupole potential, $k = 1/2$. Hyperbolic fixed points are located at $(x_N, y_N) = (\pm\sqrt{\frac{1}{2k}}, \pm\sqrt{\frac{1}{2k}})$. (Right) DN fully integrable elliptical potential, $t = 1/2$.

3.1.2.2 Danilov-Nagaitsev fully integrable solution

In this work, we only consider Quasi-Integrable lattices with an octupole potential. However, for completeness it should be noted that Danilov and Nagaitsev have found a subset of nonlinear potentials which are separable in elliptical, polar and parabolic coordinates [29]. This leads to another invariant of motion, quadratic in momenta, in addition to the Hamiltonian of the system. This results in two invariants of motion, and hence leads to a fully integrable solution in the transverse plane. A detailed derivation of the fully integrable solution is given in [29]. I will provide a brief overview of it below.

The authors started by searching for a second invariant of the form

$$I = Ap_x^2 + Bp_xp_y + Cp_y^2 + D = (ay^2 + c^2)p_x^2 - (2axy)p_xp_y + ax^2p_y^2 + D, \tag{3.12}$$

where the N denoting normalised coordinates has been omitted for clarity. Setting the constants, $a = 1$ and $c \neq 0$, the well-studied Bertrand-Darboux partial differential

equation for an integral potential [78, 79] is obtained,

$$xy\left(U_{xx}-U_{yy}\right)+\left(y^2-x^2+c^2\right)U_{xy}+3yU_x-3xU_y=0, \tag{3.13}$$

where the subscripts denote the partial derivatives of the potential, U with the respective coordinate. This partial differential equation has the general solution

$$U(x,y)=\frac{f(\xi)+g(\eta)}{\xi^2-\eta^2}, \tag{3.14}$$

for arbitrary functions, f and g and where,

$$\xi=\frac{\sqrt{(x+c)^2+y^2}+\sqrt{(x-c)^2+y^2}}{2c} \quad \eta=\frac{\sqrt{(x+c)^2+y^2}-\sqrt{(x-c)^2+y^2}}{2c}. \tag{3.15}$$

Solving Eq. 3.13 in elliptical coordinates, while continuing to satisfy the Laplace equation ($\nabla^2 U=0$), the following solution is obtained [29],

$$\begin{aligned} f_2(\xi)&=\xi\sqrt{\xi^2-1}(d+t\cosh(\xi))\\ g_2(\eta)&=\eta\sqrt{1-\eta^2}(b+t\cos(\eta)), \end{aligned} \tag{3.16}$$

where b, c, d and t are arbitrary constants. This leads to a time-independent Hamiltonian described by

$$H_N=\frac{1}{2}\left(p_x^2+p_y^2+x^2+y^2\right)+\frac{f_2(\xi)+g_2(\eta)}{\xi^2-\eta^2}, \tag{3.17}$$

and second invariant of the form

$$I=(xp_y-yp_x)^2+c^2p_x^2+2c^2\frac{f_2(\xi)\eta^2+g_2(\eta)\xi^2}{\xi^2-\eta^2}. \tag{3.18}$$

An alternative representation for the nonlinear potential was obtained in 2019 using the complex plane ($z=x+iy$) [80]. This representation is beneficial in particle tracking codes as it avoids numerical errors caused by small denominators that appear when evaluating derivatives of the potential near the mid-plane. This approach gives the potential in the form of

$$U=t\,\mathrm{Re}\left(\frac{z}{\sqrt{1-z^2}}\arcsin(z)\right), \tag{3.19}$$

where t is a constant determining the strength of the nonlinear potential. This fully integrable solution has the benefit of an infinite dynamic aperture in theory, as it is

not limited by any fixed points as was the case for the QI lattice. The potential does have two singularities at $x = \pm c$, but if the physical aperture of the beam pipe is placed at this point, then the beam dynamics is only limited by the beam pipe and not by the dynamic aperture. The Hamiltonian for the fully integrable Danilov-Nagaitsev (DN) potential is shown in Fig. 3.1(Right), using the parameterisation in Eq. 3.19 and a strength of $t = 1/2$. The singularities are located at $x = \pm 1$.

3.1.3 T-insert lattice

Now that the time-independent nonlinear potential for a QI octupole and a fully integrable elliptical potential have both been derived, we will now turn our attention to the linear optics in which these nonlinear potentials will be introduced.

In Section 3.1.2, it was assumed that the optics was symmetric and that $\beta_x = \beta_y$. Axially symmetric focusing could be provided by solenoid fields, however they have a focal length proportional to p^2 and so are impractical for higher energy machines. As quadrupole magnets affect the beta functions asymmetrically, the only other linear optics that could create equal beta functions is a drift region. However, an accelerator cannot be constructed out of only drift regions as there would be no radial confinement and the beam size would continue to grow until all the particles were lost.

Therefore, consider a lattice consisting of two parts, (1) a drift region of length L, where the beta functions are equal ($\beta_x = \beta_y$), followed by (2) a linear optics insert which provides confinement of the particle beam, while also bringing the Twiss parameters back to the same point as before the drift region but with the sign of α reversed (see Fig. 1.5). This optical insert would need the transfer matrix of a thin axially symmetric lens or 'T-insert',

$$M_T = \begin{pmatrix} 1 & 0 & 0 & 0 \\ -K & 1 & 0 & 0 \\ 0 & 0 & 1 & 0 \\ 0 & 0 & -K & 1 \end{pmatrix} \tag{3.20}$$

where $K = 1/f$ is the integrated focusing strength over the T-insert. Such an optics insert can be created with thick focusing and defocusing quadrupole magnets with the

following conditions:

1. An $n\pi$ (where n is an integer) phase advance is needed over the T-insert section.

2. The Twiss parameters must have the same magnitude at the start and end of the T-insert section (with the sign of α reversed).

The first condition of an $n\pi$ phase advance ensures periodic motion through the drift region as particles return to the same point in phase space after passing through the T-insert. This essentially makes the T-insert transparent to a single particle. Note that an $n\pi$ phase advance is a sufficient condition (as opposed to $2n\pi$) for nonlinear potentials with even powers of x_N and y_N. This is the case for the octupole potential in Eq. 3.9, which we are concerned with in this work.

The second condition ensures equal beta functions in the drift region of length L which can be described by the following formula,

$$\beta(s) = \frac{L - sK(L-s)}{\sqrt{1 - \left(1 - \frac{LK}{2}\right)^2}}, \tag{3.21}$$

where K is the integrated focusing strength of the T-insert as before and s is the position along the drift.

3.2 Designing a Quasi-Integrable lattice for IBEX

3.2.1 One-cell T-insert

A number of T-insert lattices for IBEX were designed by a previous PhD student, Lucy Martin [39]. This was a difficult procedure as the lattice was not only constrained to meeting the requirements of NIO theory, but also by the IBEX electronics and trap size. Table 3.1 lists the experimental and theory-imposed constraints.

The first two constraints in Table 3.1 arise from the theory of NIO and have been discussed already. The voltage amplifiers which amplify the trapping waveform applied to the electrodes in the IBEX Paul trap also pose additional constraints on the T-insert

lattice design. The voltage amplifiers limit the maximum voltage amplitude that can be used to create a T-insert to $\sim \pm 150$ V. Additionally, the slew rate of the amplifiers (1000 V/µs) limits the shortest pulse width of the waveform, depending on the voltage pulse height. The trap size and, more specifically, the inscribed radius of the rods limits the maximum beta function that the lattice can have. Large beta functions will lead to the loss of particles due to scraping on the rods. The original trap sizes were assumed for the T-insert design. Choosing a maximum RMS beam radius of $r_b = 2\,\text{mm}$ would avoid scraping on the rods at a radius $r_0 = 5\,\text{mm}$ and would lie within the good field region of IBEX [39]. Using $\sigma_{rms} = \sqrt{\epsilon\beta}$, and assuming an emittance of $\epsilon = 2.16 \times 10^{-9}\,\text{mrad}$ [39], a maximum beta function is obtained for the lattice of $\beta_{max} = 1850\,\text{m}$.

Furthermore, the phase advance over the drift region is a constraint on the usefulness of the nonlinear insert. In theory, the phase advance should be maximised in order to maximise the length of the drift region and hence increase the length of the region over which the octupole is applied. This will maximise the tune spread created in the particle beam for a given octupole strength and hence increase the effectiveness of decoherence. In practice, increasing the phase advance in the drift creates a large variation in $\beta(s)$ (due to Eq. 3.21), requiring a larger change in octupole strength as $K_{\text{Oct}} \sim 1/\beta^3(s)$. The increase in phase advance over the drift region also tends to increase the beta functions in the rest of the lattice, leading to the risk of scraping on the trap electrodes. A phase advance of $0.3 \times 2\pi$ was chosen by IOTA which ensures a large tune spread when the octupole is introduced into the drift region, while still being able to implement a scaling octupole potential which is acceptable within field tolerances [73]. Therefore, when designing the T-insert for IBEX, a phase advance of $0.3 \times 2\pi$ was also set to be the goal.

The lattice which was found to be the most successful at trapping ions in IBEX is referred to as L_3 in [39]. This lattice was modified slightly by myself, in order to further minimise the difference between the phase advances in x and y (0.02% improvement in the phase advances meeting the NIO conditions). Figure 3.2 plots the beta functions of this modified T-insert design and the lattice parameters are summarised in Table. 3.2.

Table 3.1: Constraints on the T-insert lattice from theory and experimental set up.

Constraint	Source
$\phi_x = \phi_y = n\pi$	NIO theory
$\beta_x = \beta_y$	NIO theory
Limit on voltage amplitude (± 150 V)	IBEX electronics
Limit on pulse width (> 50 ns)	IBEX electronics
$\beta_{max} < 1850$ m	IBEX trap inscribed radius
Maximise phase advance over drift	Maximise tune spread

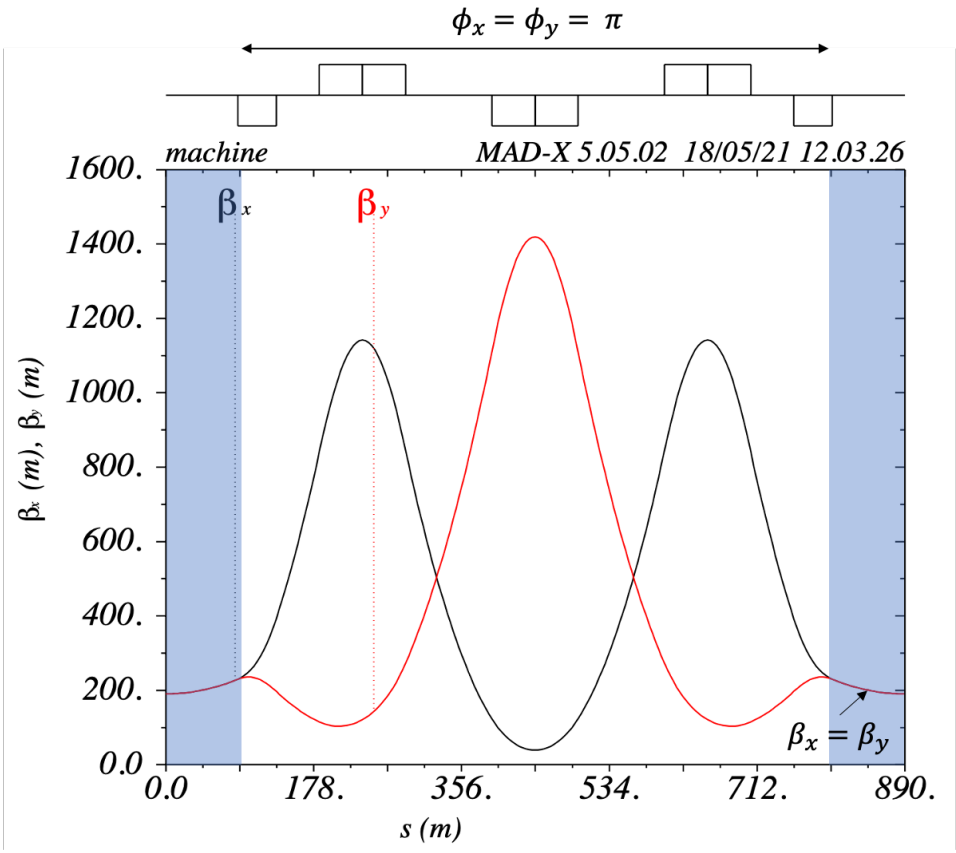

Figure 3.2: Beta functions of the T-insert lattice designed for the IBEX trap in MAD-X. The blue-shaded region is the drift region for the nonlinear insert.

The lattice consists of five quadrupoles arranged in a symmetric lattice, mirrored around the central quadrupole. The quadrupole strengths calculated from MAD-X are converted to voltages using Eq. 2.37 and the required, ideal voltage waveform is plotted in Fig. 3.3.

It should be noted that it was difficult to achieve a phase advance over the drift region close to $0.3 \times 2\pi$ without raising the beta function within the T-insert, increasing the risk of scraping on the trap electrodes. Therefore a phase advance of $0.136 \times 2\pi$ was

Table 3.2: Design parameters of the one-cell T-insert lattice.

Lattice parameter	Value
Horizontal phase advance over T-insert (2π)	0.5000
Vertical phase advance over T-insert (2π)	0.5001
Horizontal phase advance over drift (2π)	0.1358
Vertical phase advance over drift (2π)	0.1358
Equivalent lattice length (m)	889.12
Maximum β_x (m)	1141.45
Maximum β_y (m)	1419.18
Minimum β_x in drift (m)	190.50
Minimum β_y in drift (m)	190.50

settled upon.

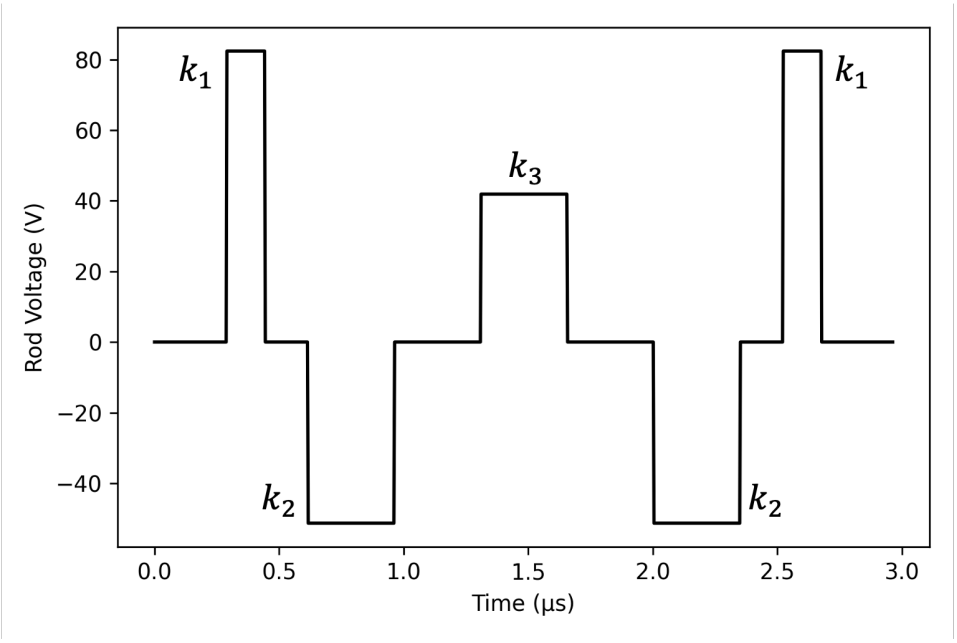

Figure 3.3: Voltage waveform applied to one pair of rod electrodes in IBEX to create the one-cell T-insert. The inverse of this waveform is applied to the other pair of electrodes.

In order to test the predictions of QI optics, a resonance needs to be excited in the lattice so that the ability of an octupole to damp this resonance can be measured. Furthermore, the lattice should also be tested near a 4th order resonance (as these are most often driven by octupoles) to determine if the quasi-integrability of the lattice has eliminated the ability for the QI octupole to drive these resonances. This one-cell lattice has a tune, $Q_x, Q_y = 0.636$ which is not close to any structural 4th order

resonance. However, in IBEX, it is possible to excite resonances using perturbations applied to the electrodes which have a frequency equal to an integer multiple of the betatron frequency. Therefore, an octupole perturbation can be applied to the plate electrodes, with a frequency of four times the betatron tune in order to simulate a 4th order resonance. This one-cell lattice is used to test QI optics in the presence of an octupole perturbation in simulation work presented in Section 5.3. This technique is unique to Paul traps as the focusing is dependent on time, in contrast to an accelerator lattice in which the focusing is dependent on the spacial positioning of the magnets.

The technique of testing QIO in IBEX, using an octupole perturbation to replicate the 4th order resonance, is itself a simulation of a resonance. Therefore, a more convincing experiment would be to test QIO at a 4th order resonance defined by the lattice structure, instead of introduced as a perturbation in time. It is for this reason, along with the extension of testing QIO with space charge, that a two-cell lattice was designed with a tune close to a 4th order resonance ($Q = 1/4$).

3.2.2 Two-cell T-insert

A main goal of NIO is to suppress space-charge-driven coherent resonances. One way to test the ability of a QI lattice to suppress such resonances is to start with a lattice that has a fractional tune close to a resonance condition. For instance, consider a linear lattice with a fractional tune $Q = 0.25 + \delta\nu$, where $\delta\nu$ is positive, so that the lattice tune is above the 1/4 integer resonance. When space charge is included, the lattice tune will be brought closer to the 1/4 integer resonance by the space-charge tune shift ΔQ_{sc} (which is always negative as the space-charge force is defocusing, see Section 1.2.2). In a linear lattice, this space-charge tune shift could drive a coherent resonance in the beam.

The goal of the QI lattice would thus be to use an octupole to suppress this coherent resonance (through Landau damping), without the octupoles driving the incoherent resonance. Therefore, I designed a T-insert with a fractional tune slightly above 0.25.

To achieve a fractional tune of ~ 0.25 in a one-cell T-insert lattice, either the beta

function in the drift has to be reduced (as $\phi(s) = \int \frac{ds}{\beta(s)}$), or the drift region needs to be made longer. Both of these methods tend to increase the beta function within the T-insert, risking scraping on the electrodes of the trap.

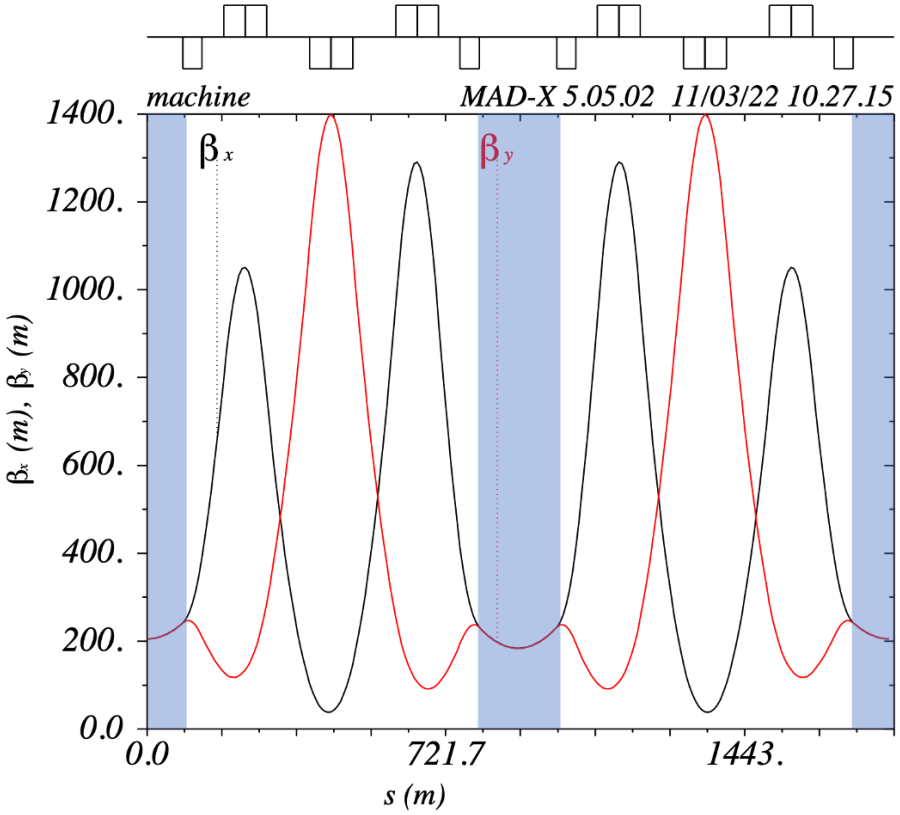

Figure 3.4: Beta functions of the two-cell T-insert lattice designed to test QIO with space charge in the IBEX trap. The blue-shaded region is the drift region for the nonlinear insert.

Instead, I decided to create a T-insert made from two cells, each cell with similar properties to the one-cell T-insert lattice, as this has already been used to trap ions in IBEX [39]. The two-cell T-insert was designed using the matching module in MAD-X and constraining the beta functions within the drift regions to be equal and the phase advance over each T-insert cell to be $0.5 \times 2\pi$. The length of the drift region in cell 2 was increased by a factor of 1.08 for two reasons. First, to increase the total fractional tune of the lattice beyond 0.25, and second to ensure that the T-insert was created from two non-identical cells. It is important for the two cells to be non-identical when particles make multiple passes through the lattice so that it acts as a super-cell (a larger

cell structure made of other cells) with fractional tune $Q_{\text{super-cell}}$ and not $Q_{\text{super-cell}}/2$. For example, if cells 1 and 2 were the same, a lattice made of 1000 'super-cells' with $Q = 0.25$ would be identical to that of a lattice made of 2000 cells of cell 1 with a tune of $Q = 0.125$. This technicality is important when it comes to driving resonances in lattices as the cell structures have different resonant-driving terms.

Table 3.3: Design parameters of the two-cell T-insert lattice.

Lattice parameter	Cell 1	Cell 2
Horizontal phase advance over T-insert (2π)	0.5111	0.4999
Vertical phase advance over T-insert (2π)	0.5118	0.5003
Horizontal phase advance over drift (2π)	0.1271	0.1496
Vertical phase advance over drift (2π)	0.1270	0.1499
Cell length (m)	889.12	902.98
Maximum β_x (m)	1290.59	1290.59
Maximum β_y (m)	1398.48	1398.48
Minimum β_x in drift (m)	205.29	184.16
Minimum β_y in drift (m)	205.50	183.75

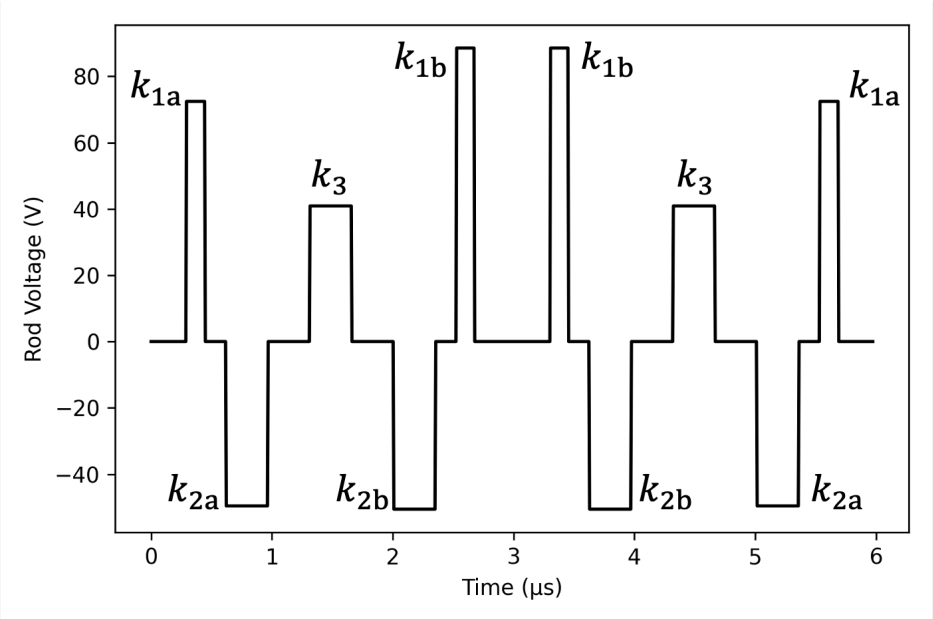

Figure 3.5: Voltage waveform applied to one pair of rod electrodes in IBEX to create the two-cell T-insert. The inverse of this waveform is applied to the other pair of electrodes.

The beta functions of the two-cell T-insert lattice are plotted in Fig. 3.4 and the lattice parameters are summarised in Table 3.3. The total horizontal and vertical tunes

of the super-cell are $Q_x = 1.276$ and $Q_y = 1.277$. The two-cell T-insert lattice consists of 10 quadrupoles and has mirror symmetry around the central drift region. The voltage waveform for the two-cell T-insert lattice is plotted in Fig. 3.5. This lattice is used in simulation to test QIO in the presence of space charge in Section 5.5.

3.2.3 Relating the octupole field in an accelerator and IBEX

Following on from Section 2.2, where the quadrupole focusing in a Paul trap was shown to be equivalent to the strong focusing in accelerators, we will now extend this comparison to octupole fields. The Hamiltonian of a particle in an accelerator consisting of quadrupole and octupole magnets is given by,

$$H_{\text{Acc}} = \frac{p_x^2 + p_y^2}{2} + \frac{1}{2}k_2\left(x^2 - y^2\right) + \frac{1}{24}k_4\left(x^4 - 6x^2y^2 + y^4\right), \tag{3.22}$$

where

$$k_m = \frac{1}{B\rho}\frac{\partial^{m-1}B}{\partial x^{m-1}}, \tag{3.23}$$

with ρ being the radius of curvature of the particle in the magnetic field B. Adding an octupole term to the Hamiltonian in a Paul trap gives the following equation,

$$H_{\text{Paul}} = \frac{p_x^2 + p_y^2}{2m} + \frac{qV_Q(t)}{r_0^2}\left(x^2 - y^2\right) + \frac{qV_O(t)}{r_0^4}\left(x^4 - 6x^2y^2 + y^4\right). \tag{3.24}$$

Using the same transformation as in Section 2.2 ($H/mc^2 \to \hat{H}$, $p/mc \to \hat{p}$) and transforming the independent variable t to $\tau = ct$, we obtain

$$\hat{H}_{\text{Paul}} = \frac{\hat{p}_x^2 + \hat{p}_y^2}{2} + \frac{qV_Q(\tau)}{r_0^2mc^2}\left(x^2 - y^2\right) + \frac{qV_O(\tau)}{r_0^4mc^2}\left(x^4 - 6x^2y^2 + y^4\right). \tag{3.25}$$

Equating the coefficients in Eq. 3.22 and Eq. 3.25 we get,

$$k_2 = \frac{2qV_Q(\tau)}{mc^2r_0^2} \quad \text{and} \quad k_4 = \frac{24qV_O(\tau)}{mc^2r_0^4}. \tag{3.26}$$

Equation 3.26 now relates the strength of the quadrupole magnet, k_2 and strength of the octupole magnet, k_4 to the voltages, V_Q and V_O in a Paul trap. In order to get an estimate of the octupole voltage required in IBEX, we need to evaluate k_4.

First, we expand the fully integrable elliptical potential so that it can be shown that the QI octupole solution is simply a truncation of this expansion. The fully integrable elliptical potential expressed in normalised coordinates can be written as

$$\begin{aligned} U\left(x_N, y_N\right) = & t \cdot \mathrm{Re}[\left(x_N + i y_N\right)^2 + \frac{2}{3c_I^2}\left(x_N + i y_N\right)^4 + \frac{8}{15c_I^4}\left(x_N + i y_N\right)^6 \\ & + \frac{16}{35c_I^6}\left(x_N + i y_N\right)^8 + \ldots], \end{aligned} \tag{3.27}$$

where t is a strength parameter that will be varied from $0 - 0.9$ in the IOTA experiment and the scaling parameter $c_I^2 = 0.01$ cm for IOTA [73]. Approximating this potential to the lowest-order term that creates a nonlinear tune spread, we arrive at the QI octupole solution,

$$U \approx \frac{2t}{3c_I^2}\left(x_N^4 - 6x_N^2 y_N^2 + y_N^4\right) = \frac{1}{\beta(s)^3}\frac{2t}{3c_I^2}\left(x^4 - 6x^2 y^2 + y^4\right), \tag{3.28}$$

where the right-hand-side of Eq. 3.28 has been converted back from normalised coordinates to Frenet-Serret coordinates. Equating the octupole coefficient in Eq. 3.22 with the coefficient in the LHS of Eq. 3.28, the octupole strength can thus be expressed as,

$$k_4 = \frac{16t}{c_I^2}\frac{1}{\beta(s)^3}. \tag{3.29}$$

If we equate this to the octupole voltage in a Paul trap in Eq. 3.26 we obtain,

$$V_O(\tau) = \frac{2}{3}\frac{mc^2 r_0^4}{q}\frac{t}{c_\mathrm{I}^2 \beta^3(\tau)}. \tag{3.30}$$

As stated above, IOTA choose a scaling parameter of $c_I^2 = 0.01$ cm, which corresponds to the singularities of the fully integrable elliptical potential at $x = \pm c_I$. IOTA chose to make their beam pipe extremely thin and almost touch the elliptical magnet poles in order to preserve as much of the physical aperture as possible [73]. To estimate a sensible value of this parameter in IBEX, a value of $c_I = r_0/\sqrt{\beta_\mathrm{drift}}$ was chosen [39] where $r_0 = 5$ mm is the inscribed radius of the trap and β_drift is the value of the beta function at the center of the drift region. This value of c_I gives an analogous physical aperture in IBEX, defined by the position of the electrodes. Thus, using Eq. 3.30 with $t = 1$ and $\beta_\mathrm{drift} = 190.5$ m, an octupole voltage of $V_O = 17.09$ V is obtained. This octupole

voltage assumes a trap configuration of 8 equally sized electrodes, equally spaced around a radius r_0. This electrode configuration however, is not practical in IBEX due to the way atoms are ionised in the trap. Therefore, the octupole voltage will be much larger in practice and will be scaled according to the trap geometry used in IBEX, described in Chapter 4.

3.3 Previous work on Nonlinear Integrable Optics

3.3.1 IOTA

The Integrable Optics Test Accelerator (IOTA) is a compact storage ring with a circumference of 40 m, located at Fermilab, US [35]. The construction of IOTA was motivated by the needs of future high-intensity accelerators and aims to test novel methods for maximizing beam intensity in hadron machines. The key research areas are (1) mitigating beam loss caused by coherent beam instabilities and (2) improving beam quality through the mitigation of space charge and beam cooling [81]. IOTA has chosen three main technologies in the pursuit of improving high-intensity machines which are Nonlinear-Integrable Optics (NIO) [82], Electron Lenses [83] and Optical Stochastic Cooling [84]. IOTA was first designed to operate with 150 MeV electrons with the goal of eventually switching to 2.5 MeV protons. The proton injector is currently being installed at the IOTA ring, with the first proton beam expected in 2023 [85]. IOTA circulated it's first electron beam in August 2018; the results discussed in this section all use an electron beam.

The IOTA ring consists of 8 main dipoles, 39 quadrupole magnets and a system of dipole and skew-quadrupole corrector magnets [35]. The small size of the ring gives rise to a large natural chromaticity which can be corrected with a series of 10 sextupoles. NIO has been found to break down in the presence of dispersion and chromaticity due to their modification of the invariants of motion [86]. However, with zero dispersion, it was found that integrability could be maintained if the horizontal and vertical chromaticities are equal [86]. Therefore, two regions were created in the lattice for nonlinear insertions

where dispersion has been made zero and the chromaticities made equal. The two regions in the ring allow for testing both Quasi-Integrable and Nonlinear Integrable optics. In one of these regions, 17 independently powered magnets approximate the scaling octupole potential for QI studies and in the other region, 18 independently powered magnets approximate the fully integrable DN nonlinear element needed to test fully integrable optics. In order to test NIO, IOTA aimed to achieve beta-functions with better than 1 % precision and better that 0.001 precision in phase advance [87]. This requires magnet alignment tolerances of 50 µm and unwanted nonlinearities in the field of less than 1 %. Octupole strength fluctuations below 10 % do not have a significant impact on the dynamics [77].

IOTA has collected data from three experimental runs, Run 1 in 2019, Run 2 in 2019/2020 and Run 3 which started in October 2020. During Run 2 it managed to circulate a single electron in the storage ring, whilst performing experimental 6D tracking of the particle's position [88]. This achievement advances experimental understanding of single-particle-dynamics as well as acting as a useful tool for machine commissioning and the verification of ring parameters.

In Run 2, testing the QI octupole showed that the amplitude-dependent tune shift of the octupole was in agreement with simulations, however the resulting dynamic aperture was smaller than expected. At the dynamic-aperture limit, a tune shift of 0.04 was measured [81], whereas simulation results seemed to suggest a maximum tune shift of 0.08 could be achieved [89]. The limiting factor in the dynamic aperture was expected to be from the strong sextupole corrections used, needed to compensate for the sextupole magnets not yet installed in the lattice. Installation of the complete set of 12 sextupole magnets in the IOTA lattice is expected to resolve this limitation [90].

The ability of Landau damping to suppress transverse instabilities was also studied using the QI lattice. IOTA reversed their damping feedback system to produce positive feedback, simulating an instability in the ring. The QI octupole strength was then increased and the anti-damping gain was measured as a function of octupole current.

These results showed that there was a two-fold increase in the instability threshold when comparing the maximum octupole strength to the case where octupoles were off [81].

In experimental testing of the DN system, it was found that the beam could cross the integer resonance while the nonlinear element had a strength parameter of $t = 0.5$. The beam could even be left circulating on the integer resonance for 110 s [81]. Previous simulation results also suggested that when crossing the integer resonance, at nonlinear strengths of $t \geq 0.5$, the beam splits into two 'beamlets' in the vertical plane [91]. This prediction was also confirmed experimentally in Run 2 [90].

Recent work by Baturin used a method for distributing the discrete nonlinear elements in the drift region of a T-insert by equal phase advance instead of equally distributed in space [92]. This allows for a better approximation of the nonlinear insert scaling to be achieved with fewer discrete magnets. This can also be extended to implement a distributed octupole lattice where single octupoles are placed at points within a FODO lattice where $\beta_x \approx \beta_y$ in order to approximate a QI lattice to within a certain degree of accuracy determined by the symplectic integration scheme. This method could allow for QI lattices to be implemented more easily in accelerators as they would not require the T-insert lattice and scaling nonlinear elements.

3.3.2 UMER

The University of Maryland Electron Ring (UMER) is a low-energy (10 keV) electron ring, designed to study beam dynamics at high space charge. When operating at a beam current of 100 mA, UMER can reach a space-charge tune depression of $Q/Q_0 = 0.14$, placing it in the extremely space-charge dominated regime [93], where Q_0 is the bare tune. This is a much larger space-charge tune depression than is achievable in IBEX. When trapping around 1×10^7 particles, a tune depression of $Q/Q_0 = 0.85$ has been measured [39]. In 2007, UMER circulated what was at that time a beam with the highest space-charge tune shift ever stored in a ring, with an integer space-charge tune shift [94]. The ring is very compact with a circumference of 11.52 m. As the ring stores low-energy

electrons it is able to utilise printed circuit board (PCB) quadrupoles [95] due to the small focusing force required to confine the beam.

A proof-of-concept octupole lattice was designed for the UMER electron ring in 2018 and extensive simulation work was undertaken to set tolerances on the lattice and octupole insert [96]. Design studies were carried out for both a distributive octupole lattice, where octupole magnets are distributed around the ring, and a single-channel octupole insert. Although the distributive octupole lattice was simpler to implement in the UMER ring, it only satisfied the quasi-integrable condition approximately. A single-channel octupole insert was also designed using 7 overlapping PCB octupoles to approximate the $1/\beta^3(s)$ strength scaling.

An experiment was proposed in 2019 to test the predictions of NIO at low-current with a low space-charge tune shift of ~ 0.005. Particle-in-cell[1] simulations showed that a maximum octupole tune spread of $\Delta Q = 0.11$ ($\Delta Q_{rms} = 0.015$) could be achieved for octupole strengths of $50\,\mathrm{T/m^3}$ [97].

Since then, new accelerator lattice designs have been made in order to test QIO in UMER while remaining close to UMER's typical operating parameters [98]. An optimization routine was developed to tune the lattice parameters within UMER until the integrability requirements were met. Tune measurements were carried out with the nonlinear octupole-channel insert and measurements of amplitude-dependent tune shifts were also attempted. However, experimental results from testing QIO were not as conclusive as the predictions from simulation. It was concluded that UMER could not meet the strict tolerance requirements needed to obtain accurate amplitude-dependent tune measurements and further work is needed for QIO to be tested experimentally [98].

3.4 Advantages of testing NIO with IBEX

So far, there have been mixed results when testing NIO. Simulations have shown promising results, however in practice experimental results have occasionally differed from

[1]Particle-in-cell (PIC) refers to the method used to solve Maxwell's equations on a grid. The particle positions are updated using the Lorentz equation of motion.

simulation and the benefits of implementing NIO have not been as clear in experiments [81, 98]. The advantage of testing NIO with IBEX is that a Paul trap offers an intermediate step between simulation work and implementing integrable lattices in accelerators. Although IBEX is a simplified model of an accelerator, only reproducing the transverse dynamics in a dispersion- and chromaticity-free environment, it can still help to test NIO experimentally.

IBEX's simplicity when compared to accelerators offers some benefits when testing NIO. As integrability can be broken by chromaticity and dispersion [86], the absence of momentum-dependent focusing in IBEX means that these effects will not interfere with experimental measurements. It also means that the lattice design is not constrained to reducing dispersion to zero and making equal chromaticities in the nonlinear insert region.

The ability to apply continuously varying voltage pulses to electrodes in IBEX also means that the octupole channel will not need to be approximated with discrete octupoles as in IOTA and UMER [77, 97]. IBEX's flexibility when it comes to creating different types of lattices means that various implementations of NIO can be tested without needing to rearrange accelerator elements or purchase new equipment. When it comes to testing NIO with space charge, the IBEX trap can create space-charge tune depressions of up to $Q/Q_0 = 0.85$. Although this tune depression is much lower than what is achievable in UMER ($Q/Q_0 = 0.14$), it is currently a much higher space charge regime than is achievable in the IOTA ring.

The IBEX trap comes with some disadvantages also, such as being sensitive to imperfections in the voltage waveform and being unable to measure beam position during the storage of ions. However, the ease with which the intensity can be changed in IBEX, along with the fact that the beam dynamics is isolated to only the transverse plane, means that IBEX has the potential to offer the first demonstration of QIO with space charge.

3.5 Chapter summary

In this chapter, the theory of NIO was laid out and the quasi-integrable and fully integrable nonlinear potentials were introduced. It was shown that the QI solution led to a time-independent Hamiltonian and thus one invariant of motion was achieved in a system with two degrees of freedom. The fully integrable elliptical potential added an additional invariant of motion, quadratic in momentum, which is being tested by the IOTA facility.

The constraints of the T-insert lattice which is needed to house the nonlinear potential were laid out in this chapter. The design of a one-cell and two-cell T-insert lattice to test QIO in the IBEX Paul trap were also presented. An introduction to the work being carried out elsewhere on the topic of NIO was given to contextualize the impact the IBEX Paul trap could have in this field. The absence of chromaticity and dispersion in IBEX, along with the ease of changing lattice design and intensity could allow for a step towards experimentally testing QIO with space charge.

In order to test QIO in IBEX, the original experimental set up laid out in Chapter 2 requires an upgrade to allow for the creation of octupole fields. In the next chapter, the design work behind the upgrade to the IBEX Paul trap is presented along with the commissioning of the new trap, IBEX-2.

Chapter 4

Design and commissioning of the nonlinear upgrade to IBEX

In this chapter I present the design work that went into the new nonlinear trap, IBEX-2. I discuss the design and manufacture of the electrodes for the IBEX-2 trap, as well as the installation and alignment tolerances. I also present the design and testing of the new HV amplifiers to drive the multipole electrodes to the desired voltages in order to provide sufficiently large octupole fields for testing Quasi-Integrable Optics (QIO). I then provide details of the commissioning of the new IBEX-2 trap. This process involved calibrating the MCP detector and optimising the transfer of ions from one section of the trap to the other.

4.1 Specifications for the nonlinear upgrade

In order to test QIO in IBEX, an upgrade to the trap was needed to allow for the creation of octupole fields in addition to the quadrupole trapping potential. This required inserting four additional electrodes in between the existing four central rods. However, due to the original trap configuration, simply adding four electrodes in between the central rods of the existing trap would be problematic as the gaps between electrodes are needed to allow for the electron gun to ionise the argon gas in the trap[1]. For this

[1]Mounting the electron gun on one of the end caps in order to introduce electrons longitudinally was considered. However, this would mean replacing the Faraday cup with an electron gun, and careful consideration would have to be put into the mounting of the gun so that electrons would not hit the MCP detector.

reason, a two-segment trap was designed. This would allow for ionisation in the linear section of the trap before ions were transferred to the nonlinear region or 'experimental region' of the trap. The experimental region would then allow for the creation of lattices with quadrupole and octupole elements. A schematic of the proposed two-section trap is shown in Fig. 4.1.

The addition of electrodes into the trap, even if grounded, will in general affect the field distribution within the trap. Therefore, careful consideration was needed to optimise the shape and placement of these electrodes to minimise unwanted non-linearities in the transverse field of the trap. The schematic shown in Fig. 4.1 is based on a similar trap design from the University of Hiroshima [99]. Before settling upon this trap design, a design study of the shape, size, and inscribed radius of the inserted electrodes was performed.

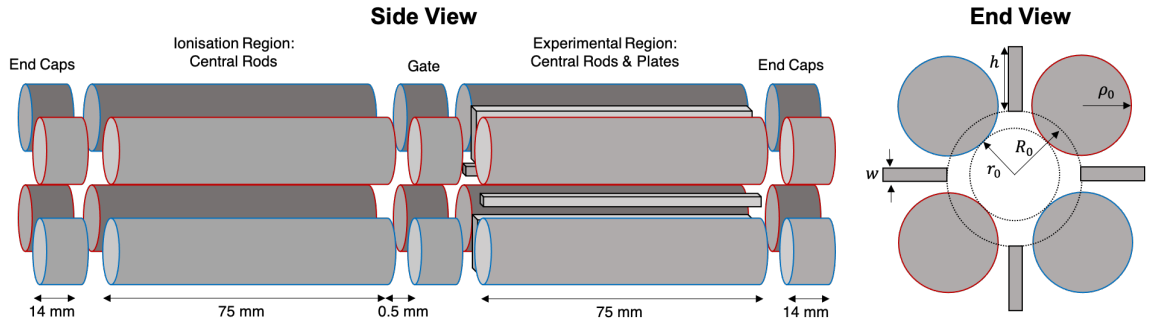

Figure 4.1: Schematic of the IBEX trap nonlinear upgrade. Opposing RF voltages are applied to the red and blue outlined rods for transverse confinement of ions. A DC voltage is applied to the end caps and gate electrodes to provide longitudinal trapping. In IBEX $r_0 = 5\,\text{mm}$ and $\rho_0 = 5.75\,\text{mm}$. Four additional rectangular plates between the rods are present in the nonlinear trap to enable the creation of octupole fields with $R_0 = 8.5\,\text{mm}$, $w = 1\,\text{mm}$ and $h = 6\,\text{mm}$.

4.2 Minimising higher-order multipoles

4.2.1 Multipole field decomposition

In order to observe the effect of introducing additional electrodes on the field quality, a multipole decomposition of the transverse field can be performed. This uses a Fourier transform to decompose the field within the trap into its multipole components.

The RF wavelength applied to the electrodes at operational frequencies of around 1 MHz is much larger than the size of the Paul trap, therefore the static-field approximation can be adopted to analyse the transverse multipole field of a specific electrode configuration. The scalar electric potential, Φ, of the trapping field can be expressed in polar coordinates (r, θ) as a sum of multipoles

$$\Phi(r,\theta) = \sum_{n=1}^{\infty} c_n (\frac{r}{r_0})^n \cos(n\theta), \tag{4.1}$$

where r_0 is the inscribed radius of the electrodes and c_n are the multipole coefficients with order n. The multipole coefficients c_n are calculated by evaluating Φ along the circumference of a circle within the trap aperture and taking the Fast Fourier Transform (FFT) of the sampled potential. The c_n components are then extracted from the peaks in the FFT spectrum. A finite element method was used in Mathematica to solve the Laplace equation in 2D, using the perimeters of the trap electrodes as Dirichlet boundary conditions. The value of Φ was evaluated at 1000 equally spaced points along a circle with an inscribed radius of $r_0 = 3\,\text{mm}$. This radius was chosen as it encompasses the transverse good-field region within the IBEX trap. The 2D multipole decomposition in this section was also performed in Mathematica, where the code has been adapted from a model of the linear IBEX trap written by D. Kelliher [55].

The quadrupolar focusing potential corresponds to the c_2 coefficient, which will be the dominant term in the multipole expansion of the quadrupole field. An ideal quadrupole field, i.e. a field with only a c_2 component, can only be created with perfect hyperbolic electrodes. Hyperbolic electrodes come with the disadvantage of narrowing (or even eliminating) the region in which electrons can pass through the electrodes to ionise the argon in the trapping region. This can be seen in Fig. 4.2, where the hyperbolic electrodes asymptotically approach one another. From this reduction in space, using hyperbolic electrodes would also make it difficult to place the multipole electrodes within the trap. It is also an engineering challenge to manufacture precise hyperbolic electrodes to within machining tolerances of $<25\,\mu\text{m}$. For these reasons, circular rod electrodes are used in

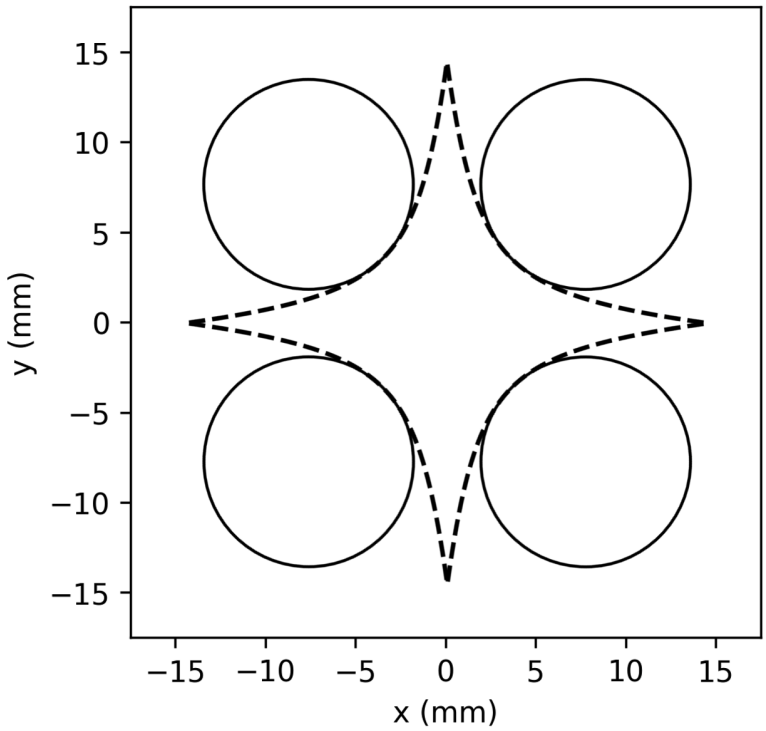

Figure 4.2: Circular rod electrodes used in IBEX (solid) compared to an ideal hyperbolic geometry truncated at ±15 mm (dashed).

IBEX, which approximate a hyperbola at the points closest to the center of the trap (see Fig. 4.2). However, circular rods introduce nonlinearities into the quadrupole field, away from the trap center. Using circular rods, with ideal alignment, only every fourth harmonic will be excited. Therefore, the next two terms in the decomposition after c_2 will be c_6 (12-pole) and c_{10} (20-pole). An example of this multipole decomposition in IBEX is shown in Fig. 4.3(Right).

To ensure that the desired multipole terms are enhanced while unwanted nonlinearities are minimised, the electrode dimensions, locations and voltages were systematically optimised to produce the most ideal operation.

4.2.2 Design of the IBEX-2 trap electrodes

The work in this section (4.2.2), designing electrodes for a multipole trap, has previously been carried out by the group in Hiroshima for the creation of their own nonlinear trap [99]. Their results have been replicated in this section using our own Mathematica

model of a transverse cross-section of the electrodes.

4.2.2.1 Quadrupole electrodes

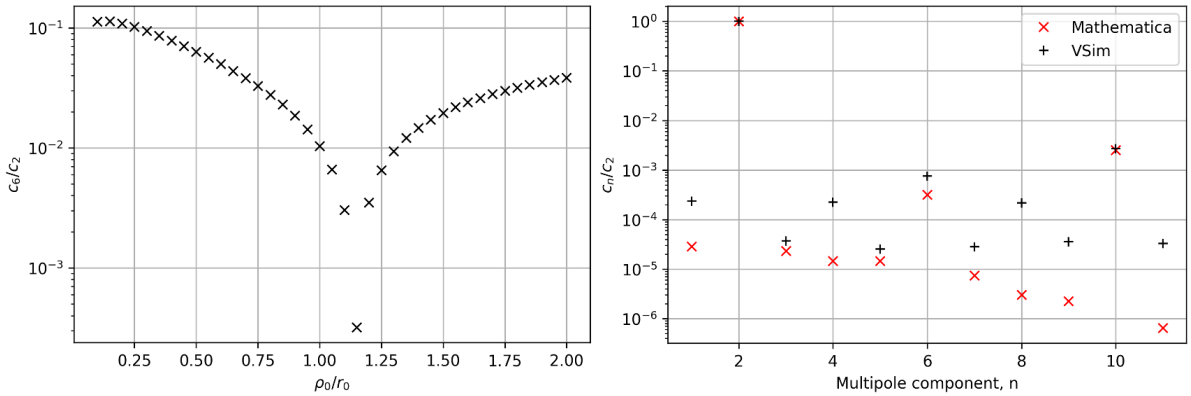

Figure 4.3: (Left) Scan of the ratio of electrode radius to inscribed radius, ρ_0/r_0, to minimise the c_6 multipole component. (Right) Multipole decomposition of the optimum circular electrode configuration, $\rho_0/r_0 = 1.15$. Decomposition was performed in both Mathematica (red, $\times$) and VSim (black, $+$).

As was seen in Section 3.1.3, designing a T-insert in the original IBEX trap was difficult as the conditions of integrability need to be met, while the maximum beta functions are constrained by the trap size and the focusing strength is limited by the slew rate and maximum output voltages of the amplifiers. Creating a larger trap for IBEX-2 (with a larger inscribed electrode radius r_0) was considered which would have increased the maximum beta function the trap could contain before scraping on the rods. However, a larger inscribed trap radius requires larger voltages for a given trapping frequency [55]. The voltage requirement can be reduced by operating at lower frequency. Although, operating at lower RF frequencies comes at the expense of simulating the motion through fewer accelerator cells or turns for a given ion storage lifetime in the trap. As well as ion losses associated with storing for larger numbers of cells, the ion lifetime in the trap will also diminish as a function of time due to factors such as collisions with residual gas.

For these reasons, and for ease of reusing as much existing hardware as possible from the original IBEX trap, the decision was made to keep the quadrupole electrode dimen-

sions of IBEX-2 the same as the original IBEX trap. Therefore, when the multipole trap was designed, the quadrupole rod dimensions of radius $\rho_0 = 5.75\,\text{mm}$ and inscribed radius $r_0 = 5.0\,\text{mm}$ were assumed, as this ratio ($\rho_0/r_0 = 1.15$) has already been shown to minimise unwanted nonlinearities in the quadrupole field [55]. For completeness, a scan of the ratio ρ_0/r_0 was performed in Mathematica and the results shown in Fig. 4.3(Left). Using the electrode dimensions of $\rho_0 = 5.75\,\text{mm}$ and $r_0 = 5.0\,\text{mm}$, a multipole decomposition spectrum for a quadrupole field is plotted up to c_{11} in Fig. 4.3(Right). This was performed both using Mathematica where the electrodes are mathematically defined as ideal circles, and VSim, where the electrode geometries were imported as tessellated cylinders. The tessellation of the electrode geometry in VSim is seen to increase nonlinearities in the trap, above that seen in Mathematica.

4.2.2.2 Design of the multipole electrodes

The simplest way to independently excite the desired multipole terms in the nonlinear trap, while maintaining a good quadrupole trapping region, is to place four additional electrodes in between the existing rods as shown in Fig. 4.4. It is important that by adding these additional electrodes that the unwanted multipole components are not enhanced in the quadrupole field. Fortunately, by careful design of the multipole electrodes, the nonlinearities in the quadrupole field can be reduced and the addition of the electrodes can even improve the field quality compared to the existing linear trap.

The voltage configuration, capable of exciting the quadrupole mode in the experimental region, is shown in Fig. 4.5 (Left). The four (smaller) multipole rods are grounded while a voltage of $\pm V_Q$ is applied to the quadrupole rod electrodes. Varying the radius of the multipole rods ρ_1, while positioned at a fixed radius $R_0 = 8.5\,\text{mm}$, the ratio of multipoles c_6/c_2 is plotted in Fig. 4.5 (Right). The nonlinear c_6 component can be minimised with multipole rods designed so that $\rho_1/R_0 \approx 0.06$. The resulting value of the c_6 component is a reduction by a factor of 10^2 when compared to perfect alignment of the linear trap (ionisation region in Fig. 4.1). In order to minimise the c_6 component

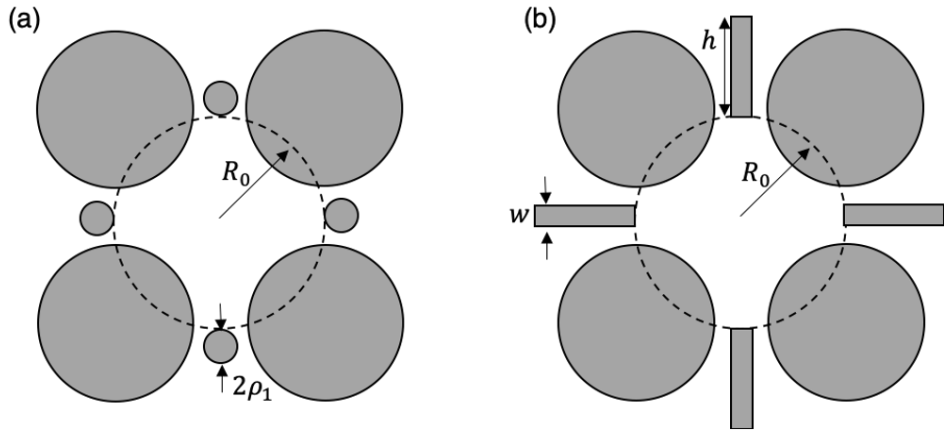

Figure 4.4: Cross sectional view of two nonlinear Paul trap designs. (Left) Nonlinear trap with multipole rods of radius ρ_1. (Right) Nonlinear trap with multipole plates of width w and height h. The inscribed radius of the multipole electrodes is given by R_0.

in the trap, with an inscribed radius of $R_0 = 8.5\,\text{mm}$, the corresponding rod radius is $\rho_1 = 0.51\,\text{mm}$. Despite the reduction in nonlinearities, such a thin rod is difficult to align and is susceptible to bending. If such a configuration were used in reality, it is likely that the benefits would be outweighed by the introduction of additional, bending-induced nonlinearities [99].

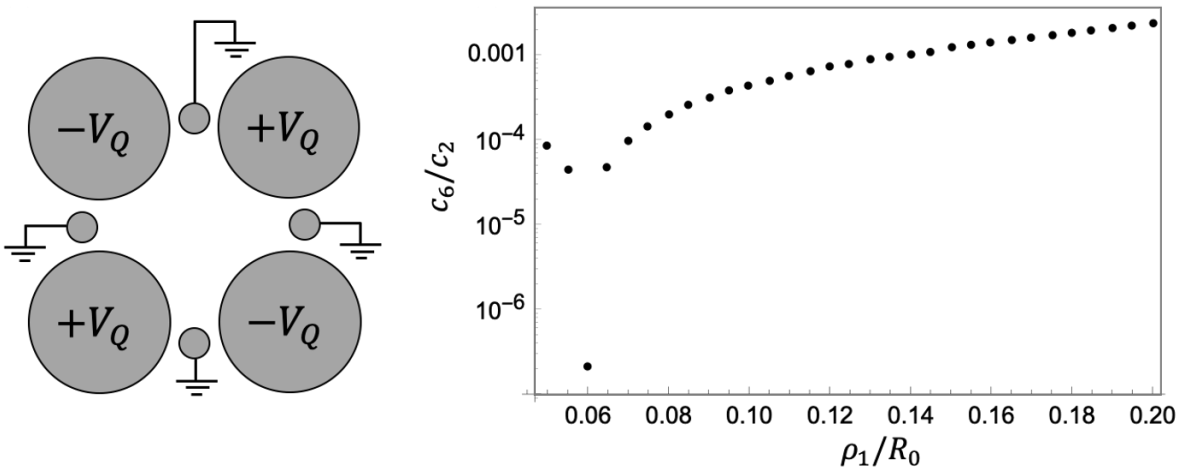

Figure 4.5: Nonlinear trap operating in quadrupole mode. (Left) Cross section of trap with the four multipole rods grounded and a voltage of $\pm V_Q$ applied to the quadrupole rod electrodes. (Right) Multipole rod radius ρ_1 is varied, and the dependence on the ratio c_6/c_2 is plotted.

Due to alignment constraints, a more practical design for the multipole electrodes is instead a flat plate, shown in Fig. 4.4b. Adopting the same voltage configuration as in

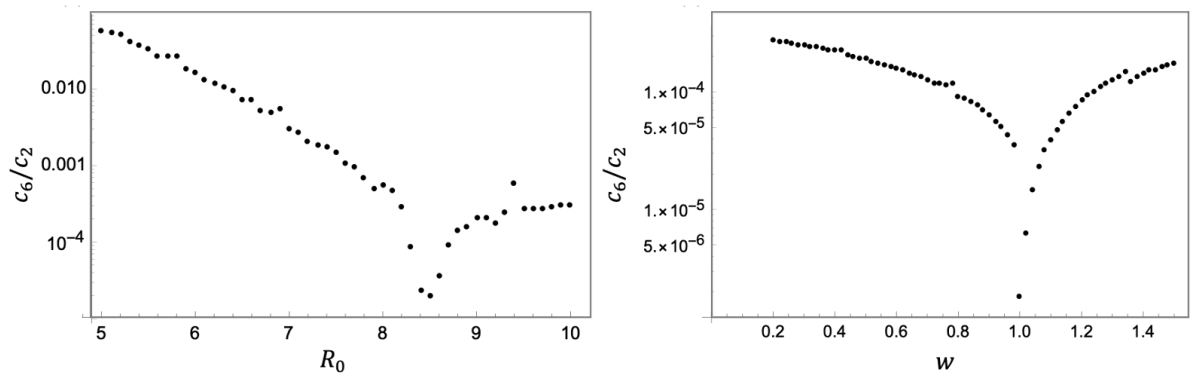

Figure 4.6: Minimising the c_6 component in a quadrupole field created in the presence of the plate electrodes. (Left) The ratio c_6/c_2 is plotted against the varying inscribed radius of the plates R_0 at $w = 1\,\text{mm}$. (Right) The ratio c_6/c_2 is plotted against the width of the plates w at $R_0 = 8.5\,\text{mm}$.

Fig. 4.5, this time using thin metallic plates of height $h = 6\,\text{mm}$, the c_6 component in the quadrupole field is minimised in Fig. 4.6. In Fig. 4.6 (Left), the inscribed radius of the plates, R_0 is varied, keeping the height and width of the plate fixed at $h = 6\,\text{mm}$ and $w = 1\,\text{mm}$ respectively. The simulations show that the optimum inscribed radius of the plates is $R_0 \approx 8.5\,\text{mm}$, in order to minimise the presence of the c_6 component in the quadrupole field.

In Fig. 4.6 (Right), a fixed inscribed radius of the plate electrodes of $R_0 = 8.5\,\text{mm}$ and height $h = 6\,\text{mm}$ is chosen, while the width of the plate is varied from $0.2 - 1.4\,\text{mm}$. At a plate width of 1 mm the c_6 component is minimised to a value $\sim 1 \times 10^{-6}$. The height of the plates was also varied, which resulted in very little change in the multipole components. A height of $h = 6\,\text{mm}$ was chosen for ease of manufacturing and alignment of the plate electrodes. These results show that the rectangular multipole plates can reduce the c_6 component by the same factor as the multipole rods, and thus a good quality quadrupole field can be maintained in the trap. A plate with a width of 1 mm and height of 6 mm is also more easily aligned in the trap when compared to the rods, leading to a reduction in unwanted nonlinearities.

4.2.2.3 Octupole operation

An octupole field can be realised in the trap when adopting the voltage configuration shown in Fig. 4.7 (Left). In this configuration, all four quadrupole rod electrodes are grounded[2], while a voltage of V_O is applied to the four plate electrodes. Due to the symmetry of the trap, when exciting the octupole mode (c_4), additional components c_n, where n is a multiple of 4, will also be excited. The c_8 component is of greatest concern as it is the lowest order unwanted nonlinearity. The voltage dependence on the octupole ($n = 4$) and 16-pole ($n = 8$) multipole components are plotted in Fig. 4.7 (Right). The multipole components can be seen to have a linear dependence on the applied voltage, with the octupole component found to be $c_4 \approx 0.034\,\widetilde{c}_2$ at a voltage of $V_O = V_Q$. Here, $\widetilde{c}_2$ is defined as the quadrupole component measured when the nonlinear trap is operating in quadrupole mode with voltage V_Q.

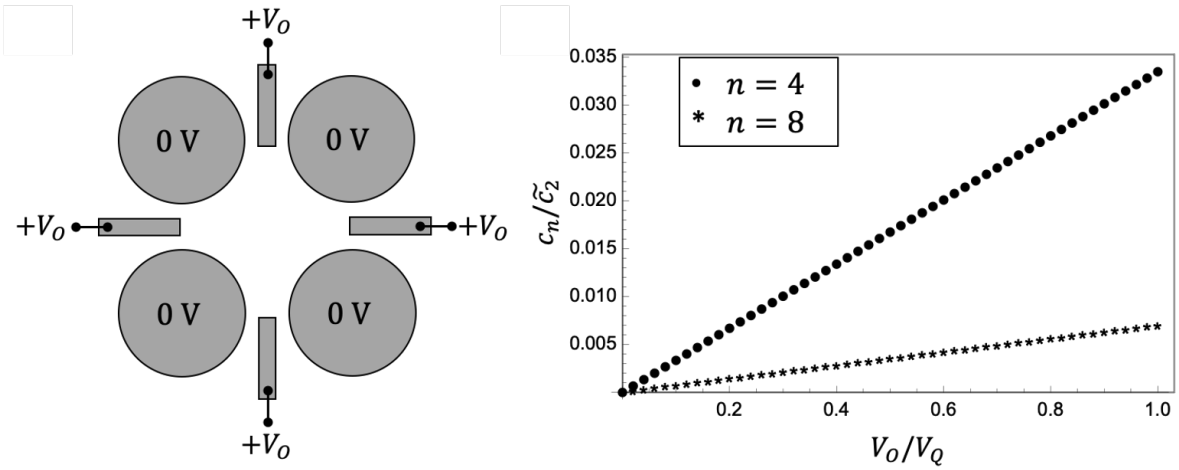

Figure 4.7: Nonlinear trap operating in octupole mode. (Left) Cross section of trap with the four quadrupole rods grounded and a voltage of V_O applied to the multipole plates. (Right) The ratio $c_n/\widetilde{c}_2$ is plotted for the octupole ($n = 4$) and 16-pole ($n = 8$) components as the voltage V_O is varied. The multipole components are normalised by $\widetilde{c}_2$ which is the quadrupole component measured when the nonlinear trap is operating in quadrupole mode with voltage V_Q.

These results agree well with the investigation carried out at Hiroshima University for the nonlinear upgrade to the S-POD trap [99] where the following, more general,

[2]Note that the quadrupole rods do not need to be grounded and can have a DC potential or a quadrupole potential applied. The resulting potential will be a superposition of the two fields.

relationship was found to minimise c_6: for a plate width of w and inscribed radius of R_0, in the presence of the quadrupole electrodes at an inscribed radius of r_0,

$$\frac{R_0}{r_0} = 1.948 + 0.153 \log(\frac{w}{r_0}). \tag{4.2}$$

The octupole strength can be increased by bringing the plates closer to the center of the trap and hence reducing R_0. However, the width of the plates, w, must also be reduced in order to continue minimising the c_6 component when operating in the quadrupole mode.

4.2.2.4 Effect of electrode misalignments

The Paul trap can never be perfectly aligned in practice, therefore it is essential to study the effects that these misalignments have on the multipole components. To investigate the effects of misalignments, all electrodes were simultaneously shifted from their ideal position by a Gaussian distributed error and the field decomposition was compared to the ideal case (no error). Table 4.1 summarises the multipole-component strengths for the linear trap and nonlinear trap with plate electrodes ($R_0 = 8.5\,\text{mm}$), operating in quadrupole mode and octupole mode. Results were averaged over 20 Mathematica simulations with randomly generated misalignments. Two different sizes of root-mean-square (RMS) alignment errors of 50 µm and 100 µm are applied to the electrodes. These alignment errors were chosen to simulate the worst-case scenario for misalignment of the new trap. The previous trap saw some misalignments in the horizontal positioning of certain electrodes of up to 168 µm, however most alignment tolerances were within 25 µm [39, 64].

All multipole components are excited once alignment errors are introduced, however they remain below 1 % of the dominant component of the field, with the exception of the dipole (c_1) component. The dipole component is not a concern in a Paul trap, as it only shifts the center of the ion distribution and will not cause any nonlinearities. Fukushima and Okamoto calculated that the dipole component caused by the largest simulated misalignments will only displace the center of the ion distribution by less than

Table 4.1: Multipole components dependence on misalignments in the trap electrodes. The multipole components (as a percentage) for alignment errors of 50 µm and 100 µm are compared to the ideal alignment case (no error) for the linear trap, the nonlinear trap operating in quadrupole mode and the nonlinear trap operating in octupole mode.

		$c_1/\widetilde{c}_2$	$c_2/\widetilde{c}_2$	$c_3/\widetilde{c}_2$	$c_4/\widetilde{c}_2$	$c_5/\widetilde{c}_2$	$c_6/\widetilde{c}_2$	$c_7/\widetilde{c}_2$	$c_8/\widetilde{c}_2$
Quadrupole mode (Linear trap)	No error	0	100	0	0	0	0.03	0	0
	50 µm	1.41	100.31	0.35	0.04	0.07	0.05	0.01	0.02
	100 µm	2.81	99.19	0.69	0.05	0.13	0.05	0.02	0.03
Quadrupole mode (Nonlinear trap)	No error	0	100	0	0	0	0	0	0
	50 µm	1.44	99.70	0.37	0.03	0.06	0.04	0.02	0.02
	100 µm	2.73	99.68	0.72	0.07	0.12	0.08	0.02	0.02
Octupole mode (Nonlinear trap)	No error	0	0	0	3.17	0	0	0	0.66
	50 µm	0.20	0.09	0.07	3.15	0.08	0.04	0.02	0.66
	100 µm	0.26	0.17	0.10	3.18	0.11	0.07	0.04	0.65

0.1 mm [99]. When compared to the 5 mm beam aperture, this amount of displacement should not cause any beam loss as the transverse beam size in IBEX is typically around 1 mm in radius. When comparing the quadrupole-field decomposition in the linear trap and quadrupole trap, it is clear that the addition of the multipole electrodes will not negatively affect the quadrupole field, within the simulated alignment errors of the trap. These results agree well with those of the Hiroshima University group although it should be noted that, in their field analysis, the multipole decomposition was taken about the electrical center of the trap (hence $c_1 = 0$) whereas in this work, the decomposition was taken about the mechanical center (hence $c_1 \neq 0$).

4.2.3 Octupole strength

Revisiting Eq. 3.30, the octupole voltage for an ideal octupole ion trap, V_O can now be converted into the voltage that needs to be applied to the plates in the IBEX trap

design, V_{plates},

$$V_{\text{plates}} = gV_O(\tau) = \frac{2}{3}\frac{mc^2 r_0^4}{q}\frac{gt}{c_{\text{I}}^2\beta^3(\tau)}, \tag{4.3}$$

where $g = \widetilde{c}_2/c_4$ is a geometrical factor accounting for the size and configuration of the electrodes. For an ideal octupole potential with 8 identical electrodes with equal inscribed radius, $g = 1$. However, with the chosen configuration of smaller plate electrodes, at a larger inscribed radius when compared to the rod electrodes, the geometrical factor $g > 1$, requiring a larger voltage applied to the plates to achieve the same V_O. From the results in Fig. 4.7, $g = \widetilde{c}_2/c_4 = 1/0.034$ for plates of $w = 1\,\text{mm}$ and inscribed radius of $R_0 = 8.5\,\text{mm}$. Calculating the necessary plate voltage with a strength parameter $t = 1$ and $\beta_{\text{drift}} = 190.5$ m, we get $V_{\text{plates}} = V_O/0.034 = 502.65$ V.

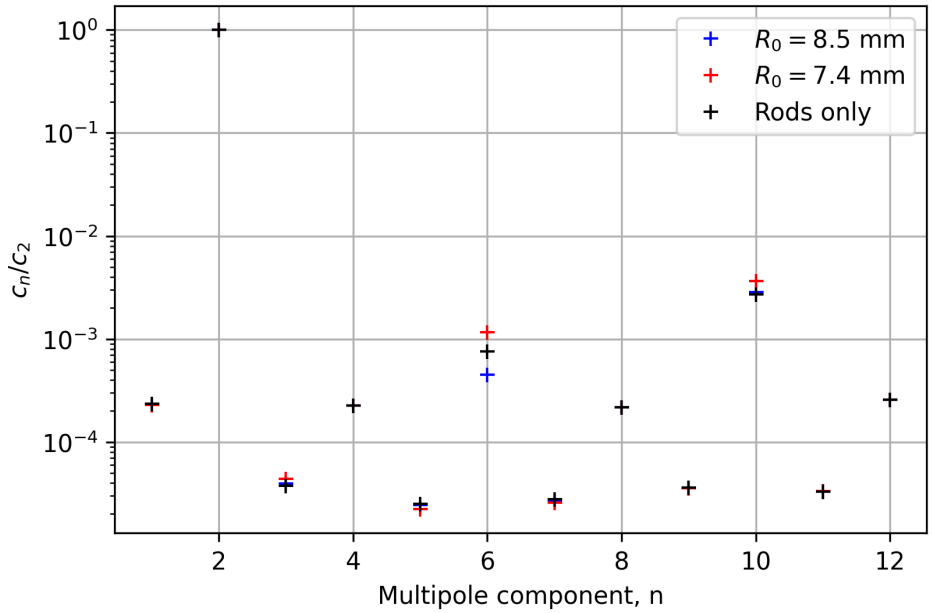

Figure 4.8: Multipole decomposition for the transverse quadrupole field in IBEX normalised to c_2. The decomposition was performed with no plate electrodes and $w = 1\,\text{mm}$ plate electrodes inserted at an inscribed radius of 8.5 mm and 7.4 mm.

As the trap was being designed in parallel with the high-voltage amplifiers that would drive the electrodes, it was not guaranteed that the amplifiers would reach the design voltage of ~ 500 V in order to create the desired octupole field strength. Therefore, it was decided that some flexibility would be built into the trap design in order to reach higher octupole strengths if needed. For this reason, two sets of plates were manufactured so

that they could be installed at two different inscribed radii, 8.5 mm and 7.4 mm. The set of plate electrodes with an inscribed radius of 7.4 mm (with $g = 1/0.085$) would give the option of providing a larger octupole field for a given voltage applied to the electrodes. For the same octupole strength as before, plates at this inscribed radius would only need an applied voltage of $V_{\text{plates}} = V_O/0.085 = 201.06$ V. As the minimum width of the plates was set to 1 mm due to manufacturing and alignment constraints, the 7.4 mm inscribed radius would have the drawback of increasing the c_6 component in the field. Figure. 4.8 shows the multipole decomposition performed for a quadrupole field in the multipole trap with no plate electrodes (four rod electrodes only), and 1 mm plate electrodes inserted at a radius of 8.5 mm and 7.4 mm. This multipole decomposition was performed using a 2D model of IBEX that I created in VSim. An inscribed radius of $R_0 = 8.5$ mm can be seen to reduce the c_6 component below that of the linear trap (four rod electrodes only). Due to the plate width not being decreased as the inscribed radius, R_0, is reduced according to Eq. 4.2, an inscribed radius of 7.4 mm can be seen to increase the c_6 component, above that of the linear trap configuration. Despite this increased c_6 component, the ability to reach higher octupole strengths in the future may be useful.

4.3 Engineering of the nonlinear trap

The new nonlinear section of the IBEX trap could have been manufactured and integrated with the existing linear section of IBEX. However, it was decided that a full redesign of the trap would be best in order to improve upon previous manufacturing tolerances and alignments. The trap configuration in Fig. 4.1 was decided upon with the final parameters summarised in Table 4.2.

These specifications were given to the ISIS design division and the engineering design was carried out by Ross Turnley in collaboration with Galen Aymar (Accelerator Design Group) and Dave Wilsher (Dimensional Metrology and Additive Manufacturing Facility). The Intense Beams group and I worked closely with the engineers throughout

the design process to ensure that it would meet our requirements and to help build flexibility into the trap design.

The goal was to design and manufacture the multipole trap to within mechanical and alignment tolerances of 10 µm. This is a significant improvement over the original IBEX trap design which had the majority of components to within 25 µm tolerances [39]. The CAD design of the new trap, created by Ross Turnley, is shown in Fig. 4.9.

Table 4.2: Parameters for the design of the multipole trap.

Parameter	Symbol	Value (mm)
Rod inscribed radius	r_0	5
Rod electrode radius	ρ_0	5.75
Plate inscribed radius	R_0	8.5, 7.4
Plate width	w	1
Plate height	h	6

The previous IBEX trap design had a separate ceramic body to hold each set of electrodes (i.e. end caps and central rods) as seen in Fig. 2.7. This made alignment from one set of electrodes to the next very difficult. The center bodies in the previous IBEX design were also square and the electrodes were pulled into the ceramic body to have two points of contact in order to align the electrode. It is difficult to reach <10 µm tolerances with this alignment technique as it is a manufacturing challenge to make two 90° flat surfaces of ceramic for the electrode to be pulled up against.

A centerpiece of the new design was the ceramic center body (labeled in Fig. 4.9 and photographed in Fig. 4.10). This center body was designed to align and position the gate electrodes and both sets of central electrodes. This ensures much better alignment between the ionisation region and the experimental region of the trap, and also improves the alignment between the central electrodes and end-cap electrodes. Figure 4.10 shows a photograph of this ceramic center body housing the central rod electrodes and new plate electrodes designed by the engineers. The center bodies were precision engineered out of Alumina, using jig grinding to get within 1 µm tolerance in orientation and form and within 5 µm tolerance in positioning of the holes to house the electrodes. The electrodes

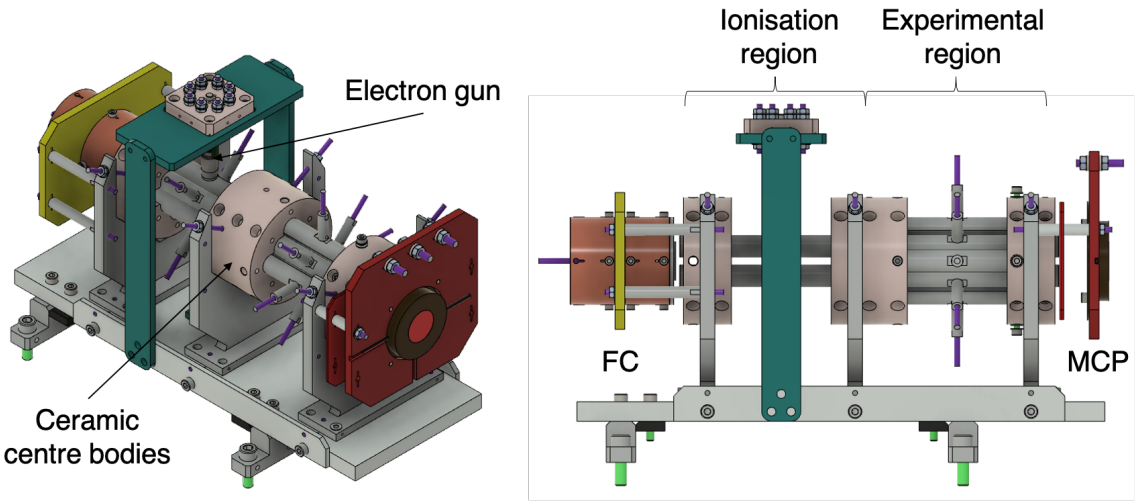

Figure 4.9: Engineer's CAD design of the new multipole IBEX trap.

were then pulled against the curved surface of the center body as the point of contact. This was a tried and tested technique of MTD Precision Engineering who make custom precision ceramic components for mass spectrometers [100]. The ceramic chosen for the new trap was Alumina as it is much less brittle than Macor which was previously used for IBEX-1.

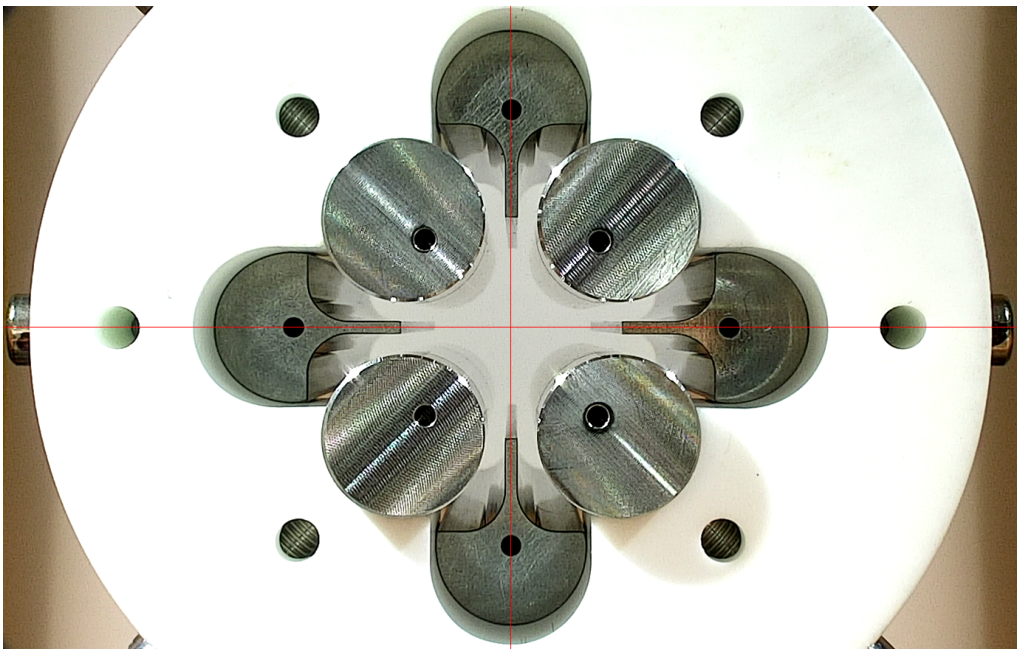

Figure 4.10: Photograph of assembled rods and plate electrodes in the new multipole trap. A cross hair is added to show alignment of the plate electrodes.

The plate electrodes were precision engineered using Electrical-Discharge Manufacturing (EDM) and were designed with a semi-circular top to aid manufacture and alignment (see Figure 4.10). Performing a multipole decomposition of the quadrupole field in a 2D VSim model of IBEX shows that the Engineer's plate design does not increase any nonlinearities when compared to the simple plate design, as shown in Fig. 4.11. Two sets of plates were manufactured, one with an inscribed radius of $R_0 = 8.5\,\text{mm}$ and another with $R_0 = 7.4\,\text{mm}$ to allow for the possibility of increased octupole strengths.

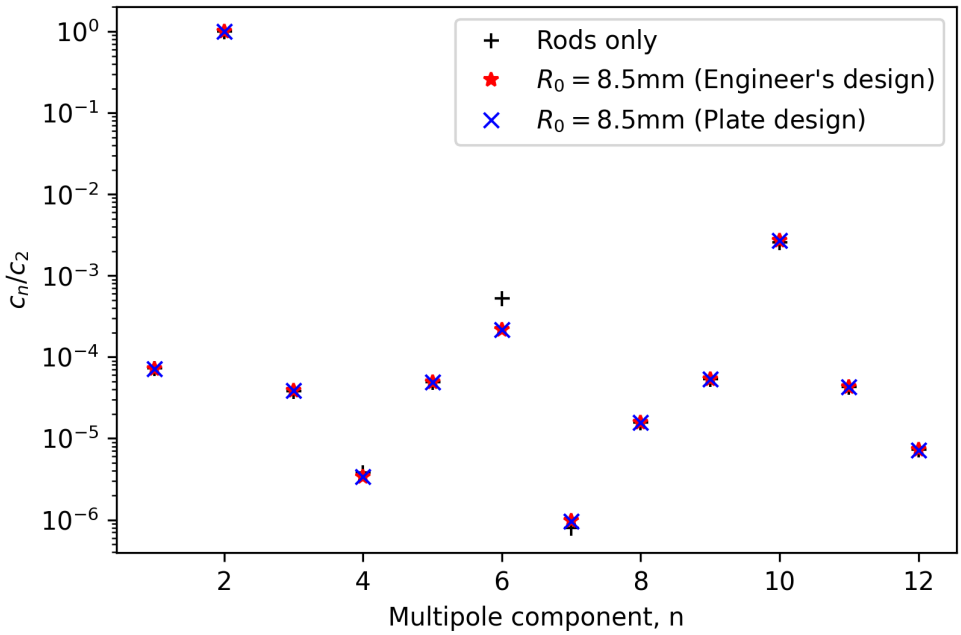

Figure 4.11: Multipole decomposition for the transverse quadrupole field in IBEX normalised to c_2. The decomposition was performed with no plate electrodes, the original $w = 1\,\text{mm}$ plate electrodes inserted at an inscribed radius of 8.5 mm and the engineer's plate electrodes design with a semi-circle top (see Figure 4.10).

After the new trap was manufactured, the machining tolerances for each component were measured by Dave Wilsher using a Coordinate Measuring Machine (CMM). The trap was then assembled and further CMM measurements were taken to confirm alignment tolerances. Nearly all components achieved a machining tolerance within 10 µm with the exception of the plate electrodes form[3] (or 'straightness') falling within

[3]Form tolerance is a geometric tolerance that constrains how straight a component must be made.

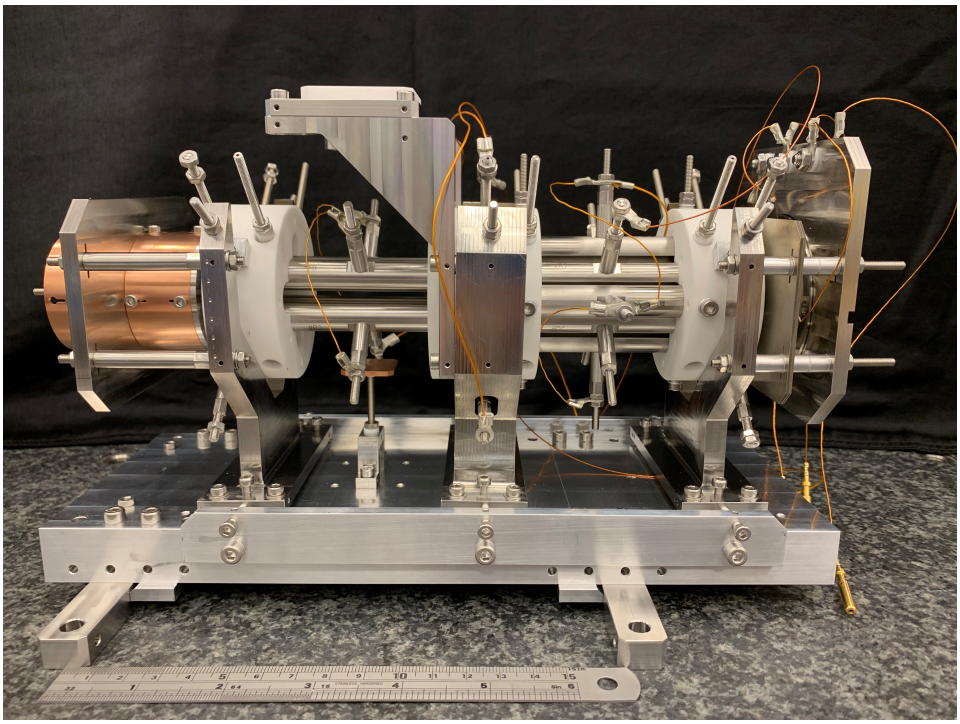

Figure 4.12: Photograph of the assembled multipole trap, IBEX-2 with a 15 mm ruler for scale.

a tolerance of <18 µm for the $R_0 = 8.5$ mm plates and a tolerance of <27 µm for the $R_0 = 7.4$ mm plates. Despite this, all transverse alignment tolerances of the electrodes were met (<10 µm) with the exception of the horizontal distance between the plate electrode 1 and rod electrode 1 (<12 µm). Overall the tolerances achieved for IBEX-2 were a significant improvement over the original IBEX trap. The mechanical and alignment tolerances in IBEX are summarised in Appendix A.

The new trap was then installed into the IBEX vacuum vessel and the electrodes and detectors were wired up to the respective flange ports. The trap was then baked out at 130°C to outgass while the vacuum vessel was pumped down to a pressure of $\sim 5 \times 10^{-10}$ mbar.

4.4 Design and commissioning of the high-voltage amplifiers

In addition to the precise manufacture and alignment of the trap electrodes, in order to trap ions and accurately test accelerator lattices, a precise, high-slew-rate amplifier is needed to drive the electrode voltages. Three additional amplifiers were required to drive the two pairs of central rods in the experimental region (ER) and the plate electrodes. The requirements for the octupole pulse applied to the plate electrodes is a 578 ns width pulse with a peak voltage of 500 V from the T-insert design in Section. 3.2. This requires a slew rate of greater than 1700 V/µs.

The previous, custom-built high-voltage (HV) amplifiers were designed and built for IBEX by Adam Baird from the Oxford Physics Central Electronics Group. These amplifiers used an APEX PA98 operational amplifier [68] with a peak-to-peak voltage of 450 V (± 225 V) and a typical slew rate of 1000 V/µs. This operational amplifier (op amp) would not meet the requirements for the octupole pulse and therefore the improved implementation of the APEX PA98, the APEX PA194, was chosen instead [101]. This new operational amplifier has a peak-to-peak voltage operation of 900 V (± 450 V) and slew rates of up to 2100 V/µs (1700 V/µs typically), with very low noise. Four PA194's (one for testing and three for the new amplifiers) were purchased from APEX technology and the amplifiers were again designed and manufactured by Adam Baird. My contribution involved performing the initial circuit simulations with LTspice in order to find suitable values for the circuit components and to test the PA194's slew rate and bandwidth. I was also involved in the testing stages of the circuit, along with Adam Baird, throughout the design process.

4.4.1 Design of the HV amplifier circuit

Figure 4.13 presents a schematic of the PA194 circuit which I simulated in the electronic circuit simulator software LTspice [102]. Values given in Fig. 4.13 are set to the optimum values found through simulation in this section. The rod electrodes were measured to

have a capacitance of 50 pF and hence each pair has a capacitance of 100 pF. As each pair of rod electrodes is driven by a single amplifier, a 100 pF capacitance is added to the circuit as a load with a 1 kΩ resistor. The HV power supplies are labelled 'PS+' and 'PS-', with voltages given in volts, and are shown off to the side in Fig. 4.13 for clarity. Due to the voltage bias across the PA194 being limited to 900 V, the largest symmetrical voltage bias for the power supplies is +450 V/−450 V. To get the required 500 V plate voltage, an asymmetrical bias, for example +550 V/−350 V, is needed. It should be noted that although this asymmetrical voltage bias can achieve higher positive voltages (up to 860 V with +860 V/−40 V), this cannot be applied in the negative direction as the negative power supply terminal is limited to −450 V and each pin needs a supply of at least 40 V [101].

A SPICE (Simulator Program with Integrated Circuit Emphasis) model of the PA194 op amp was downloaded from the APEX website [101]. The input signal (V_{in}) to the amplifier originates from a power supply which simulates the output voltage from the Arbitrary Waveform Generator (AWG). This input signal is connected to the negative terminal of the op amp labelled "-IN", resulting in the amplifier operating as an inverting op amp. This means that the input signal is inverted as well as amplified and the gain of the circuit is defined by

$$A = -\frac{R_{\text{F}}}{R_{\text{in}}} = \frac{V_{\text{out}}}{V_{\text{in}}}, \tag{4.4}$$

where R_{in} is the resistance on the input, R_{F} is the resistance of the feedback resistor, and V_{in} and V_{out} are the input and output voltage signals respectively. In electronics, the gain of an amplifier is often measured on a logarithmic scale and given in dB using the following relation,

$$A_{\text{dB}} = 20 \log_{10} \left(\frac{V_{\text{out}}}{V_{\text{in}}} \right). \tag{4.5}$$

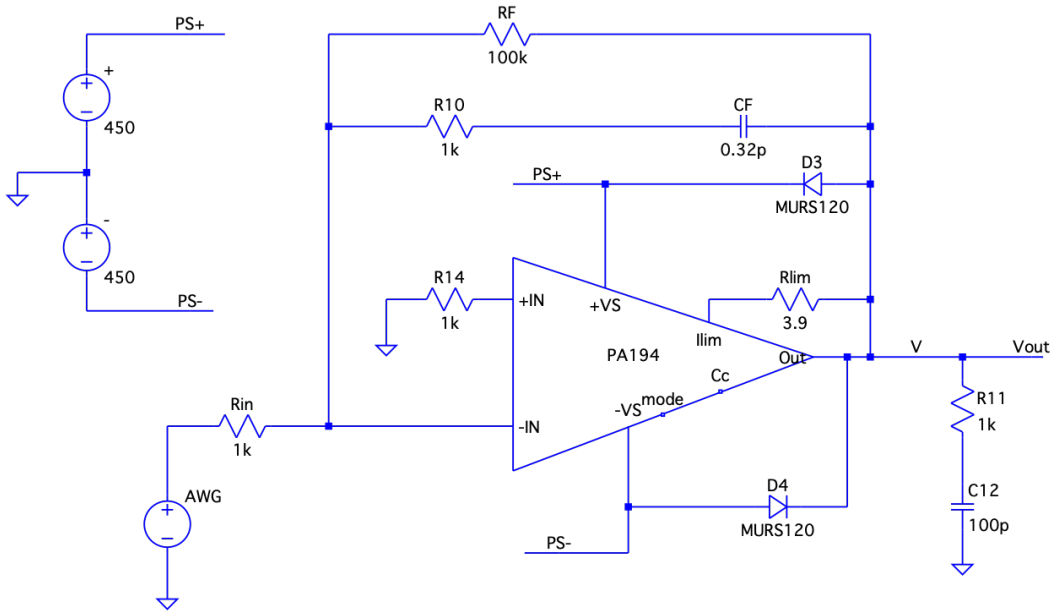

Figure 4.13: LTspice circuit diagram for the APEX PA194 operational amplifier. Resistors are labelled 'R' and given in units of Ohms, capacitors are labelled 'C' and capacitance is given in Farads, and diodes are given the symbol 'D'. Components are set to the optimal values as found in this section.

4.4.1.1 Reducing ringing

The amplifier for the plate electrodes needed to have a gain of at least 100 (40 dB) so that it could convert a 5 V pulse from the AWG (max. output voltage is ± 5 V) into a 500 V output pulse to create the desired octupole field strength. To achieve this gain, simulations were initially run with an input resistance of $R_{\text{in}} = 500\,\Omega$ and a feedback resistor of $R_{\text{F}} = 50\,\text{k}\Omega$ to give a gain of 100. Initial simulations also did not include a feedback capacitor C_{F}. This resulted in high-frequency ringing of the signal as seen in Fig 4.14(Bottom) in magenta for the octupole waveform and again in Fig 4.15(Top) in magenta for the T-insert waveform. The addition of a feedback capacitor can reduce the amplification of high-frequency noise and therefore reduce ringing in the amplified waveform. This is an in-loop compensation technique, meaning that it is applied within the amplification loop and is referred to as Miller compensation [103].

In Fig. 4.14(Top) a 2.25 V QI octupole pulse was amplified with a gain of 100 by an ideal op amp with infinite slew rate (green) and the PA194 with varying levels of feedback

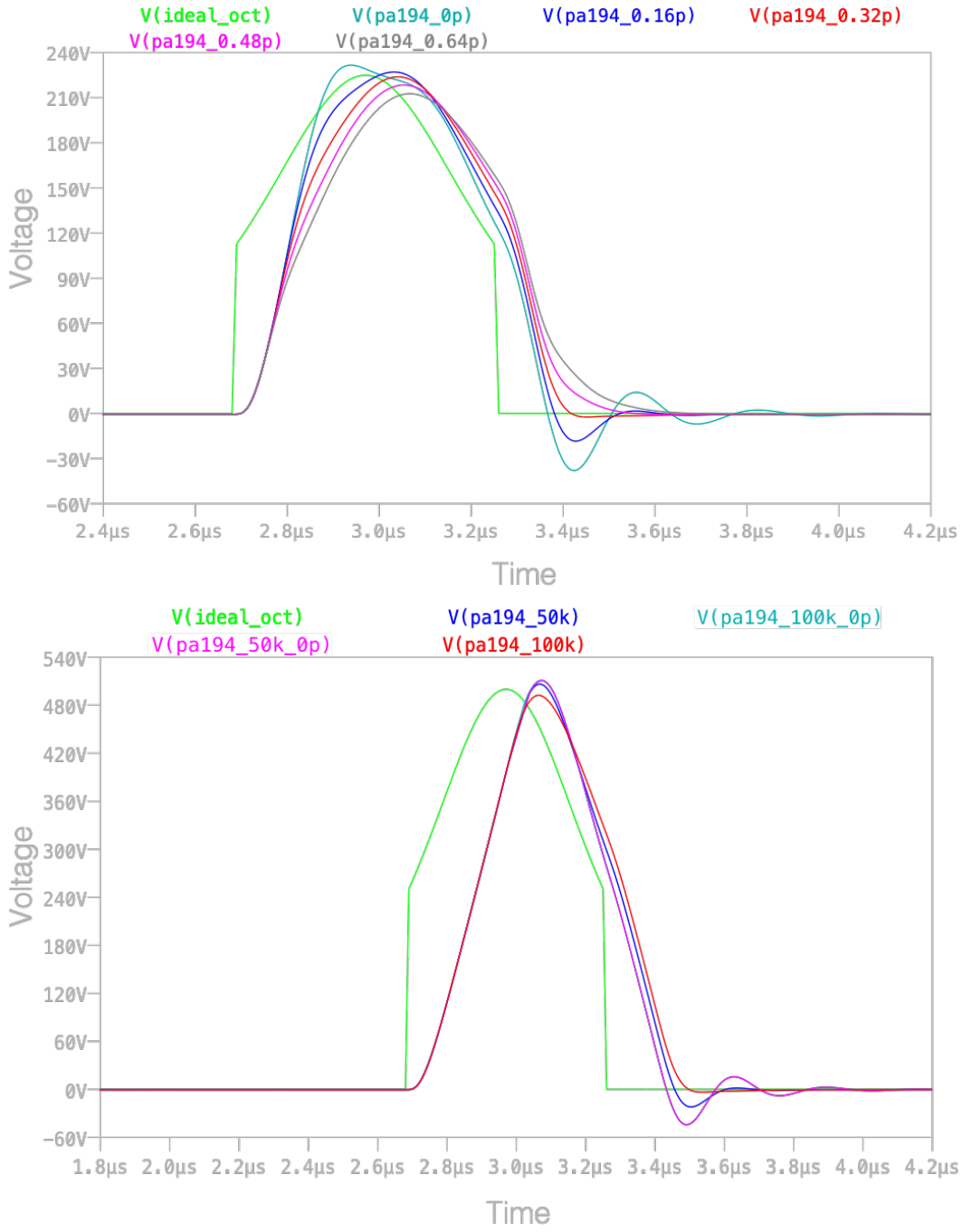

Figure 4.14: Amplified QI octupole waveform simulated in LTspice. (Top) A 2.25 V octupole pulse is amplified 100 times by an op amp with infinite slew rate (green) and compared to the PA194 op amp with a feedback capacitance of 0 - 0.64 pF. (Bottom) A 5 V octupole pulse is amplified 100 times by an op amp with infinite slew rate (green) and compared to the PA194 op amp with $R_F = 50\,\text{k}\Omega$, $C_F = 0.32\,\text{pF}$ (blue), $R_F = 100\,\text{k}\Omega$, $C_F = 0\,\text{pF}$ (cyan), $R_F = 50\,\text{k}\Omega$, $C_F = 0\,\text{pF}$ (magenta), and $R_F = 100\,\text{k}\Omega$, $C_F = 0.32\,\text{pF}$ (red).

capacitance $C_F = 0.0 - 0.64\,\text{pF}$. When the feedback capacitor is set to $C_F = 0.0\,\text{pF}$, (cyan) the amplified octupole pulse is seen to overshoot the desired peak voltage of 225 V in Fig 4.14(Top) and a large amount of ringing is seen after the octupole pulse. Increasing the capacitance of the feedback capacitor leads to the damping of high frequency ringing in the octupole pulse. However, adding too much capacitance can over-damp the ringing as seen with a capacitance of $C_F = 0.48\,\text{pF}$ (magenta) and $C_F = 0.64\,\text{pF}$ (grey). A capacitance of $C_F = 0.32\,\text{pF}$ can be seen to damp the ringing without over-damping and without compromising significantly on slew rate (see Section 4.4.1.2 for slew-rate measurements).

Figure 4.14(Bottom) plots a 5.0 V QI octupole pulse, again amplified by an ideal amplifier with a gain of 100 (green). The power-supply bias was changed from ±450 V to +550 V/−350 V in order to reach an output pulse of 500 V. The circuit was simulated with the PA194 op amp having an $R_{in} = 500\,\Omega$ and a feedback resistor of $R_F = 50\,\text{k}\Omega$; with $C_F = 0\,\text{pF}$ (magenta) and with $C_F = 0.32\,\text{pF}$ (blue). Fig. 4.14(Bottom) also shows the circuit simulated with $R_{in} = 1\,\text{k}\Omega$ and $R_F = 100\,\text{k}\Omega$; with $C_F = 0\,\text{pF}$ (cyan) and with $C_F = 0.32\,\text{pF}$ (red). With no feedback capacitance ($C_F = 0\,\text{pF}$), high-frequency ringing can again be seen after the pulse for the overlapping cyan and magenta voltage signals. Therefore, whether the gain is achieved by $A = 50\,\text{k}\Omega/500\,\Omega$ or $A = 100\,\text{k}\Omega/1\,\text{k}\Omega$, the ringing is dominated by high frequencies. When the feedback resistor of $C_F = 0.32\,\text{pF}$ is added in parallel with the feedback resistor (as shown in Fig. 4.13), the ringing is damped. However, we can see that the circuit with $R_{in} = 1\,\text{k}\Omega$ and $R_F = 100\,\text{k}\Omega$ (red) reduces ringing more than the circuit with $R_{in} = 500\,\Omega$ and $R_F = 50\,\text{k}\Omega$.

The same effect is seen in Fig. 4.15(Top) for the T-insert waveform, where the configuration of $R_{in} = 1\text{k}\,\Omega$ and $R_F = 100\,\text{k}\Omega$ with $C_F = 0.32\,\text{pF}$ (red) reduces ringing and overshoot of the signal when compared to the circuit with $R_{in} = 500\,\Omega$ and a $R_F = 50\,\text{k}\Omega$ with $C_F = 0.32\,\text{pF}$ (blue) and compared to having no feedback capacitor (magenta).

Finally, the PA194 with the circuit configuration in Fig. 4.13 is compared to the LTspice model of the PA98 op amp in Fig. 4.15(Bottom) for an amplified T-insert wave-

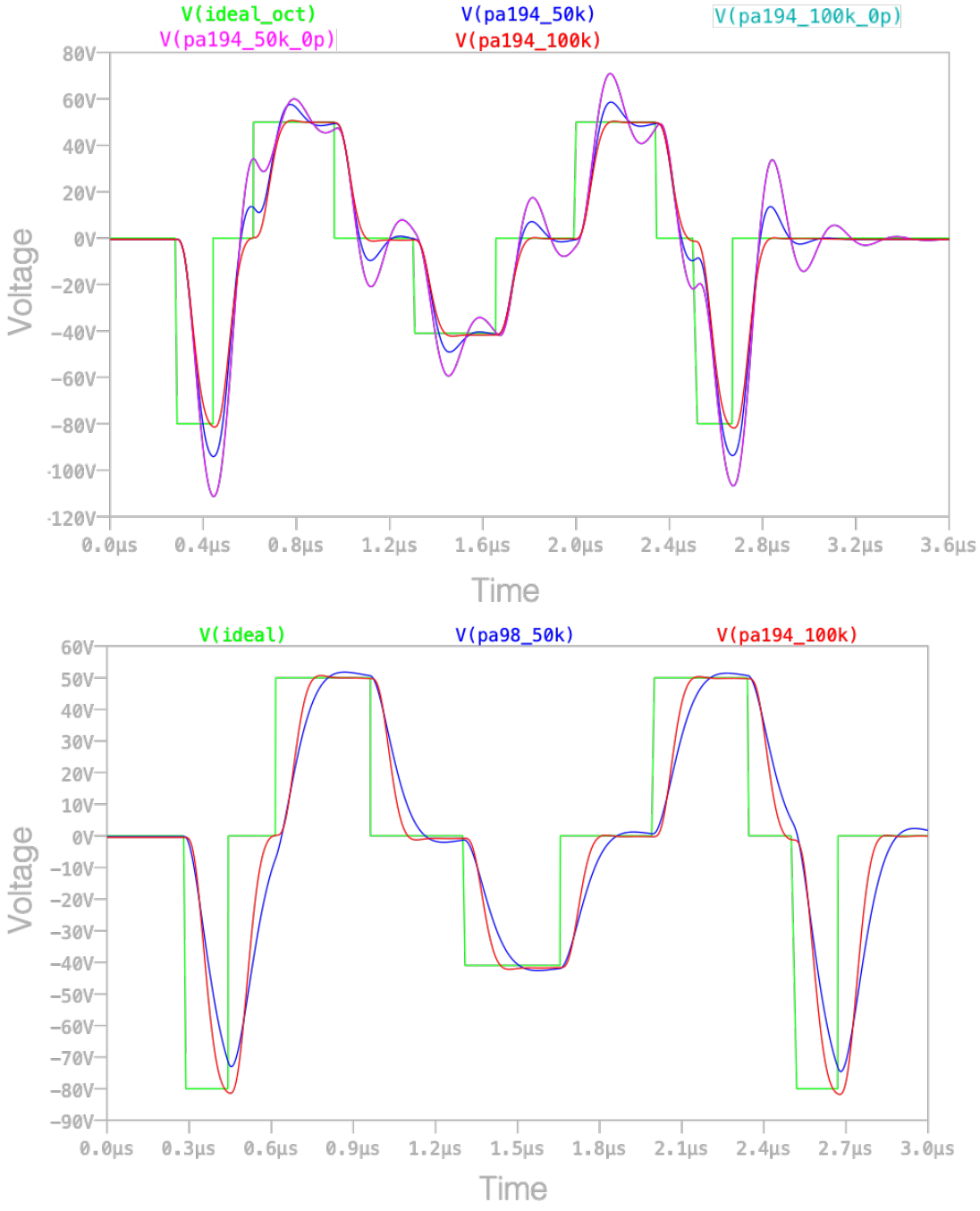

Figure 4.15: Amplified one-cell T-insert waveform simulated in LTspice. (Top) T-insert waveform amplified 100 times by an op amp with infinite slew rate (green) and compared to the PA194 op amp with $R_F = 50\,\mathrm{k\Omega}$, $C_F = 0.32\,\mathrm{pF}$ (blue), $R_F = 100\,\mathrm{k\Omega}$, $C_F = 0\,\mathrm{pF}$ (cyan), $R_F = 50\,\mathrm{k\Omega}$, $C_F = 0\,\mathrm{pF}$ (magenta), and $R_F = 100\,\mathrm{k\Omega}$, $C_F = 0.32\,\mathrm{pF}$ (red). (Bottom) T-insert waveform amplified by an op amp with infinite slew rate (green), PA98 op amp $R_F = 50\,\mathrm{k\Omega}$ (blue) and PA194 op amp $R_F = 100\,\mathrm{k\Omega}$, $C_F = 0.32\,\mathrm{pF}$.

form. The input waveform into the PA98 op amp was twice as large as the input into the PA194, as the gain of the PA98 amplifiers designed by Adam Baird was only 50. The LTspice simulations show a greater slew rate for the waveform amplified by the PA194 op amp, achieving a better approximation of the square wave T-insert waveform. In the following section we will quantify and compare the simulated bandwidth and slew rates of the PA98 and PA194.

4.4.1.2 Simulating bandwidth and slew rate of PA98 and PA194

The gain of the PA98 and PA194 op amps was simulated across a frequency range of 100 Hz to 10 MHz to compare the bandwidth of the amplifiers. The bandwidth is taken to be the frequency at which the gain has fallen by 3dB compared to its mean value at low frequencies. The results are shown in Fig. 4.16. The PA98 op amp was designed to have a gain of 50 (33.98 dB) and can be seen to achieve this gain for frequencies of 100 Hz to around 1 MHz where the gain starts to drop off. At a frequency of 3 MHz, the PA98 only has a gain of 63 % of its design value. In comparison, Fig. 4.16 shows that the frequency drop off of the PA194 op amp occurs later.

We can see that for the PA194 op amp with no feedback capacitor ($C_{\mathrm{F}} = 0\,\mathrm{pF}$), the gain increases at frequencies higher than 1 MHz to a maximum of 199 (46 dB) at a frequency of 3.6 MHz. Adding a feedback capacitor of $C_{\mathrm{F}} = 0.32\,\mathrm{pF}$ to the circuit, we can see that the bandwidth of the amplifier is effectively reduced from approximately 6 MHz to 5 MHz, but with the advantage of damping ringing in the circuit. At a frequency of 3 MHz, the PA194 op amp with $C_{\mathrm{F}} = 0.32\,\mathrm{pF}$ still has a gain of 88 (38.9 dB) which is 88 % of the design value.

The phase between the input waveform and the output waveform of the amplifier is also plotted in Fig. 4.16. As the simulated circuits are inverting op amps, the output signal is 180° out of phase with the input at 0 Hz. The phase difference starts to lag around 10 kHz and by 300 kHz the amplified signal from the PA194 has a 170° phase offset with the input signal. The phase delay between the input and output signal

becomes a problem when driving voltages in the electrodes of a Paul trap if different amplifiers are used with different phase delays. At a frequency of 1 MHz, the phase delay between the PA98 op amp and PA194 op amp is 6.5°, which can be accounted for with an initial phase offset of the input waveform. However, when driving a waveform with multiple frequency components, this cannot be easily corrected, as the phase delays are frequency dependent. This problem is minimised by ensuring that the same amplifiers are always used on adjacent pairs of rods in the trap.

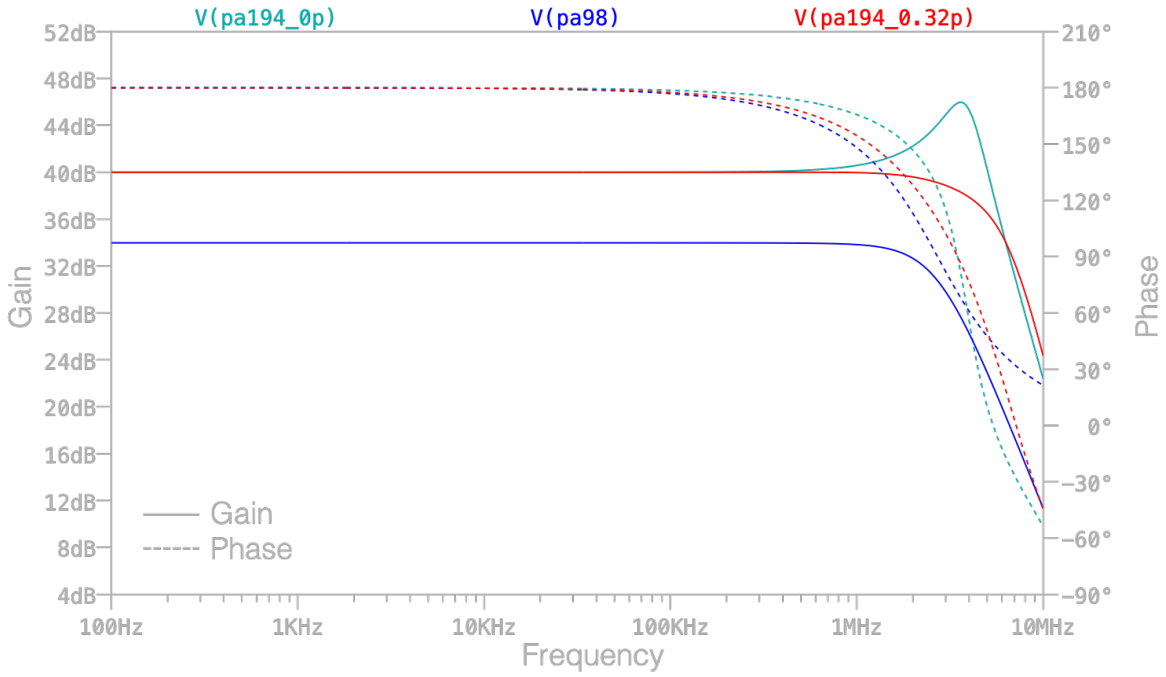

Figure 4.16: Simulated bandwidth and phase of the PA194, $C_F = 0.32\,\text{pF}$ (red), PA194, $C_F = 0.0\,\text{pF}$ (cyan) and PA98 (blue) op amp. Gain is plotted in dB (bold) and phase between the input and output signal is shown in degrees (dashed).

The rising and falling slew rates for the PA98 and PA194 op amps were also simulated in LTspice. In this chapter, I define the rising slew rate as

$$\text{Slew rate} = \frac{\Delta V_{10\%\text{ - }90\%}}{t}, \tag{4.6}$$

where $\Delta V_{10\%\text{ - }90\%}$ is the voltage increase from 10 % of the voltage pulse amplitude to 90 % and t is the rise time taken. The PA194 op amp slew rate was measured at three different power-supply biases, +225 V/-225 V, +450 V/-450 V and +550 V/-350 V. The input

pulse was set to be a square wave with amplitudes of 2 V, 4.5 V and 5 V respectively for the three power-supply configurations for the PA194 with a gain of 100. The PA194 op amp was also tested with and without a feedback capacitor of $C_F = 0.32\,pF$. The PA98 was only tested with a 4 V input pulse (as it has a gain of 50), with a power-supply bias of +225 V/-225 V as it can only operate with a maximum of 450 V across the terminals.

The slew rates measured in LTspice are summarised in Table 4.3. At a power-supply bias of +225 V/-225 V, the PA194 op amp can be seen to have around a 30 % larger slew rate than the PA98, even when the feedback capacitor is included. With this power-supply configuration, the difference in rising and falling slew rate for the PA194 without the feedback capacitor is seen to be around 8.9 %. This difference is reduced to only 1.2 % for the PA194 with $C_F = 0.32\,pF$. The slew rate improvement of the PA194 over the PA98 increases by around 60 % for power-supply biases of +450 V/-450 V and +550 V/-350 V. Operating at an asymmetrical power-supply bias of +550 V/-350 V does not seem to significantly affect the difference in rising and falling slew rates. The slew rates simulated with LTspice for the PA194 appear slightly lower than the typical values of slew rate quoted in the manual of up to 1700 V/µs. It is suspected that the slew rate for the LTspice model of the PA194 is set to a conservative value. Experimental results testing the performance of the amplifier circuit are presented in the next section.

Table 4.3: Simulated rising (+) and falling (−) slew rates for the PA98 and PA194 om amps. The PA194 is tested with and without a feedback capacitor, C_F and is tested at three different power-supply biases (+PS/-PS).

Op Amp	Slew rate (V/ µs)		
	+225 V/-225 V	+450 V/-450 V	+550 V/-350 V
PA98	+1027, -1027	-	-
PA194 ($C_F = 0.0\,pF$)	+1322, -1440	+1620, -1627	+1651, -1662
PA194 ($C_F = 0.32\,pF$)	+1293, -1309	+1591, -1594	+1642, -1646

4.4.2 Testing and commissioning of HV amplifiers

Figure 4.17 compares the simulated LTspice waveform amplified by the PA194 op amp, to the measured amplified signal from a PA194 test circuit. The LTspice circuit was the

same as that presented in Fig. 4.13 but with $C_F = 0\,\text{pF}$; the experimental circuit was set up to be the same as the simulated circuit. The power-supply bias was set to +450 V/-450 V in both cases. Due to the omission of the feedback capacitor, a large amount of ringing is seen on both the simulated and the experimental amplified signals. The LTspice model predicts the ringing in the circuit well as can be seen from the fairly good agreement of simulated and experimental data in Fig. 4.17.

Experimental data for the final PA194 circuit design is presented in Fig. 4.18 for the T-insert waveform and is compared to the current amplifiers using the PA98 op amp. For this test, the power-supply bias was set to +225 V/-225 V for both the PA98 and PA194 amplifiers. It is clear from Fig. 4.18 that the inclusion of a feedback capacitor (as well as other circuit compensation techniques that are beyond the scope of this thesis) have significantly reduced the ringing in the circuit when compared to Fig. 4.17. However, inspecting Fig. 4.18(Bottom), it is clear that there is still more overshoot and undershoot of the waveform in comparison to the amplified waveform from the PA98 amplifiers.

In Fig. 4.19, a QI octupole input pulse is compared to the amplified signal from the PA194 amplifier for a power-supply bias of +450 V/-450 V. The amplified signal has been overlaid over the input signal for comparison and hence is not indicative of the phase delay between the signals. Figure. 4.19 shows a good approximation of the octupole pulse.

The slew rates for the PA98 and PA194 amplifiers were also measured using a 1 MHz square-wave pulse with a duty factor of 30 % (i.e. the pulse is on for 0.3 µs and off for 0.7 µs). The slew rate is again defined by Eq. 4.6, where the voltage increase is measured between 10 % and 90 % of the maximum pulse voltage. The slew rate of the PA98 amplifier was tested at a power-supply bias of +225 V/-225 V and was found to have a rising slew rate of +1006 V/µs and a falling slew rate of +1005 V/µs. These values agree within 2 % of the simulated values presented in Table 4.3. The PA194 amplifier was tested at a power-supply bias of +450 V/-450 V and was found to have a rising slew rate of +1659 V/µs and -1643 V/µs. These slew rates are an improvement of around 4 % over

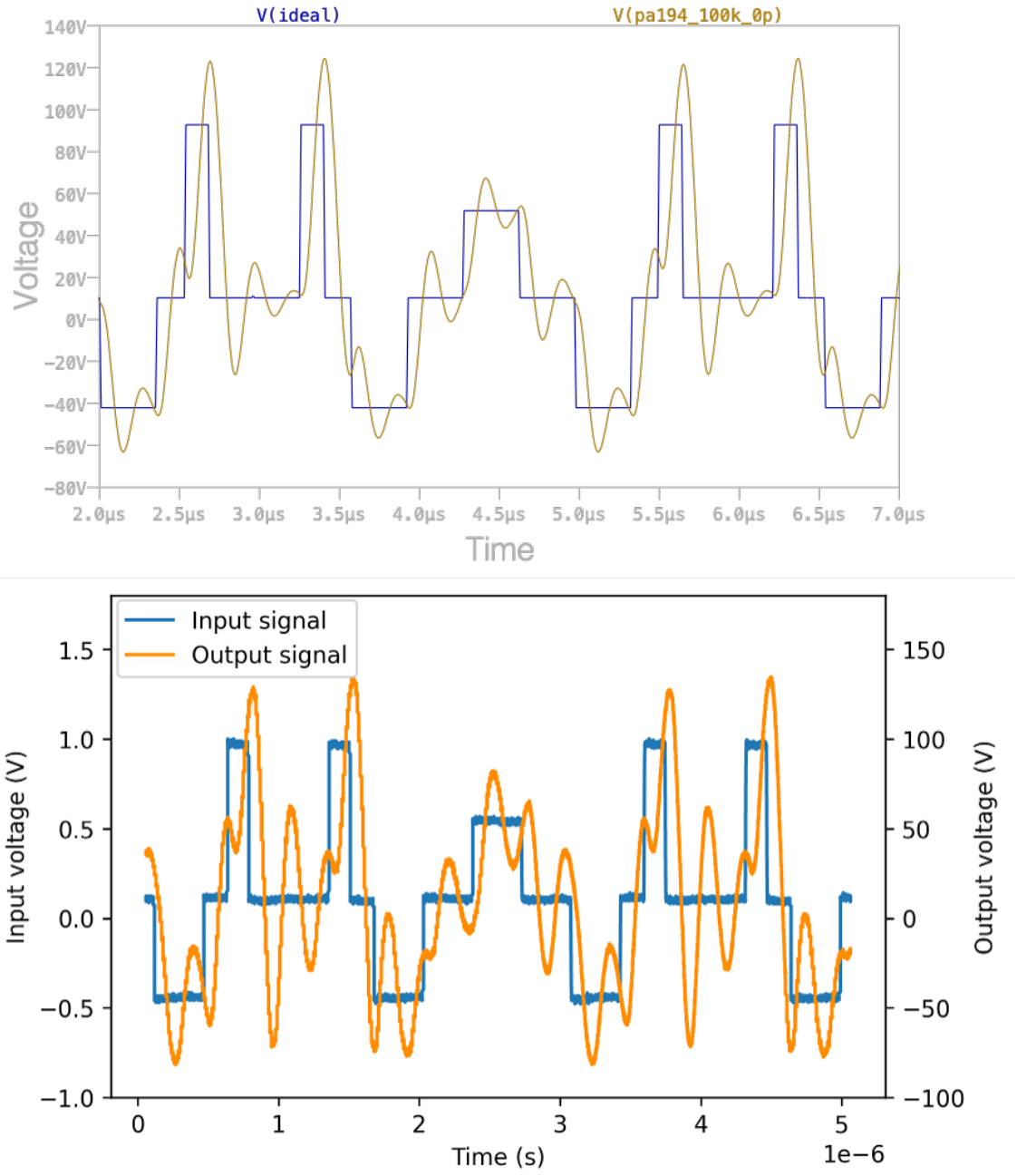

Figure 4.17: (Top) Simulated amplified signal of a T-insert waveform through an ideal amplifier (blue) and the PA194 op amp with $C_F = 0.0\,\text{pF}$ (brown). (Bottom) Measured input waveform from an AWG (blue) and measured amplified signal through an APEX PA194 op amp test circuit with $C_F = 0.0\,\text{pF}$ (orange).

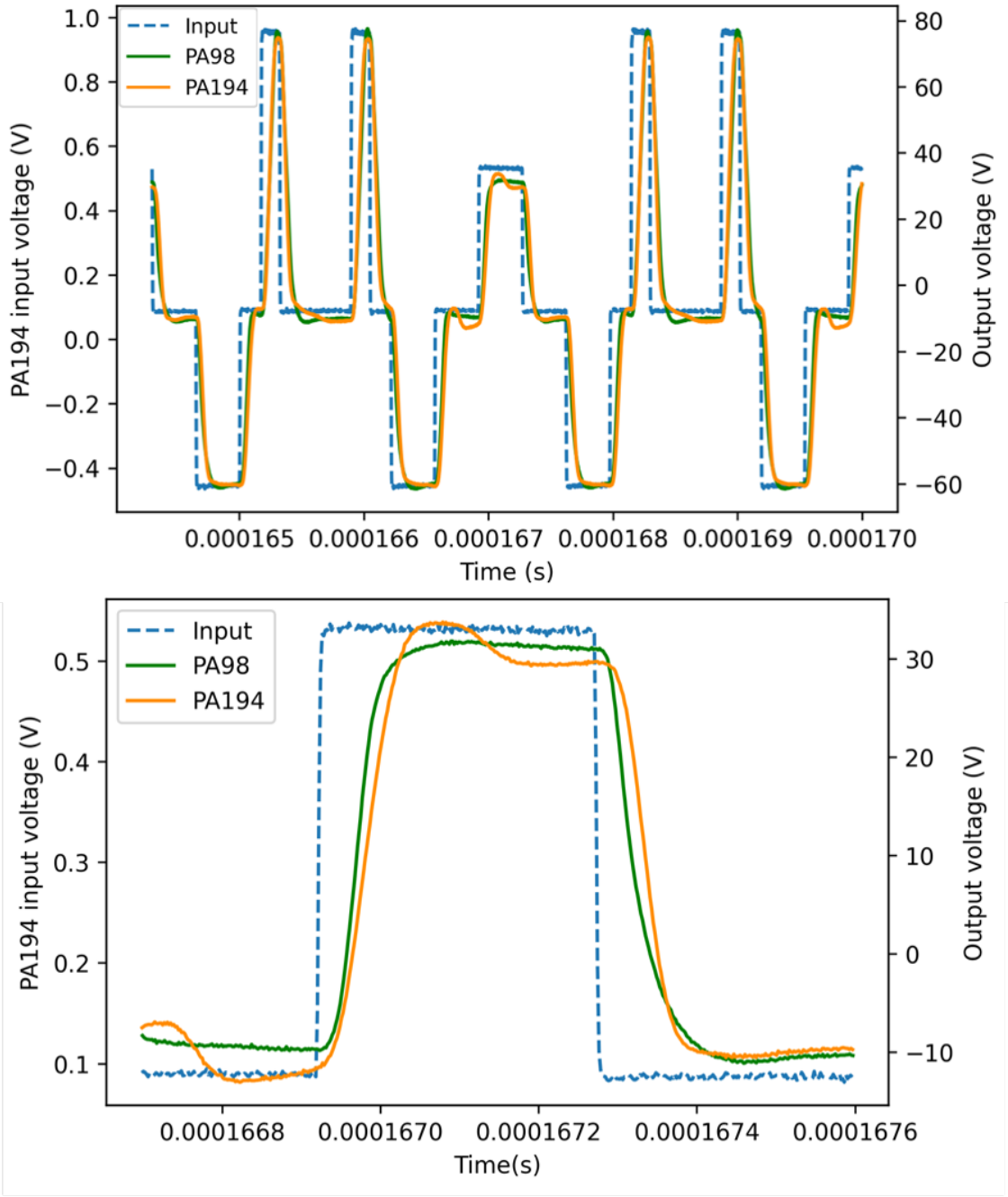

Figure 4.18: Experimental data of T-insert waveform. Input waveform for the PA194 amplifier is plotted in blue, dashed (input voltage to PA98 is twice as large due to its gain of 50 instead of 100). Amplified signal from the PA98 circuit is plotted in green and the amplified signal from the final PA194 design is plotted in orange. (Top) One and a half T-insert cells. (Bottom) Zoomed-in plot from the central square-wave pulse.

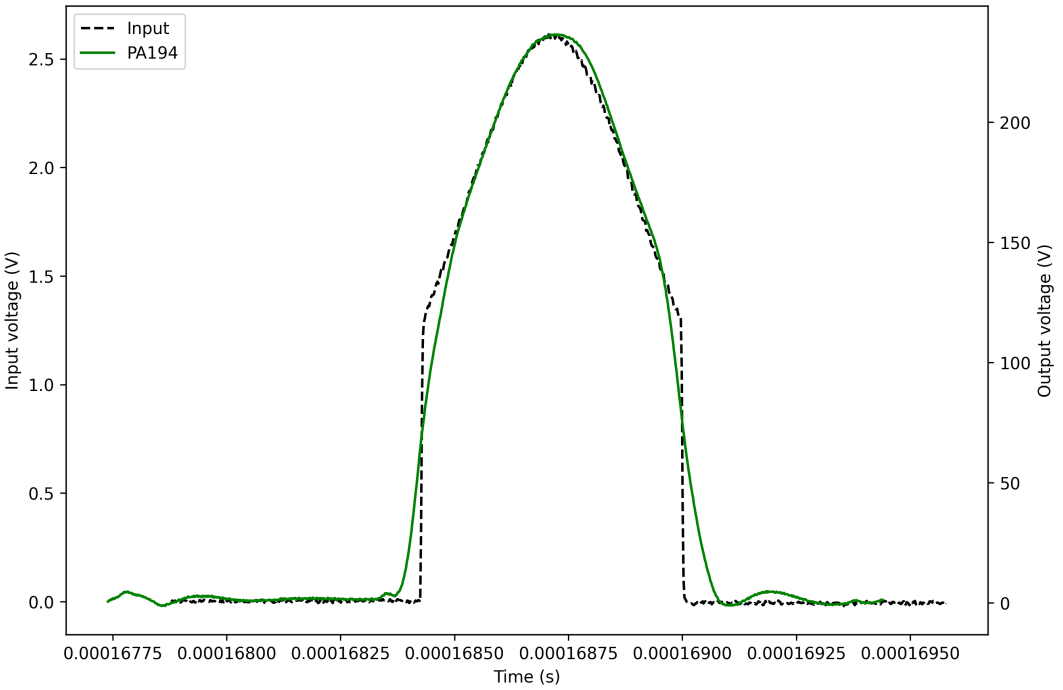

Figure 4.19: Octupole input waveform into the PA194 (black, dashed). Amplified octupole pulse from the final PA194 design (green). Waveforms have been overlaid onto one another.

the values predicted from simulation when the feedback capacitor was included. They agree to within 4 % with simulation values of the slew rate when no feedback capacitor was included in the circuit.

4.5 Commissioning the nonlinear trap: IBEX-2

A schematic of the normal trapping set up for IBEX-2 is shown in Fig. 4.20(Top). Argon gas is introduced into the vacuum vessel and an electron gun, positioned over the ionisation region (IR), ionises the argon, while RF voltages are applied to the electrodes in the IR, trapping the singly charged ions. A DC voltage of 25 V is applied to the Faraday Cup (FC) end caps and to the gate electrodes, shown in Fig. 4.20 for longitudinal confinement. Note that the detectors are not shown in the schematic but the FC detector would be located on the left-hand side, whereas the MCP detector would be on the right. After ionisation, the gate electrode DC voltage is dropped to the same DC voltage as the electrodes in the Experimental Region (ER). Due to a DC offset between the IR and ER, δV_{DC}, ions which were previously trapped in the IR will now be able to pass into the ER. After a certain time, determined experimentally in Section 4.5.4, the gate DC voltage is increased back to 25 V and the ions are stored in the ER for the desired experiment time. After the desired time has elapsed, the DC voltage on the MCP end caps is dropped to 0 V to accelerate the ions onto the MCP detector where they are measured destructively. The voltage waveforms were created in a Python script and sent to the Arbitrary Waveform Generators (AWGs) via a LabView program.

The new IBEX-2 trap was installed in the vacuum vessel in June 2022. At this point in time, the amplifier design was still ongoing and so there were not enough amplifiers to power each pair of electrodes separately. In order to start the commissioning of the trap without the new amplifiers, a different trapping mode, more closely resembling the previous trap, was initially implemented. This trapping mode is referred to as 'Long trapping mode' and is shown in a schematic in Fig. 4.20(Bottom). As shown in the schematic, the same DC bias is applied to the gate, IR and ER electrodes, allowing ions to be trapped and stored across the entire length of the trap[4]. For this experimental setup, each pair of electrodes (outlined in blue and red in Fig. 4.20) for the gate, IR

[4]Note that this trapping mode is not useful for applying octupole voltages to the plates as the ions will only experience these fields half of the time as they bounce back and forth between the IR and ER.

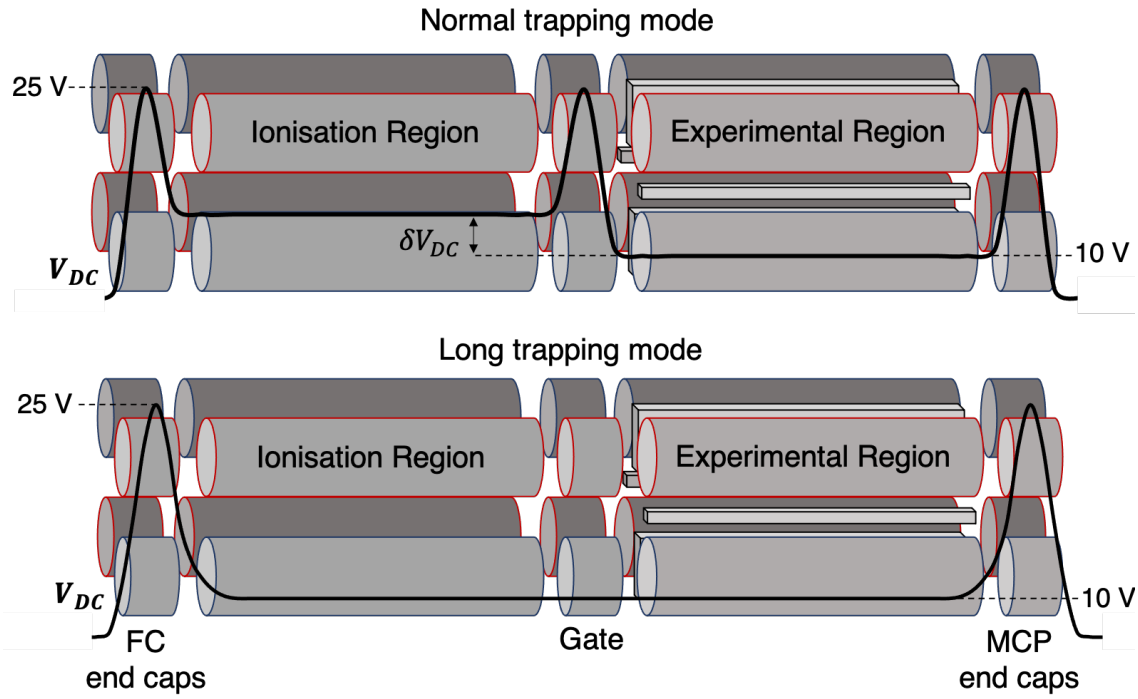

Figure 4.20: Longitudinal confinement in IBEX-2. (Top) Normal trapping mode where a DC voltage on the gate electrodes is dropped and raised to allow ions to be stored in the experimental region (ER) only. δV_{DC} is the DC bias between the ER and IR. (Bottom) Long trapping mode where the DC voltages applied in the ionisation region, experimental region and gate electrodes are all the same. In this configuration, ions are stored throughout the trap.

and ER were shorted together, external to the vacuum chamber. One Falco WMA-300 amplifier was used for each pair of opposing electrodes, meaning that only two amplifiers were needed to drive all six pairs of the gate, IR and ER electrodes. Another two WMA-300 amplifiers were used, one for each pair of electrodes on the MCP end caps, as these required a DC voltage of 25 V. This DC voltage needed to be dropped at a specific time to allow ions to be detected in the MCP, and therefore required a different input waveform to that applied to the central rods. A DC power supply was used to apply a constant DC voltage of 25 V to the FC end caps, as these voltages are not changed throughout the experiment and do not require an RF waveform to be applied. The setup on the MCP end caps and FC end caps can be switched in order to detect ions on the FC instead of the MCP detector.

Long trapping mode was used to calibrate the new MCP detector against the Faraday-

cup detector. Normal trapping mode was used to optimise the transfer of ions from the IR to the ER. Unless otherwise stated, normal trapping mode will be assumed throughout the rest of the experimental work with IBEX-2.

4.5.1 MCP signal

As described in Section 2.4, the MCP detector amplifies an incident ion signal onto the input plate with an electron cascade in the micrometer-diameter channels. Note that the MCP was only used in 'ion counting mode' and not 'imaging mode' throughout this thesis. The number of electrons that reach the phosphor screen is determined by the number of ions incident onto the detector, as well as the gain of the MCP. An example of a signal from the MCP detector measuring ions trapped in IBEX-2 is shown in Fig. 4.21. When the DC voltage on the MCP end caps is dropped from 25 V to 0 V, ions are accelerated towards the MCP detector. However, the drop in DC voltage also induces a voltage in the MCP detector, shown in black in Fig. 4.21. This induced voltage must be subtracted from the raw signal (green) to get the signal in blue. The ion number can be calculated from the integrated signal, I_{signal} using the equation,

$$N_{Ions} = \frac{I_{signal}}{eA(\text{Gain})_{\text{MCP}}}, \tag{4.7}$$

where e is the charge of the electron, $A = 5.74 \times 10^6\,\Omega$ is the gain of the phosphor screen amplifier and $(\text{Gain})_{\text{MCP}}$ is the gain of the MCP, defined in the next section in Eq. 4.8.

4.5.2 Calibrating the MCP detector

A new two-stage Hamamatsu P43 phosphor MCP [69] was fitted when the IBEX-2 trap was installed. The new MCP was very similar to the previous MCP, except that the bias angle on the micro-channels is now 12°, compared to the previous MCP which had a bias angle of 8°[5]. The previous MCP detector was calibrated by Lucy Martin [39]. Although both MCP detectors should have the same gain, because it was a new piece of

[5]Note that the bias angle does not affect the gain of an MCP but it will affect the detector efficiency [69].

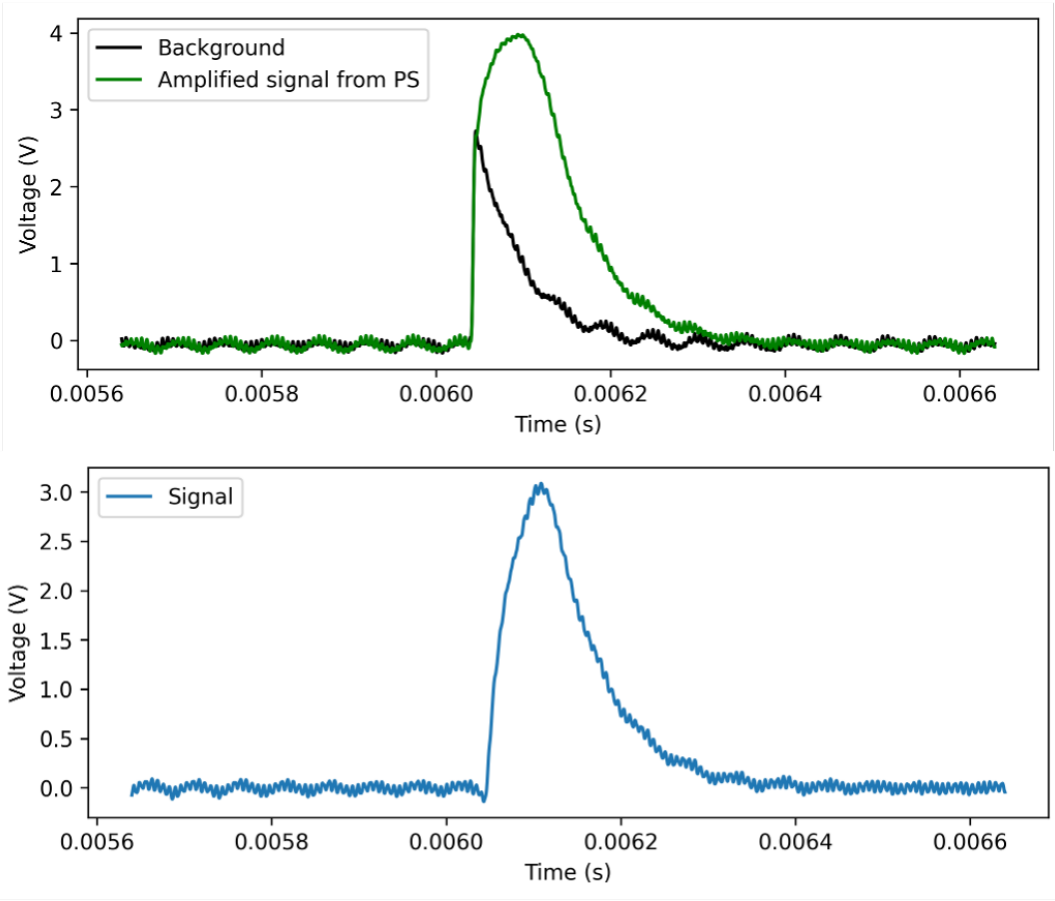

Figure 4.21: (Top) Oscilloscope trace of the signal detected on MCP when the electron gun is on is plotted in green. The background signal (from the MCP end-cap DC being dropped) when the electron gun is off is plotted in black. (Bottom) The signal plotted in blue is the subtraction of the background signal from the raw signal in the above plot.

equipment I performed a calibration to the FC detector to check if it differed from the previous calibration.

A simple model for the gain of a two-stage MCP detector is defined as [39],

$$(\text{Gain})_{\text{MCP}} = \left(\frac{U_{\text{MCP}}}{V_0 \alpha b}\right)^{\frac{\alpha}{2}}, \tag{4.8}$$

where $U_{\text{MCP}} = U_{\text{OUT}} - U_{\text{IN}}$ is the potential difference between the input and output plates of the MCP (see Fig. 2.9). The parameter $\alpha = L/d$ is the ratio of channel length (L) to the diameter of the channel (d) and for a standard MCP is often between 40 – 60 [69]. The parameter b is a property of the MCP material called the 'inherent secondary emission factor' which determines how many secondary electrons are emitted from the walls of the channels and V_0 is the initial energy of the emitted secondary electron

($\sim 1\,\mathrm{eV}$ [104]). The model of the MCP gain in Eq. 4.8 assumes that the detector acts as a series of dynodes (electron multipliers) [104, 105].

Therefore, for a given bias between the two plates in the MCP, U_{MCP}, each incident ion will correspond to multiple electrons. In order to convert between an electron number and an ion number, the MCP signal should be calibrated against the Faraday cup (FC) detector.

A FODO lattice with a cell tune of $Q_x = Q_y = 0.15$ was created in IBEX to store ions for 50,000 cell periods before the end-cap voltage was dropped and the ions were directed onto either the MCP or FC detector. This tune has previously been found to be optimum for storing ions during ionisation and hence remaining at this tune for the duration of the experiment does not require ramping to different electrode voltages [39]. The electron gun was turned on for 300 ms in each experiment, and the pressure of argon leaking into the vacuum vessel was varied from 1.2×10^{-7} – $1.6 \times 10^{-6}\,\mathrm{mbar}$ in order to vary the number of ions stored in the trap.

The number of ions measured on the FC and number of electrons measured on the MCP detector are plotted in Fig. 4.22. Each data point is the mean number of ions or electrons measured on the detector from 10 experiments. The standard deviation in number of particles detected is much larger for the FC detector when compared to the MCP detector. This is expected to be the case from the statistical error (proportional to $1/\sqrt{N}$, where N is the number of particles detected), as two orders of magnitude more particles are measured with the MCP, compared to the FC. However, the standard deviation in particles measured with the FC was further increased by a large amount of noise on the detector. This noise was found to be induced from a wire carrying a voltage to an end-cap electrode which passes over the wire carrying the FC signal, within the vacuum vessel. This wiring will be corrected the next time the vacuum vessel is brought back up to atmospheric pressure.

From calculating the gradient of a linear fit to the data in Fig. 4.22, the MCP gain, $(\mathrm{Gain})_{\mathrm{MCP}}$, for the given MCP bias, U_{MCP} can be obtained. The gains were found to

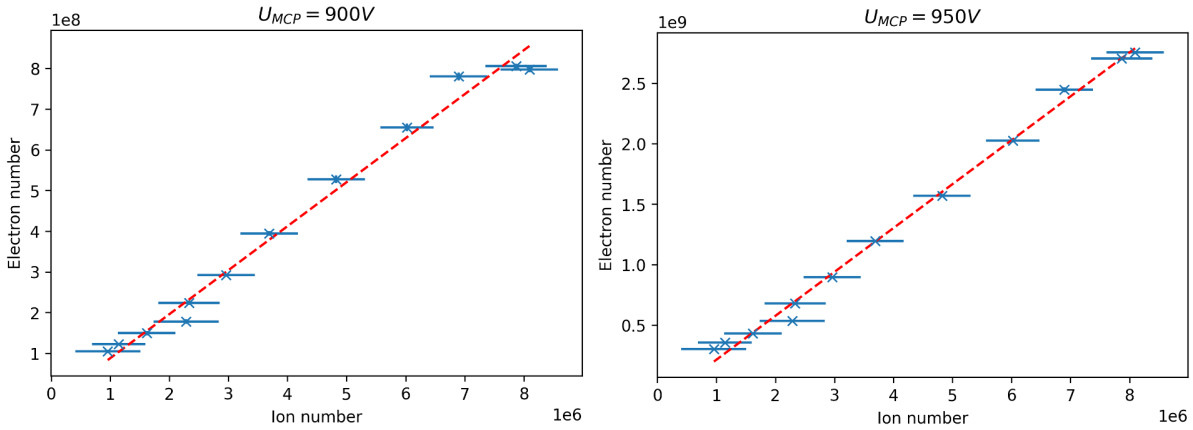

Figure 4.22: The number of electrons measured by the MCP detector, plotted against the number of ions measured with the FC detector for gas pressures between 1.2×10^{-7} mbar – 1.6×10^{-6} mbar. Each data point is averaged over 10 experiments for both the MCP and FC and the standard deviation in measured particles is indicated by the error bar. (Left) MCP bias set to $U_{\mathrm{MCP}} = 900\,\mathrm{V}$. (Right) MCP bias set to $U_{\mathrm{MCP}} = 950\,\mathrm{V}$.

be 108(4) for $U_{\mathrm{MCP}} = 900\,\mathrm{V}$ and 363(9) for $U_{\mathrm{MCP}} = 950\,\mathrm{V}$. Now the MCP bias can be varied for a constant ion number in the trap, in order to measure the MCP gain over a range of U_{MCP}. The MCP gain was measured in relation to the two known gains calculated from Fig. 4.22.

From the curve fit, the parameters $\alpha = 38.4(8)$ and $b = 9.13(2)$ were found from Eq. 4.8. The value of $\alpha = 38.4(8)$ is close to the value of 40 stated in the MCP data sheet. It also agrees, within the uncertainty, with the value of $\alpha = 37.74$ measured for the previous MCP [39]. The secondary electron emission factor can vary depending on material and the energy of the primary electron [106]. For most metals, the secondary-emission factor is between 1–2, however metal alloys can have an emission factor of between 6 to 20 [107]. It was difficult to find published values of the secondary electron emission factor for Inconel, however in [39] it is stated that the secondary emission factor of Inconel should be between 9.5 and 10. The calculated value of $b = 9.13(2)$ was found to be 8 % lower than the value obtained for the previous MCP of $b = 9.97$ [39].

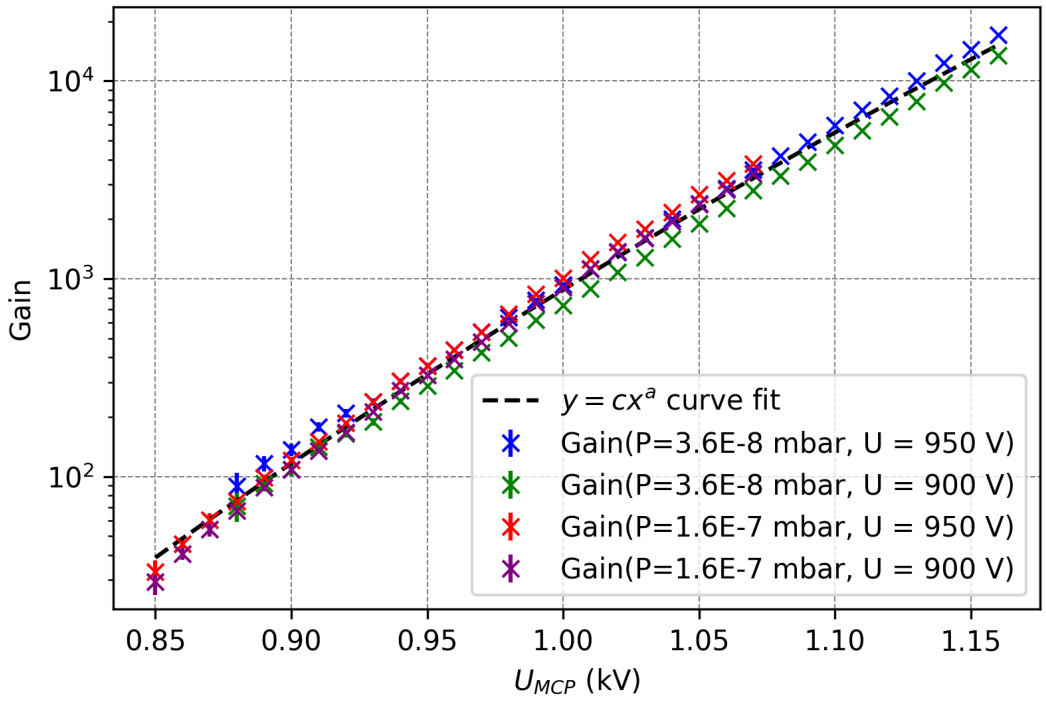

Figure 4.23: MCP gain for a given potential bias U_{MCP}. The gain was measured for two different ion numbers using an argon pressure of 3.6×10^{-8} mbar and 1.6×10^{-7} mbar. It was also measured using both the calibration point at $U_{\mathrm{MCP}} = 900\,\mathrm{V}$ and $U_{\mathrm{MCP}} = 950\,\mathrm{V}$. A curve with an equation of $y = cx^a$ was fitted to all data to calculate values for α and b from Eq. 4.8.

4.5.3 Synchronising multiple Arbitrary Waveform Generators

In order to successfully achieve 'Normal trapping mode' (Fig. 4.20(Top)), multiple Arbitrary Waveform Generators (AWGs) are required to supply the HV amplifiers with the desired trapping waveforms. The previous trap, IBEX-1, only needed a single, 4-channel AWG to supply all the trap electrodes. Therefore, the 4 channels were synchronised internally to the AWG. The allocation of AWG channels and amplifiers for IBEX-1 are summarised in Table 4.4. However, the new trap, IBEX-2, has twice the number of independently powered rod electrodes, plus the plate electrodes. This requires the use of three separate Tabor AWGs (two WW2074 and one WW1074) to allow for individual waveforms to be sent to each pair of electrodes. The allocation of AWG channels and amplifiers for IBEX-2 is summarised in Table 4.5. At this point it should be noted that the custom amplifiers with the PA98 op amp were chosen to drive the central rods in

the experimental region instead of using the new amplifiers with the PA194 op amp. This is due to the PA98 amplifiers having less ringing on the T-insert waveform when compared to the PA194 amplifiers, as was shown in Section 4.4.2, Fig. 4.18. The custom amplifiers with the PA194 op amp were instead used for the gate electrodes.

Table 4.4: AWG and amplifier setup for IBEX-1.

Electrode	Waveform source	Amplifier
Central rod: 1&3	AWG1: Ch1	Custom (PA98)
Central rod: 2&4	AWG1: Ch2	Custom (PA98)
MCP EC: 1&3	AWG1: Ch3	WMA-300
MCP EC: 2&4	AWG1: Ch4	WMA-300
FC EC: 1&3	DC power supply	-
FC EC: 2&4	DC power supply	-

Table 4.5: AWG and amplifier setup for IBEX-2.

Electrode	Waveform source	Amplifier
IR: 1&3	AWG2: Ch1	WMA-300
IR: 2&4	AWG2: Ch2	WMA-300
ER: 1&3	AWG1: Ch1	Custom (PA98)
ER: 2&4	AWG1: Ch2	Custom (PA98)
Gate: 1&3	AWG1: Ch3	Custom (PA194)
Gate: 2&4	AWG1: Ch4	Custom (PA194)
MCP EC: 1&3	AWG2: Ch3	WMA-300
MCP EC: 2&4	AWG2: Ch4	WMA-300
Plates	AWG3: Ch1	Custom (PA194)
FC EC: 1&3	DC power supply	-
FC EC: 2&4	DC power supply	-

The use of multiple AWGs requires coupling of the instruments so that all the channels output synchronised waveforms. For the Tabor instruments, this first requires connecting 'SCLK-OUT' and 'COUPLE-OUT' on the primary instrument to 'SCLK-IN' and 'COUPLE-IN' on the subordinate instrument with SMB connectors [108]. If three AWGs are to be synchronised, the connections can be daisy chained. There is then a software requirement in order to initiate the synchronisation procedure. The AWGs need to be connected to the same network via LAN and the primary instrument should be given the

IP address of the subordinate instrument. The coupling command must then be communicated to the instruments in order to complete the synchronisation. These instructions are communicated to the instruments via SCPI commands[6]. This is a straightforward process when using the Tabor user interface 'ArbConnection' [109]. However, this synchronisation procedure proved difficult to implement with the Tabor-provided LabView subVI (virtual instrument). After trying for several months to integrate this synchronisation procedure into the existing LabView control program for IBEX, I discovered that the Tabor-provided LabView subVI, 'wx218x Configure Output Enabled.vi' [110] was faulty. This was confirmed to be the case after communication with Tabor and a potential fix was created by the company. However, I did not have time to test and implement this potential fix into the IBEX LabView program and I instead synchronised the instruments manually by first wiring the AWGs together as described above. Then the desired waveforms were loaded to the two AWGs via the IBEX LabView program. Then the desired instrument was set to be a subordinate instrument manually on the AWG. This bypasses the need to send SCPI commands to the instrument to instruct them to couple. The disadvantage of this solution is that this requires a manual step in the setup of an IBEX experiment, in an otherwise automated process. This significantly increases the time needed to perform experiments where the voltage waveform is varied from experiment to experiment (i.e. tune scans). Therefore, a more efficient solution to synchronise the AWGs should be implemented in the future. However, with the AWGs synchronised, the IBEX-2 trap could now be successfully operated in 'Normal trapping mode'.

4.5.4 Optimising ion transfer between IR and ER

Previously in IBEX-1, a DC voltage of 25 V was applied to the end caps for longitudinal confinement, and a DC voltage of 10 V was applied to the central rods. The DC voltage on the central rods aids extraction onto the detector when the end-cap DC voltage is

[6]Standard Commands for Programmable Instruments.

dropped to 0 V. These values were kept the same for the experimental region (ER) in IBEX-2. In order to maximise the number of ions transferred from the ionisation region (IR) to the experimental region in IBEX-2, two parameters need to be optimised. The first is the DC bias between the IR and the ER, δV_{DC}, which aids the transfer of ions from one section to the other. The second parameter is the time that the DC voltage on the gate electrode is dropped to allow ions to pass into the ER. This parameter will be referred to as the 'transfer time'. A typical timings chart for IBEX-2 operating in 'Normal trapping mode' is shown in Fig. 4.24.

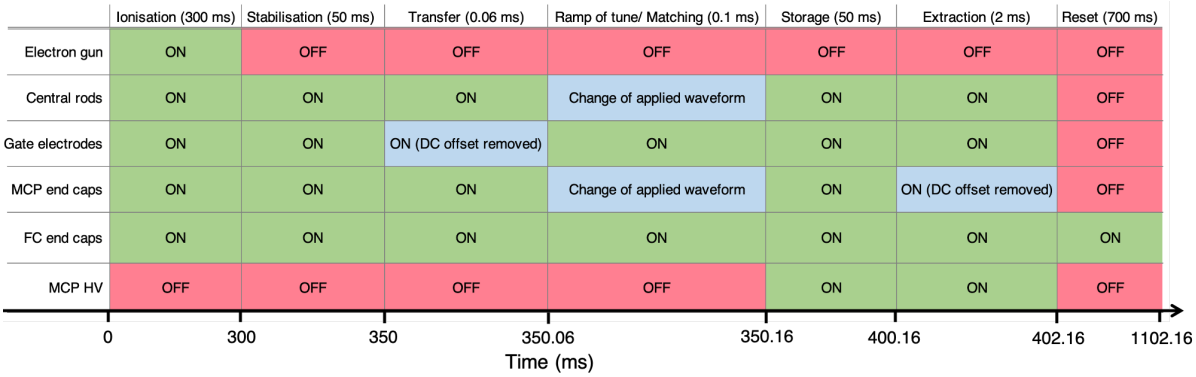

Figure 4.24: Timings chart of an IBEX-2 experiment, operating in 'Normal trapping mode'. A transfer section has been added compared to the previous timings chart.

Again, a FODO lattice with cell tunes of $Q_x = Q_y = 0.15$ was created to store ions for 50,000 cell periods before the end-cap voltage was dropped and the ions were detected on the MCP detector. The electron gun was on for 300 ms and the argon pressure was 1.6×10^{-7} mbar. An initial DC bias between the IR and ER of $\delta V_{DC} = 1$ V was chosen as a starting point and the time the gate voltage was dropped (transfer time) was varied. The number of ions detected, averaged over 10 experiments, is plotted in Fig. 4.25(Left) for a transfer time of 0 ms to 2 ms. A peak ion number of $\sim 2 \times 10^6$ can be seen in Fig. 4.25(Left) at around 0.06 ms. This is followed by a minima in ion number with a transfer time of around 0.12 ms, twice the optimum transfer time.

The form of Fig. 4.25(Left) is suspected to be caused by the majority of the ion distribution taking approximately 0.06 ms to drift from the IR to the ER. However, in twice that time, the distribution can travel back into the IR, creating a minima in the

number of ions detected. As the transfer time is increased past 0.25 ms, the number of ions detected on the MCP seems to approach about half the peak number of ions, i.e. $\sim 1 \times 10^6$. The reason for this is believed to be due to the ion distribution having time to spread out and fill both the IR and ER and so only around 50 % of ions get trapped in the ER when the gate voltage is returned to 25 V. These hypotheses need to be confirmed in the future by studying the transfer of ions from the IR to ER in a longitudinal simulation of IBEX.

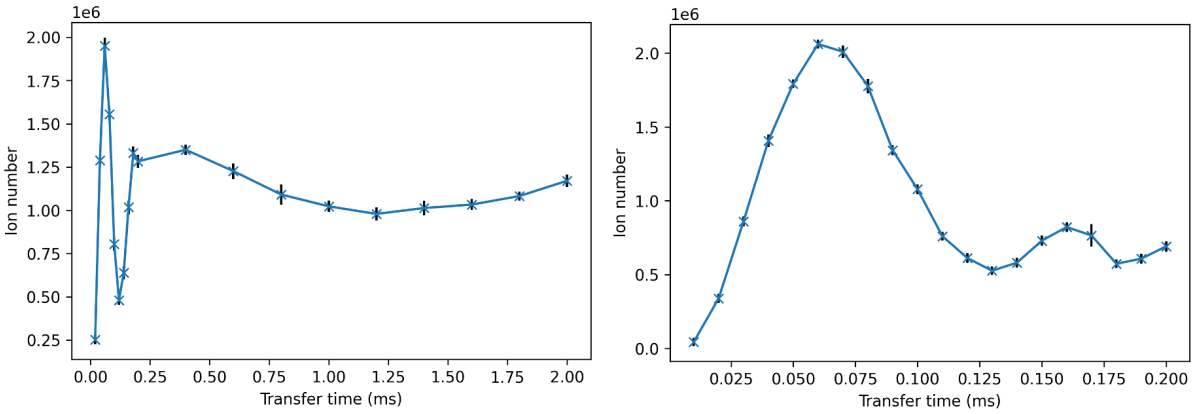

Figure 4.25: Ion number measured on the MCP as a function of time the gate voltage is dropped (transfer time).

In Fig. 4.25(Right), a finer resolution scan of the ion number as a function of transfer time was performed. Again, the optimum transfer time is seen to be 0.060(5) ms. This transfer time was adopted for the rest of the experimental work in this thesis.

As the DC bias of $\delta V_{DC} = 1$ V was chosen arbitrarily, the transfer time should now be fixed while the δV_{DC} is varied. The DC voltage on the ER central rods was fixed at 10 V and the DC of the IR central rods was varied from 9.5 V–13 V. The results presented in Fig. 4.26 show that a DC bias of $\delta V_{DC} = 1$ V is still consistent with being the optimal value, for a transfer time of 0.06 ms, within the granularity of the scan. A finer scan in the future could improve on this transfer efficiency.

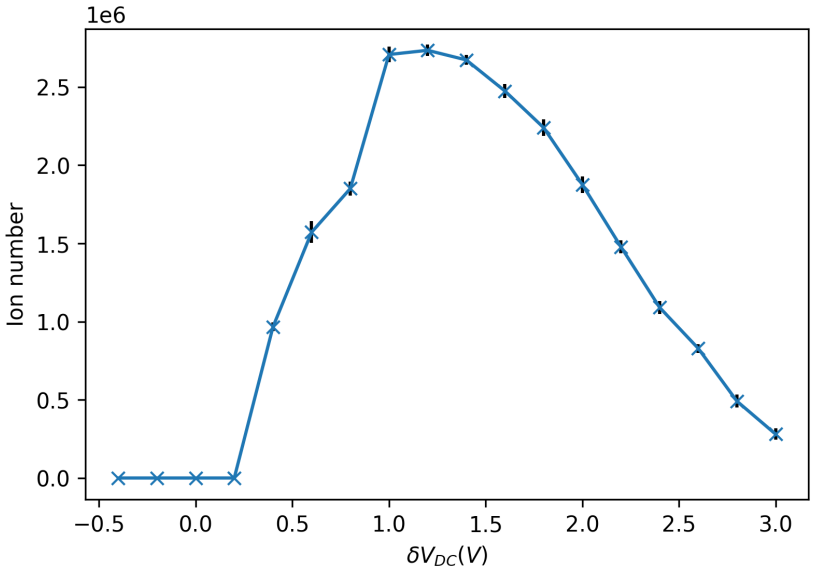

Figure 4.26: Ion number measured on the MCP as a function of the DC bias between the IR and ER, δV_{DC}.

4.6 Chapter summary

In this chapter the design for the upgraded IBEX-2 trap was presented. A design for the multipole trap was decided upon which was similar to the S-POD trap at Hiroshima [99]. The addition of the multipole plate electrodes was seen to reduce the c_6 component of the quadrupole field by a factor of 100 when compared to the linear trap. The design of IBEX-2 was brought to fruition by the ISIS design division, who manufactured and aligned the trap to tolerances within 10 µm. The design and testing of the HV amplifiers needed to supply the voltages to the additional rod and plate electrodes was also presented in this chapter. The work behind the commissioning of the new trap was discussed. This involved the calibration of the MCP detector along with the synchronisation of AWGs and optimisation of ion transport between the two trapping regions. Further optimisation of the trap parameters can be performed in the future to ensure that the transfer efficiency between the IR and ER is maximised.

Chapter 5

Simulation of Quasi-Integrable Optics in a Paul trap

A quasi-integrable lattice has a time-independent Hamiltonian and hence one invariant of motion for a two-dimensional system. The benefit of a quasi-integrable lattice is that it is robust to small perturbations while maintaining a large dynamic aperture. A quasi-integrable lattice has been studied at IOTA [81, 89], but quasi-integrable optics (QIO) has yet to be tested with space charge. In this chapter I explain how I tested the benefits of QIO through simulation, first with a perturbation in a one-cell T-insert lattice and then with space charge in a two-cell T-insert. These simulations are designed to be experimentally verifiable with the IBEX-2 trap.

In order to test QIO, a 2D model of the IBEX trap was created in the simulation software VSim 11 [111]. The T-insert waveform was applied as a voltage to the trap electrodes and the distribution of particles was simulated with particle-in-cell tracking. Perturbations which excite the 2nd order and 4th order resonances were applied to the T-insert to induce particle loss. The octupoles were then turned on in the drift region to damp these instabilities and show the reduction of particle loss due to the creation of tune spread in the beam. The particle loss from the quasi-integrable lattice, where the octupole strength scales as $1/\beta^3$, was then compared to two octupole scalings that were perturbed from the integrability condition. The first is a normal constant-strength octupole (square-wave pulse). The second is an octupole which scales with β^3. A scaling of β^3 was chosen to exaggerate the wrong scaling of the octupole strength. This work has

previously been published in the International Particle Accelerator Conference (IPAC) 2021 proceedings [112] and the 61st ICFA ABDW on High-Intensity and High-Brightness Hadron Beams 2021 (HB 2021) [66].

Finally, the theory of QIO is extended to include space charge and a T-insert lattice is tested with different intensities and hence varying amounts of space-charge tune spread. This work has been published though IPAC 22's light peer review process [67] and presented at the 5th ICFA Mini-Workshop on Space Charge 2022 [113].

I start this chapter by deriving a formula with the aim of quantifying how closely the conditions of integrability are met in an arbitrary T-insert lattice design. I then test the predictions of this new formula with simulation results.

5.1 Measure of integrability

In the literature, if an accelerator lattice meets the conditions of (quasi-)integrability it is said to be a Quasi-Integrable lattice, otherwise it is non-integrable. However, in reality a Quasi-Integrable lattice can never be implemented perfectly as it will always have some error in the phase advance over the T-insert, the equality of the beta functions in the drift region, and the octupole scaling with $1/\beta^3(s)$. Therefore, it is important to be able to quantify how closely a lattice meets the conditions of integrability, as this will determine how stable and bounded the particle motion will be in practice.

There are methods to study the beam dynamics of lattices that deviate from the integrability conditions, which often involve measuring the relative standard deviation of an invariant of the system [114]. This has been done previously with quasi-integrable lattices with sextupole and octupole inserts, by measuring the fluctuation in Hamiltonian [92]. When the invariant is an emittance, the standard deviation in this quantity is often referred to as the 'smear' or 'jitter' [73,114]. However, measuring the fluctuation in these invariants often involves performing simulations. As far as I am aware, at the time of writing, there is not an analytical measure of how closely a T-insert lattice meets the integrability conditions, given errors in the lattice design parameters.

Therefore, in this section I propose a way to quantify analytically how "integrable" a quasi-integrable lattice is, assuming small perturbations away from the ideal lattice. In other words, given a T-insert lattice with arbitrary errors in the phase advance, beta functions in the drift region, and octupole scaling, I want to assign a numerical value that describes how close to integrable that lattice will be, without the need for extensive simulation testing of that lattice. I start by deriving a formula used to quantify the "measure of integrability", before testing the theory's predictions against simulation results where the fluctuation in the Hamiltonian is measured.

5.1.1 Deriving a measure of integrability

The Hamiltonian for a single particle in a T-insert lattice, with a quasi-integrable (QI) octupole applied in the drift region is given by

$$H = \frac{p_x^2 + p_y^2}{2} + K(s)\left(x^2 + y^2\right) + V(x, y, s), \tag{5.1}$$

where the QI octupole potential can be written as

$$V(x, y, s) = \frac{k}{\beta_x^{3/2}(s)\beta_y^{3/2}(s)}\left(\frac{x^4}{4} - \frac{3}{2}x^2y^2 + \frac{y^4}{4}\right), \tag{5.2}$$

where k is a constant defining the strength of the octupole and where we have not assumed that $\beta_x = \beta_y$ in the drift region. The QI octupole scaling of $1/\beta^3(s)$ is expressed explicitly in terms of the horizontal and vertical beta functions (β_x, β_y).

Substituting the normalised coordinate transformation, $x_N = \frac{x}{\sqrt{\beta_x(s)}}$ and $y_N = \frac{y}{\sqrt{\beta_y(s)}}$ into Eq. 5.2 we get,

$$\begin{aligned} V(x_N, y_N, s) &= \frac{k}{\beta_x^{3/2}(s)\beta_y^{3/2}(s)}\left(\frac{x_N^4\beta_x^2(s)}{4} + \frac{y_N^4\beta_y^2(s)}{4} - \frac{3}{2}x_N^2y_N^2\beta_x(s)\beta_y(s)\right) \\ &= k\left(\frac{x_N^4}{4}\frac{\sqrt{\beta_x(s)}}{\beta_y^{3/2}(s)} + \frac{y_N^4}{4}\frac{\sqrt{\beta_y(s)}}{\beta_x^{3/2}(s)} - \frac{3}{2}x_N^2y_N^2\frac{1}{\sqrt{\beta_x(s)}\sqrt{\beta_y(s)}}\right), \end{aligned} \tag{5.3}$$

and using the relation below from Section 3.1.2,

$$U(x_N, y_N) = \sqrt{\beta_x(\phi)}\sqrt{\beta_y(\phi)}V(x_N\sqrt{\beta_x(\phi)}, y_N\sqrt{\beta_y(\phi)}), \tag{5.4}$$

we obtain a normalised potential which is still dependent on s if $\beta_x \neq \beta_y$,

$$U(x_N, y_N, s) = k\left(\frac{x_N^4}{4}\frac{\beta_x(s)}{\beta_y(s)} + \frac{y_N^4}{4}\frac{\beta_y(s)}{\beta_x(s)} - \frac{3}{2}x_N^2 y_N^2\right). \tag{5.5}$$

When $\beta_x(s) = \beta_y(s)$ this equation becomes independent of s as previously seen in Section. 3.1.2,

$$U(x_N, y_N) = k\left(\frac{x_N^4}{4} + \frac{y_N^4}{4} - \frac{3}{2}x_N^2 y_N^2\right), \tag{5.6}$$

and therefore the Hamiltonian, expressed in normalised coordinates (Eq. 3.11) is also s-independent and thus integrable.

If we assume the octupole scaling with beta function is imperfect and deviates from the ideal scaling as a function of $g(s)$, then we can modify Eq. 5.5 to become,

$$U(x_N, y_N, s) = \frac{g_x(s) + g_y(s)}{2}k\left(\frac{x_N^4}{4}\frac{\beta_x(s)}{\beta_y(s)} + \frac{y_N^4}{4}\frac{\beta_y(s)}{\beta_x(s)} - \frac{3}{2}x_N^2 y_N^2\right), \tag{5.7}$$

where the functions $g_x(s)$ and $g_y(s)$ denote an arbitrary deviation from the ideal octupole scaling in relation to $\beta_x(s)$ and $\beta_y(s)$, respectively. If the beta functions in the drift region are equal so that $\beta_x(s) = \beta_y(s) = \beta(s)$ and the octupole strength scaling is exactly $1/\beta^3(s)$, then $g_x(s) = g_y(s) = 1$ and Eq. 5.7 becomes time-independent. Substituting action-angle coordinates (see Section 2.1.4), $x(s) = \sqrt{2J_x\beta_x(s)}\cos\phi_x$ and $y(s) = \sqrt{2J_y\beta_y(s)}\cos\phi_y$, into the normalised coordinates transformations we get

$$x_N = \sqrt{2J_x}\cos\phi_x, \quad y_N = \sqrt{2J_y}\cos\phi_y. \tag{5.8}$$

Substituting these normalised coordinates, now expressed in terms of action-angle variables (J, ϕ) into Eq. 5.7, the following potential can be obtained,

$$\begin{aligned} U(J_x, J_y, \phi_x, \phi_y, s) =& \frac{g_x(s) + g_y(s)}{2}k(J_x^2\frac{\beta_x(s)}{\beta_y(s)}\cos^4\phi_x + J_y^2\frac{\beta_y(s)}{\beta_x(s)}\cos^4\phi_y \\ &- 6J_xJ_y\cos^2\phi_x\cos^2\phi_y), \end{aligned} \tag{5.9}$$

where J_x and J_y are the horizontal and vertical actions and ϕ_x and ϕ_y are the horizontal and vertical phase advances over the T-insert. To simplify this equation, we can use the substitution, $\hat{\beta}(s) = \frac{\beta_x(s)}{\beta_y(s)}$,

$$\begin{aligned} U(J_x, J_y, \phi_x, \phi_y, s) =& \frac{g_x(s) + g_y(s)}{2}k(J_x^2\hat{\beta}(s)\cos^4\phi_x + J_y^2\frac{1}{\hat{\beta}(s)}\cos^4\phi_y \\ &- 6J_xJ_y\cos^2\phi_x\cos^2\phi_y). \end{aligned} \tag{5.10}$$

Taking the partial derivative of Eq. 5.10 with respect to the function that describes the deviation from the ideal octupole scaling, $g(s)$ and the phase advance ϕ, the following equations are obtained,

$$\frac{\partial U}{\partial g_x(s)} = \frac{k}{2}(J_x^2\hat{\beta}(s)\cos^4\phi_x + J_y^2\frac{1}{\hat{\beta}(s)}\cos^4\phi_y - 6J_xJ_y\cos^2\phi_x\cos^2\phi_y), \tag{5.11}$$

$$\frac{\partial U}{\partial g_y(s)} = \frac{k}{2}(J_x^2\hat{\beta}(s)\cos^4\phi_x + J_y^2\frac{1}{\hat{\beta}(s)}\cos^4\phi_y - 6J_xJ_y\cos^2\phi_x\cos^2\phi_y), \tag{5.12}$$

$$\frac{\partial U}{\partial \phi_x} = \frac{g_x(s)+g_y(s)}{2}k(-4J_x^2\hat{\beta}(s)\sin\phi_x\cos^3\phi_x + 12J_xJ_y\sin\phi_x\cos\phi_x\cos^2\phi_y), \tag{5.13}$$

$$\frac{\partial U}{\partial \phi_y} = \frac{g_x(s)+g_y(s)}{2}k(-4J_y^2\hat{\beta}(s)\sin\phi_y\cos^3\phi_y + 12J_xJ_y\sin\phi_y\cos\phi_y\cos^2\phi_x). \tag{5.14}$$

Then to calculate the deviation in the potential from the ideal QI lattice, the parameter errors are added in quadrature,

$$\delta U = \sqrt{\left(\frac{\partial U}{\partial g_x(s)}\right)^2\delta g_x^2 + \left(\frac{\partial U}{\partial g_y(s)}\right)^2\delta g_y^2 + \left(\frac{\partial U}{\partial \phi_x}\right)^2\delta\phi_x^2 + \left(\frac{\partial U}{\partial \phi_y}\right)^2\delta\phi_y^2} \tag{5.15}$$

where the deviations in each of the parameters have been defined to be the following,

$$\delta g_x(s) = \int \sqrt{<(1/\beta_x^3(s))^2> - <g_x^2(s)>}\,ds, \tag{5.16}$$

$$\delta g_y(s) = \int \sqrt{<(1/\beta_y^3(s))^2> - <g_y^2(s)>}\,ds, \tag{5.17}$$

$$\delta\phi_x = n\pi - \phi_x, \tag{5.18}$$

$$\delta\phi_y = n\pi - \phi_y. \tag{5.19}$$

In Eq. 5.16 and 5.17, the RMS difference is taken between the ideal octupole scaling in the drift region ($1/\beta^3(s)$), and the octupole scaling, $g(s)$ achieved in practice. The RMS

difference, $\delta g(s)$ is integrated over the entire drift region of length L that the octupole is applied over.

Equations 5.18 and 5.19 define the error in the phase advance over the T-insert section of the lattice. As was shown in Section 3.1.3, the phase advance over the T-insert should be $n\pi$ where n is an integer. If, for example, $\phi_x = \phi_y = \pi$ then Eq. 5.18 and 5.19 equal zero, and the two terms which depend on the error in ϕ in Eq. 5.15 also go to zero. Equation 5.15 still holds if the phase advance over the T-insert is $n\pi$ and $n > 1$ as each term in Eq. 5.13 and 5.14 depends on a $\sin\phi$ term which equals zero if $\phi = \pm n\pi$. However, if the phase advance over the T-insert was to be a multiple of $m\pi/2$ where m is an odd integer, Eq. 5.13 and 5.14 would again go to zero due to each term also depending on a $\cos\phi$ term. This is, of course, not a property of NIO theory but is instead a limitation of Eq. 5.15 to quantify the measure of integrability for large errors in the phase advance. This is not surprising as Eq. 5.15 assumes small perturbations away from the ideal QI lattice, therefore it should be noted that this equation will assume $\delta\phi = n\pi - \phi << \pi/2$.

Equation 5.15, which in the rest of this thesis is referred to as the "measure of integrability," therefore gives an estimate of how much the potential U deviates from its ideal integrable form, given a set of lattice errors in the octupole scaling, $\delta g(s)$ and the phase advance over the T-insert, $\delta\phi$. As the Hamiltonian of the system is given by $H_N = \frac{1}{2}(p_{x_N}^2 + p_{y_N}^2) + \frac{1}{2}(x_N^2 + y_N^2) + U$, an error in the potential, δU will correspond to the equivalent error in the Hamiltonian $\delta H = \delta U$.

5.1.2 Testing the measure of integrability formula with simulation

In order to test the usefulness of the measure of integrability formula derived in Eq. 5.15, its predictions must first be compared to simulation results. Future work should also benchmark the predictions of this formula against experimental measurements. The ability to apply the octupole field as a continuously varying voltage makes the new

IBEX-2 trap the perfect tool to carry out these experimental results. However, in this work we will only benchmark with simulations.

A 1D particle-tracking code written in Mathematica by Stas Baturin [92] was used as the simulation comparison. This code tracks single particles through a T-insert lattice with a scaling octupole potential in the drift region. The T-insert lattice is assumed ideal and is applied as a transfer matrix, given in Eq. 3.20. The nonlinear region in the drift is implemented as a "drift-kick", where the scaling octupole potential is approximated as a series of discrete thin-lens octupole "kicks" spaced by short drift sections. The octupole kick updates the particle coordinates (x_N, p_{N_x}) by an amount determined by the derivative of the octupole potential (Eq. 3.10) with respect to x_N, taken at the position of the thin lens. I adapted this code to compute the Hamiltonian of each particle and calculate the deviation of the Hamiltonian, $\delta H = (\mathrm{H_{max}} - \mathrm{H_{min}})/2$ over a given number of turns through the lattice. The aim of using this tracking code was to calculate the deviation in the Hamiltonian over a number of turns through the lattice, for a given perturbed octupole strength scaling, i.e. deviations away from the $1/\beta^3(s)$ scaling.

Figure 5.1 plots the phase space trajectories of particles in a Poincaré map[1] through a T-insert lattice and $L = 1\,\mathrm{m}$ drift region with a fractional tune of $Q = 0.246$, close to the 4th order resonance. Thirty particles with incrementally increasing amplitude were tracked over 1000 turns through the lattice. In Fig. 5.1a, no octupole element was applied in the drift region and hence the lattice is completely linear. The particles exhibit regular, bounded motion and the lattice has an infinite dynamic aperture. In Fig. 5.1b, a single thin-lens octupole is placed at the center of the drift region. As the tune is close to the 1/4 integer resonance, this octupole drives the 4th order resonance and islands of instability can be seen in the phase space plot. The axes in Fig. 5.1b have been scaled up to show the resonant islands, therefore a dashed grey box indicates the scale of the other five plots in Figure 5.1.

[1] A Poincaré map or first recurrence map shows a cross section in phase space of a periodic particle orbit.

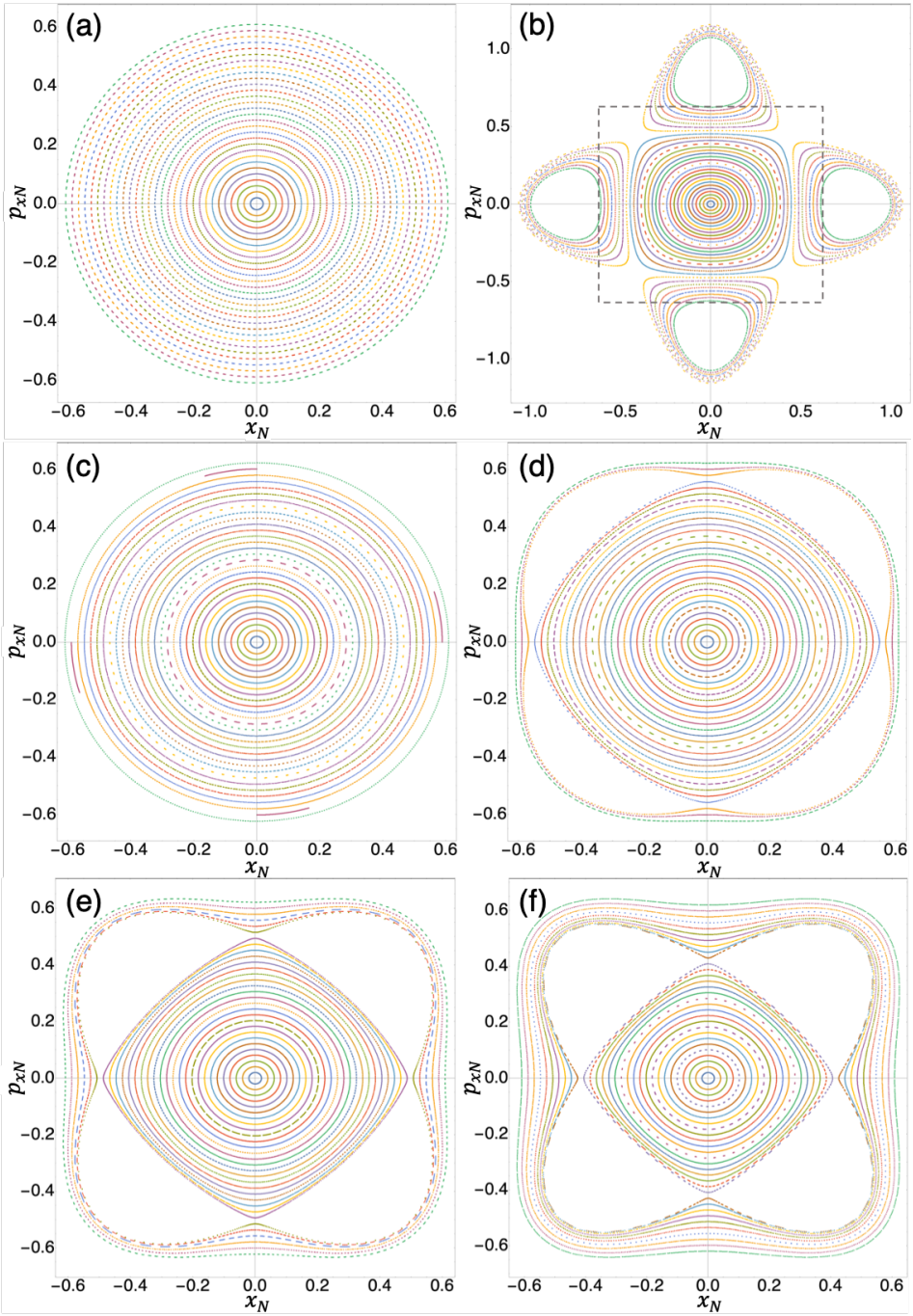

Figure 5.1: Poincaré map in normalised coordinates, plotted for 1000 turns through a T-insert lattice and drift region with fraction tune $Q = 0.246$. The octupole element in the drift region is varied over the 6 plots. (a) Drift region only, no octupole. (b) Single thin-lens octupole at center of drift. (c) QI octupole scaling, $1/\beta^3(s)$, approximated with 20 thin-lens octupoles. (d) Octupole strength scaling with $1/\beta^2(s)$. (e) Constant octupole strength scaling. (f) Octupole strength scaling with $\beta^3(s)$. Dashed box in (b) marks the scale of the other plots.

Figure 5.1c displays the phase space trajectories of the lattice with a QI octupole scaling ($1/\beta^3(s)$) in the drift region. The octupole scaling was approximated in the Mathematica simulation with 20 equally spaced, thin-lens octupoles and the strength was normalised over plots (b)-(f). The phase space in Figure 5.1c has been almost entirely returned to regular bounded motion, similar to what was seen in Fig. 5.1a for the linear lattice. This is a helpful visualisation of how the QI octupole scaling shrinks the effective width of the 4th order resonance to almost zero. This demonstrates how the quasi-integrable lattice can essentially eliminate the 4th order resonance. This is due to the octupole scaling with beta function cancelling out the $s-$dependence in the Hamiltonian. Therefore the Hamiltonian is time-independent and so the octupole potential does not drive the 4th order resonance.

In Fig. 5.1d, e and f, the octupole scaling was perturbed from the $1/\beta^3(s)$ scaling. Figure. 5.1d shows the phase space from an octupole scaling of $1/\beta^2(s)$, Fig. 5.1e has a constant octupole scaling across the drift region, and the octupole in Fig. 5.1f scales as $\beta^3(s)$. These octupole scalings with the beta function are plotted along the length of the drift region in Fig. 5.3. From Fig. 5.1d-f, it is clear that deviating away from the ideal octupole scaling prescribed by NIO, distorts the phase space trajectories. The trajectories are however still bounded which is not necessarily the case at larger particle amplitudes.

Figure 5.2 plots the phase space trajectories over a larger range of particle amplitudes. The 30 particle initial positions have been increased by a factor of ~ 10 compared to Fig. 5.1, whereas the octupole strength has been scaled down by a factor of 10. Figure 5.2a shows regular bounded motion for all particles when the QI octupole scaling is implemented, with the exception of two thin islands shown in red. The fact that islands appear in the phase space of the QI octupole in 1D is due to the approximations made in the simulation, namely the approximation of the octupole scaling as 20 discrete thin-lens octupoles. In Fig. 5.2b some particles begin to exhibit chaotic, unbounded motion with an octupole scaling of $1/\beta^2(s)$. As the octupole scaling is further perturbed away

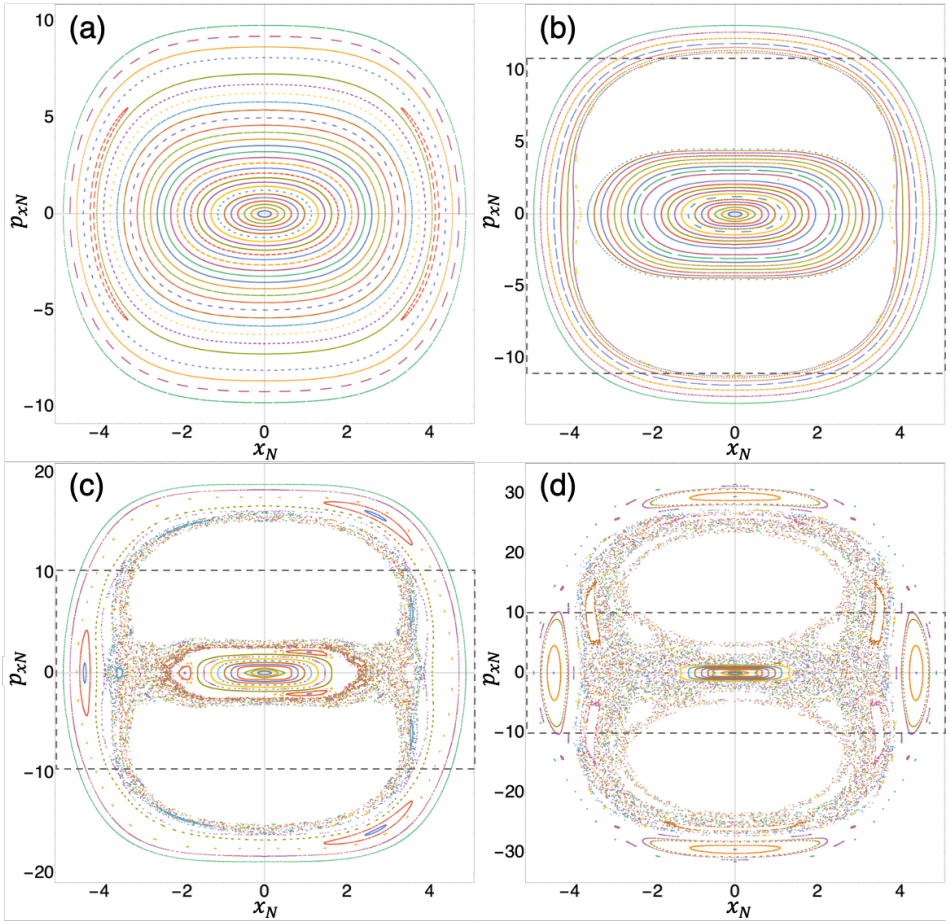

Figure 5.2: Poincaré map in normalised coordinates, plotted for 1000 turns through a T-insert lattice and drift region with fraction tune $Q = 0.246$. The octupole scaling in the drift region was varied: (a) QI octupole scaling, $1/\beta^3(s)$. (b) Octupole strength scaling with $1/\beta^2(s)$. (c) Constant octupole strength scaling. (d) Octupole strength scaling with $\beta^3(s)$. The grey dashed boxes in (b)-(d) indicate the scale used in plot (a).

from $1/\beta^3(s)$ in Fig. 5.2c and d (constant octupole and $\beta^3(s)$ scaling respectively), more chaotic motion and resonant islands can be seen in the phase space plots.

As the measure of integrability formula (Eq. 5.15) was derived assuming small perturbations from the QI lattice, it is not capable of predicting or describing the resonant island dynamics seen in Fig. 5.1 and Fig. 5.2. For this reason, in order to make a fair comparison between the theory and simulation, 30 particles were simulated, all with initial particle amplitudes of $x_N < 0.4$. This avoids any unbounded or significantly distorted phase space trajectories. These particles were then tracked through 5000 turns of the lattice. Various different octupole scalings were implemented in the drift region and

are plotted in Fig. 5.3. All octupole scalings were approximated as 20 thin-lens octupoles in the Mathematica simulation.

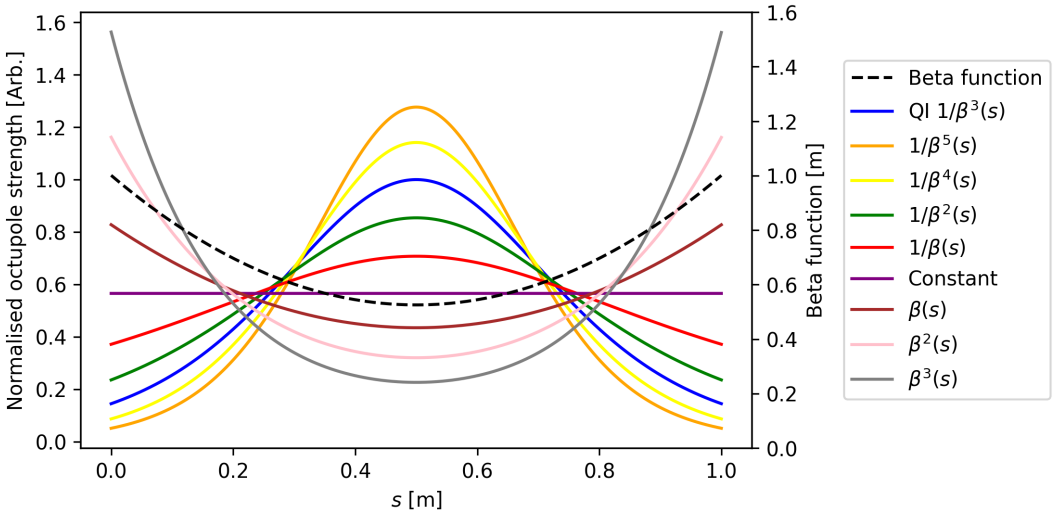

Figure 5.3: Beta function and the normalised octupole strength scalings within the drift region.

Table 5.1: RMS deviation from ideal octupole scaling, $\delta g_x(s)$ used for the theoretical measure of integrability calculation.

Octupole scaling	$\delta g_x(s)$
$1/\beta^3(s)$	0.0
$1/\beta^4(s)$	0.03609
$1/\beta^2(s)$	0.04296
$1/\beta(s)$	0.18081
1	0.41746
$\beta(s)$	0.74358
$\beta^2(s)$	1.14044
$\beta^3(s)$	1.58628

The Hamiltonian was calculated once per turn for each particle, over 5000 turns through the lattice. An example of the Hamiltonian of a single particle tracked through the QI octupole lattice is shown in Fig. 5.4. The deviation of the Hamiltonian for this particle amplitude was then calculated using $(\mathrm{H_{max}} - \mathrm{H_{min}})/2$. This deviation in Hamiltonian was then compared to the predicted deviation in Eq. 5.15. This calculation was repeated for multiple particle amplitudes (or actions) and for the 8 different octupole

scalings shown in Fig. 5.3. The normalised particle amplitude is related to the action in Eq. 5.8.

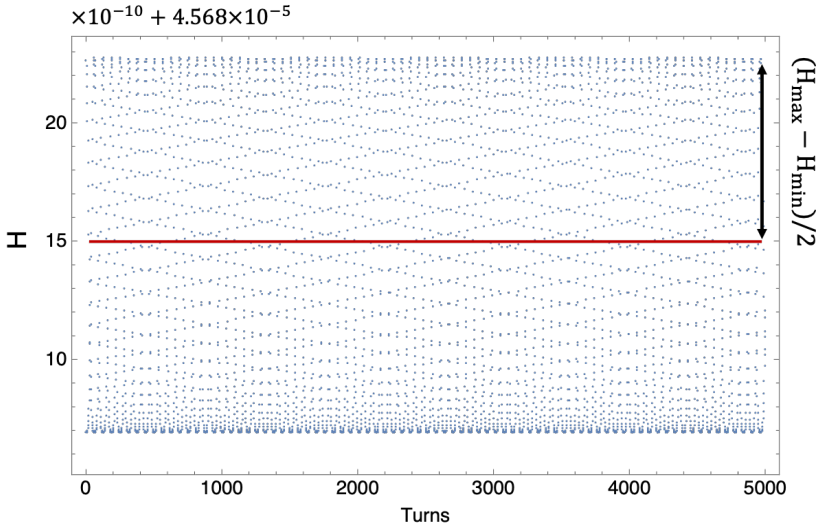

Figure 5.4: Hamiltonian of a single particle plotted at each turn through a QI lattice. Red line shows the average Hamiltonian over 5000 turns and the amplitude of the fluctuation of this Hamiltonian is estimated by $(\mathrm{H_{max}} - \mathrm{H_{min}})/2$.

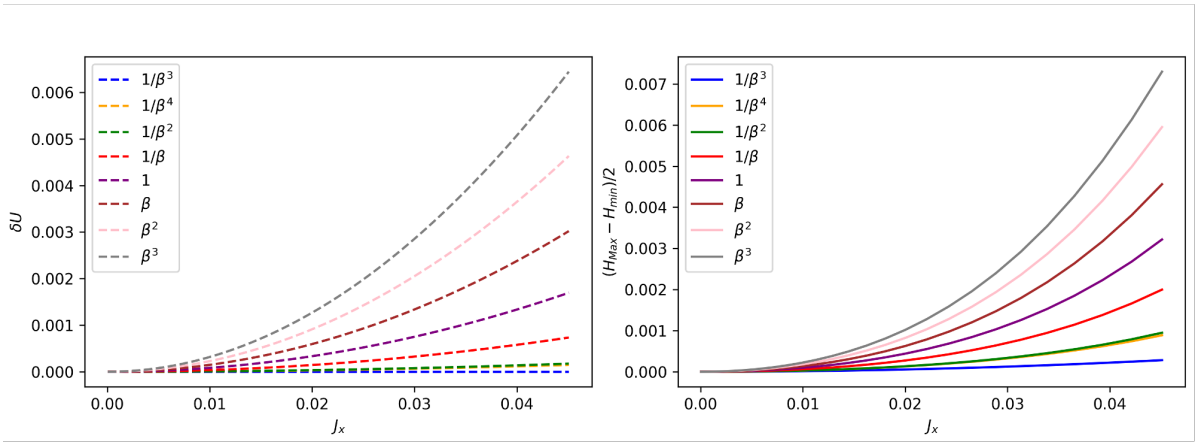

Figure 5.5: (Left) Theoretical deviation in octupole potential or "Measure of Integrability" calculated with Eq. 5.5 for various octupole scalings at a range of actions. (Right) Deviation in Hamiltonian calculated from Mathematica simulations, as a function of action J_x for various octupole scalings.

In Figure 5.5, the deviation in Hamiltonian $\delta H = (\mathrm{H_{max}} - \mathrm{H_{min}})/2$, calculated from Mathematica simulations is compared to the measure of integrability δU, calculated from Eq. 5.15. The simulation was performed in 1D with no phase advance error and hence the only non-zero term of Eq. 5.15 is the one dependent on $g_x(s)$. The value of $\delta g_x(s)$

was found by calculating the RMS difference between the $1/\beta^3(s)$ octupole scaling and the given octupole scaling in Fig. 5.3. These values are summarised in Table 5.1. These values neglect the error introduced by the discrete thin-lens octupoles used in simulation. The theoretical predictions in Fig. 5.5 (Left) are shown to be in reasonable agreement with the simulation results on the right of Fig. 5.5. A notable discrepancy is the J_x dependence in the QI ($1/\beta^3(s)$) simulation results compared to the $\delta U = 0$, predicted by theory. This discrepancy can be seen more clearly in Fig. 5.6 where only the ideal QI, $1/\beta^4(s)$ and $1/\beta^2(s)$ octupole scalings are plotted. This discrepancy is expected as the measure of integrability, $\delta U = 0$ is set by definition as ideally matching the conditions of quasi-integrability. However, the Mathematica simulation approximated the octupole potential as a series of 20 "drift-kick" elements which introduces error into the simulation, giving rise to the discrepancy.

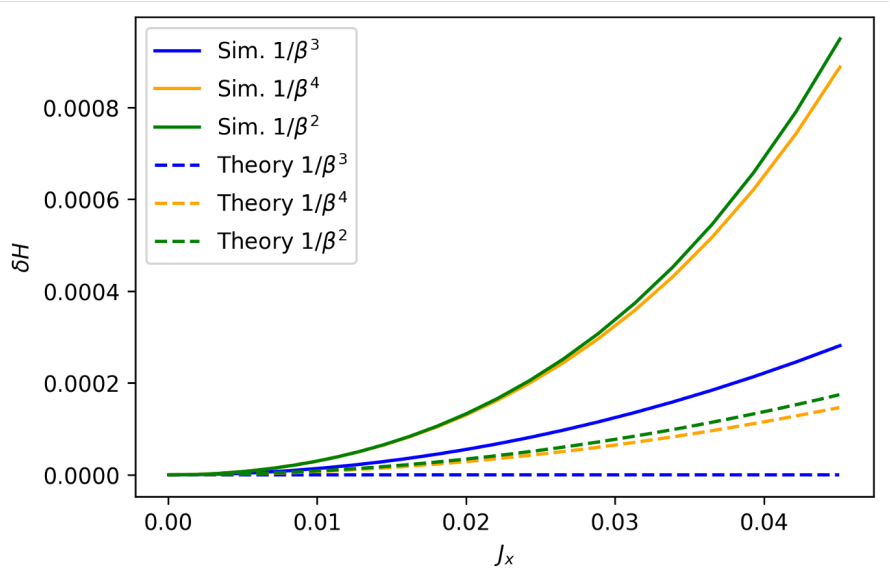

Figure 5.6: Fluctuation in Hamiltonian δH plotted for theory and simulation. Ideal QI octupole scaling, $1/\beta^3(s)$ (blue). $1/\beta^4(s)$ octupole scaling (yellow). $1/\beta^2(s)$ octupole scaling (green).

Despite the magnitudes of the fluctuation in Hamiltonian for theory and simulation not agreeing completely, the relative magnitudes between the fluctuation in Hamiltonians predict correctly which scalings are worse than others. In Fig. 5.6, the formula in Eq. 5.15 predicts that a $1/\beta^2(s)$ octupole scaling (green) will deviate further from an integrable

lattice than a $1/\beta^4(s)$ scaling (yellow) which is indeed what is seen in simulation. This is an example of when the trade-off between a scaling of $1/\beta^2(s)$ and $1/\beta^4(s)$ may not be intuitive when designing a QI lattice and so the designer would ordinarily need to perform simulations to test which is better. However, an analytical formula such as the one in Eq. 5.15 could allow for faster determination of how close the lattice is to integrable.

The error in the Mathematica simulation can be modeled as a perturbation added to the variation in the Hamiltonian, so that $\delta H = \delta U + aJ_x^2$ where a is some fitting parameter that depends on the error in the simulation. If this error is taken into account when calculating the measure of integrability, then theory and simulation results agree remarkably well across three order of magnitude of particle action, as seen in Fig. 5.7. In Fig. 5.7 a fitting parameter of $a = 0.07$ was used to give $\delta H = \delta U + 0.07J_x^2$.

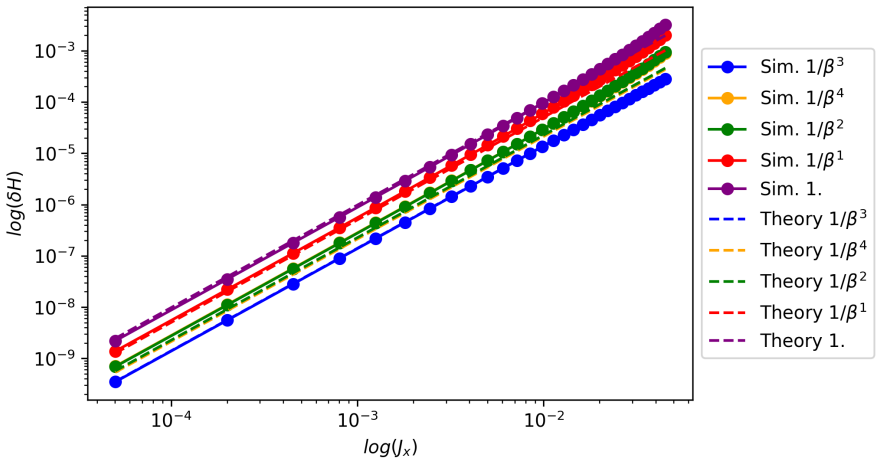

Figure 5.7: Fluctuation in Hamiltonian δH plotted against action, J_x, for theory and simulation with logarithmic axes. Theoretical values were calculated using $\delta H = \delta U + aJ_x^2$, where a was fit to simulation data and found to be $a = 0.07$.

The measure of integrability formula derived in Eq. 5.15 needs further benchmarking against simulation results which include error in the phase advance over the T-insert and extend the simulation to 2D. In addition, as mentioned above, the newly upgraded IBEX-2 could potentially be used to test predictions from the measure of integrability formula. The ease at which different lattices parameters can be scanned over in IBEX

makes it ideal for such experiments. In the meantime, from the results presented in this section, Eq. 5.15 can be used as a convenient estimate as to how close to integrable a T-insert lattice design will be, given errors in the octupole scaling.

5.2 PIC code VSim

The rest of the simulation work in this chapter used the simulation software VSim. The aim of these simulations was to create a model of the IBEX trap to simulate a T-insert lattice, with an octupole field applied in the drift region, created using voltages that could be achieved practically in the laboratory. The goal was then to test predictions from quasi-integrable optics with these simulations before testing experimentally with the IBEX-2 trap. The electromagnetic code VSimEM [111] was used to simulate a 2D cross-section of a 3D model of the Experimental Region (ER) in IBEX-2. As IBEX is essentially a 2D analog simulation of the alternating focusing in an accelerator, a 2D VSim model is sufficient to study the transverse beam dynamics we are interested in for testing quasi-integrable optics.

VSim is a commercial software made by Tech-X Corporation (Boulder, Colorado, USA) and the underling code is called VORPAL [115]. It uses a combination of Finite-Difference Time-Domain (FDTD) to solve Maxwell's equations and Particle-In-Cell (PIC) for particle tracking and space-charge effects. VSim is commonly used for plasma simulations such as RF antennas, plasma surface reactions [116] and plasma acceleration [117] but has also previously been used to study space-charge compensation in RF multipole traps [118].

The licence for VSim was provided by RAL, STFC and simulations were run in parallel on the SCARF high-performance computing cluster. The majority of simulations were run on one node with 16 cores for between an hour and multiple days, depending on the number of particles in the simulation and for how many lattice periods they were tracked.

A 3D model of the IBEX trap was created in AutoCAD and was imported into VSim as an '.stl' file[2]. The electrode material was set to a Perfect Electrical Conductor (PEC) and the rest of the space in the simulation was assumed to be a perfect vacuum. No residual gas was added to the simulation in order to reduce computational time so no residual-gas collisions with neutral argon atoms were taken into account in the simulations. A 2D, transverse slice of the electrodes was taken in VSim and a particle distribution with matched Twiss parameters to the simulated lattice was generated with Python code, before being loaded into the VSim simulation. The time-varying voltage waveforms were defined in Python and then applied as a potential to the trap electrodes. No longitudinal effects were studied in these simulations. This greatly reduces computational time, however, it means that processes such as the transfer of ions from the ionisation region to the experimental region were not simulated.

The grid size of the 2D simulations was set to 1000 × 1000 grid cells for an 18 mm × 18 mm boundary, encompassing a transverse cross-section of the electrodes and trapping region in IBEX. The number of grid cells was increased until there was negligible difference in the quadrupole-field multipole decomposition shown in Fig. 4.8. For correct tracking, a given particle in the simulation should not travel more than one grid cell per time step [119]. This sets a maximum speed for the particles, v_{max} in the simulation to be

$$v_{max} = \frac{L_{\text{cell}}}{t_{\text{step}}}, \tag{5.20}$$

where t_{step} is the time step of the simulation and L_{cell} is the length of a grid cell. The time-step of the simulation was set to 1/1000th of a cell period, i.e. a step size of 2.9 ns for a 2.9 µs cell period (where the cell period is treated as one turn through our accelerator). This put a reasonable maximum transverse speed on the particles of $v_{max} = 6081\,\text{m/s}$. Average transverse velocities in trap are below $v = 3000\,\text{m/s}$.

[2] An STL (stereolithography) is a file type commonly used in computer-aided design (CAD) software.

5.2.1 Matched distribution benchmark

The initial particle distribution was defined using the beta function of the lattice, given by MAD-X, and an assumed RMS emittance of 2.16×10^{-9} m rad [39]. In order to check the matching of the distribution in the VSim simulation, the RMS beam size was calculated at 50 points over the the one-cell and two-cell T-insert lattice. The RMS emittance, ϵ_{rms} of the distribution was also calculated at each point, using a Python script. The beta function can then be calculated at each point using $\beta = \sigma_{rms}^2/\epsilon_{rms}$ to see whether the distribution is correctly matched to the lattice.

The reconstructed beta functions for both the one-cell and two-cell T-insert lattice are plotted in Fig. 5.8 (Top) and are seen to agree well with the MAD-X beta functions plotted in Fig. 3.2 and Fig. 3.4 in Section 3.2. The percentage difference between the beta functions measured in VSim and the MAD-X beta functions are plotted in Fig. 5.8 (Bottom) and are seen to agree to within 2 – 3 %.

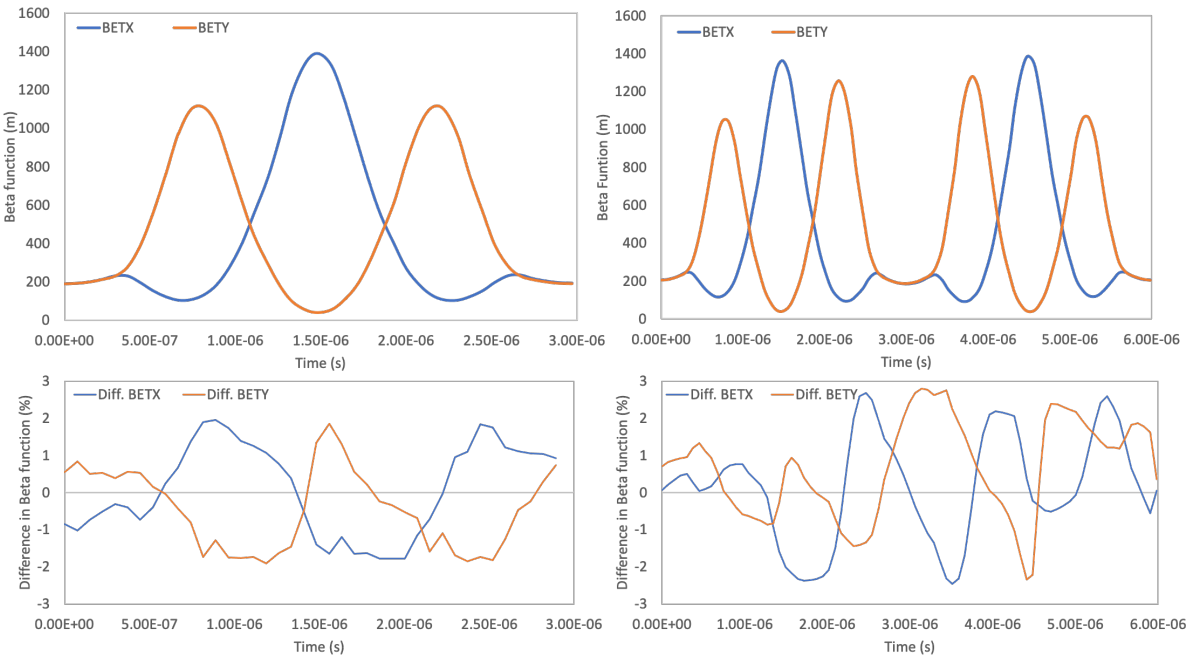

Figure 5.8: Reconstructed beta functions for the one-cell T-insert (Left) and two-cell T-insert (Right) calculated from VSim. Percentage difference between the beta functions measured in VSim and the MAD-X beta functions are plotted in the insert below.

5.2.2 KV distribution space-charge benchmark

In a KV (Kapchinskij-Vladimirskij) distribution [120], particles are randomly distributed on a 4D hyper-ellipsoid in phase space, defined by the beam size and emittance. This means that any 2D projection of this hyper-ellipsoid onto any pair of coordinates (x, x', y, y') will result in a uniform distribution where the space-charge force within this distribution is linear. This results in all particles oscillating with exactly the same betatron frequency (tune) which means that when space-charge forces are increased, this shifts all the particle tunes down evenly, which in theory does not cause any tune spread. A KV distribution was used to benchmark the space-charge tune shift in VSim against the analytical formula.

Assuming a cylinder with length L with a uniform distribution of N particles with charge e, then the maximum space-charge tune shift in a Paul trap [39] with an applied RF voltage with wavelength, λ_{RF} is

$$\Delta Q_{max} = \frac{\lambda_{RF}}{2\pi} \frac{e^2}{4\pi\varepsilon_0 mc^2} \frac{N}{L\epsilon_{100}}, \tag{5.21}$$

where ϵ_{100} is the 100 % emittance (i.e. it encompasses 100 % of the particle distribution). A matched KV distribution of 25,000 macro particles was loaded into VSim with an emittance of $\epsilon_{100} = 2.16 \times 10^{-9}\,\mathrm{m\,rad}$. The ratio between macro and physical particles was initially set to 1:1.

The distribution was tracked through the two-cell T-insert for 100 turns and the particle tunes were measured by taking the Fourier transform of the particle positions using the NAFF algorithm [121], implemented with pyNAFF [122]. This was repeated for increasing numbers of physical particles and the maximum space-charge tune shift, ΔQ_{max} from the nominal tune was measured. These values were compared to the theoretical maximum tune shift values, calculated from Eq. 5.21 and are plotted in Fig. 5.9. Figure 5.9 shows good agreement between the theoretical and simulation results for space-charge tune shift in a KV beam in VSim. The error bars in simulation indicate the tune spread in the distribution that was observed to increase at higher space charge.

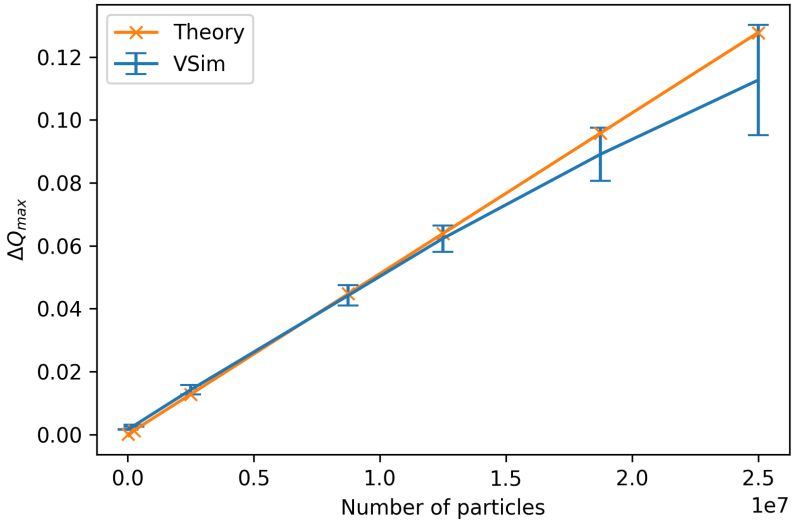

Figure 5.9: Theoretical maximum tune shift calculated from Eq. 5.21 plotted against the number of particles. This is compared to the calculated maximum tune shift from a KV distribution in VSim for various numbers of particles. Error bars indicate the RMS tune spread observed in simulation.

5.3 Testing Quasi-Integrable Optics with a 4th order perturbation

In an accelerator, perturbations are determined by the spatial positioning of magnets in the lattice. The perturbation's frequency is governed by the lattice periodicity. When the betatron oscillation frequency or its harmonics become close to the frequency of the lattice periodicity, a resonance occurs between the lattice and the beam, which leads to unstable motion of the beam. In IBEX, on the other hand, perturbations can be introduced independently from the lattice structure. A resonance can be introduced as a sinusoidal perturbation superimposed over the voltage waveform defining the lattice structure in IBEX. When the frequency of the perturbation becomes close to the betatron frequency (tune) or its harmonics, a resonance occurs. Using this technique, a perturbation with quadrupole-like potential can drive a 2nd order resonance and a perturbation with an octupole-like potential can drive a 4th order resonance, without the need for the lattice tune to be close to the 1/2 or 1/4 integer.

These perturbations have been shown to excite resonances in Paul traps in previous experiments [61]. In previous simulation work, I have also shown that 2nd order resonances driven by a small perturbation are damped in a T-insert lattice with a QI octupole insert [112]. In this section, I will concentrate on the results from damping a 4th order resonance in the T-insert lattice as this more clearly shows the benefits of quasi-integrable optics, i.e. the ability for a quasi-integrable lattice to eliminate the 4th order (octupole) resonance. For the rest of this work, 'perturbation' will refer to a sinusoidal perturbation created with an octupole potential and frequency close to four times the lattice tune.

5.3.1 4th order perturbation

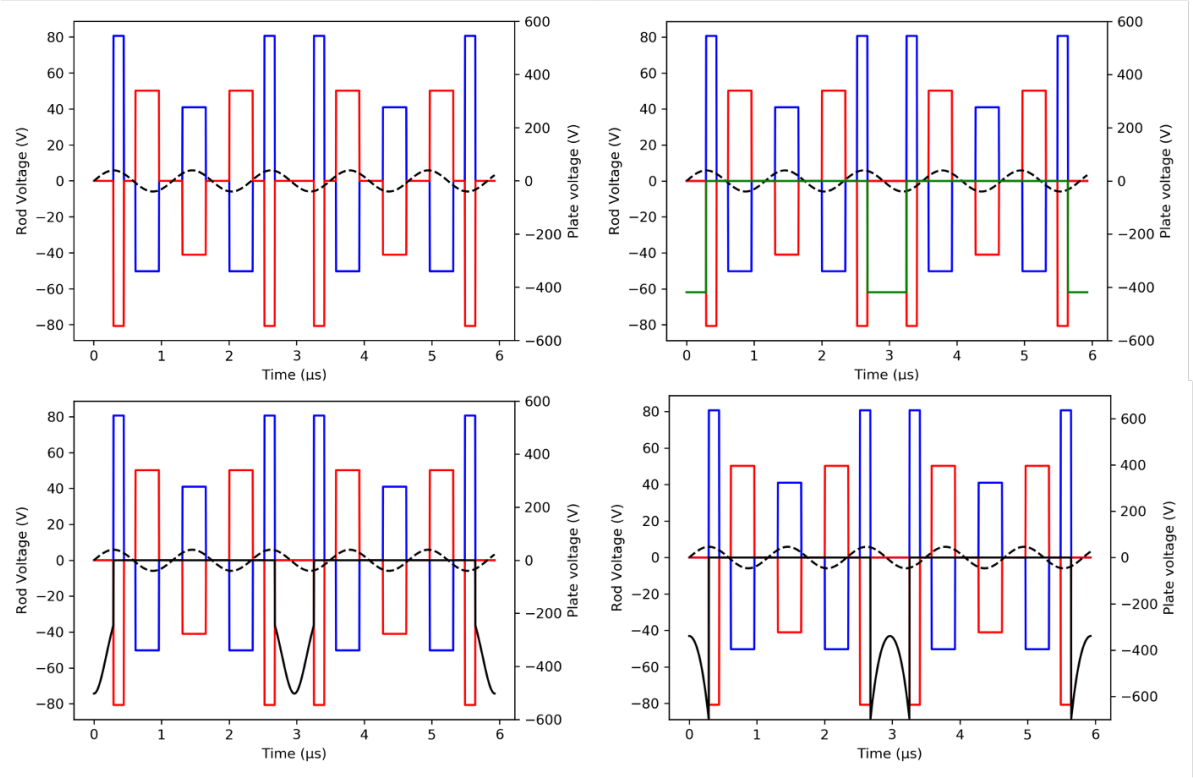

Figure 5.10: Two periods of the voltage waveform, applied to the rods in IBEX (red and blue) to create the T-insert lattice. A 5.88 V perturbation is applied to the plates to excite the 4th order resonance (black, dashed). **Top Left:** No octupoles applied in drift region. **Top Right:** Constant square-wave octupole pulse applied in drift region (green). **Bottom Left:** Octupole pulse with $1/\beta^3$ strength scaling (black, solid). **Bottom Right:** Octupole pulse with β^3 strength scaling (black, solid).

VSim 11.0 [111] was used to simulate a perturbation with an octupole-like potential applied to the T-insert lattice in order to excite the 4th order resonance. Figure 5.10 plots the voltage waveform applied to the rod electrodes in IBEX to create the one-cell T-insert lattice designed and presented in Section 3.2. The perturbation is plotted as the black dashed line and corresponds to a sinusoidal voltage of $\mathrm{V} = A\sin(4 \cdot 2\pi Q/T)$ applied to the plate electrodes where $A = 5.88\,\mathrm{V}$ is the amplitude of the perturbation, $Q = 0.6356$ is the horizontal and vertical tune of the lattice and $T = 2.966\,\mu\mathrm{s}$ is the lattice time period. In the top-left plot of Fig. 5.10, no octupole is applied in the drift region, only the perturbation is present (black dashed). In the top-right plot of Fig. 5.10, a constant octupole field is applied in the drift region (green) in the presence of the perturbation. The plate voltage required to create this octupole strength is around 419 V. As the octupole strength does not vary with the beta function, this lattice is no longer time-independent and is non-integrable. The bottom right plot of Fig. 5.10 shows an alternative non-integrable lattice, where an octupole scaling as $\beta^3(s)$ is applied in the nonlinear region of the perturbed T-insert lattice (black, solid). The bottom left plot of Fig. 5.10 shows the quasi-integrable lattice, where an octupole scaling as $1/\beta^3(s)$ is applied in the nonlinear region of the perturbed T-insert lattice (black, solid). This octupole pulse requires a peak plate voltage of 502 V. All three octupole pulses had their integrated octupole strength adjusted so that they each created the same tune spread of $\Delta Q = 0.015$.

A 2D, non-truncated, Gaussian distribution of 25,865 Ar^+ particles was tracked in a VSim 11 model of IBEX for 200 T-insert lattice periods. The ratio of macro particles to real particles was 1:1. As VSim solves the Laplace equation at each time step to calculate the electrostatic field in the simulation, space-charge effects between the charged particles cannot be turned off. Therefore, a low number of particles was chosen to avoid space-charge effects in these simulations. Figure 5.11 shows the initial phase space (x, x') of the particle distribution as well as the phase space after 50, 100 and 200 turns for the T-insert lattice with perturbation but without octupole (Fig. 5.10, top left). The four

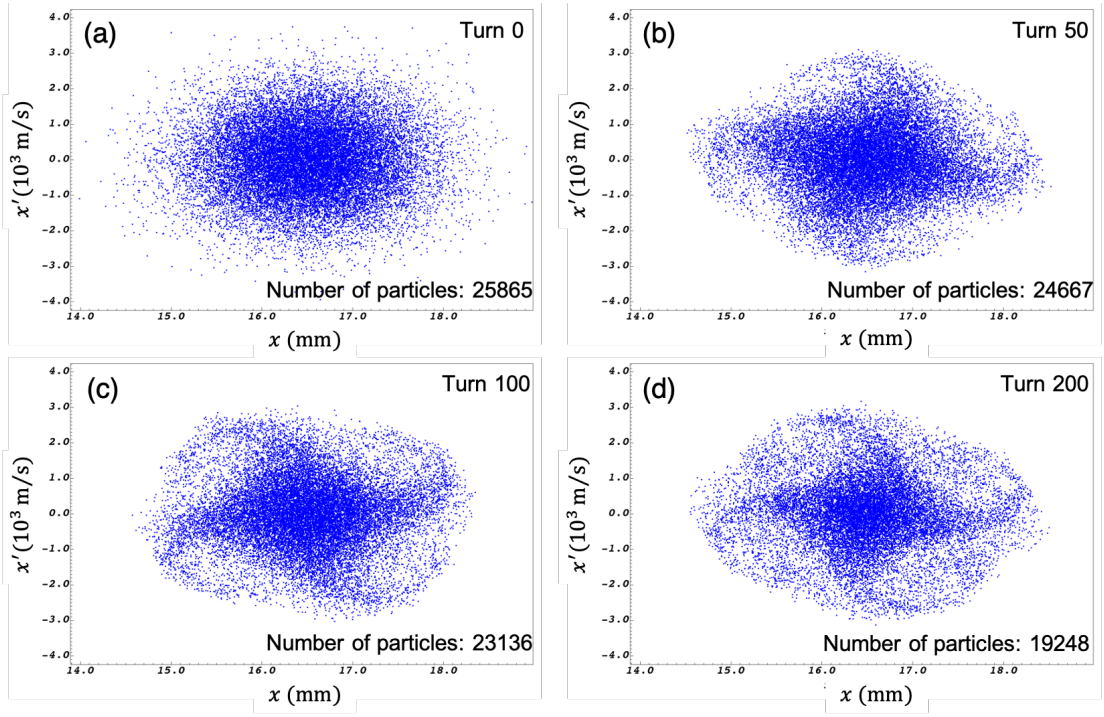

Figure 5.11: Phase space evolution when a 4th order perturbation is applied to the T-insert lattice, at a frequency proportional to $4Q$, with the octupole potential switched off.

tails forming in the phase space distribution show that the 4th order resonance is being excited by the perturbation. Over the 200 lattice periods, 25.6(3) % of particles were lost in the simulation.

Figure 5.12 shows the evolution of the phase space distribution for the perturbed, quasi-integrable lattice. An octupole with a strength that scales with $1/\beta^3(s)$ is applied in the drift region (Fig. 5.10, bottom left). The phase space distribution has been restored to one that resembles the initial distribution. A similar result is seen in the (y, y') phase space which has been omitted from this thesis to avoid repeating plots. The particle loss over the 200 lattice periods has been reduced from 25.6(3) % to 5.1(1) %. These results show that the T-insert lattice, with the correctly scaled octupole insert, can successfully damp the instability excited by the perturbation with voltages that can be realistically achieved in the nonlinear IBEX trap.

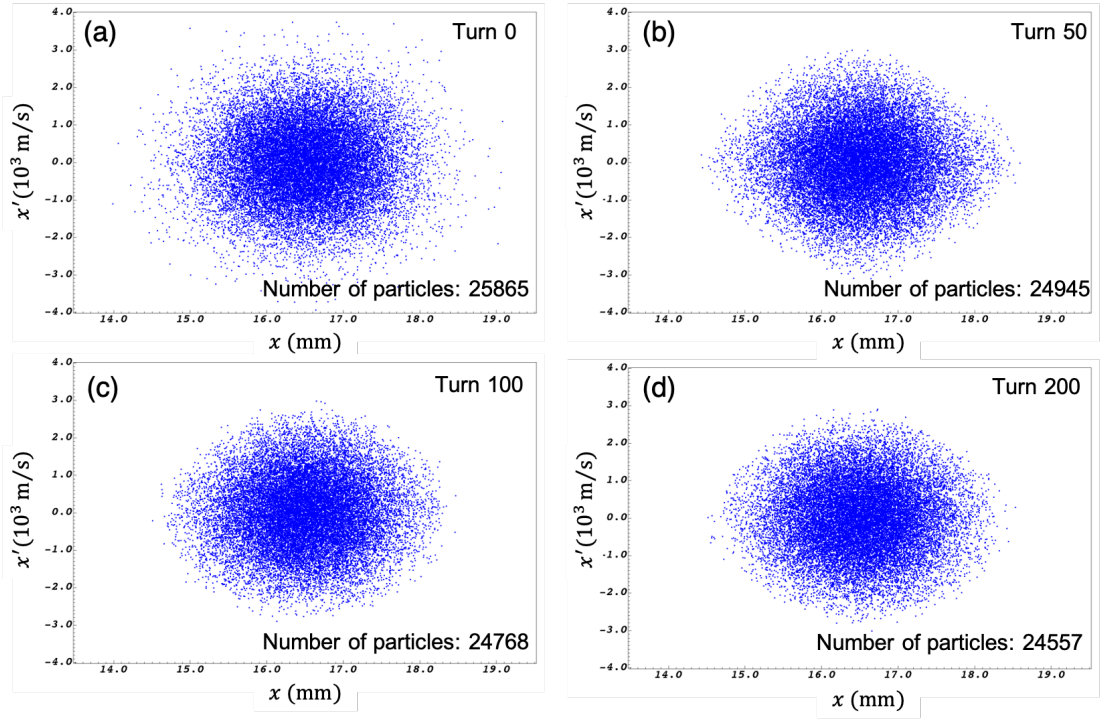

Figure 5.12: Phase space evolution when a 4th order perturbation is applied to the T-insert lattice, at a frequency proportional to $4Q$, with the QI octupole potential switched on.

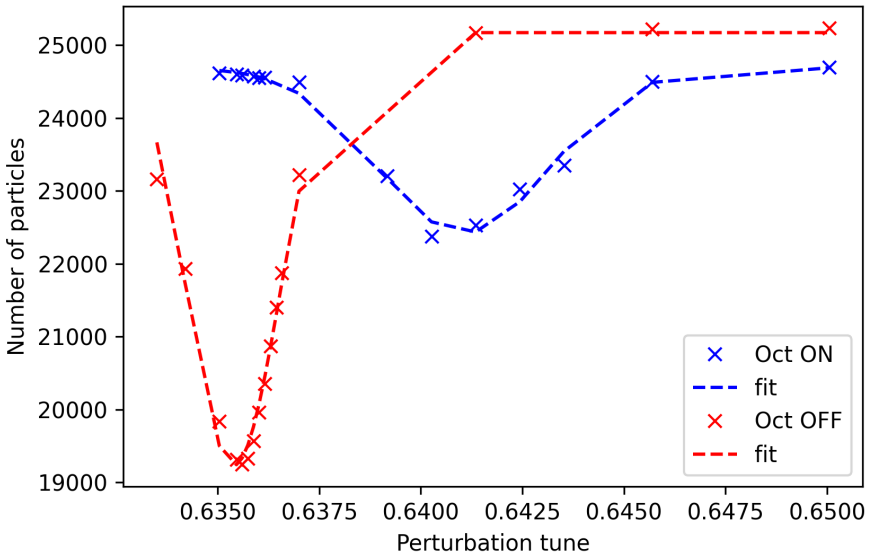

Figure 5.13: Number of particles plotted against the perturbation tune corresponding to the perturbation frequency.

5.3.1.1 Perturbation tune scan

Simulation results were also taken at a number of perturbation frequencies, analogous to scanning the tune in an accelerator lattice. The results from the perturbation tune scan are presented in Figure 5.13. The number of particles remaining after the 200 lattice periods is plotted against the corresponding tune of the applied perturbation. The T-insert lattice without octupoles, with the 4th order perturbation applied, is plotted in red, whereas the octupole perturbation plus the QI octupole turned on in the drift region is plotted in blue. The plate voltage applied to create the octupole again had a peak voltage of 503 V and was estimated to generate a tune spread of $\Delta Q = 0.015$. Turning on the QI octupole shows that the peak in particle loss is shifted over to the right. The peak amount of particle loss is reduced from 26 % when octupoles are off to 13 % when octupoles are on. The resonance width in the case when the octupoles were turned on is broadened due to the tune spread created by the octupole. Taking the standard deviation of the Gaussian curve fitted to the data, we get a value of $\sigma = 0.001$ for octupoles off and $\sigma = 0.002$ for octupoles on. The peak in particle loss occurred at a tune of 0.635 for octupoles off, whereas the peak loss has shifted to a value of 0.641 when the octupoles are turned on.

5.3.1.2 Comparison with a non-integrable lattice

In order to demonstrate the true benefits of quasi-integrable optics (not just the benefits of including an octupole), we must compare the quasi-integrable lattice to a lattice that creates an equal tune spread but is non-integrable. The simplest way to do this is with a lattice where a constant octupole is applied in the drift region, with an integrated octupole strength equal to the quasi-integrable lattice (Fig. 5.10, top right).

An octupole with a scaling of β^3 (Fig. 5.10 bottom right) was also designed to exaggerate the effect that the octupole pulse has on the integrability of the lattice. This time a 2D Gaussian distribution of 51,730 Ar^+ particles was tracked in the quasi-integrable lattice (Fig. 5.10 bottom left), constant octupole lattice (Fig. 5.10 top right) and $\beta^3(s)$

octupole scaling lattice (Fig. 5.10 bottom right) for 2000 T-insert lattice periods with the perturbation applied. The number of particles surviving over the 2000 lattice periods is plotted in Fig. 5.14 and is also compared to a T-insert lattice with the octupoles turned off in the drift, with and without a 4th order perturbation applied.

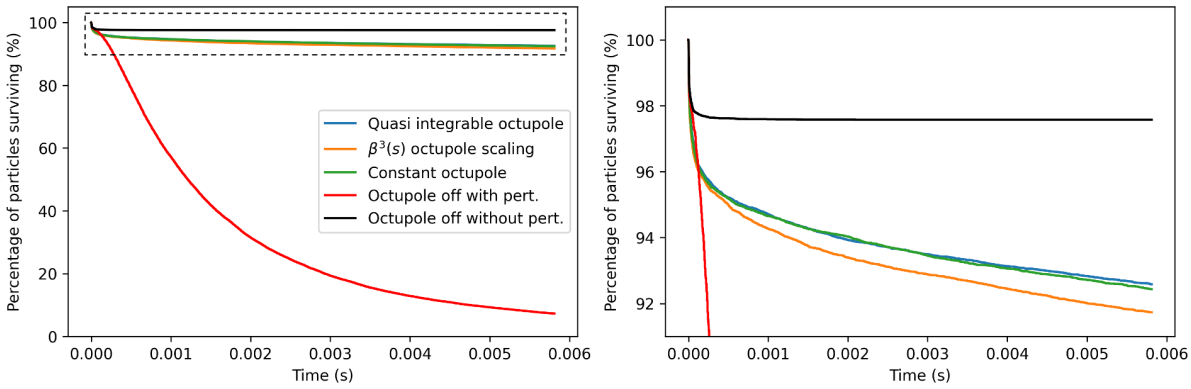

Figure 5.14: VSim simulations of the number of particles surviving after 2000 T-insert lattice periods. (Left) Three different octupole scalings (with 4th order perturbation applied) are compared to octupoles off with no perturbation (black) and octupoles on with 4th order perturbation (red). Dashed box indicates the scale of the figure on the right. (Right) The T-insert lattice with the quasi-integrable ($1/\beta^3$ strength scaling) octupole pulse is compared to the T-insert lattice with a constant square-wave octupole and β^3 octupole scaling.

When the perturbation is applied to the T-insert lattice with the octupoles turned off in the drift region, a particle loss of 93.0(2) % over 2000 lattice periods is seen (Fig. 5.14 (red)). This is compared to only 2.4(1) % particle loss for the linear lattice, with no perturbation applied. A small amount of loss is still seen in the linear lattice with no perturbation applied because the Gaussian distribution is not truncated. These particles are scrapped on the rod electrodes within the first 30 cell periods of the simulation.

When the quasi-integrable octupole pulse is turned on, with the 4th order perturbation present, the particle loss is reduced from 93.0(2) % to only 7.4(1) %. In comparison, the particle loss for the lattice with the constant, square-wave octupole pulse was found to be 7.6(1) % and for the lattice whose octupole strength scales as β^3, a particle loss of 8.3(1) % was observed. The reason behind the similar particle loss for all three octupole lattices is thought to be because of the comparatively flat nature of the beta function

in the drift region (see Fig. 3.2 in Section 3.2). If the beta function in the drift region is flat, then the lattice is less sensitive to the $1/\beta^3$ strength scaling condition of QIO. However, Fig. 5.14 (Right) also shows that the difference between the particle loss seen in the three different octupole scalings is diverging. This means that for a synchrotron which could circulate particles for hundreds of thousands of turns, the octupole scaling will become increasingly important.

Another contributing factor to why little difference was seen in particle loss between the QI lattice and two lattices that broke the $1/\beta^3$ octupole scaling is due to the perturbation itself affecting the applied octupole field in the lattice. As the perturbation applied to the plate electrodes is superimposed onto the octupole field applied in the drift region, the perturbation will therefore reintroduce a small time dependence back into the Hamiltonian, moving the system away from integrability. Deviations in the octupole field strength are studied further in Section 5.4. In order to avoid breaking the conditions of integrability with the perturbation, a T-insert lattice is later studied in the absence of a perturbation, with the resonance driven by the interaction of space charge and the lattice in Section 5.5.

The results presented in this section suggest that the quasi-integrable octupole scaling of $1/\beta^3$ is indeed the ideal case, as theory suggests, and perturbations away from this scaling will lead to larger particle loss. The difference in particle loss is still relatively small over the time scale studied. These results suggest that for relatively flat beta functions in the drift region, or for short storage times, a good approximation of QIO could be achieved with constant strength octupoles. This would greatly simplify the lattice for use in accelerators as multiple, independently powered octupoles would no longer be needed to create the $1/\beta^3$ scaling.

5.3.2 Dynamic aperture

The theory of QIO states that instabilities can be damped with an octupole tune spread, while maintaining a large dynamic aperture (DA). The results presented so far in this

chapter have shown that a quasi-integrable (QI) lattice can indeed damp instabilities and reduce the particle loss associated with these resonances. However, we now turn to investigating the DA of the QI lattice, and comparing it to the linear case, with and without perturbation, and the β^3 octupole scaling, with perturbation. In this section the DA is defined as the largest initial particle amplitude which survives the simulation.

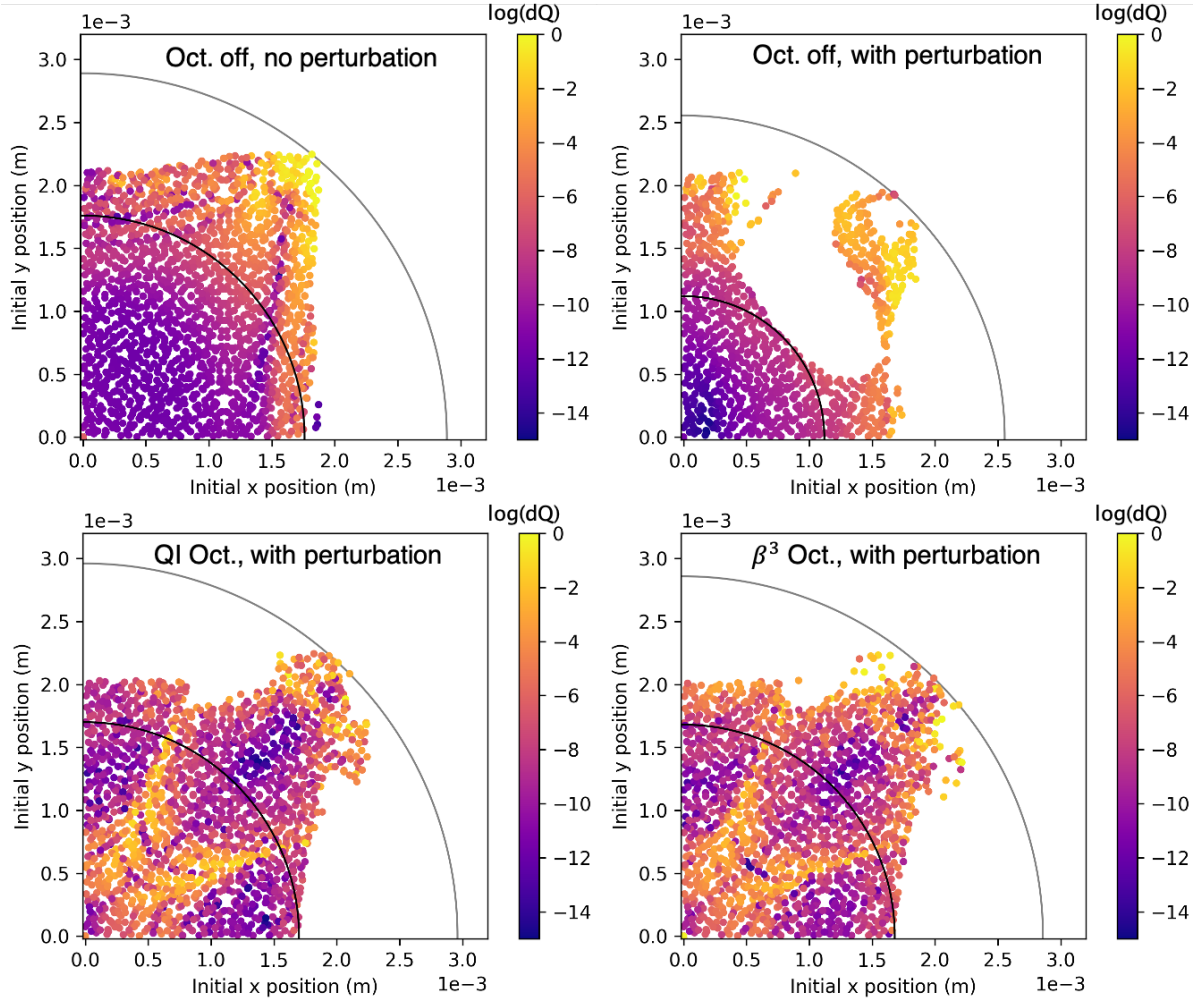

Figure 5.15: Dynamic aperture plot of T-insert simulated for 200 lattice periods in the VSim IBEX model. Inner black circle is the measured DA whilst the outer grey circle is the largest stable orbit observed. **Top Left:** No octupoles applied in drift region and no perturbation applied. **Top Right:** No octupoles applied in drift region but a perturbation is applied to lattice. **Bottom Left:** T-insert with perturbation, octupole pulse with $1/\beta^3$ strength scaling (quasi-integrable). **Bottom Right:** T-insert with perturbation, octupole pulse with β^3 strength scaling (non-integrable).

Figure 5.15 displays the region of initial (x, y) coordinates in configuration space where a particle survives 200 T-insert lattice periods. Note that just the positive quad-

rant of the (x, y) space is plotted as it is symmetrical in the x and y planes. The points are coloured based on the log of the change in particle tune (dQ), calculated by comparing the tune in the first 100 lattice periods to the tune in the last 100 periods. Particles with a large, negative $\log(dQ)$ have very little change in tune. Particles with a $\log(dQ)$ of close to 0 have a large change in tune and are considered less stable. The VSim simulation started with a uniform particle distribution with a size of 5 mm × 5 mm which fills around 31.8 % of the physical aperture of the trap, defined by the trap electrodes. Only particles that survived the full 200 turns are plotted in Fig. 5.15. The DA, defined as the largest radius in (x, y) in which all particles have survived the simulation, is plotted as the inner black quadrant of a circle. The radius of the largest stable orbit is plotted by the outer grey circle.

The top-left plot of Fig. 5.15 shows the DA of the T-insert with octupoles off and no perturbation applied to the lattice. The DA was calculated to be 1.76×10^{-3} m and had a largest stable particle orbit of 2.89×10^{-3} m. The average $\log(dQ)$ was calculated to be -10.47, suggesting stable particle orbits, as expected from a linear lattice free from perturbations.

Table 5.2: Table summarising the DA, largest stable orbit and average $\log(dQ)$ for the four different lattices shown in Fig. 5.15.

Lattice	DA (mm)	Largest stable orbit (mm)	$\log(dQ)$
No Octupole, no perturbation	1.76	2.89	-10.47
No Octupole + perturbation	1.12	2.55	-9.30
QI Octupole + perturbation	1.70	2.96	-9.44
β^3 Octupole + perturbation	1.68	2.86	-9.28

A perturbation was applied to the lattice, while the octupole in the nonlinear region remained off (Fig. 5.10, top left); the resulting DA is plotted in the top-right plot of Fig. 5.15. The DA was reduced to 1.12×10^{-3} m and the largest stable orbit recorded was 2.55×10^{-3} m. This shows the reduction in DA caused by the excitation of the 4th order resonance. The average $\log(dQ)$ was reduced to -9.30, which shows that there are

also less stable particles still present in the distribution.

The QI octupole pulse which scales as $1/\beta^3$ (Fig. 5.10, bottom left) created the DA plot in the bottom left of Fig. 5.15. The DA was calculated to be 1.70×10^{-3} m, comparable to the DA on the linear lattice without the perturbation applied. The largest stable orbit was found to be 2.96×10^{-3} m which is slightly larger than that of the lattice with octupoles off and no perturbation. The average $\log(dQ)$ was -9.44, an increase in stability over the lattice with the perturbation applied but octupoles turned off.

As a comparison to the QI octupole, the DA for the non-integrable octupole with β^3 scaling (Fig. 5.10, bottom right) is plotted in the bottom right of Fig. 5.15. The DA was measured to be 1.68×10^{-3} m, slightly smaller than the DA of the QI lattice but still an improvement over the lattice with the perturbation applied but octupoles off in the nonlinear region. The largest stable orbit was found to be 2.86×10^{-3} m and the average $\log(dQ)$ was found to be -9.28, suggesting the particles that do remain are on average less stable than in the other three lattices. These values are summarised in Table 5.2.

It should be noted that the asymmetry in the DA plotted in Fig. 5.10 is a result of the different maximum beta functions in the horizontal and vertical axes. This in turn leads to asymmetrical scraping on the rods.

These results confirm that not only does the presence of an octupole in the drift region damp the 4th order resonance created by the perturbation, but the QIO lattice also restores the DA to within 3.4 % of the linear lattice with no perturbation applied.

5.4 Octupole field quality

In order to test these simulation results in the nonlinear IBEX trap we must first test the sensitivity of QIO to fluctuations in the octupole strength. Figure 5.16 plots six lattice periods of the T-insert with the QI octupole pulse applied in the nonlinear region. For this simulation, the octupole strength was randomly fluctuated by a value from a Gaussian distribution with standard deviation σ.

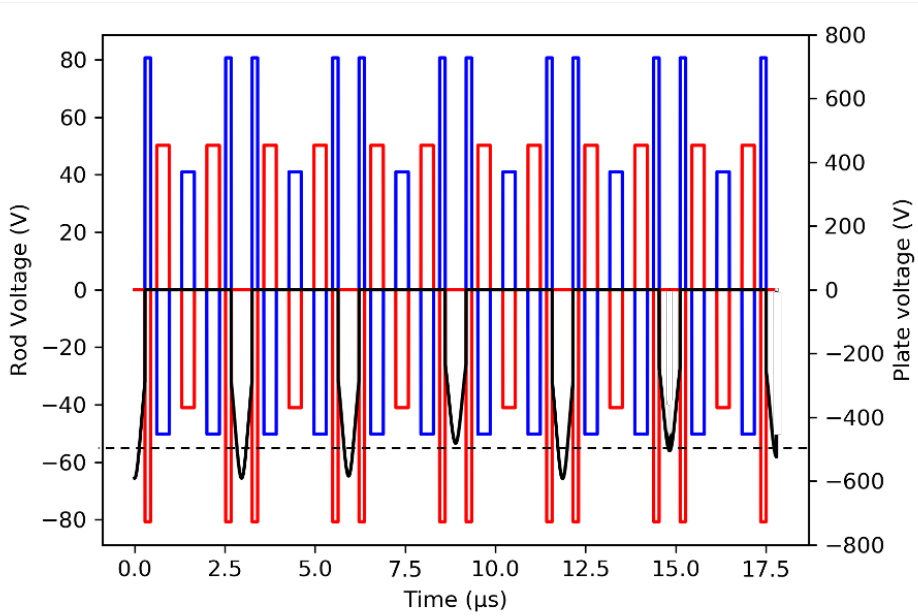

Figure 5.16: Six cells of the T-insert lattice waveform are shown with the quasi-integrable octupole turned on. The T-insert lattice waveform applied to the rods is plotted in red and blue. The peak strength of the octupole is given a random error from a Gaussian distribution with standard deviation σ. Black dashed line indicates the nominal octupole strength.

Table 5.3: Particle loss after 200 T-insert lattice periods for a given Gaussian random error deviation, σ in octupole strength.

Standard deviation of error (σ_{rms})	Particle loss (%)
0.0	3.8(1)
0.05	4.3(1)
0.1	5.1(1)
0.2	8.0(1)
0.5	20.3(2)

Figure 5.17 plots the number of particles surviving after passing 200 cells of the T-insert with octupoles on in the drift region. The octupole strengths have been randomly varied by RMS standard deviations of 0.0, 0.05, 0.1, 0.2 and 0.5 of the nominal octupole strength. The particle loss at the end of the 200 lattice periods is summarized in Table 5.3. As expected, the particle loss increases as the average error in the octupole strength is increased. Increasing the error to a standard deviation of 0.1 only increases the particle loss by 1.3(1) %. This agrees with results from IOTA which found that octupole-field errors on the order of 10 % can be tolerated and should not alter the dy-

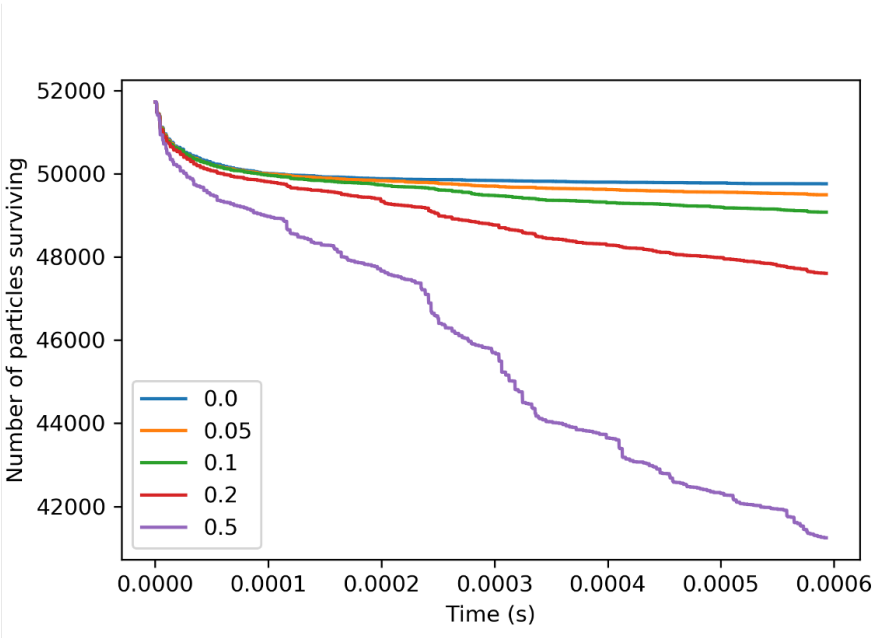

Figure 5.17: Number of particles surviving 200 T-insert lattice periods with octupole random error deviation ranging from 0.0 to 0.5.

namics of the system [77]. This is a generous tolerance and experimentally we expect to have an octupole strength error of less than 1 % in IBEX.

5.5 Quasi-Integrable Optics with space charge

The previous results showed that a QI lattice could damp a perturbation analogous to magnet misalignment or field errors which would excite the 4th order incoherent resonance. However, the most important goal of QIO is to damp coherent resonances, driven by space charge, while also not exciting any octupole resonances. Therefore, the next step is to test a QI lattice in the presence of space charge. In this section, the resonances will be driven by the lattice structure itself (or the interaction between the lattice and beam core), not by an external perturbation. This is a more realistic comparison to resonances in accelerators.

The idea is to create a lattice close to the 1/4 integer resonance as this resonance is driven predominately by octupoles. An intensity will be chosen to create a space-charge tune shift which will overlap with the stopband of the 2nd order coherent resonance. In

a linear lattice (i.e. no octupoles) this should excite a 2nd order coherent resonance. A QI lattice will be tested to see if it is capable of damping the 2nd order coherent resonance, without also exciting the 4th order incoherent resonance. A non-QI lattice, where the applied octupole breaks the conditions of integrability, will also be compared to test whether this lattice excites the 4th order incoherent resonance.

5.5.1 T-insert lattice design

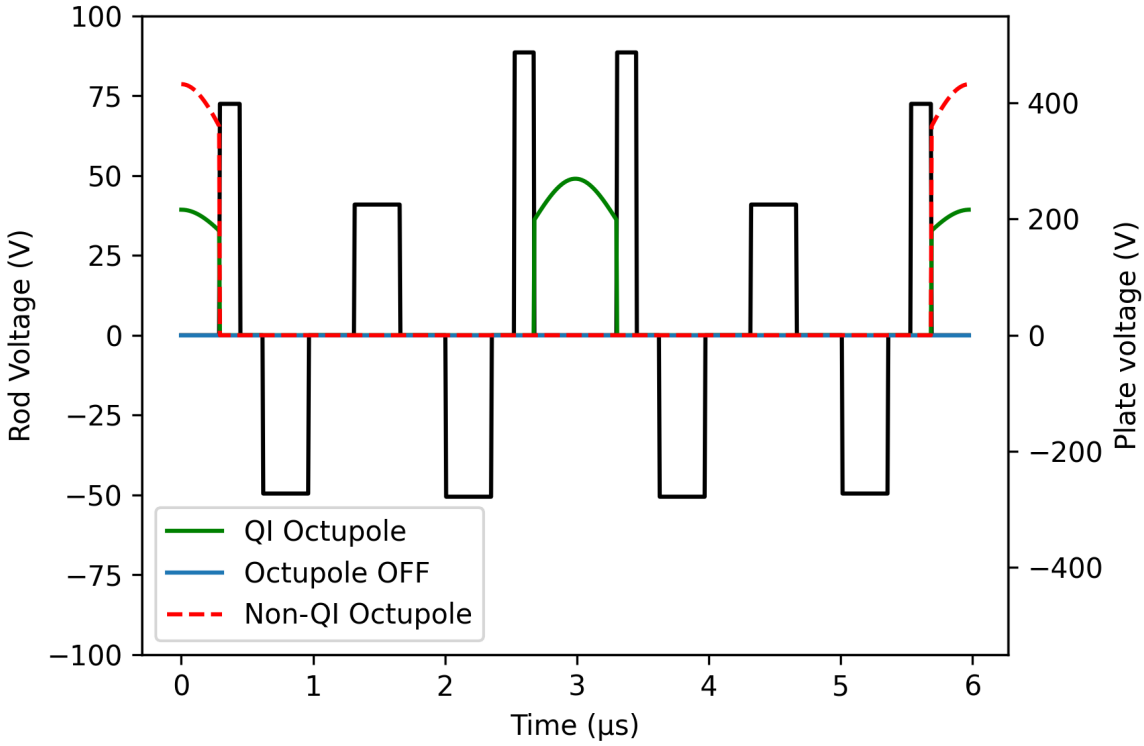

Figure 5.18: Voltage waveform applied to the rods in IBEX (black) to create the two-cell T-insert super-period. Coloured waveforms indicate the voltage applied to the plates. **Blue:** No octupoles applied in the drift region. **Green:** Octupole pulse with $1/\beta^3$ strength scaling applied in the drift region to create Quasi-Integrable lattice. **Red (dashed):** Octupole pulse with $1/\beta^3$ strength scaling with twice the strength but applied only once per super-period, hence non-integrable.

VSim 11.0 was used to create the T-insert lattice in a 2D simulation of the IBEX trap. Figure 3.4 shows the beta functions of the non-identical, two-cell lattice. The octupole is positioned in the shaded blue region where the beta functions are equal. The lattice was designed to have a π phase advance through the T-insert region and equal

horizontal and vertical beta functions within the drift region. Two distinct cells with mirror symmetry were designed to create a super-period with tunes of $Q_x = 1.276$ and $Q_y = 1.277$, close to the 1/4 integer resonance. The decision to create a two-cell lattice with the first cell being distinct from the second was to ensure the resonant driving term of the octupole would be the same if the octupole was applied once per drift region or every other drift region.

Figure 5.18 plots the voltage waveform applied to the rod electrodes in IBEX to create the two-cell T-insert lattice. The black waveform is the quadrupole focusing applied to the rod electrodes. The coloured waveforms indicate what is being applied to the plate electrodes to create the octupole field in the lattice. In blue is the T-insert lattice with no octupole applied in the drift region. In green is the Quasi-Integrable (QI) lattice where the octupole is turned on in the drift region and varies as $1/\beta^3(s)$. In red (dashed), a comparison lattice is used where the octupole is turned off every other cell (while the strength still varies as $1/\beta^3(s)$). The octupole strength is twice as large in this lattice to make the integrated octupole strength the same as the QI lattice, however this lattice is non-integrable.

The way in which the non-QI lattice breaks integrability can be thought of in two ways. If we first consider the Hamiltonian, it is conserved over the first cell, but then as the octupole is turned off in the drift of the second cell, the Hamiltonian will have a different value and therefore is not conserved over the two-cell structure. The second way to view the non-QI lattice is that the two-cell lattice creates a larger one-cell T-insert where the phase advance over the linear region is now $2\pi + \phi_{drift}$. As $\phi_{drift} = 0.13 \times 2\pi$, the $n\pi$ condition is broken over the linear region of the T-insert and thus the lattice is no longer integrable. A lattice was chosen that broke the integrability condition by a larger amount then simply changing the octupole scaling. This is due to simulation results presented in Section 5.3.1.2 which showed that changing the octupole scaling in the designed lattice did not have a significant effect on particle loss over the length of simulation studied. As previously mentioned, this is most likely due to the relatively

flat beta function in the drift region.

5.5.2 Gaussian particle distribution

5.5.2.1 Coherent resonance condition

A 2D non-truncated Gaussian distribution, with a beam size of $\sigma_{rms} = 0.66\,\text{mm}$ and RMS emittance of $2.16 \times 10^{-9}\,\text{m rad}$, was matched to the Twiss parameters at the center of the drift region in the two-cell T-insert lattice. The particle distribution contained 25,000 Ar^+ macro particles and was tracked in a VSim 11 model of IBEX for 1000 T-insert lattice super-periods (2000 cell periods). The ratio of macro particles to physical particles was 1:1000. The distribution of 2.5×10^7 physical particles created a theoretical incoherent space-charge tune shift of $\Delta Q_{rms} = -0.034$ (tune depression of $\eta = 0.97$). This tune shift was chosen to excite coherent oscillations which satisfied the following resonant condition [123]:

$$Q_0 + C_2 \Delta Q_{rms} = \frac{1}{2}(\frac{5}{2}) \tag{5.22}$$

where Q_0 is the nominal tune and the coherent mode factor is $C_2 = 3/4$ [19] (see Section 1.2.2.1).

For the Gaussian distribution, the incoherent space-charge tune shift was calculated from simulation data. In Fig. 5.19 a tune space diagram is plotted for the 2D, Gaussian particle distribution of 2.5×10^7 particles. Using the relation between the RMS tune shift and the maximum tune shift [124]

$$\Delta Q_{rms} = \frac{1}{2}\Delta Q_{max}, \tag{5.23}$$

with $\Delta Q_{x_{max}} = -0.06275$ and $\Delta Q_{y_{max}} = -0.07146$ obtained from Fig. 5.19 ($\Delta Q_{max} = Q_{max} - Q_0$), the horizontal and vertical RMS tune shifts are found to be $\Delta Q_{x_{rms}} = -0.0314$ and $\Delta Q_{y_{rms}} = -0.0357$ respectively.

The RMS incoherent tune shift for a Gaussian distribution can also be calculated theoretically using the following formula

$$\Delta Q_{rms} = -\frac{1}{2}\frac{\lambda_{RF}}{2\pi}\frac{e^2}{8\pi\varepsilon_0 mc^2}\frac{N}{L\epsilon_{rms}} \tag{5.24}$$

where $\lambda_{RF} = 1792$ m is the length of the two-cell lattice, e is the charge of an electron, ε_0 is the vacuum permittivity, $m = 39.948 \times 1.660\,539 \times 10^{-27}$ kg is the mass of an argon ion, c is the speed of light in a vacuum, $\epsilon_{rms} = 2.16 \times 10^{-9}$ m rad is the initial RMS emittance and N/L is the longitudinal particle line density. Note that as the VSim simulations are 2D, the number of particles is already a transverse cross-section and so can be thought of as 'number of particles per unit of longitudinal length'. Using this equation, we get a value of $\Delta Q_{rms} = -0.03193$ which agrees well with the values from simulation.

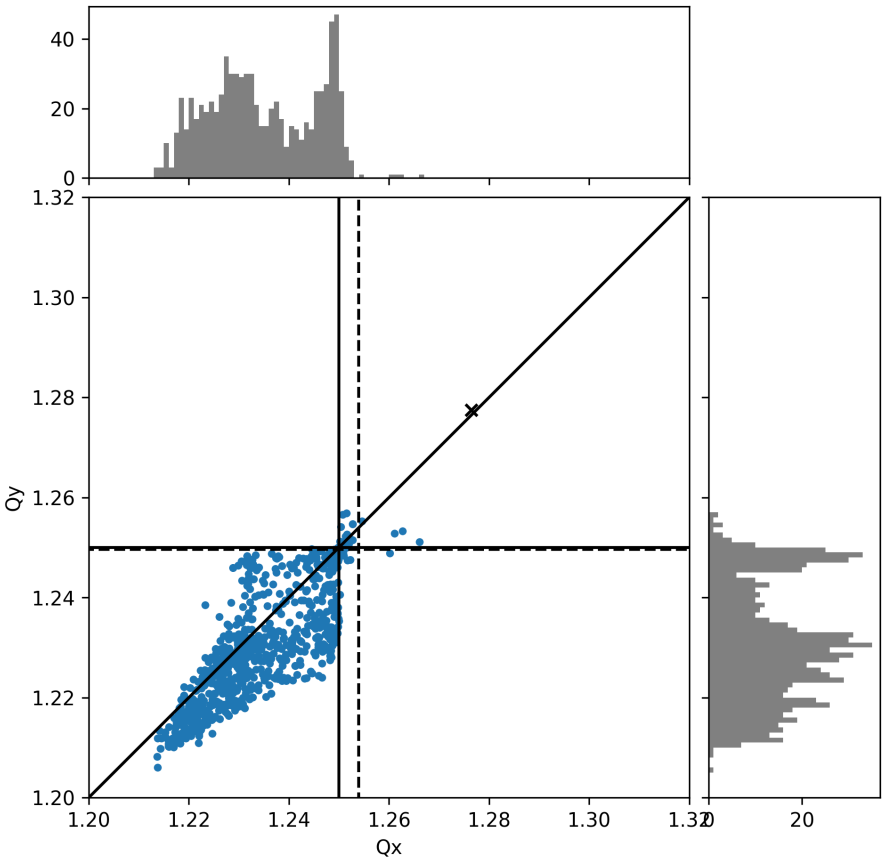

Figure 5.19: Tune shift diagram for a 2D Gaussian distribution of 2.5×10^7 physical particles (blue). Nominal tune is indicated with a black cross. The black horizontal and vertical lines show the 2nd order coherent resonance (overlapping with the 1/4 incoherent resonance). Black dashed lines indicate how close the distribution is to the coherent resonance condition from Eq. 5.22.

5.5.2.2 Particle loss

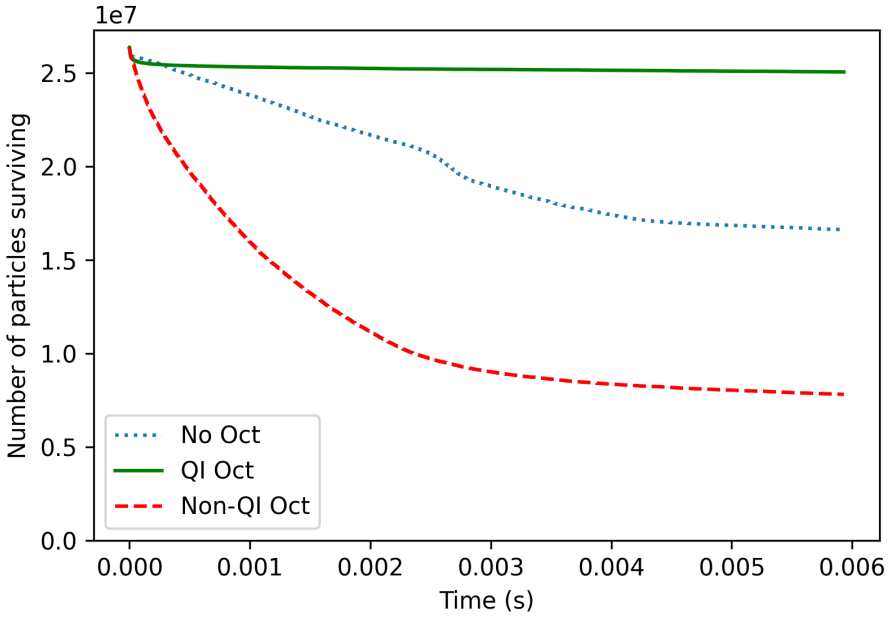

Figure 5.20: Rate of particle loss over 1000 super-periods of the T-insert lattice. (Blue, dotted) No octupoles applied in the drift region. (Green, solid) Octupoles turned on in the drift region which meet the quasi-integrability condition. (Red, dashed) Octupoles turned on with twice the strength but applied only once per super-period, hence non-QI.

The number of particles surviving over 1000 T-insert super-periods is plotted against time in Fig. 5.20. The linear T-insert lattice with no octupoles applied is plotted in blue (dotted) and can be seen to lose 36.9(3) % of the initial distribution of particles. When the octupoles are turned on and they meet the quasi-integrability condition (green), the particle loss is reduced to 5.0(1) %. If we compare the QI lattice to the non-QI lattice, we get 70.4(3) % particle loss, which is plotted in red (dashed) in Fig. 5.20.

The mechanisms behind the particle loss can be observed from the phase space plotted in Fig. 5.21. Figure 5.21a is the (x, x') phase space of a matched Gaussian distribution of 25,000 macro particles with no space charge (ratio of macro particles to physical particles was 1:1, where space charge is negligible). The phase space is plotted after 500 super-periods of the linear lattice and resembles the initial Gaussian distribution.

In Fig. 5.21b the phase space is plotted after 500 super-periods through the linear

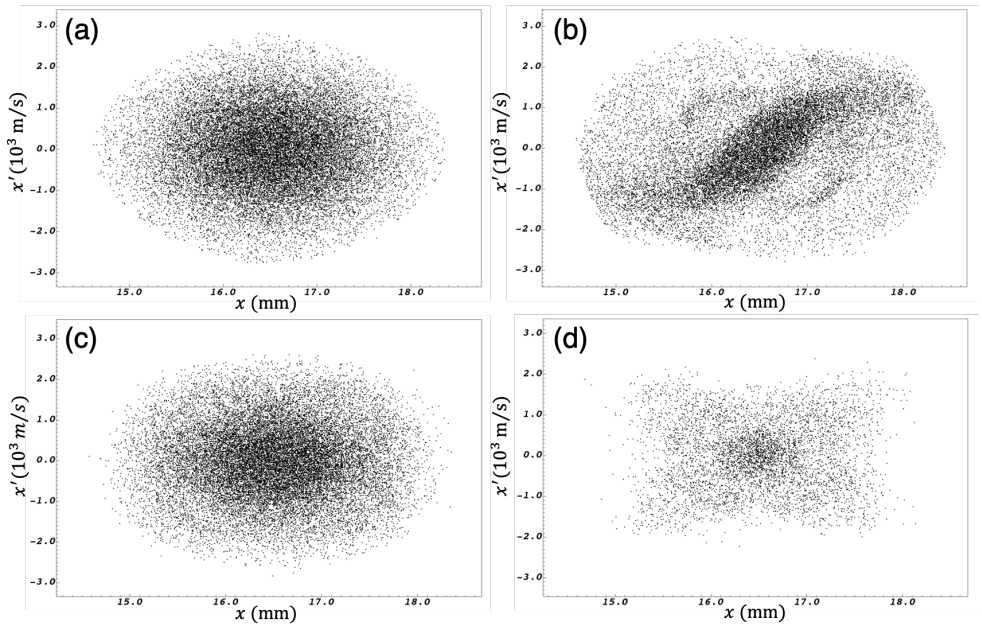

Figure 5.21: (x, x') phase space plotted after 500 super-periods of the T-insert lattice. (a) Octupoles off in the drift region (negligible space charge). A space-charge tune shift of $\Delta Q_{rms} = -0.032$ is present in simulations (b)-(d). (b) Octupoles off in the drift region. (c) Octupoles on and QI conditions met. (d) Octupoles on but QI conditions broken.

lattice, now with space charge. Due to the resonant condition in Eq. 5.22 being met, the 2nd order coherent resonance is excited. This can be seen from the two arms forming in the phase space of Fig. 5.21b.

Figure 5.21c shows the phase space of the lattice when the octupoles are turned on and the quasi-integrability condition is met. The coherent resonance caused by the space-charge tune shift has been damped by the octupole field and the particle distribution is returned to what resembles a Gaussian distribution. It is comparable to the phase space in Fig. 5.21a when negligible space charge was present.

In order to show the benefits of Quasi-Integrable Optics (QIO) over the use of ordinary octupoles to damp this coherent resonance, I also compared a lattice which broke the integrability condition (Fig. 5.18, red dashed). Figure 5.21d shows the phase space when just one octupole of twice the strength is turned on per two-cell super-period. The four arms that appear in the phase space show that the 4th order incoherent resonance is being excited and is responsible for the significant particle loss seen in Fig. 5.20. The

4th order incoherent resonance is being excited by the octupole as it is no longer meeting the conditions of integrability. This is in comparison to the QI lattice, which did not excite the 4th order incoherent resonance, due to the lattice being quasi-integrable.

5.5.2.3 Coherent spectrum

To calculate the single-particle tune, the Fourier transform of the particle's position, sampled over N turns, is taken to give the frequency at which the particle oscillates. The 2nd order coherent tune can be calculated by performing a Fourier transform on the RMS beam size, to see the frequency at which the beam oscillates collectively. Note that in the beam halo model, the beam core oscillates at twice the frequency of the single particle [20]. Figure 5.22 plots this coherent spectrum, in order to see how prominent the 2nd order coherent amplitude is in the particle distribution. The coherent spectrum was calculated using NAFF [121] with the RMS beam size calculated from VSim, once per cell for 400 cell periods (200 super-periods). This was calculated for a particle distribution with three different amounts of particles to simulate three different space-charge tune shifts. These were with $N_p = 2.5 \times 10^4$, $\Delta Q_{rms} = 3.19 \times 10^{-5}$ below the coherent resonance, $N_p = 2.5 \times 10^7$, $\Delta Q_{rms} = 0.0319$ at the coherent resonance and with $N_p = 5 \times 10^7$, $\Delta Q_{rms} = 0.0639$ above the coherent resonance.

In Fig. 5.22 (Top), the coherent spectrum is plotted for a particle distribution with negligible space-charge tune shift ($\Delta Q_{rms} = 3.19 \times 10^{-5}$). Both the horizontal (Fig. 5.22 (Top, left)) and vertical (Fig. 5.22 (Top, right)) spectra show little response around the coherent resonance at $Q_{\text{coh.}} = 5/2$. This is expected as there is not enough space-charge tune shift to bring the beam close to the resonance condition to excite a coherent resonance.

When the number of particles is increased to $N_p = 2.5 \times 10^7$, the resulting space-charge tune shift of $\Delta Q_{rms} = 0.0319$ brings the particle distribution onto resonance and a large peak in the spectrum is seen in Fig. 5.22 (Middle) at $Q_{\text{coh.}} = 5/2$ when no octupoles are applied. This peak in the coherent frequency spectrum is significantly reduced when both the QI octupole (green) and non-QI octupole (red) are turned on.

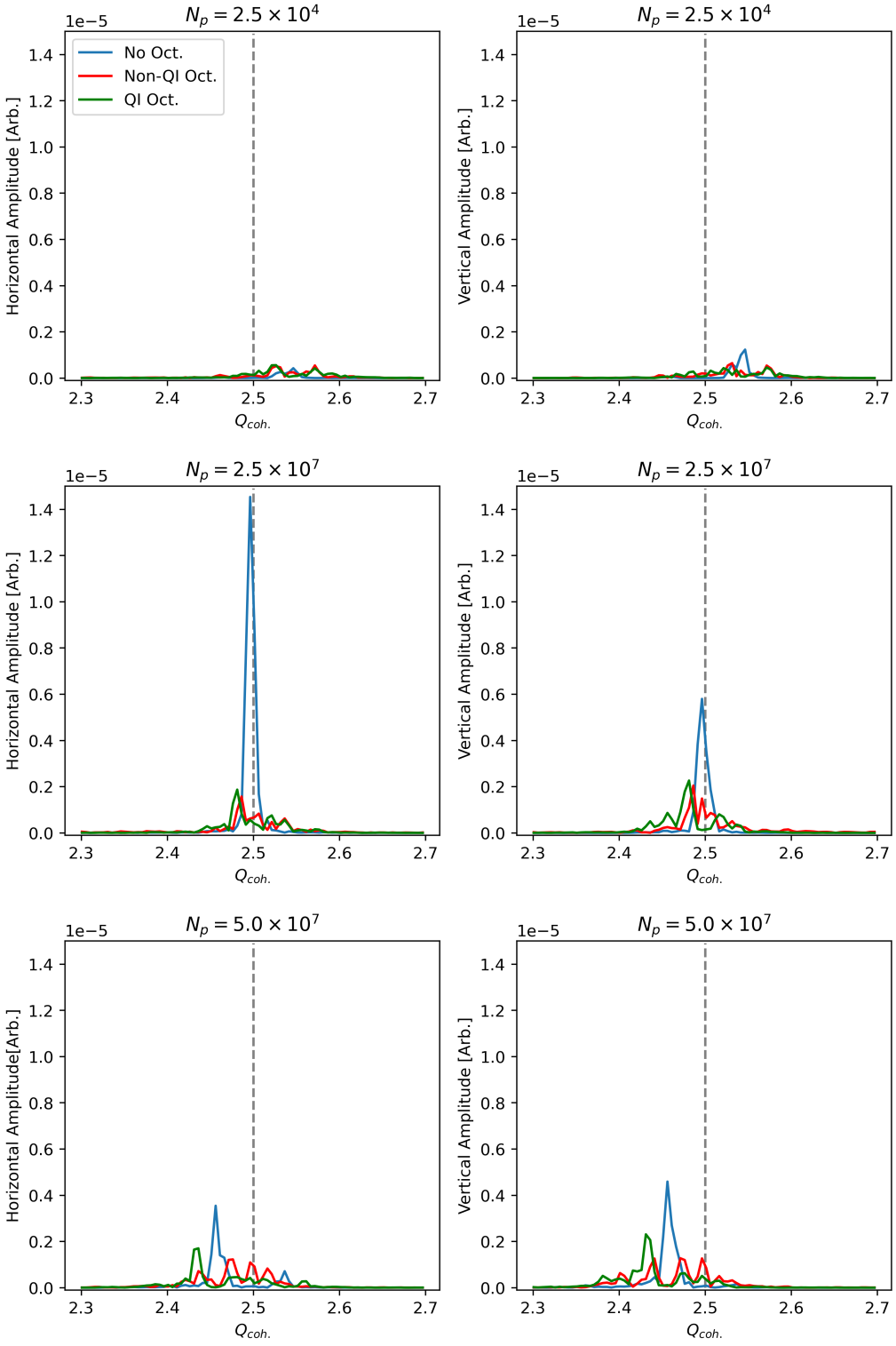

Figure 5.22: Horizontal (Left) and vertical (Right) coherent spectra computed for no octupoles (blue), non-QI octupole turned on (red) and the QI octupoles turned on (green). (Top) Below resonance, $N_p = 2.5 \times 10^4$. (Middle) At resonance, $N_p = 2.5 \times 10^7$. (Bottom) Above resonance, $N_p = 5 \times 10^7$. Grey dashed line marks the $Q_{\text{coh.}} = 5/2$, 2nd order coherent resonance.

The coherent amplitude is seen to be reduced by almost an order of magnitude in the horizontal spectrum and by around 2/3rds in the vertical spectrum. As these results were taken over 200 super-periods of the lattice, the coherent amplitude for the lattice with octupoles off is expected to increase further, as particle loss was only seen to plateau in Fig. 5.20 after around 650 lattice periods. Nevertheless, the results in Fig. 5.22 clearly show the coherent amplitude suppressed when the octupoles are tuned on, showing the benefits of introducing decoherence. The fact that the non-QI octupole was also seen to damp the coherent amplitude by the same amount as the QI octupole shows that the particle loss seen for the non-QI lattice in Section 5.5.2.2 was not caused by the 2nd order coherent resonance. This gives further evidence that the non-QI octupole is indeed exciting the 4th order incoherent resonance and that that is the mechanism behind the particle loss seen in this lattice.

Figure 5.22 (Bottom) shows that as the particle number and space-charge tune shift are increased further, the coherent amplitude decreases and is shifted past the $Q_{\text{coh.}} = 5/2$ 2nd order coherent resonance. Turning on the octupoles in the lattice is still seen to damp this coherent amplitude in both the horizontal and vertical spectrum.

5.5.3 Gaussian distribution: intensity scan

In order to get a complete picture of the particle loss caused by the coherent resonance and the ability of the QI octupole to both damp the coherent resonance and avoid exciting the 4th order incoherent resonance, we should scan over the entire resonance. This can be done by fixing the intensity and varying the tune of the lattice, or alternatively by fixing the lattice tune and scanning over a range of intensities. The latter was chosen in this work due to the difficulties in re-tuning the T-insert lattice to meet both the integrability conditions and the constraints of the IBEX trap. This also more accurately simulates what would happen in an intense hadron machine, as the lattice tune will be held constant, and the intensity of the machine increased.

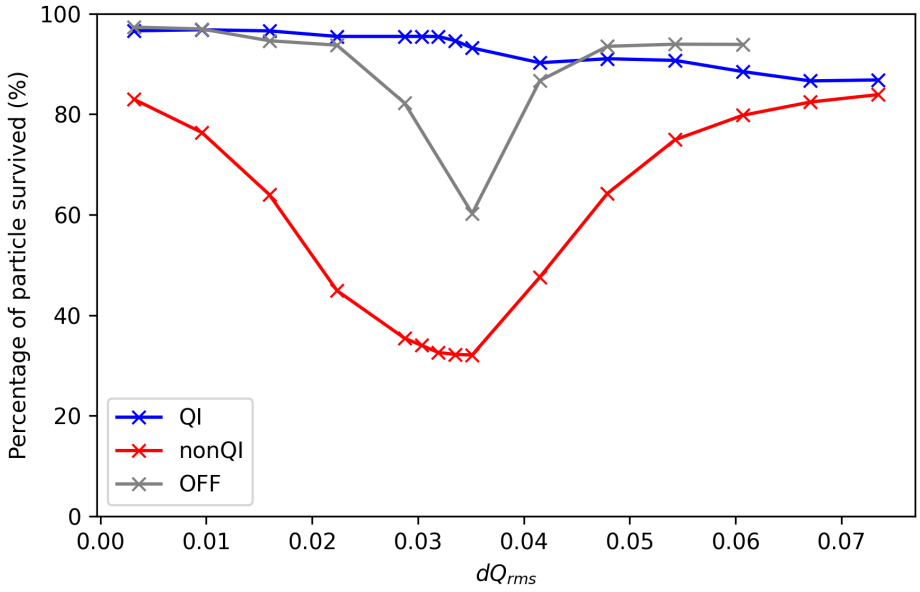

Figure 5.23: Percentage of particles surviving 650 T-insert super-periods plotted against RMS space-charge tune shift, ΔQ_{rms} for an initial Gaussian distribution. Quasi-Integrable lattice (blue), linear T-insert with octupoles turned off (grey) and non-Quasi-Integrable lattice (red).

Figure 5.23 shows the number of particles surviving 650 super-periods of the simulation at varying space-charge tune shifts (intensities) for the Quasi-Integrable (QI) and non-Quasi-Integrable (non-QI) lattice, as well as the linear lattice where octupoles are turned off. The RMS tune shift, ΔQ_{rms}, is calculated using Eq. 5.24, using the initial emittance of 2.16×10^{-9} m rad. In reality, this emittance will grow throughout the simulation when the distribution is close to resonance and therefore ΔQ_{rms} should be considered an initial value only.

In Fig. 5.23, a maximum dip in particle loss of 39.8(3) % is seen to occur in the linear lattice (octupoles turned off) around $\Delta Q_{rms} = 0.036$. The space-charge tune spread of $\Delta Q_{rms} = 0.036$ is as predicted from Eq. 5.22 and is consistent with exciting the 2nd order coherent resonance. The QI lattice can be seen to damp the coherent resonance caused by space charge and the particle loss remains below 10 % throughout the scan. In comparison, the non-QI lattice excites the 4th order incoherent resonance and results in up to 67.8(3) % particle loss. The QI lattice does not excite the 4th order incoherent

resonance as the Hamiltonian is time-independent. The stopband width of the resonance has been reduced to essentially zero within the resolution of this data. This is a huge benefit for machine operation as this QI lattice could damp coherent resonances without the risk of driving 4th order incoherent resonances.

It can be seen in Fig. 5.23 that, as the space-charge tune shift increases past the resonance, the particle loss observed in the QI lattice continues to increase. This is believed to arise from the space-charge tune shift starting to break the integrability of the QI lattice. One condition for the integrability of the lattice is that there should be an $n\pi$ phase advance over the linear section of the lattice. With high space-charge tune shifts, this condition is deviated from significantly in these simulations and the particle loss starts to approach that of the non-QI lattice. To avoid this, and to keep a QI lattice at high space-charge tune shifts, the lattice would have to be re-tuned to account for space charge.

5.5.4 KV distribution: intensity scan

Gaussian distributions have a nonlinear charge-density distribution and hence the space-charge tune shift that a given particle experiences can vary over the distribution. This leads to a space-charge tune spread (seen in Fig. 5.19) as well as a space-charge tune shift. Therefore, because Gaussian distributions with space charge already have a tune spread, this decoherence introduced into the distribution can act as a natural damping mechanism.

In order to isolate the benefits of damping the coherent resonance from the tune spread created from octupoles, and from any tune spread effects in the distribution itself, the results can be repeated for a KV distribution. A KV distribution is uniform and so has a linear space-charge force across the whole distribution. This leads to every particle in the distribution getting the same tune shift and hence there should be no tune spread in the spectrum. Therefore in this section, the intensity scan across the 1/4 integer resonance was repeated, using a KV distribution.

A matched KV distribution with a 100 % emittance of $\epsilon_{100} = 2.16 \times 10^{-9}$ m rad was created in VSim. The number of particles surviving after 1000 super-periods is plotted against the initial maximum space-charge tune shift (see Eq. 5.21) in Fig. 5.24.

Over the 1000 super-periods, a maximum particle loss of 1.79(8) % was observed when the octupoles were turned off. This was reduced to a maximum of 0.36(4) % when the QI octupoles were turned on. In comparison, a maximum of 17.5(3) % of particles were lost for the non-QI lattice. It should be noted that the dip in particle loss for the QI and non-QI lattice occurs in the same place as they have the same tune and octupole tune spread. However, the QI lattice has a time-independent Hamiltonian and so the resonance stopband width is reduced to almost zero. The two dips in the QI particle loss plot are expected to be from exciting the horizontal and vertical resonances as the tunes are not exactly identical ($Q_x = 1.276$, $Q_y = 1.277$). The three dips that are seen when the octupoles are turned off in Fig. 5.24 are suspected to be from a combination of the 4th order incoherent resonance and 2nd order coherent resonance being excited in the linear lattice. The 4th order resonance can be driven by small octupole nonlinearities in the quadrupole field. However, further simulation work is needed to confirm the mechanism behind the three dips.

Note that the particle loss observed was significantly smaller for the KV distribution than the Gaussian distribution as the emittance of the initial distribution was smaller. The KV and Gaussian distributions in these two simulations are not equivalent beams[3].

These simulation results confirm that a coherent resonance can be damped in a KV distribution as well as Gaussian distributions with octupoles, when arranged in a lattice prescribed by QIO. The results also show that deviating from the conditions of quasi-integrability can result in the octupole driving its own set of 4th order resonances. The IBEX Paul trap has undergone an upgrade to allow for the creation of octupole fields within the trap with the aim to confirm these simulations with detailed experiments.

[3]To create equivalent beams for a given number of particles, the emittance of the KV distribution needs to be scaled to give the same tune shift as the Gaussian distribution.

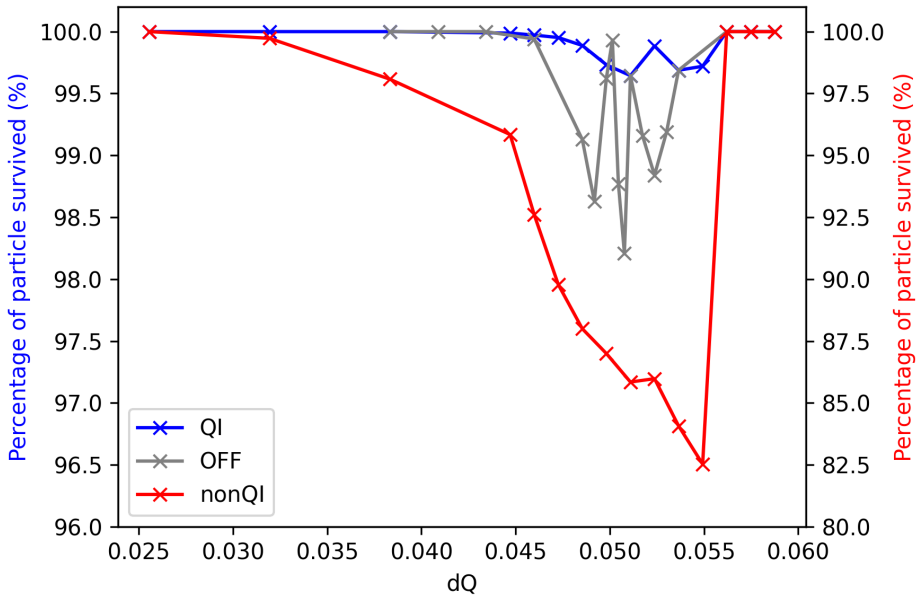

Figure 5.24: Percentage of particles surviving the simulation plotted against max tune shift, ΔQ_{max} for an initial KV distribution. The percentage of particles surviving the Quasi-Integrable lattice (blue) and octupoles turned off (grey) should be read from the axis on the left. Particle survival for the non-QI lattice (red) can be read from the axis on the right.

5.6 Chapter summary

In this chapter, I first derived an equation to measure the integrability of a lattice design given errors in the octupole scaling, beta functions in the drift region and phase advance over the T-insert. The predictions from the equation were tested using a lattice simulated in Mathematica where the octupole scalings were varied. Simulation and theory agree well for small actions and small deviations away from the ideal QI lattice.

I also presented simulation results using a 2D model of the IBEX trap created in the particle-in-cell software VSim. These results have shown that a quasi-integrable lattice can successfully damp a 4th order perturbation, designed to excite the 4th order resonance. The tune spread of the octupole is able to damp the resonance through decoherence of the particle betatron tunes, increasing the fraction of surviving particles and maintaining a large DA.

The QI lattice was also compared to lattices with two other pulses that deviated

away from the integrable $1/\beta^3$ octupole scaling, namely the constant strength octupole pulse and β^3 scaling pulse. It was shown that the QI lattice had the lowest amount of particle loss (7.4(1) %) over 2000 lattice periods with the 4th order perturbation applied. This is compared to the constant octupole with 7.6(1) % loss and β^3 octupole scaling with 8.3(1) %. The QI lattice was also shown to restore the DA to within 3.4 % of the unperturbed linear lattice.

I also show that the T-insert can be created with realistic voltages for IBEX and that fluctuations in the octupole strength on the order of 10 % can be tolerated without leading to significant particle loss.

I then tested a QI lattice with space charge and scanned across the 2nd order coherent resonance for both a Gaussian and KV distribution. With the octupoles turned off, the 2nd order resonance was clearly excited and 36.9(3) % of particles were lost over 1000 super-periods for the Gaussian distribution. This particle loss was reduced to 5.0(1) % when the QI octupoles were turned on. This is a significant improvement and shows how a QIO lattice can be used to damp a coherent instability without exciting the 4th order incoherent resonance. To further show the benefits of using a QI lattice, a non-QI lattice was also compared at this resonance and lost 70.4(3) % of particles over the same tracking time. This shows that when the QI condition is broken, the 4th order incoherent resonance can be excited by the octupoles.

Coherent spectrum analysis was used to confirm that the coherent resonance was being damped by both the QI octupole and the non-QI octupole. This further indicated that the particle loss in the case of the non-QI octupole was indeed due to the 4th order incoherent resonance. An intensity scan over the resonance was performed for both a Gaussian and for a KV distribution, showing the benefits of the QI octupole in damping the coherent resonance, without exciting a 4th order incoherent resonance, over the entire tune scan studied. However, as the space-charge tune shift is increased, the phase advance over the T-insert lattice will be altered so that it will deviate from the conditions of integrability. Therefore for large space-charge tune shifts, the linear

T-insert lattice will have to be appropriately tuned.

Chapter 6

Experimental investigation into Quasi-Integrable Optics in a Paul trap

In this chapter I present the first experimental results from the newly commissioned IBEX-2 multipole trap. The IBEX-2 trap was installed in the vacuum vessel in June 2022 and the full commissioning was completed in March 2023. The experimental results discussed in this chapter were taken from April 2023 to July 2023. Unless otherwise stated, all experimental work was carried out by myself. The aim of this experimental run with IBEX-2 was to test the simulation results that were presented in Chapter 5. First, the one-cell T-insert was perturbed with a 4th order perturbation to excite particle loss. The QI octupole pulse which scales as $1/\beta^3(s)$ was then turned on to create decoherence with the goal of damping the 4th order resonance created by the applied perturbation. Second, the two-cell T-insert lattice was created and the ion density in the trap was increased in order to excite the space-charge-induced 2nd order coherent resonance in the linear lattice. The QI octupole was turned on to test whether the decoherence created in the distribution could damp the coherent resonance without exciting the 4th order resonance. The particle survival for the QI lattice was then compared to two lattices that break the conditions of integrability to see if these would excite the 4th order resonance.

6.1 Experimental setup

Normal trapping mode (see Fig. 4.20(Top)) was used for the data collected in this chapter. A typical timings flow chart of an experiment, where ions are stored in a T-insert lattice, is shown in Fig. 6.1. During the ionisation stage, a FODO lattice with a tune of $Q_x, Q_y = 0.15$ was applied to the rod electrodes in the ionisation region (IR) of the trap. This was achieved with a 1 MHz square-wave waveform with an amplitude of 42 V. The resulting time period for one FODO cell was therefore 1 µs.

Control over the initial number of ions created in the trap was accomplished through a combination of adjusting the gas pressure and varying the length of time that the electron gun was on. The electron gun was turned on for a duration between 100 – 500 ms (100,000 – 500,000 FODO cell periods). Argon gas was continually leaked into the vacuum vessel to maintain a pressure of between 1.5×10^{-8} – 6.8×10^{-7} mbar. The ions were left in the IR for a further 50 ms, whilst the electron gun was turned off, to allow the ion distribution to stabilise [39]. The DC voltage on the gate electrodes was then dropped from 25 V to 10 V for 0.06 ms to allow ions to pass into the experimental region (ER). The same FODO RF waveform was applied to the gate electrodes and ER electrodes as the ions were transferred. The gate DC voltage was returned to 25 V and a matching section was applied to the ER rod electrodes to match the Twiss parameters from the FODO lattice to the T-insert lattice [39].

The T-insert lattice waveform was then applied to the ER electrodes for the desired storage time. In Fig. 6.1, a one-cell T-insert lattice with a cell period of 2.96 µs was assumed, and a storage time of 5000 cells was chosen. It is during this storage time that the experimental stage is reached, where perturbations or octupole voltages can be applied to the plate electrodes. After the desired storage time, the DC voltage on the MCP end-caps was dropped from 25 V to 0 V and ions were extracted onto the MCP detector, while the T-insert waveform was continually applied to the MCP end-cap electrodes. For the results presented in this chapter, the procedure detailed above

was repeated 10 times. Each data point was averaged over these 10 experiments and the error bars indicate the standard deviation in ion number across those 10 experiments.

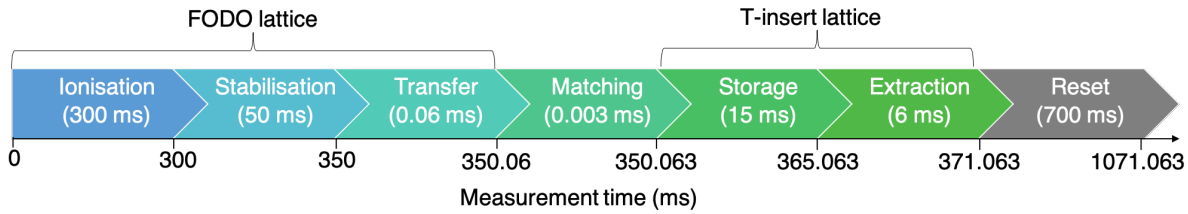

Figure 6.1: Timings flow chart of a typical experiment in IBEX-2. Ions are stored for 5000 cells of the T-insert lattice.

6.2 Testing Quasi-Integrable Optics with a 4th order perturbation

6.2.1 Creation of the One-cell T-insert in IBEX

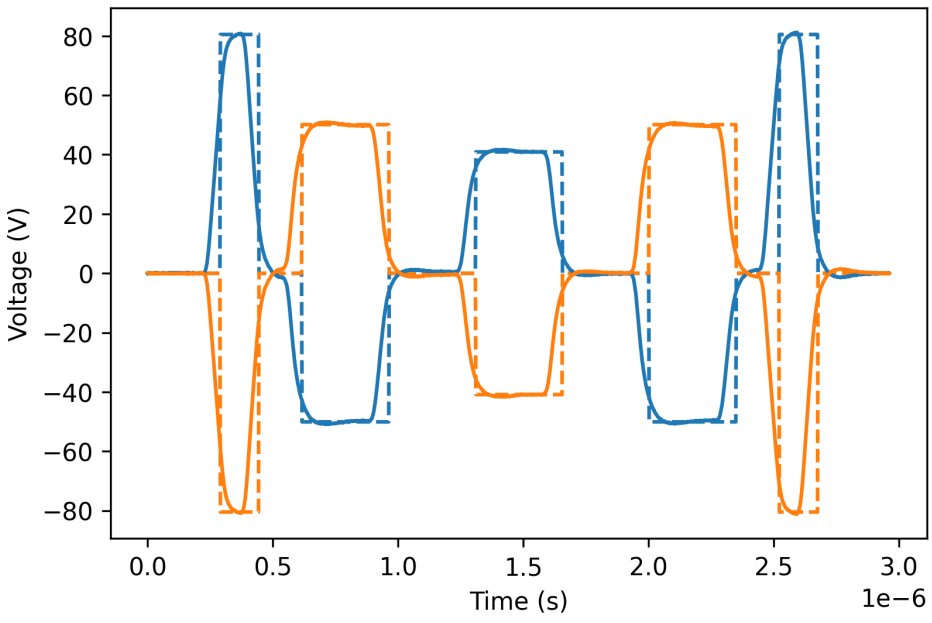

Figure 6.2: Oscilloscope trace of the one-cell T-insert waveform created by the PA98 amplifiers (solid). The ideal waveform is shown as a dashed line.

In this section, the one-cell T-insert waveform, created by amplifying a square-wave input waveform, is analysed to estimate the lattice tune and beta functions. Figure. 6.2

compares the amplified T-insert waveform applied to both pairs of electrodes in the ER of the trap to the ideal square-wave T-insert waveform. Note that the 10 V DC voltage applied to the central rod electrodes in the ER has been removed in the Python code for the analysis detailed below. The input T-insert waveform was created with 296 points and loaded to an AWG with a sample rate set to 99.805 MS/s to give the correct lattice period of 2.9658 µs. Ideally, more points would have been used, however the sample rate was limited to the slowest AWG which was 100 MS/s. Because the three AWGs used in this experiment required synchronisation, all three AWGs were therefore limited to this sample rate[1].

A Python script was used to split the waveform in Fig. 6.2 into 1000 time steps of $dt \approx 2.96$ ns, corresponding to a lattice segment length of $l \approx 0.888$ m. For each section of the waveform the electrode voltage was converted to a quadrupole focusing strength, K using Eq. 2.37. A transfer matrix (see Section 2.1.6) for each segment of the lattice was then created and multiplied together to give a transfer matrix corresponding to the one-cell T-insert applied to the trap electrodes. The tune, Q of the transfer matrix, M can then be calculated using $\mathrm{Tr}(M) = 2\cos(2\pi Q)$, where $\mathrm{Tr}(M)$ is the trace of the matrix, M. For the waveform in Fig. 6.2, the horizontal and vertical tunes of $Q_x = 0.634$ and $Q_x = 0.633$ were calculated which agree with the designed tunes from MAD-X ($Q_x, Q_y = 0.636$) to within 0.5 %.

The transfer matrix of each segment of the one-cell T-insert can also be expressed in terms of the Twiss parameters, and the beta function at each point in the waveform can be calculated. This calculation uses the assumption that the T-insert waveform is periodic. The reconstructed beta function from the waveform plotted in Fig. 6.2 is shown in Fig. 6.3(Top). The difference in beta functions between the T-insert lattice applied to the trap electrodes and the lattice designed in MAD-X is plotted in Fig. 6.3(Bottom). The percentage error in the beta functions for the one-cell T-insert created in IBEX was found to be up to 18 % in β_x and 13 % in β_y. This was reduced down from discrepancies

[1]Replacing the Tabor WW1074 AWG with another Tabor WW2074 would therefore increase the maximum sample rate to 200 MS/s and thus 592 points could be used to define the T-insert waveform.

of up to 300 % in the beta functions by correcting the T-insert input voltage by a factor of $f = 1/1.01$. This voltage correction factor ensured that the experimentally measured tune (calculated in the next section) agreed with the designed tune.

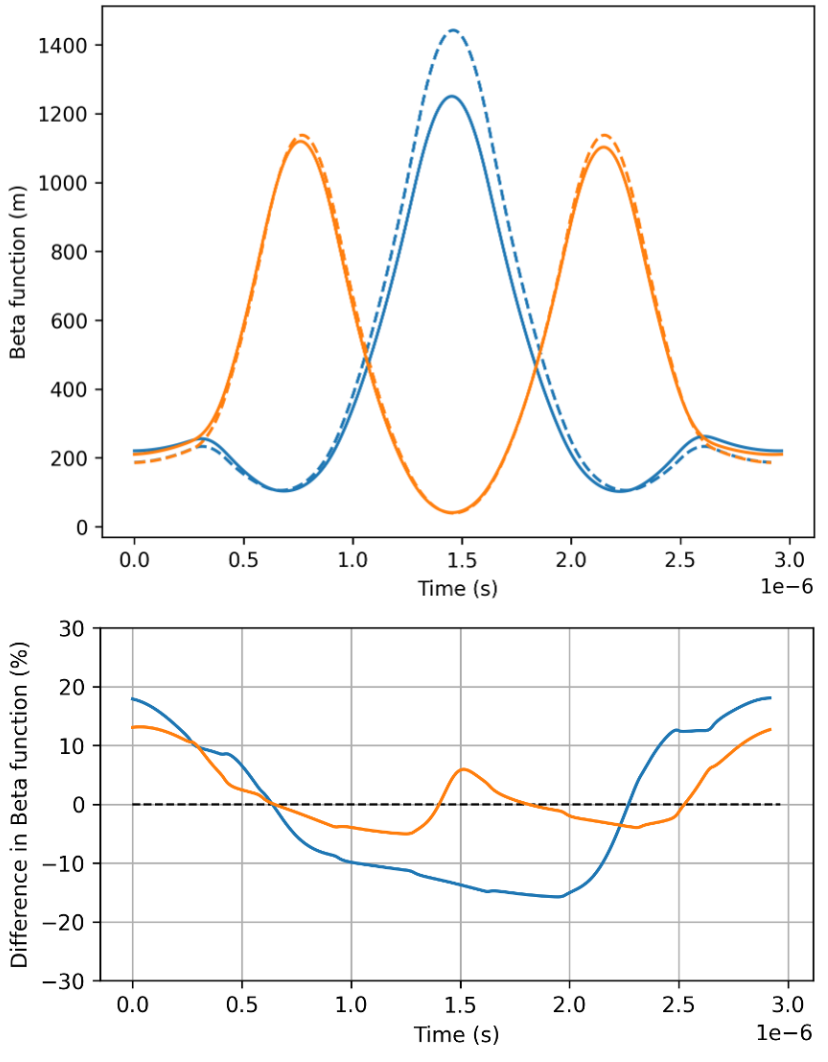

Figure 6.3: (Top) Recreated beta functions from the voltage waveform applied to the electrodes to create the one-cell T-insert lattice. Dashed lines show the MAD-X beta functions. (Bottom) Percentage difference in beta functions between the lattice created in IBEX and MAD-X.

Reconstructing the beta functions using the method described above will only give an estimate of the actual beta functions of the ion distribution stored in the trap. This is due to errors in the oscilloscope probes and the oscilloscope trace voltage reading. In the future, an experimental measurement of the beta functions within the T-insert should be taken using the method proposed in [125]. In this paper, the beta function was

measured in a Paul trap by applying a dipole kick to the trapped ions in order to scrape ions on the electrodes at various points in the lattice. This allowed for an experimental reconstruction of the beta function within the trap. In order to achieve this in IBEX-2, one pair of the ER electrodes would need to be independently powered in order to apply a dipole kick. This would require an additional HV amplifier and was thus not possible at the time of writing.

Currently, the beta functions of the T-insert lattice cannot be directly measured experimentally, however we are able to experimentally verify the tune of the lattice. This was achieved by applying an octupole perturbation (or 4th order perturbation) to the plate electrodes[2]. Ions will be lost if the applied perturbation frequency is twice or four times the lattice tune (see Appendix B). These results are discussed in more detail in the next section as well as the effect of turning on the QI octupole in order to damp the applied 4th order perturbation.

6.2.2 Trapping Argon

The 4th order perturbation experiment, applied to the one-cell T-insert lattice, was first carried out with argon as the trapped ion species, as this has been the default experimental setup. The next section repeats this experiment with nitrogen ions (N_2^+), a lighter species which requires only 70 % of the quadrupole and octupole focusing strengths compared to those required for argon. More details explaining the switch are described later.

Argon ions were stored in the one cell T-insert for 5000 cell periods, after an electron-gun ionisation time of 0.3 s. The timing structure of this experiment was identical to that in Fig. 6.1. A low gas pressure of 1.5×10^{-8} mbar was used to store a small number of ions in the trap ($<1 \times 10^5$) in order to minimise space-charge effects. The T-insert lattice was tested with and without the QI octupole applied, in the case of a 4th order perturbation with an amplitude of 5.88 V applied to the plates (Pert. ON) and with the perturbation

[2]Note that a 2nd order perturbation can be excited by applying a quadrupole perturbation to the rod electrodes. This has previously been done in [39] to measure the tune experimentally.

turned off (Pert. OFF). The octupole strength used in this experiment was $t = -0.8$, corresponding to a plate voltage of $-402\,\mathrm{V}$. This should create a theoretical octupole tune spread of 0.012. The frequency of the perturbation was varied from 390 – 455 kHz, corresponding to exciting twice the betatron frequency in the one-cell T-insert. When dividing the perturbation frequency by two, this corresponds to a cell tune of between 0.58 and 0.67. In simulations, the 4th order perturbation was applied at four times the T-insert cell tune. Experimentally, it was chosen to apply the perturbation frequency at twice the T-insert cell tune, which is shown to be equivalent in Appendix B. From the simulation results presented in Section 5.3, we expect that turning on the octupoles will create an amplitude-dependent tune spread, introducing decoherence in the particle tunes. This decoherence is expected to damp the applied 4th order perturbation, and reduce the maximum ion loss at the resonance.

The results from scanning over the 4th order perturbation frequency are presented in Fig. 6.4. When the perturbation was not applied, the ion number remains fairly constant at around 70.000, fluctuating by less than $\pm 4\,\%$ over the duration of the experiment. When the 4th order perturbation was applied to the plates, a dip in the measured ion number can be seen at a tune of $Q = 0.636$, in good agreement with the predicted values of the tune from MAD-X (dashed lines in Fig. 6.4). The maximum loss observed when the octupoles were off and the perturbation was on was found to be $54(2)\,\%$. When the octupoles were turned on, in the presence of the 4th order perturbation, a dip in ion number was observed that was shifted to the right of the octupoles-off dip. The maximum particle loss observed for the octupoles-on case was $50(3)\,\%$, within the error of the percentage loss when no octupoles were applied. The broadening of the dip for the case of octupoles-on suggests that the octupoles were creating some tune spread within the ion bunch; however, this may not be enough to damp the applied 4th order perturbation through decoherence.

Larger negative octupole strengths were not possible with the current amplifiers as the negative power supply was limited to $-450\,\mathrm{V}$ and could practically only reach about

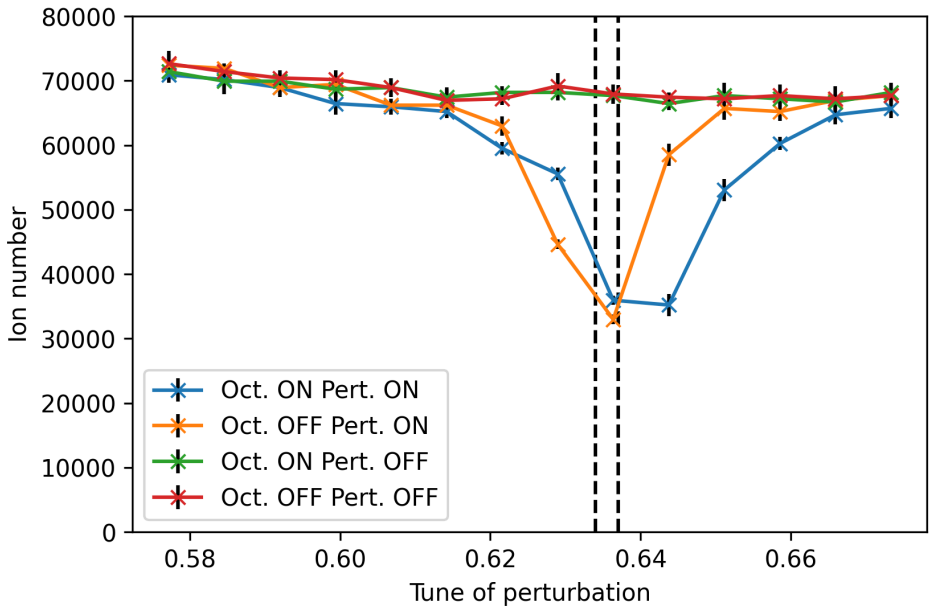

Figure 6.4: Tune scan of the 4th order perturbation applied over 5000 cells of the one-cell T-insert lattice. Number of ions surviving is plotted for QI octupoles turned on in the drift region with and without the perturbation applied, and octupoles turned off, with and without the perturbation applied. Dashed lines represent the nominal zero-current horizontal and vertical tunes of the T-insert lattice, predicted with MAD-X.

90 % of this maximum value. In addition, due to the limited slew rate of the current amplifier, larger octupole voltages increase the overlap of the octupole pulse with the T-insert waveform. This means that the octupole was no longer just applied in the drift region, but was also on while the T-insert waveform was being applied and hence when $\beta_x \neq \beta_y$. This breaks the integrability conditions and is another possible explanation as to why turning on the octupoles was not seen to create a significant reduction in particle loss in Fig. 6.4.

In order to test this T-insert lattice with a lower octupole voltage for a given octupole strength, two options were considered. The first option was switching to the second set of plate electrodes, with an inscribed radius of $R_0 = 7.4\,\text{mm}$ (see Section 4.2.3), which would have allowed for the same tune spread to be created using only 40 % of the voltage compared to using the current $R_0 = 8.5\,\text{mm}$ plates. However, this would have involved lifting the lid of the vacuum vessel, disassembling the IBEX-2 trap to replace the electrodes and realigning the trap. In addition, as mentioned in Section 4.2.3, the plate

electrodes with $R_0 = 7.4\,\text{mm}$ increase the unwanted c_6 component in the quadrupole field decomposition. The second option to achieve a larger tune spread in the trap for a given octupole voltage was to trap a lighter ion species. As shown in Section 3.2.3, the octupole strength, k_4 is equal to,

$$k_4 = \frac{24qV_O(\tau)}{mc^2r_0^4}, \tag{6.1}$$

where q is the charge of the ion, $V_O(\tau)$ is the time-dependent octupole voltage, and m is the mass of the ion species. Hence, for a singly charged ion with a smaller mass, m, a larger octupole strength can be achieved for a given voltage V_O. The IBEX trap has previously trapped nitrogen (N_2^+ ions) and already has the gas bottle and gas line set up in the laboratory. The mass ratio between a nitrogen molecule and an atom of argon is $m_{N_2}/m_{Ar} = 0.701$. This means that for a given octupole focusing strength, nitrogen would only require 70 % of the octupole voltage required for argon. Similarly, the quadrupole potential is also proportional to the inverse of the trapped ion mass, and therefore the quadrupole trapping potential would also be 70 % of that of the potential needed to trap argon. Due to the relative ease with which the ion species could be changed over from argon to nitrogen, it was decided to switch to trapping nitrogen (N_2^+), and repeat this 4th order perturbation scan.

6.2.3 Trapping Nitrogen

The 4th order perturbation experiment was repeated with nitrogen as the trapped ion species. All RF electrode voltages were scaled down by a factor of 0.701, while the DC voltages were kept the same as before. The perturbation was again applied for 5000 T-insert cells for both a focusing and defocusing octupole, i.e. a positive and negative plate voltage. The octupole strength parameter for this experiment was $t = \pm 0.6$, corresponding to a plate voltage of $V_{\text{plates}} = \pm 300\,\text{V}$. This octupole strength should create a theoretical tune spread of 0.013 with nitrogen as the trapped ion species. Both a focusing and defocusing octupole can be made QI with a $1/\beta^3(s)$ strength scaling, however they will have tune shifts with amplitude of opposite sign. Figure 6.5 illustrates

the tune spread created in a one-cell T-insert lattice in simulation with a negative plate voltage (Left) and a positive plate voltage (Right).

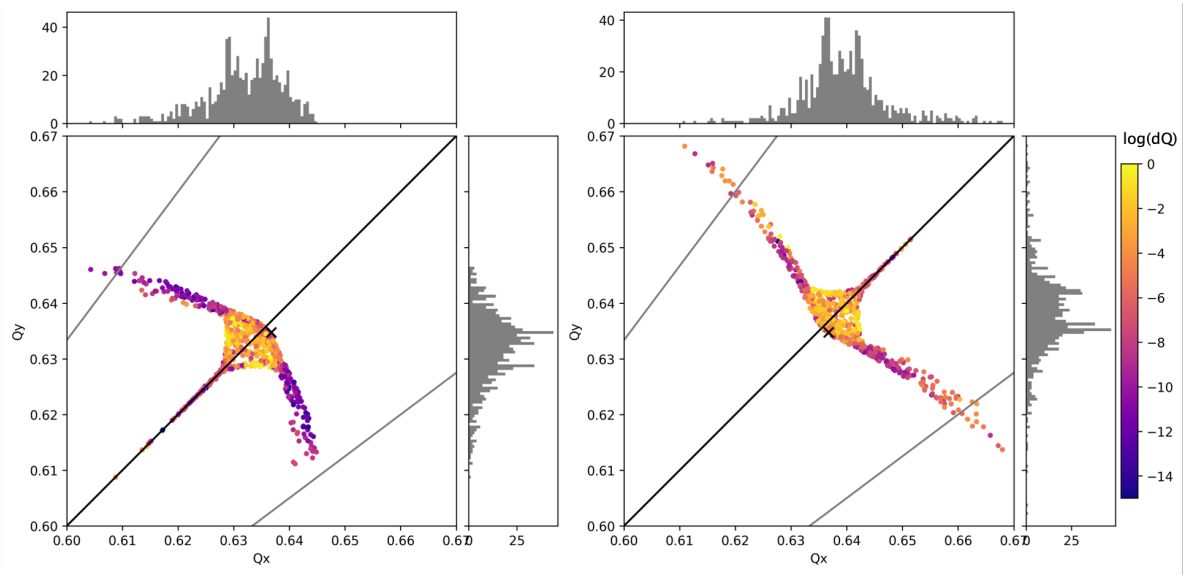

Figure 6.5: Tune diagram created from a VSim simulation of a one-cell T-insert lattice. The black cross indicates the nominal tune. The trapped ion species in this simulation was argon. (Left) Octupole tune spread from a negative plate voltage of −500 V. (Right) Octupole tune spread from a positive plate voltage of 500 V.

The results of the perturbation scan are shown in Fig. 6.6, where the negative octupole voltage was applied in the top figure and a positive octupole voltage was applied in the bottom figure. The percentage of ions surviving was calculated from the difference in the number of ions measured with the perturbation turned on and off and octupoles turned on and off. A fit was applied to the data assuming the dip in particles surviving approximates a Gaussian distribution, with a standard deviation that is proportional to the tune spread in the ion distribution. The tune spread cannot be described solely by the standard deviation of the fit as the width of the resonance excited by the perturbation will also affect the width of dip.

In Fig. 6.6(Top), when the perturbation was applied and octupoles were off, a maximum loss of 78(2) % occurred at a perturbation frequency corresponding to a tune of $Q = 0.636$. When the QI octupoles were turned on, this loss was reduced to 60(3) % and the peak loss has shifted to a tune of $Q = 0.641$. When no octupoles were applied the

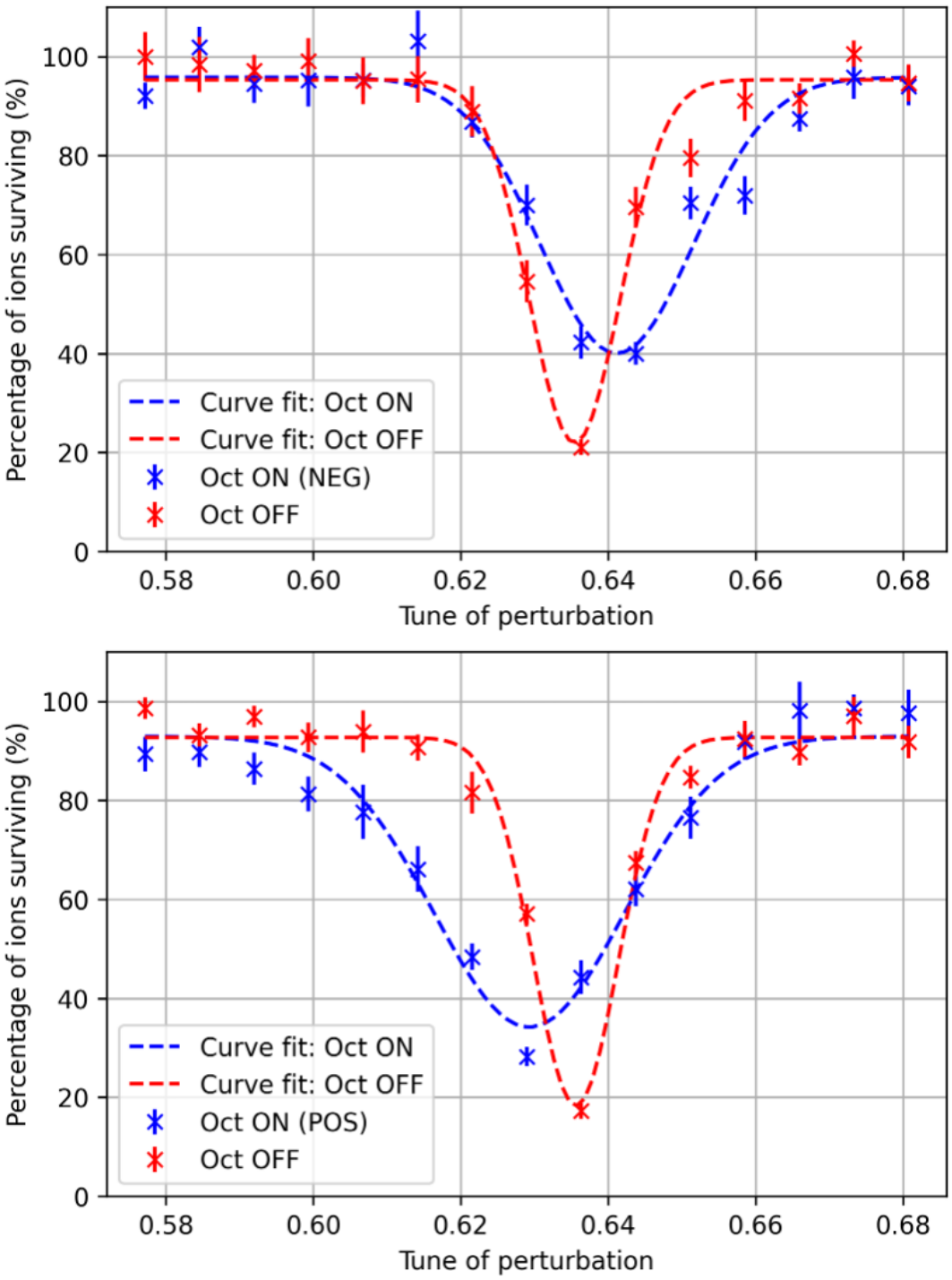

Figure 6.6: Tune scan of the 4th order perturbation applied over 5000 cells of the one-cell T-insert lattice. Percentage of ions surviving is plotted for QI octupoles turned on (blue) and off (red) in the drift region. (Top) Negative octupole, $t = -0.6$, $V_{\text{Plates}} = -302\,\text{V}$. (Bottom) Positive octupole, $t = +0.6$, $V_{\text{Plates}} = +302\,\text{V}$.

standard deviation of the Gaussian curve fit was found to be 0.006(1). The curve fit for when the negative octupoles were turned on was found to have a standard deviation of

0.010(1), showing evidence of a tune spread being created. It is the tune spread created by the octupole that is expected to damp the 4th order resonance, as seen in the simulation results presented in Section 5.3. This experimental perturbation scan agrees well with the perturbation scan simulated in VSim shown in Fig. 5.13. In these simulation results, the negative octupole was also seen to shift the octupole dip to a tune of 0.641, while the standard deviation was seen to be twice as large for octupoles on compared to when octupoles were turned off.

The experiment was repeated, this time testing a positive octupole voltage applied to the plate electrodes. The results for the positive octupole are shown in Fig. 6.6(Bottom). In this experiment, a maximum particle loss of 82(2) % was seen at a tune of 0.636 when the octupoles were turned off. Turning on the positive octupole reduced this particle loss to 66(4) % (calculated from the minimum of the fit) and occurred at a tune of 0.629. The standard deviation was seen to be larger when compared to turning on the negative octupole. With a standard deviation of 0.013, this tune spread agrees with the theoretical tune spread of 0.013. The positive octupole is seen to create a negative shift in tune, whereas the negative octupole was seen to create a positive shift in tune. The results are summarised in Table. 6.1.

Table 6.1: Table summarising the results from the 4th order perturbation scan in Fig. 6.6.

	Negative Oct.		Positive Oct.	
	Oct. ON	Oct. OFF	Oct. ON	Oct. OFF
Maximum ion loss (%)	60(3)	78(2)	66(4)	82(2)
Tune	0.641	0.636	0.629	0.636
Standard deviation	0.010(1)	0.006(1)	0.013(1)	0.006(1)

These experimental results show the first demonstration of ions stored in a QI T-insert lattice in a Paul trap. Turning on the QI octupole was seen to create a tune spread within the ion distribution which helped damp the applied 4th order perturbation. A reduction in the maximum ion loss of up to 30(7) % was seen when the QI octupole was turned on. These benefits of the QI T-insert lattice were seen despite the estimated errors in beta function within the lattice, which indicates the robustness of this lattice.

In the future, it is expected that, by improving the accuracy of the T-insert lattice created within IBEX, the benefits of QIO could be further demonstrated.

6.3 Testing Quasi-Integrable Optics in the presence of space charge

In this section, the two-cell T-insert lattice, with a designed tune close 1.25, is tested in the presence of space charge.

6.3.1 Creation of the Two-cell lattice in IBEX

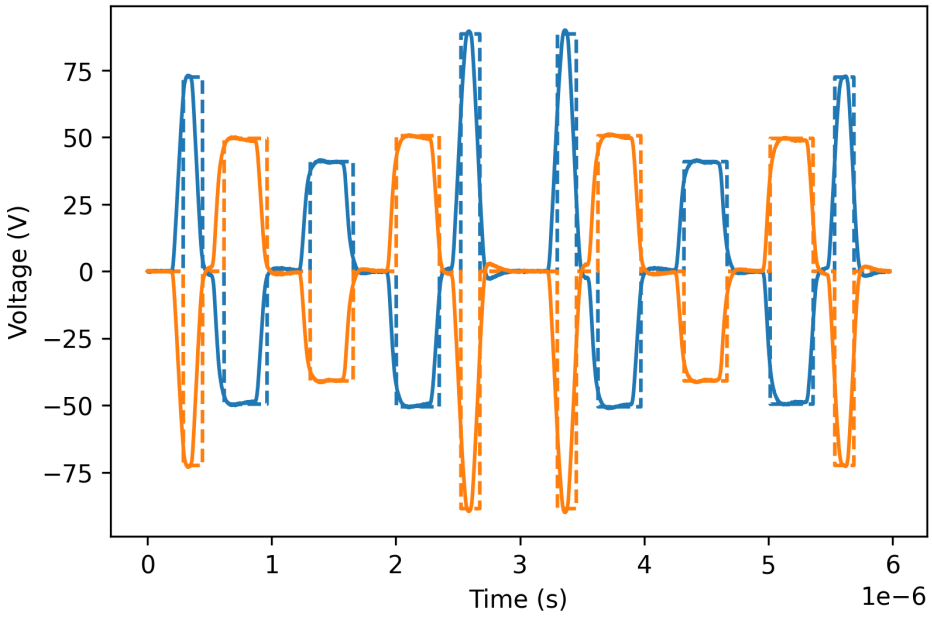

Figure 6.7: Oscilloscope trace of the two-cell T-insert waveform created by the PA98 amplifiers (solid). The ideal waveform is shown as a dashed line.

In this section, the two-cell T-insert waveform created by amplifying the square-wave input waveform is analysed, as was done in Section 6.2.1 for the one-cell lattice. The two-cell T-insert lattice waveform applied to the ER electrodes is compared to the ideal square-wave waveform in Fig. 6.7. The horizontal and vertical tunes calculated from this waveform were found to be $Q_x = 1.277$ and $Q_y = 1.278$, which agree within 0.1 % of the MAD-X design values ($Q_x = 1.276$ and $Q_y = 1.277$).

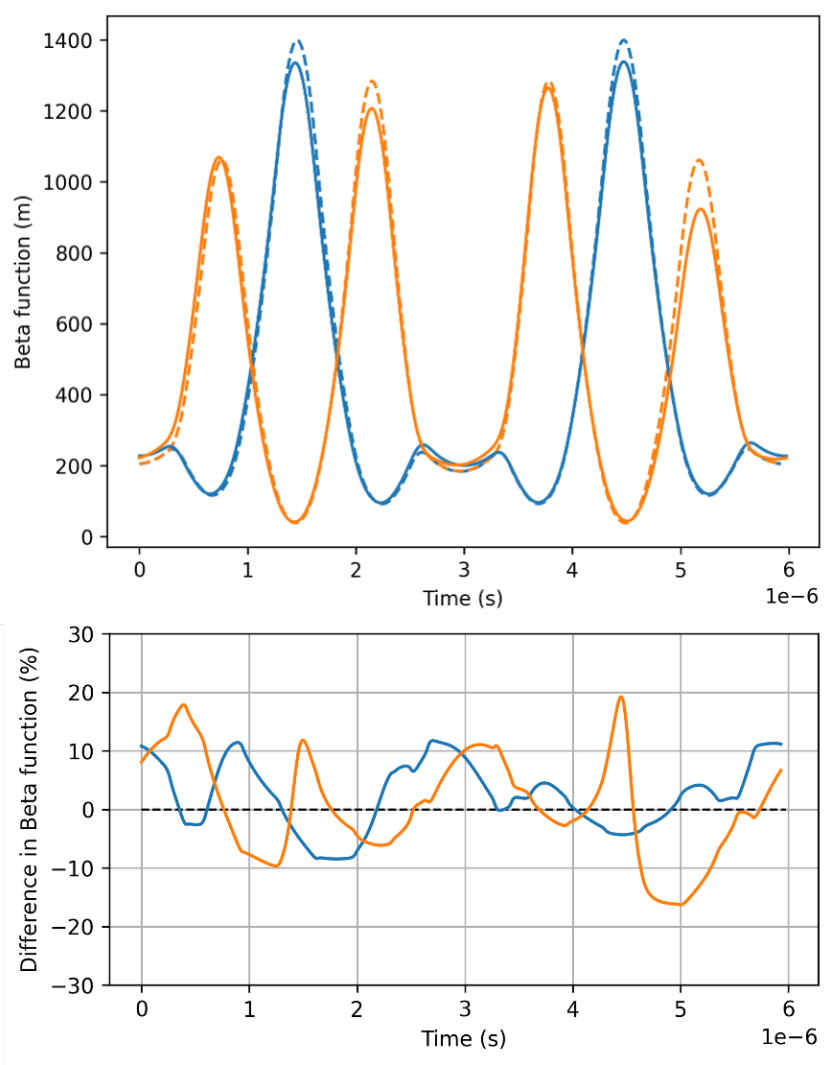

Figure 6.8: (Top) Recreated beta functions for the two-cell T-insert lattice. Dashed lines show the MAD-X beta functions. (Bottom) Percentage difference in beta functions between the lattice created in IBEX compared to the MAD-X beta functions.

The reconstructed beta functions from the two-cell T-insert waveform in Fig. 6.7 are plotted in Fig. 6.8. These beta functions show a discrepancy of up to 12 % in β_x and 19 % in β_y. A 4th order perturbation was applied to the plate electrodes to experimentally confirm the lattice tune in the next section. A voltage correction factor of $f = 1/1.022$ was used to adjust the input voltages so that the experimentally measured tune (calculated in the next section) agreed with the designed tune.

6.3.2 Space-charge tune shift

In this section, an investigation is carried out to measure the space-charge tune shift in the trap for a given ion number. The goal was to see if a sufficient space-charge tune shift could be achieved in the two-cell T-insert lattice in order to reach the 2nd order coherent and 4th order incoherent resonances. The results presented in this section were collected before the gas line was switched over to nitrogen and hence the trapping species in this section was argon. Ions were stored for 2000 two-cell T-insert super-periods while a 4th order, sinusoidal perturbation with an amplitude of 5.88 V was applied to the plate electrodes. The frequency of this perturbation was scanned from 415 – 436 kHz in 1 kHz steps. This corresponds to scanning the tune of the perturbation from 1.24 – 1.30. This perturbation scan was repeated at several different intensities, created by adjusting the argon gas pressure in the vessel and the length of time for which the electron gun was turned on. Figure 6.9 presents the results from the perturbation scan at different intensities, where the same data is plotted in the top and bottom plots using both a linear and logarithmic scale.

Operating at an argon pressure of $P = 1.5 \times 10^{-8}$ mbar, with the electron gun turned on for 0.2 s (Fig. 6.9, dark blue), around 70,000 particles remained after 2000 T-insert super-periods. The theoretical space-charge tune shift at this ion number is ~ 0.001. Operating at this low-space-charge regime, the dip in the ion number was seen to occur at a tune of $Q = 1.276$, which agrees well with the MAD-X values of the lattice tune, plotted as dashed lines in Fig. 6.9.

In order to test the QI two-cell T-insert with space charge, a large enough space-charge tune spread must be created ($\Delta Q_{rms} \approx 0.036$) in order to excite the 2nd order coherent resonance. The intensity of the ion distribution was increased up to an argon gas pressure of $P = 6.8 \times 10^{-7}$ mbar and the electron gun was turned on for up to 0.5 s. Practically, these are the upper limits of pressure and time the electron gun can be on for because the ion number saturates if either of these parameters is further increased. At the highest intensity, the maximum ion loss was observed at a perturbation tune of

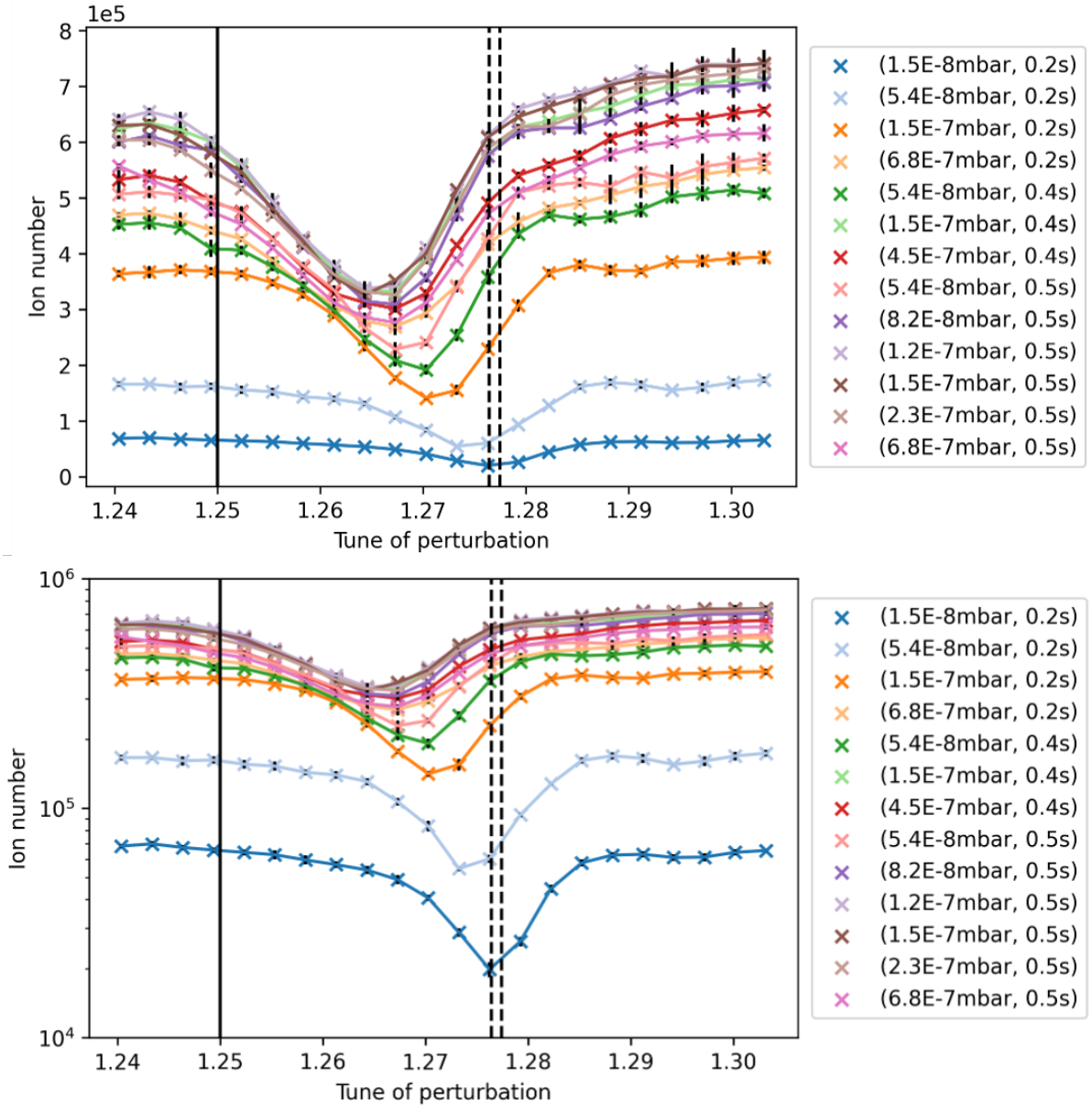

Figure 6.9: Tune scan of the 4th order perturbation applied over 2000 super-periods of the two-cell T-insert lattice. The argon pressure was varied between 1.5×10^{-8} – 6.8×10^{-7} mbar and the length of time the electron gun was on was varied between 0.2 – 0.5 s to increase the intensity, and therefore space-charge tune shift, of the ion distribution. Dashed lines represent the nominal, zero current horizontal and vertical tunes of the T-insert lattice, predicted with MAD-X. The solid line indicates the location of the 4th order incoherent resonance. (Top) Linear y-axis. (Bottom) Logarithmic y-axis.

1.265 as seen in Fig. 6.9. The maximum space-charge tune shift measured was 0.011, only around 31 % of the desired space-charge tune shift. At first sight, from these results it seems as though not enough ions can be stored in the trap to create the desired space-

charge tune shift. A potential reason behind this is that the ion loss was dominated by residual-gas collisions. As argon gas was leaked continuously throughout the experiment to maintain the desired gas pressure, at the higher gas pressure required for creating more ions, the stored ions were more likely to collide with the background argon gas. These residual-gas collisions could limit how many ions can be stored in this T-insert and for how long.

An additional loss mechanism is the 1/4 integer resonance at 1.25. As the ion number was increased to be closer to the 4th order incoherent resonance at $Q = 1.25$, ions would be lost as the 4th order incoherent resonance would be driven by nonlinearities in the quadrupole field. In simulation, the ion loss in the linear T-insert was not dominated by this 4th order incoherent resonance as the electrodes were perfectly aligned and hence nonlinearities were small. This 4th order incoherent resonance was studied in the previous IBEX trap, where ion loss was observed at cell tunes of 0.25 [39].

Another scenario is that as the intensity in the trap was increased, space-charge tune shifts of up to $\Delta Q_{rms} \approx 0.036$ were achieved and the 2nd order coherent resonance was excited. This ion loss would reduce the intensity and hence the space-charge tune shift, resulting in an apparent reduction. In reality, all of the loss mechanisms discussed above could be contributing at the same time.

In order to see whether enough ions could be stored in the trap initially to create a large-enough space-charge tune shift, the perturbation scan was repeated for a shorter storage time. This would reduce ion loss from any of the mechanisms described above and would be able to capture an earlier measurement of the space-charge-shifted tune. The results from storing for 200 two-cell T-insert super-periods while a 4th order perturbation with an amplitude of 10.0 V was applied to the plate electrodes are shown in Fig. 6.10. The perturbation amplitude was increased from 5.88 V to 10.0 V to increase the ion loss as the perturbation was being applied over a shorter storage time. When storing for this shorter time of 200 super-periods, tune shifts of up to $\Delta Q_{rms} = 0.025$ were seen when operating at a gas pressure of $P = 2.3 \times 10^{-7}$ mbar and electron-gun active time of 0.3 s.

This put the tune of the ion distributions on the 4th order incoherent resonance.

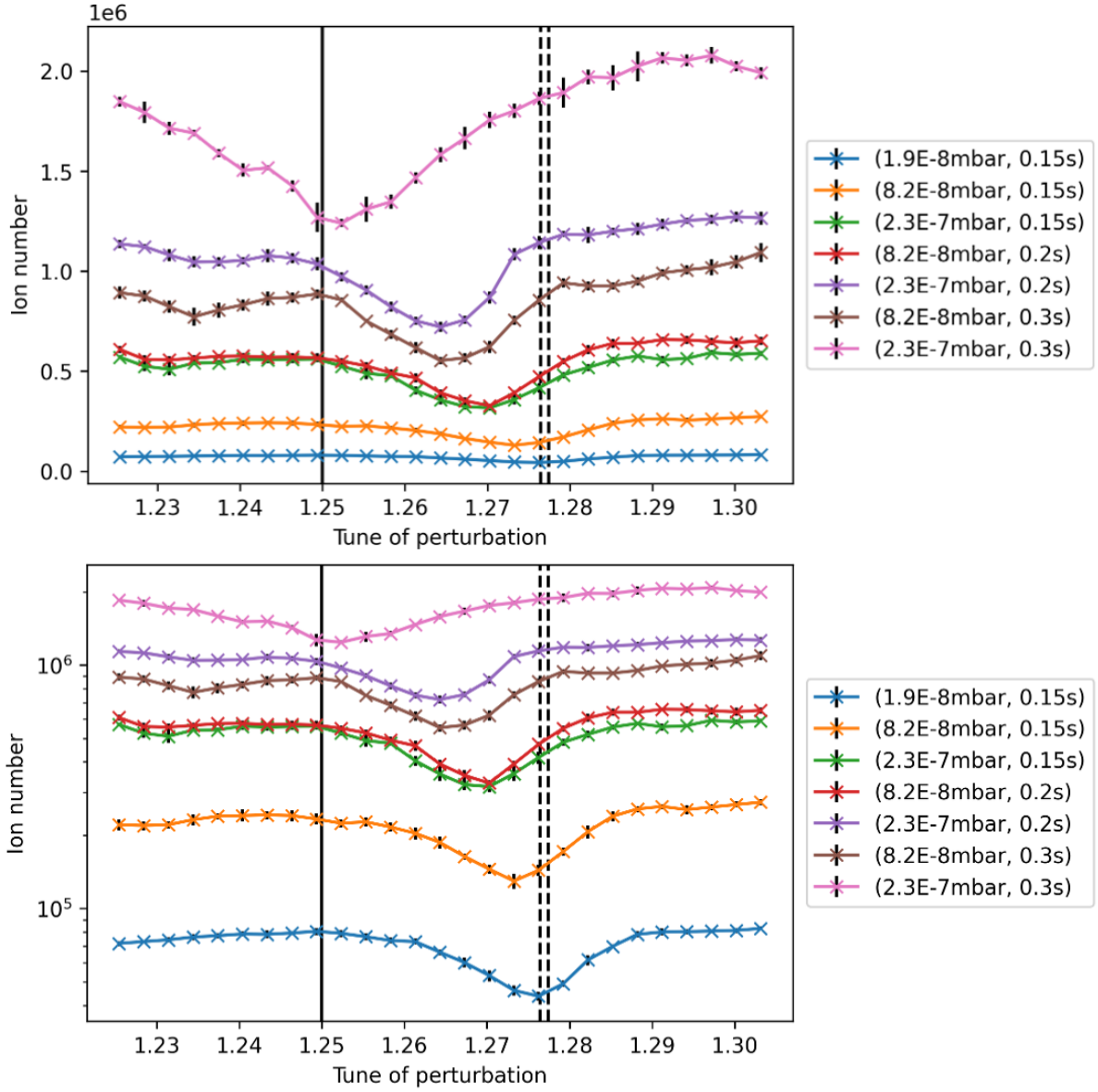

Figure 6.10: Tune scan of the 4th order perturbation applied over 200 super-periods of the two-cell T-insert lattice. The argon pressure was varied between 1.9×10^{-8} – 2.3×10^{-7} mbar and the time the electron gun was on was varied between 0.15 – 0.3 s to increase the intensity, and therefore space-charge tune shift, of the ion distribution. Dashed lines represent the nominal zero-current horizontal and vertical tunes of the T-insert lattice, predicted with MAD-X. The solid line indicates the location of the 4th order incoherent resonance. (Top) Linear y-axis. (Bottom) Logarithmic y-axis.

Note that the 2nd order coherent resonance condition is given by $Q_0 + C_2 \Delta Q_{rms} = \frac{1}{2}(\frac{5}{2})$, where Q_0 is the nominal tune and C_2 is the coherent mode factor (see Section 1.2.2.1 and Section 5.5.2.1). If C_2 were to equal 1, then the 2nd order coherent and 4th order

coherent resonances would entirely overlap and a space-charge tune shift of $\Delta Q_{rms} \approx 0.025$ would be sufficient to reach both resonances. However, as $C_2 = 3/4$, a theoretical space-charge tune shift of $\Delta Q_{rms} \approx 0.036$ is needed to reach the 2nd order coherent resonance. In practice, these resonances have finite stopband widths and so they can overlap.

The experimental space-charge tune shifts are plotted against ion number in Fig. 6.11. In this figure, the ion number plotted on the $x-$axis is an average ion number of the first five data points, at each given pressure and electron-gun time, shown in Fig. 6.10. This gave an estimate of the number of ions surviving 200 super-periods away from resonance. Using Eq. 5.24, a theoretical space-charge tune shift was calculated using the same ion number.

The RMS emittance was assumed to be 2.16×10^{-9} m rad, as was found in [39]. In the setup in [39], a low number of ions was stored in a FODO lattice with a tune of 0.1. The assumption of an emittance of 2.16×10^{-9} m rad only holds for low ion numbers, as the emittance of the distribution is expected to grow for larger space-charge forces. The theoretical and experimental space-charge tune shifts in Fig. 6.11 both show a good linear relationship between ion number and space-charge tune shift. However, a discrepancy of up to 30 % is seen in the gradients of these two linear fits. This could easily be attributed to an experimental emittance which is 30 % larger than the emittance of 2.16×10^{-9} m rad that was initially assumed. Therefore, it is likely that the emittance in the trap is closer to 2.8×10^{-9} m rad. This means that experimentally, around 30 % more particles would need to be stored in the trap than was previously calculated in order to reach a desired space-charge tune shift. Future work could estimate the emittance in the T-insert at larger ion numbers by looking at the Full-Width-Half-Maximum (FWHM) of the ion distribution, imaged on the phosphor screen with the CCD camera. This was done for the previous trap in [39].

An important note when comparing the ion number in experiment to the number of particles in simulation should be stated here. As the VSim simulations presented in

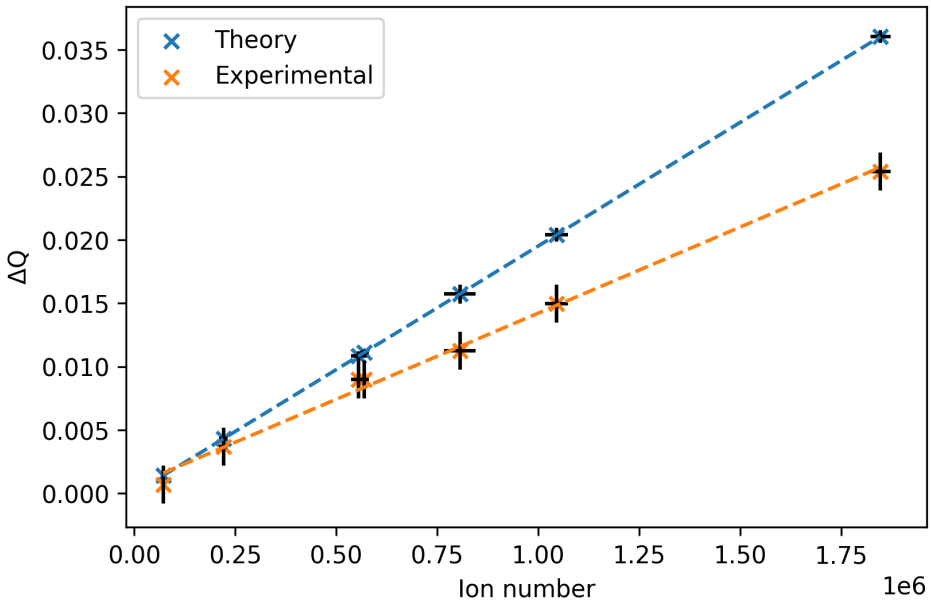

Figure 6.11: Space-charge tune shift plotted against the initial ion number. Theoretical values are calculated using Eq. 5.24 assuming an emittance of 2.16×10^{-9} m rad. Experimental values were calculated after 200 super-periods from Fig. 6.10.

Section 5.5.3 were 2D simulations, the 'number of particles' is technically a longitudinal line density, i.e. 'number of particles per meter'. In IBEX, there is a 3D charge distribution, with a longitudinal bunch length of 65.5 mm [39]. Therefore, assuming a uniform longitudinal bunch distribution in the trap, 2.5×10^7 particles per meter in VSim (needed to reach the 2nd order coherent resonance) would correspond to around 1.64×10^6 ions stored in IBEX.

In this section it was shown that space-charge tune shifts of up to $Q_{rms} = 0.025$ have been observed experimentally when trapping ions for 200 super-periods of the two-cell T-insert. Tune shifts of this magnitude will put the particle distribution on the 4th order incoherent resonance at 1.25, and close to the 2nd order coherent resonance. Extrapolating the experimental data in Fig. 6.11, approximately 2.3×10^6 particles are needed to shift the tune onto the 2nd order coherent resonance. This number of particles is shown to be stored in IBEX (at least initially) in Section 6.3.3. In the next section, the intensity was scanned, without applying any perturbation to excite ion loss. The goal of this intensity scan was to excite the 2nd order coherent resonance and observe

whether turning on a QI octupole would damp this resonance, without exciting the 4th order incoherent resonance.

6.3.3 Intensity scan

The experimental results collected in this section aimed to test the simulation results presented in Section 5.5.3. The goal of these experiments was to increase the ion density within the trap in order to increase the space-charge tune shift, which would then cause the ion distribution to reach the 4th order incoherent resonance and the 2nd order coherent resonance. In simulation, turning on a QI octupole was seen to be able to damp the 2nd order resonance, without exciting the 4th order resonance, whereas breaking the conditions of integrability was seen to excite the 4th order incoherent resonance. Two different loss mechanisms were seen in the experimental results presented in this section, namely resonant losses and residual-gas collision losses. Residual-gas losses reduce the ion survival at high gas pressures. Resonant losses are observed from comparing the differences in the total number of particles surviving the storage time.

In these experimental results, the ionisation time was kept constant while the argon gas pressure was varied. In order to get an estimate of the initial number of ions in the trap for a given argon gas pressure, the number of ions was measured on the MCP after storing for ten two-cell T-insert super-periods (see Fig. 6.13(Top)). Ten super-periods were chosen as this was long enough that any loss due to scraping on the rods would have occurred but short enough that any resonances would not have had time to cause significant ion loss. Four different lattices were tested, namely 'Oct OFF' where no octupole element was applied, 'Oct ON QI' where the QI octupole is turned on in the drift regions, and two lattices with octupole elements that break the integrability conditions. The two-cell T-insert lattice waveform along with the octupole voltages applied to the plates can be found in Fig. 5.18. An additional lattice to what was initially presented in Section 5.5.3 was also tested, where the octupole was simply turned off every other lattice period and the integrated octupole strength was not corrected. This lattice is

labeled as 'Oct ON nonQI half' as it has half the octupole strength and hence half the octupole tune spread of either the 'Oct ON QI' and 'Oct ON nonQI' lattice.

In the simulation results presented in Section 5.5.3, a positive QI octupole voltage was applied to the plates. However, it was found experimentally that a negative QI octupole voltage had a larger ion survival than with a positive octupole voltage and thus a negative octupole strength was used throughout the rest of these experimental results (see Appendix. C for results from an octupole strength scan). Interestingly, simulation results show the opposite, with a positive plate voltage leading to a larger ion survival as shown in Fig. 6.12. Table 6.2 summarises the simulated percentage particle loss in Fig. 6.12. Note that residual-gas collisions were not included in these simulations. However, the total particle loss is not as important as the relative losses between lattices, which stays the same for both a positive and negative octupole.

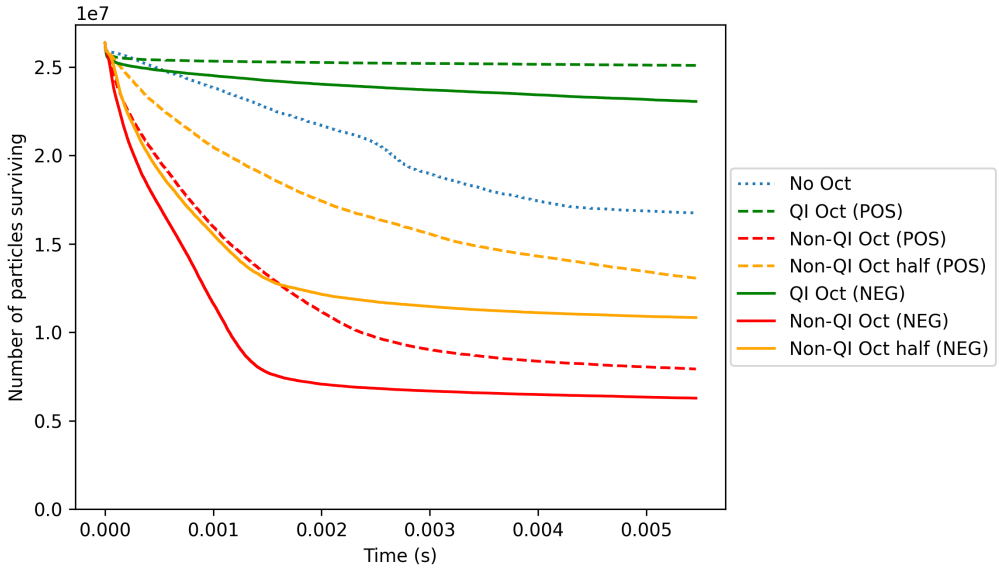

Figure 6.12: VSim simulation of rate of particle loss over 920 super-periods of the two-cell T-insert lattice at the 2nd order coherent resonance. (Blue) No octupoles applied in the drift region. (Green) Octupoles turned on in the drift region which meet the quasi-integrability condition. (Orange) Octupoles turned on but applied only once per super-period, hence non-QI. (Red) Octupoles turned on with twice the strength but applied only once per super-period, hence non-QI. Dashed lines indicate positive octupole plate voltage (presented in Section 5.5.3), solid lines indicate negative plate voltage.

In Fig. 6.13(Top) the ion number after storing for ten two-cell T-insert super-periods

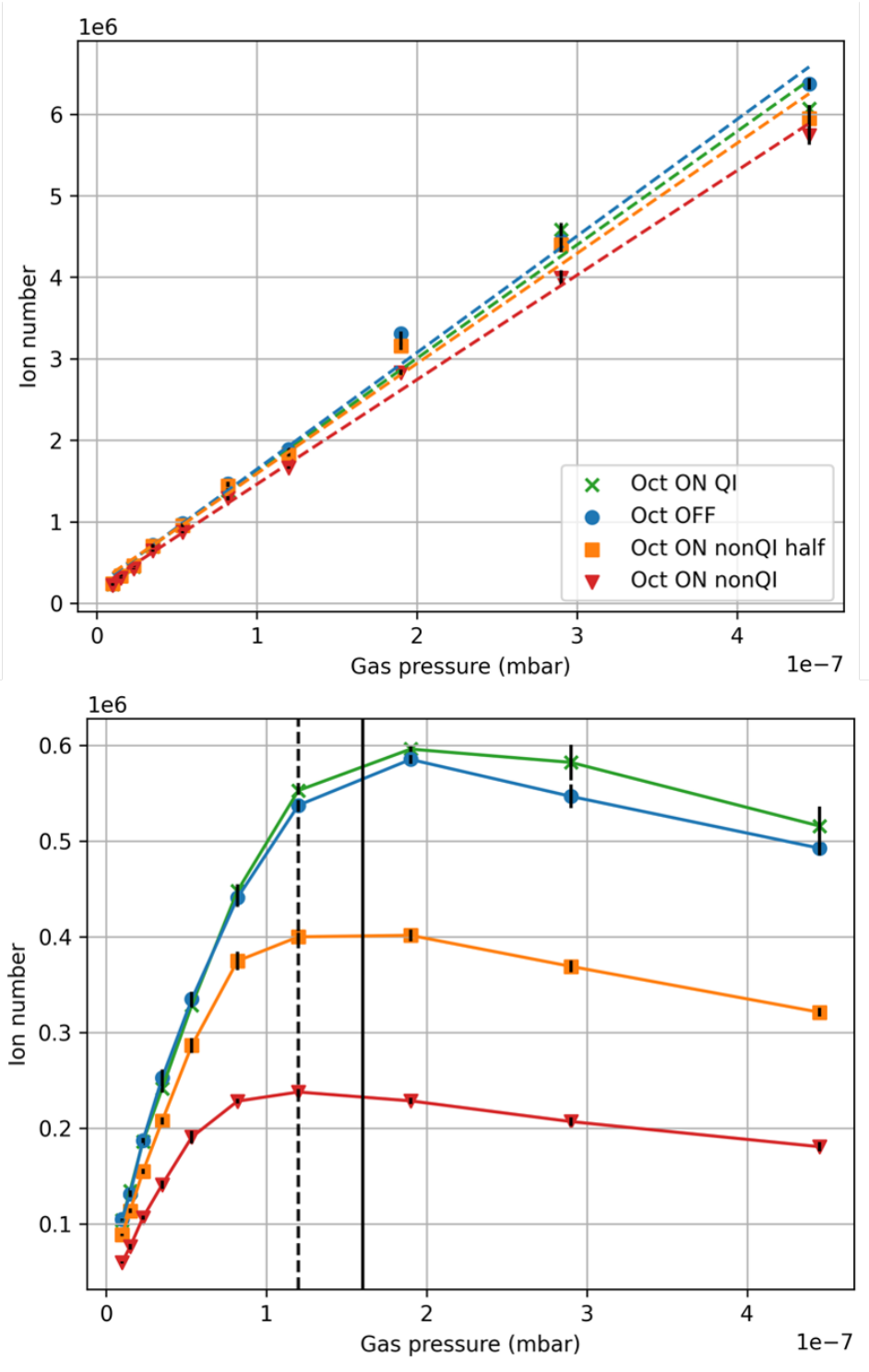

Figure 6.13: Ion number plotted against argon gas pressure at an electron-gun time of 0.3 s. (Top) Ion number after 10 two-cell T-insert lattice super-periods. Linear fit to the data is plotted as a dashed line. (Bottom) Ion number after 2000 two-cell T-insert lattice super-periods. Dashed black line indicates predicted location of 4th order incoherent resonance. Solid black line indicates predicted location of 2nd order coherent resonance.

Table 6.2: VSim simulated particle loss over 920 super-periods of the two-cell T-insert lattice at the 2nd order coherent resonance.

Octupole element	Percentage particle loss (%)
Oct. OFF	36.5(3)
QI Oct. (POS)	5.0(1)
QI Oct. (NEG)	11.0(2)
non-QI Oct. half (POS)	51.6(3)
non-QI Oct. half (NEG)	59.2(3)
non-QI Oct. (POS)	70.4(3)
non-QI Oct. (NEG)	76.2(3)

for varying argon gas pressures is plotted for the linear T-insert lattice (Oct OFF), QI octupoles turned on (Oct ON QI), and two lattices that break the integrability conditions. From Fig. 6.13(Top) the ion number measured after 10 T-insert super-periods is seen to increase linearly with the argon gas pressure introduced into the vessel for all four lattices, as expected. The results were then repeated, storing the ions for 2000 T-insert super-periods, shown in Fig. 6.13(Bottom). For an argon gas pressure of $P = 0.82 \times 10^{-7}$ mbar, corresponding to an initial ion number of around 1.4×10^6, the number of ions surviving 2000 T-insert super-periods can be seen to plateau in both of the non-QI lattices. This suggests that the octupoles in these lattices, which do not meet the conditions of QIO, are exciting the 4th order incoherent resonance. Interpolating from the line of best fit to experimental data in Fig. 6.11, this number of particles should create a space-charge tune shift of around $Q_{rms} = 0.020$, shifting the ion distribution close to the 1/4 integer resonance at 1.25. Therefore, the results shown in Fig. 6.13(Bottom) are consistent with the non-QI octupoles exciting the 4th order incoherent resonance. The number of particles surviving the 'Oct ON nonQI' lattice is approximately half of that of the 'Oct ON nonQI half' lattice. This is because the strength of the octupole for 'Oct ON nonQI' lattice is twice that of 'Oct ON nonQI half' and hence the driving term for the resonance is twice as large. The fact that all four curves in Fig. 6.13(Bottom) see the ion number not just plateau, but also start to decrease, suggests that at larger gas pressures, residual-gas collisions are contributing to the ion loss over these time scales

(2000 lattice super-periods).

In the absence of octupoles (Oct OFF), the ion number is seen to plateau at a gas pressure of $P = 1.2 \times 10^{-7}$ mbar, corresponding to an initial ion number of 1.9×10^6. The fact that this plateau in ion number occurs slightly after the plateau seen for the non-QI lattices suggests that this ion loss could be due to the coherent resonance condition being reached. It was predicted earlier that around 2.3×10^6 ions would be needed in order to create an experimental space-charge tune shift large enough to reach the 2nd order coherent resonance, therefore it is plausible that at ion numbers of 1.9×10^6 the edge of the 2nd order coherent resonance stopband has been reached. Similarly, when the QI octupoles are turned on (Oct ON QI), the ion number is seen to plateau at the same place. At this point it should be noted that introducing the QI octupole to the lattice does not excite the 4th order incoherent resonance to anywhere near the same extent as the non-QI lattices. A maximum of $0.596(3) \times 10^6$ ions were seen to survive 2000 two-cell T-insert super-periods with the QI octupole switched on, compared to a maximum of $0.402(6) \times 10^6$ in the 'Oct ON nonQI half' lattice and $0.238(3) \times 10^6$ in the 'Oct ON nonQI'. Therefore, these results show that by introducing the octupole using the method prescribed by QIO, up to 60 % more particles were stored when compared to a non-QI lattice with the same octupole strength, and 33 % more particles were stored when compared to a non-QI lattice with the half the octupole strength.

When comparing the results of the T-insert lattice with octupoles off and QI octupoles on in Fig. 6.13(Bottom), a marginal improvement of up to 6(4) % is seen when turning the QI octupole on. The fact that the number of ions surviving both lattices are so close shows the promising result that introducing the QI octupole has not further excited the 4th order resonance and has not made the lattice worse than the linear lattice alone. However, the results do not show the same improvement in reducing ion loss from damping the coherent resonance, as was seen in simulation (Section 5.5.3). Using the difference between the number of particles surviving 2000 super-periods and 10 super-periods, a percentage of ions surviving is calculated as a function of the initial

number of particles stored in the trap and plotted in Fig. 6.14.

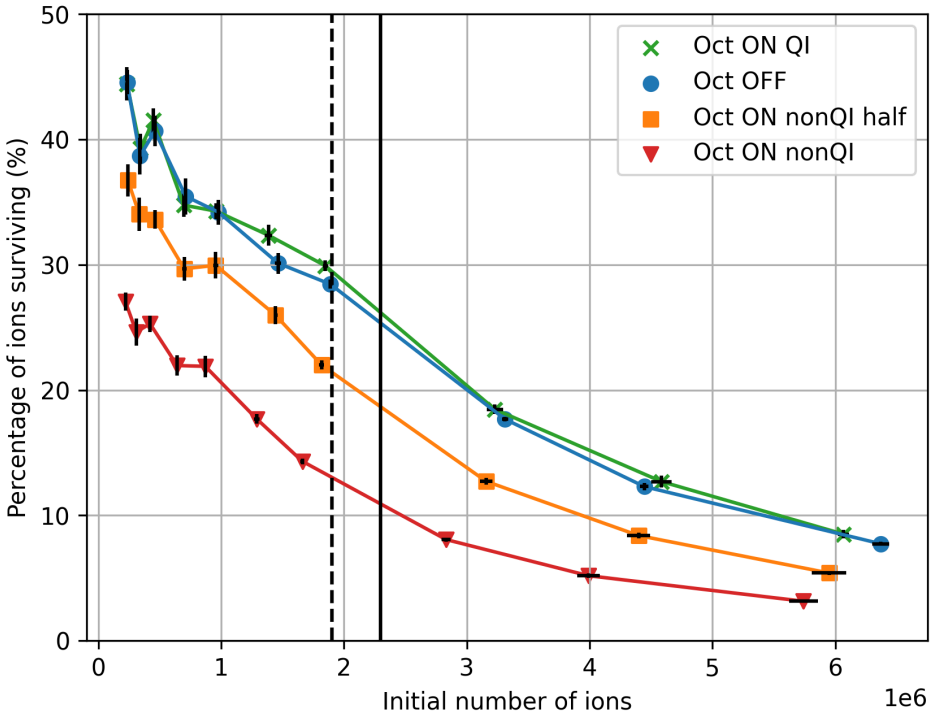

Figure 6.14: Percentage of ions surviving 2000 two-cell T-insert super-periods as a function of initial number of ions stored in the trap (after 10 super-periods). The dashed black line indicates the predicted location of the 4th order incoherent resonance. The solid black line indicates the predicted location of the 2nd order coherent resonance.

One possible explanation for the similar ion loss seen for QI octupoles on and off is that the ion loss is dominated by residual-gas collisions at the larger gas pressures needed to create larger initial numbers of ions within the trap. If residual-gas collisions were the dominant source of ion loss, this could mask the benefits of the QI octupole, when compared to having octupoles off, in the presence of the 2nd order coherent resonance. It is also possible that the ion loss created from the residual-gas collisions is preventing a high-enough intensity of ions being trapped, which is needed for the coherent resonance to form. In this case, turning the QI octupoles on would not help as there would be no coherent resonance to damp. To quantify the extent to which the residual gas is affecting the ion loss in the trap, the mean free path of argon ions was calculated for typical gas pressures in IBEX. The mean free path, ℓ, can be calculated for a pressure, P, using the following formula:

$$\ell = \frac{k_{\mathrm{B}} T}{\sqrt{2}\pi d^2 P}, \tag{6.2}$$

where k_{B} is the Boltzmann constant, T is the temperature of the gas and d is the kinetic diameter of the particle. Taking the gas within the vessel to be at the room temperature of the lab, $T = 291.15\,\mathrm{K}$ and assuming a kinetic diameter of 340 pm [126, 127], the mean free paths of an argon ion are calculated for typical gas pressures in IBEX in Table 6.3.

Table 6.3: Mean free path calculated for typical argon pressures in IBEX. A vacuum pressure of 5.0×10^{-10} mbar is typical when no argon is being leaked into the vessel.

Pressure (mbar)	Mean Free Path (m)
5.0×10^{-10}	157×10^{3}
1.5×10^{-8}	5.22×10^{3}
2.3×10^{-7}	340
4.5×10^{-7}	174
6.8×10^{-7}	115

In order to calculate how far a typical argon ion would travel in the trap during a total storage time[3] of 68 ms, the average velocity of the ion needs to be estimated. Assuming the trapped ions have a thermal energy of 0.3 eV (measured in [39]), then the average velocity of a particle in the trap is found to be around $v = 1360\,\mathrm{ms}^{-1}$. This gives an average distance an ion has travelled during a storage time of one experiment as 92.5 m. This distance travelled in the trap is comparable to the mean free path of ions at the larger gas pressures used. Assuming that an ion is expelled from the trap if it collides with a residual gas molecule, then there is expected to be significant ion loss at these higher gas pressures. In order to confirm these calculations, further experiments should be carried out in IBEX which measure the percentage of particles surviving as a function of the time stored in the trap for various gas pressures. This would help conclude the impact of residual-gas collisions on these experimental results.

[3]The total storage time was calculated from the point the electron gun was switched off to the end of extraction.

Nevertheless, despite the ion loss being dominated by residual-gas collisions, these results still indicate that when the octupole is introduced into the lattice, following the conditions of QIO, the dominant source of loss in the lattice is no longer from the octupole exciting the 4th order resonance.

In order to reduce the effect of residual-gas collisions in the trap, two steps were taken. First, the time the electron gun was turned on for was increased from 0.3 s to 0.4 s. This should allow more ions to be created for a lower argon pressure. This is seen to be the case when comparing the ion number stored after ten two-cell T-insert lattice super-periods, plotted against argon gas pressure, for the two ionisation times in Fig. 6.13(Top) and in Fig. 6.15(Top). Using an ionisation time of 0.4 s, ion numbers of up to 5.8×10^6 could be reached at a pressure of $P = 3.6 \times 10^{-7}$ mbar, whereas the same ion number could only be reached with a gas pressure of over $P = 4.0 \times 10^{-7}$ mbar for an ionisation time of 0.3 s (Fig. 6.13(Top)). In Fig. 6.15(Top), the ion number is seen to saturate above $P = 3.6 \times 10^{-7}$ mbar and hence pressures of between $P = 9.9 \times 10^{-9}$ – 3.6×10^{-7} mbar were used in the linear fit.

Figure 6.15(Bottom) plots the number of ions surviving after 1000 two-cell T-insert lattice super-periods. Again, the ion numbers for the non-QI lattice start to plateau as the initial ion number reaches around 1.5×10^6. This corresponds to a tune shift of around 0.02 which is consistent with exciting the 4th order incoherent resonance. This time, the QI octupole is seen to be able to store up to 10(2) % more particles when compared to when the octupoles are off, over the 1000 T-insert super-periods studied. These results suggest that storing ions for fewer T-insert lattice periods, and avoiding the highest argon gas pressures, can reduce the residual-gas collisions sufficiently in order to start to see the benefits of the QI octupole.

For completeness, the percentage of particles surviving 1000 two-cell T-insert super-periods is plotted against initial ion number in Fig. 6.16. The percentage of ions surviving the lattice when the QI octupoles are turned on is up to 2.1(7) % more than when the octupoles are turned off. As the percentage of the initial number of ions surviving is

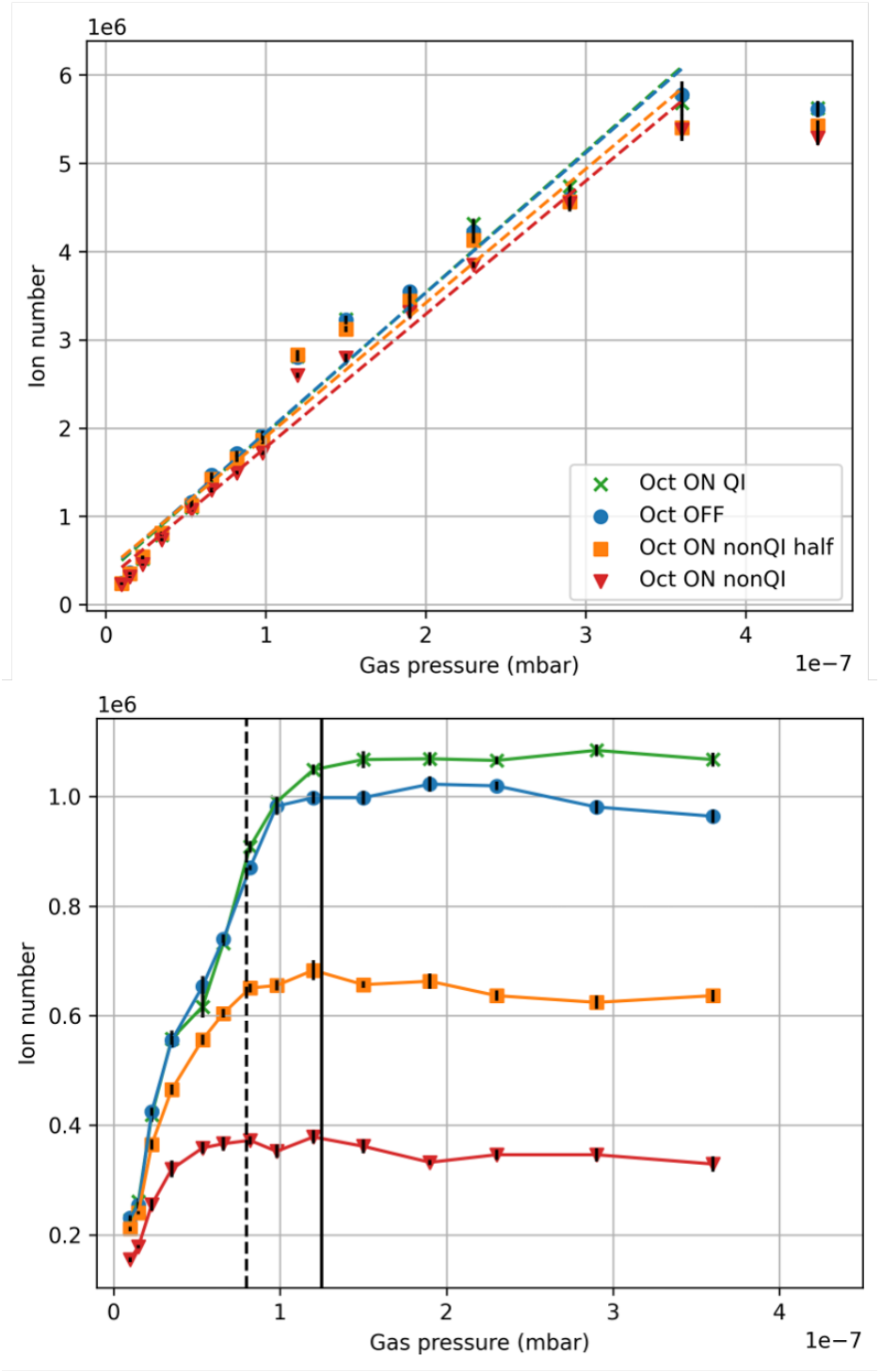

Figure 6.15: Ion number plotted against argon gas pressure at an electron-gun time of 0.4 s. (Top) Ion number after 10 two-cell T-insert lattice super-periods. Linear fit to the data is plotted as a dashed line, where the data point at $P = 4.5 \times 10^{-7}$ mbar has been excluded from the fit as the ion number has saturated. (Bottom) Ion number after 1000 two-cell T-insert lattice super-periods. The dashed black line indicates the predicted location of the 4th order incoherent resonance. The solid black line indicates the predicted location of the 2nd order coherent resonance.

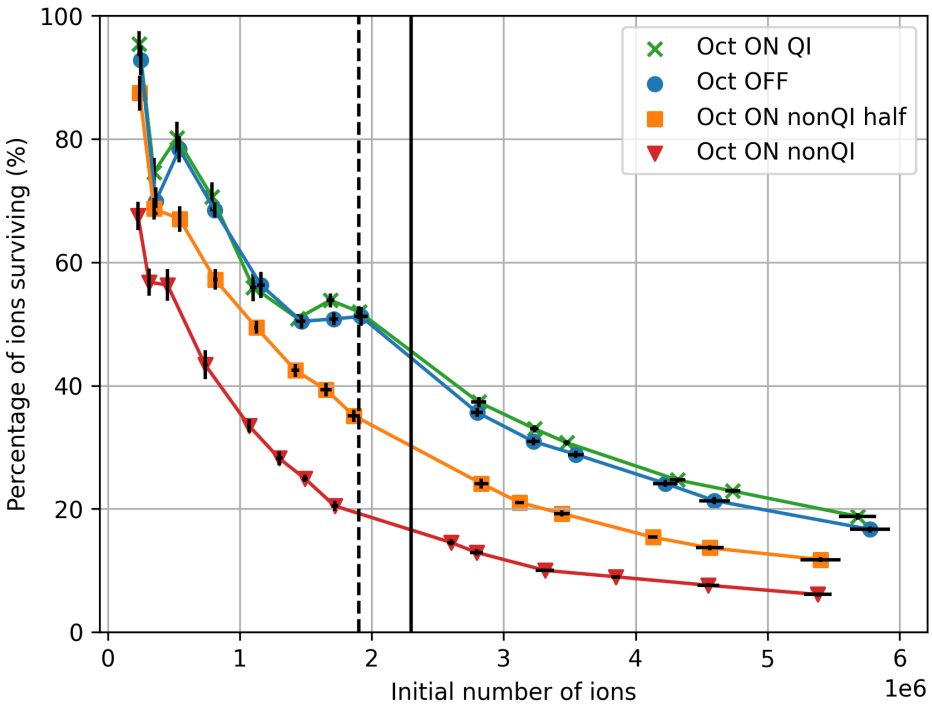

Figure 6.16: Percentage of ions surviving 1000 two-cell T-insert super-periods as a function of initial number of ions stored in the trap. The initial number of ions was assumed to be the number of ions detected after storing for 10 two-cell T-insert super-periods (Fig. 6.15(Top)).

around 20 %, this corresponds to 11.0(4) % more particles stored in the lattice where QI octupoles are turned on, when accounting for the initial number of ions in the trap. The percentage of particles surviving plotted in Fig. 6.16 is not seen to increase as the particle number is increased beyond the 4th order incoherent and 2nd order coherent resonances, as was seen in simulation (Section 5.5.3). The reason for this is suspected to be due to losses in the trap, with residual-gas collisions likely to still be dominating. Hence, even if enough particles are initially created in the trap in order to create a space-charge tune shift taking it beyond the resonances, due to ion losses over the 1000 super-periods, the ion distribution will be brought back onto the 2nd order coherent resonance. In comparison to simulation results, the particle loss after crossing the 2nd order resonance was around 2 % for octupoles off and between 5-10 % for octupoles on. This particle loss is much less than what is seen in experiment (up to 83 % for octupoles off after 1000 super-periods) and therefore a large enough space-charge tune shift cannot

be created in the trap to reach beyond the 2nd order resonance. This is thought to be a limitation from residual-gas collisions.

The results in this section have illustrated the benefits of introducing octupoles described by the theory of QIO, in the presence of space charge. The results show promising potential benefits to using QI octupoles in a lattice in order to damp 2nd order coherent resonances. An absolute number of 10(2) % more particles survived 1000 two-cell T-insert super-periods when compared to when octupoles were off. When comparing the QI lattice to two non-QI lattices the results show that the QI lattice does not excite the 4th order resonance. The 4th order resonance was confirmed to be present from the particle loss seen in both the non-QI lattices.

6.4 Chapter summary

In summary, these experimental results have shown the first demonstration of ions trapped in a QI T-insert lattice both in a low-space-charge regime ($\Delta Q_{rms} \sim 0.001$) and with space charge ($\Delta Q_{rms} \sim 0.025$ and above). In the low-space-charge regime, the QI octupole was shown to create tune spreads of up to 0.013 and was able to damp an externally applied 4th order perturbation. Turning on the QI octupole was seen to reduce the maximum ion loss by up to 30(7) %. These results agreed well with what was seen in simulation.

The two-cell T-insert lattice, with tunes of $Q_x = 1.276, Q_y = 1.277$ was tested with space charge with the aim to create space-charge tune shifts to bring the ion distribution close to the 4th order incoherent resonance and 2nd order coherent resonance. The QI octupole generated improved ion survival at higher intensities compared to when the octupoles were turned off. It was suspected that the benefits of the QI octupole were limited due to residual-gas collisions dominating ion loss. This additional loss mechanism would continuously reduce the space-charge tune shift, moving the tune distribution across the resonance and not giving time for the 2nd order coherent resonance to fully form. Despite this, the QI octupole was shown to no longer be the dominant source of

ion loss in the vicinity of the 4th order incoherent resonance. This was confirmed by testing two non-QI lattices, which were shown to excite the 4th order resonance.

In the future, the T-insert lattice created in IBEX could be improved to meet the conditions of integrability more closely. This could be done by creating higher slew-rate amplifiers, optimising the input waveform to more closely create the desired output waveform, or by redesigning the T-insert lattice in an attempt to reduce the slew-rate requirements. Experimental verification of the beta functions within the trap should also be carried out to better quantify how well the conditions of integrability are met within the trap.

Automating these experiments would also allow for higher-resolution scans to be carried out, and would increase the efficiency of data collection. In order to fully automate experiments on IBEX-2, the synchronisation of the AWGs should be integrated into the existing LabView program. This was not possible with the current LabView subVIs provided by Tabor, as described in Section 4.5.3. Automating the synchronisation procedure would also reduce errors in phase offsets, caused by synchronising the octupole waveform manually on the AWG.

In order to overcome challenges with residual-gas collisions, future experiments could look at 'topping up' the charge distribution within the trap by turning on the electron gun again before dropping the gate DC voltage briefly to allow more ions into the ER. This process would first need to be studied and understood in simulation. An alternative solution could look at injecting a 'bubble' of gas into the vacuum vessel. This would introduce gas into the vessel while the electron gun was on and then stop the flow of gas during the rest of the storage time. This would minimise the amount of residual gas within the trap during the experiment. However, this would require a leak valve that could be opened and closed on a time scale of less than 0.1 s. The current VAT leak valve operates on the time scale of seconds. In addition to the solutions mentioned above, reducing the effective length of the trap could also be studied as a potential method of increasing the space charge within the trap at a fixed ion number and hence

gas pressure. This could be achieved by increasing the DC voltages applied to the end caps in order to reduce the effective longitudinal length of the experimental trapping region. According to Eq. 5.24, a shorter longitudinal effective length within the trap would increase the space-charge tune shift for a given number of particles.

Despite the challenges of testing QIO in the newly commissioned IBEX-2 trap, the experimental results presented in this chapter show promising benefits of using QIO lattices in future experiments. We hope that future experimental runs of IBEX can further build on these results.

Chapter 7

Conclusions and Future work

Paul traps are a useful tool for research in accelerator physics due to the equivalence between the transverse Hamiltonian of ions in a trap and the transverse Hamiltonian of particles in an accelerator. Due to this equivalence, the Intense Beams Experiment (IBEX) can be used as an analogue simulation of the transverse beam dynamics in an alternating-gradient accelerator. There are several benefits to using IBEX for this purpose. IBEX stores low-energy ions so that space-charge-dominated beams can be studied in a fraction of the time that it would take to run a computer simulation to recreate the intricate Coulomb forces between particles. Furthermore, when compared to using accelerators to study intense beams, the flexibility of IBEX allows for a large parameter space to be covered, without the risk of damaging or activating components if ions are lost. For example, it is quick and simple to change the number of ions stored in the trap and hence to change the space-charge tune shift. In addition, the type of accelerator lattice being studied can be altered simply by changing the amplitude and time structure of voltage waveform applied to the electrodes. For the research described in this thesis, these advantages of IBEX were used to test experimentally the theory of Nonlinear Integrable Optics (NIO), which proposes a method of constructing an accelerator lattice using nonlinear elements which avoids exciting the resonances associated with these elements.

One of the obstacles to achieving higher-intensity beams is that space-charge forces can excite coherent resonances and thus lead to beam loss in accelerators. Along with re-

ducing the efficiency of the accelerator, these losses can be damaging and costly. While octupoles can be used to damp coherent resonances through Landau damping, they can also pose an additional problem as they lead to non-integrable lattices where the Hamiltonian is not conserved. This can lead to the octupole elements driving 4th order resonances. Nonlinear Integrable Optics offers a potential solution to this issue as it introduces a way to create decoherence in a beam while maintaining integrability. Fulfilling the conditions of NIO requires a complicated elliptical potential in order to create the two invariants of motion, which is necessary to produce fully integrable motion in the transverse plane. This thesis focused on Quasi Integrable Optics (QIO), which is a method of using carefully placed, strength-scaling octupoles in a T-insert lattice in order to conserve the Hamiltonian while still introducing decoherence. Because a QIO lattice has a time-independent Hamiltonian, the octupoles should not excite 4th order resonances.

In order to test Quasi Integrable Optics, an upgrade to the IBEX trap was required which added four additional multipole electrodes, capable of creating the octupole fields needed for studying QIO. Prior to attaining experimental results, simulations were carried out that, as described in Chapter 5, showed the ability of the QIO lattice to damp a 2nd order coherent resonance without exciting the 4th order resonance. By contrast, breaking the conditions of integrability while maintaining the same octupole tune spread showed that the 4th order resonance was excited. Simulations were also used to benchmark a proposed method of quantifying how close a lattice will be to integrable, given errors in the octupole scaling, beta functions, and phase advance. Further work is needed to test the measure of integrability formula against errors in the phase advance, and in the future IBEX could be used to test this formula experimentally.

Following the promising simulation results, the IBEX Paul trap was redesigned to allow for octupole fields to be created in the trap. This full redesign of the trap enabled us to reach alignment tolerances of $<10\,\mu m$ for nearly all components. This thesis has described in detail the design work and commissioning of the new trap, as well as the

new high-voltage, high-slew-rate amplifiers that were required to supply the voltages to the additional electrodes. With the completion of the upgrade, I was then able to experimentally test QIO on the newly commissioned IBEX-2 multipole trap. The experiments discussed in this thesis demonstrated the first successful trapping of ions in a T-insert lattice with a quasi-integrable scaling octupole, within a Paul trap.

Particle loss was excited in a one-cell T-insert lattice with a 4th order perturbation applied to the plate electrodes. Turning on an octupole with a strength that scales with $1/\beta^3$ was shown to create a tune spread in the beam, reducing the peak particle loss by up to 30(7) % when compared to leaving the octupoles off. I was also able to test QIO with space charge in a two-cell T-insert lattice by increasing the intensity of the stored ions in order to excite the 2nd order coherent resonance. Due to ion loss being dominated by residual-gas collisions at large gas pressures, the benefits of damping the 2nd order coherent resonance could not be measured in their entirety. However, improvements in ion survival of up to 10(2) % were seen over 1000 T-insert super periods for when the QI octupole was turned on, compared to when it was off. Despite being limited by residual-gas collisions, the Quasi Integrable scaling octupole was shown to avoid further exciting the 4th order incoherent resonance, and was therefore not the dominant source of ion loss. In contrast, breaking the integrability conditions was shown to lead to more ion loss caused by exciting the 4th order resonance.

7.1 Future work

The results described in this thesis lay the foundation for multiple trajectories of future work with IBEX to further investigate QIO and NIO. Next steps should include optimising the input T-insert waveform to ensure that the waveform applied to the electrodes in the trap more closely meets the conditions of integrability. Experimental verification of the beta functions within the trap is also an important next step to further quantify how close to integrable the T-insert lattice can be made in IBEX. It would also be beneficial

to improve the slew rate of the amplifiers, as doing so would help achieve better agreement of the T-insert waveform and octupole pulse. Another approach to allow IBEX to explore QIO further would involve seeking to reduce the residual-gas collisions that hinder the formation of the 2nd order coherent resonance. This might be possible through the introduction of a 'bubble' of argon or nitrogen gas using a triggered, high-speed leak valve. This would aim to minimise ion collisions with the neutral gas. We could also gain a more thorough understanding of the practical applications of QIO by implementing a distributed octupole scheme as described in [92], in IBEX. The space-charge tune shift within the trap can also be increased for a given number of ions by trapping ions with smaller mass-to-charge ratios or by decreasing the effective longitudinal length of the trap. These methods would allow for higher space-charge tune shifts to be studied in the trap without increasing losses due to residual-gas collisions.

IBEX-2 also has the potential to further explore effects such as Landau damping. A recent paper describes a method for measuring the strength of Landau damping at the LHC [128]. A similar experiment could be performed with IBEX using a dipole perturbation to create coherent oscillations of the ion distribution. Octupoles could be turned on and the damping of the oscillations measured.

In addition to IBEX, and the other operational Paul traps for studying accelerator physics discussed in this thesis, a new trap has been proposed at Brookhaven National Laboratory (BNL) [129]. The goal of this experiment is to laser cool the trapped ions in order to study ultra-low emittance bunches. This has application in high luminosity collider experiments, as well as potential quantum-computing applications [130].

Finally, it is worth noting that IBEX-2 has potential for studying subjects beyond NIO and QIO. For example, the additional multipoles could be used to create skew quadrupole terms and higher-order terms to allow for experiments to study the dynamics of FFAs (Fixed-Field alternating gradient Accelerators). The IBEX trap could also be adapted for explorations of other space-charge mitigation techniques such as electron lenses. For example, research into trapping quasi-neutral plasma in RF multipole traps

has previously been studied [118], however this has yet to be applied to Paul traps studying accelerator physics. Along with the research described in this thesis, these are just a few possible areas of research that demonstrate the exciting potential of both the theory of Nonlinear Integrable Optics and the IBEX Paul Trap for pushing the frontiers of high-intensity accelerator physics.

Appendix A

IBEX-2 trap alignment

In this appendix the CMM dimensional metrology report for the machining tolerances and alignment tolerances of the recently assembled IBEX-2 trap is presented. Table A.1 summarises the machining and alignment tolerances of the electrodes, measured at the Faraday cup end caps. Table A.2 summarises the machining and alignment tolerances of the rod and plate electrodes in the experimental region of the trap.

Table A.1: Electrode and alignment tolerances measured at the Faraday cup end caps.

Parameter	Actual (mm)	Nominal (mm)	Deviation (mm)
Diameter of end cap 1	11.4980	11.4965	0.0015
Diameter of end cap 2	11.5004	11.4965	0.0039
Diameter of end cap 3	11.5005	11.4965	0.0040
Diameter of end cap 4	11.5040	11.4965	0.0075
Roundness of end cap 1	0.0023	0.0000	0.0023
Roundness of end cap 2	0.0017	0.0000	0.0017
Roundness of end cap 3	0.0025	0.0000	0.0025
Roundness of end cap 4	0.0025	0.0000	0.0025
Inner diameter	9.9933	9.9925	0.0008
Roundness of inner diameter	0.0039	0.0000	0.0039
Horizontal coaxiality of IR to ER	-0.0039	0.0000	-0.0039
Vertical coaxiality of IR to ER	-0.0492	0.0000	-0.0492

Table A.2: Electrode and alignment tolerances measured at the end of the experimental region.

Parameter	Actual (mm)	Nominal (mm)	Deviation (mm)
Diameter of rod 1	11.4923	11.4965	-0.0042
Diameter of rod 2	11.4985	11.4965	0.0020
Diameter of rod 3	11.4949	11.4965	-0.0016
Diameter of rod 4	11.4962	11.4965	-0.0003
Roundness of rod 1	0.0024	0.0000	0.0024
Roundness of rod 2	0.0019	0.0000	0.0019
Roundness of rod 3	0.0019	0.0000	0.0019
Roundness of rod 4	0.0025	0.0000	0.0025
Inner diameter	9.9947	9.9950	-0.0003
Roundness of inner diameter	0.0012	0.0000	0.0012
Plate 1 blade thickness	1.0018	1.0000	0.0018
Plate 2 blade thickness	1.0022	1.0000	0.0022
Plate 3 blade thickness	1.0000	1.0000	0.0000
Plate 4 blade thickness	1.0005	1.0000	0.0005
Plate 1 radius from center	8.4932	8.5000	-0.0068
Plate 2 radius from center	8.5014	8.5000	0.0014
Plate 3 radius from center	8.5025	8.5000	0.0025
Plate 4 radius from center	8.5006	8.5000	0.0006

Appendix B

4th order perturbation: Interaction between the rod and plate electrodes

In this appendix the 4th order perturbation applied to the plate electrodes experimentally in Section 6.2 is explained in more detail. Problems with an induced voltage in the plate electrodes from the rod electrodes are also discussed.

The horizontal amplitude of a particle is defined by $x = \sqrt{2J_x\beta_x}\cos\phi_x$. As the octupole potential is proportional to x^4 (see Eq. 2.39), the particle amplitude becomes dependent on $\cos^4\phi_x$. This can be expanded as,

$$\cos^4\phi_x = \frac{1}{2}\cos 2\phi_x + \frac{1}{8}\cos 4\phi_x + \frac{3}{8}. \tag{B.1}$$

Hence, from the expansion above we can see that an octupole (or 4th order) perturbation can drive particles to larger amplitudes if the frequency of the perturbation is either four times the phase advance over the cell or twice the phase advance over the cell. In other words, a resonance will be excited if the 4th order perturbation frequency matches twice or four times the betatron frequency.

This can clearly be seen from Fig. B.1, where a FODO lattice with tunes $Q_x, Q_y = 0.15$ stored ions for 50,000 cell periods in IBEX while a 4th order perturbation was applied to the plate electrodes. The frequency of the sinusoidal perturbation was varied from 220 kHz – 740 kHz and two distinct dips in ion number can be seen when the perturbation frequency is twice and four times the betatron frequency. The other smaller

dips in ion number seen in Fig. B.1 are suspected to be caused by other frequency components in the perturbation voltage, caused by the induced voltage in the plate electrodes from the rod electrodes.

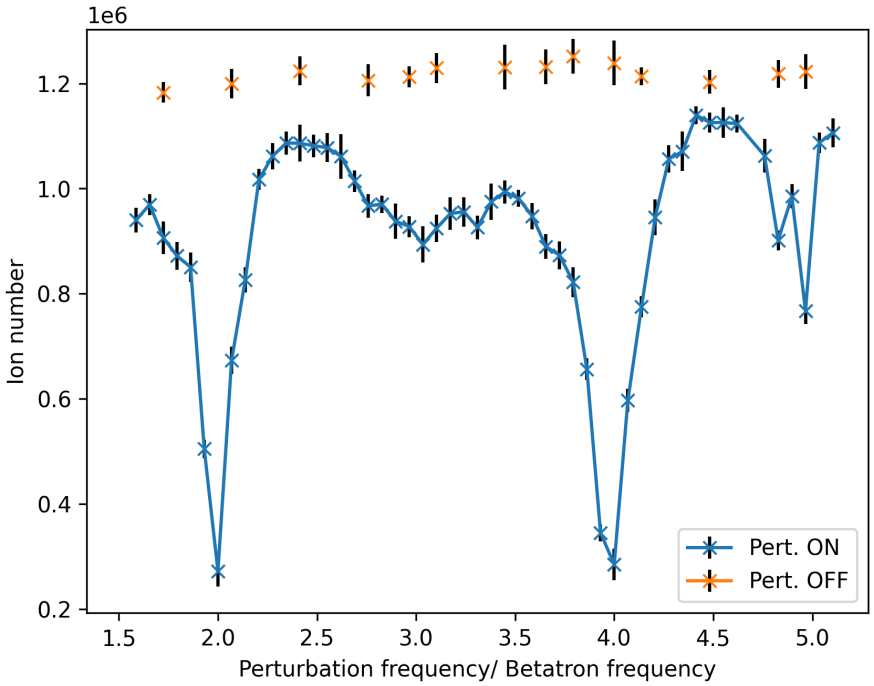

Figure B.1: Experimental 4th order perturbation frequency scan for a FODO lattice with cell tunes $Q_x, Q_y = 0.15$. (Blue) Perturbation with an amplitude of 10 V applied. (Orange) No perturbation applied

In simulation, a perturbation frequency of four times the betatron frequency was chosen. However, when collecting experimental perturbation data it was chosen to excite the 4th order perturbation at twice the betatron frequency for the reasons described below.

Figure B.2 shows the oscilloscope trace of a 420 kHz sine wave with an amplitude of 5 V, being applied experimentally to the plate electrodes, while the rod electrodes are grounded. A perturbation frequency of 420 kHz corresponds to a frequency which is twice the betatron frequency of the two-cell T-insert lattice.

If a voltage waveform is applied to the rod electrodes at the same time as the 420 kHz perturbation is applied to the plates, the induced voltage from the rod electrodes to the plates is seen to affect the applied perturbation. This is shown in Fig. B.3. The

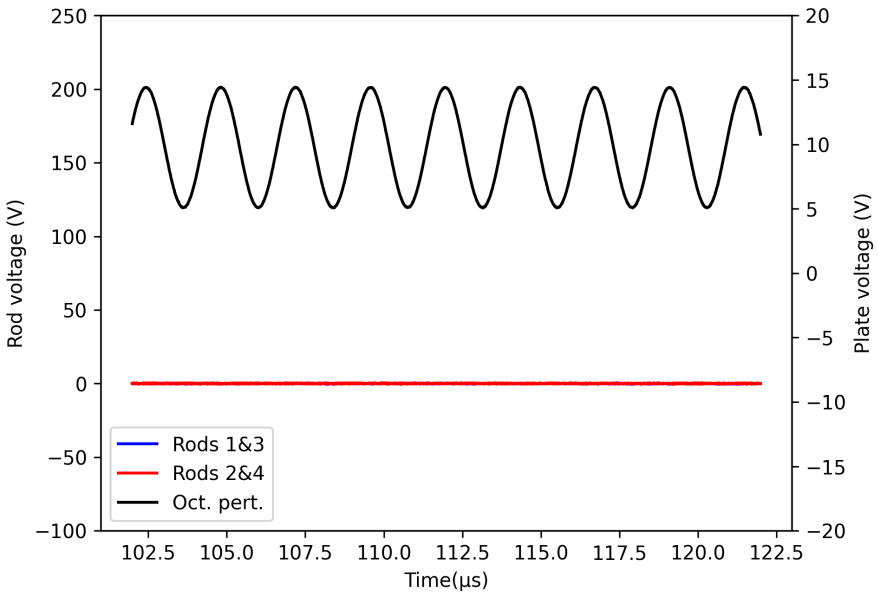

Figure B.2: Oscilloscope trace of 4th order perturbation applied at 420 kHz to the plate electrodes while the rod electrodes in the experimental region are grounded at 0V.

induced voltage seen in the plates occurs due to the close proximity of the rod and plate electrodes, as well as the relatively large voltage applied to the rod electrodes ($\sim \pm 80\,\mathrm{V}$), when compared to the perturbation voltage applied to the plates ($\sim \pm 5\,\mathrm{V}$). It was thus decided to perform the 4th order perturbation scans at lower frequencies to avoid this high-frequency induced noise. Therefore, frequencies around twice the betatron frequency were used in experiment instead of four times the betatron frequency.

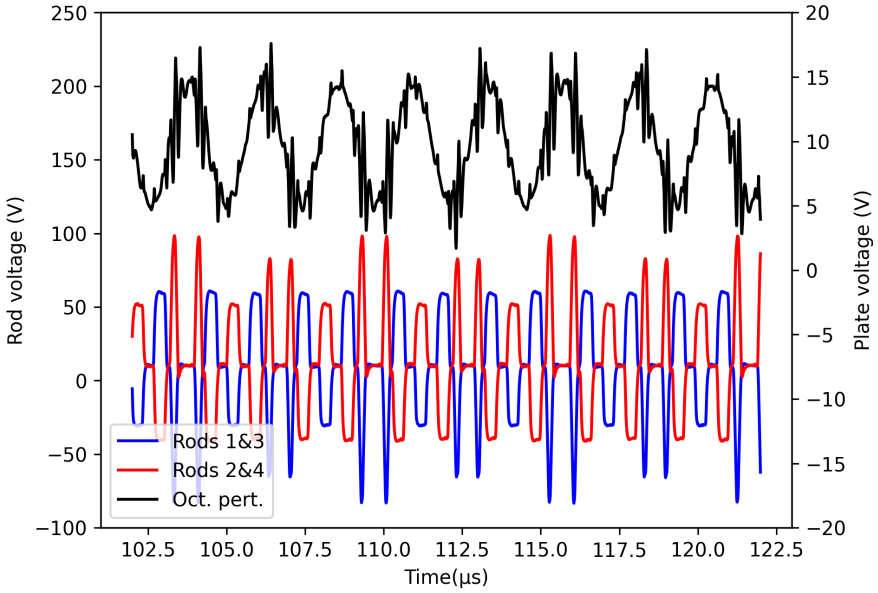

Figure B.3: Oscilloscope trace of 4th order perturbation applied at 420 kHz to the plate electrodes while a T-insert lattice is applied to the rod electrodes in the experimental region

Appendix C

Octupole Strength Scan

Throughout this thesis the octupole strength has mainly been kept constant. However, the strength of the applied octupole field is important for fine tuning the amplitude-dependent tune shift required to damp resonant behaviour. An experimental scan of the octupole strength was carried out for the two-cell T-insert lattice with a fixed ion number. The ionisation time was set to 0.4 s and the argon gas pressure was fixed at 2.3×10^{-7} mbar. This gave an initial number of particles (measured after 10 two-cell periods) of around 4×10^6, creating an initial theoretical space-charge tune shift of around 0.08. The number of particles surviving 2000 two-cell T-insert lattice periods was measured on the MCP for varying octupole strengths of the QI lattice and two non-QI lattices. The results are presented in Fig C.1.

The QI octupole can be seen to increase ion survival over the linear lattice (Oct OFF) for negative octupole strengths below $t = -0.5$. A maximum increase of 6(1) % of ions remaining was observed at an octupole strength parameter of $t = -0.2$. Increasing the QI octupole strength to larger negative values past $t = -0.5$ is seen to start decreasing the ion survival, below that of the linear lattice. This is suspected to be caused by a combination of two effects. First, the degradation of the $1/\beta^3(s)$ octupole scaling as the octupole strength is increased. This is due to the limited slew rate of the amplifiers not being able to recreate the $1/\beta^3(s)$ scaling and thus perturbing the lattice away from being integrable. Second, the dynamic aperture is expected to be reduced due to the fixed points being proportional to $t^{-0.5}$, i.e. $(x_N, y_N) = (\pm\sqrt{\frac{1}{2t}}, \pm\sqrt{\frac{1}{2t}})$, as was presented

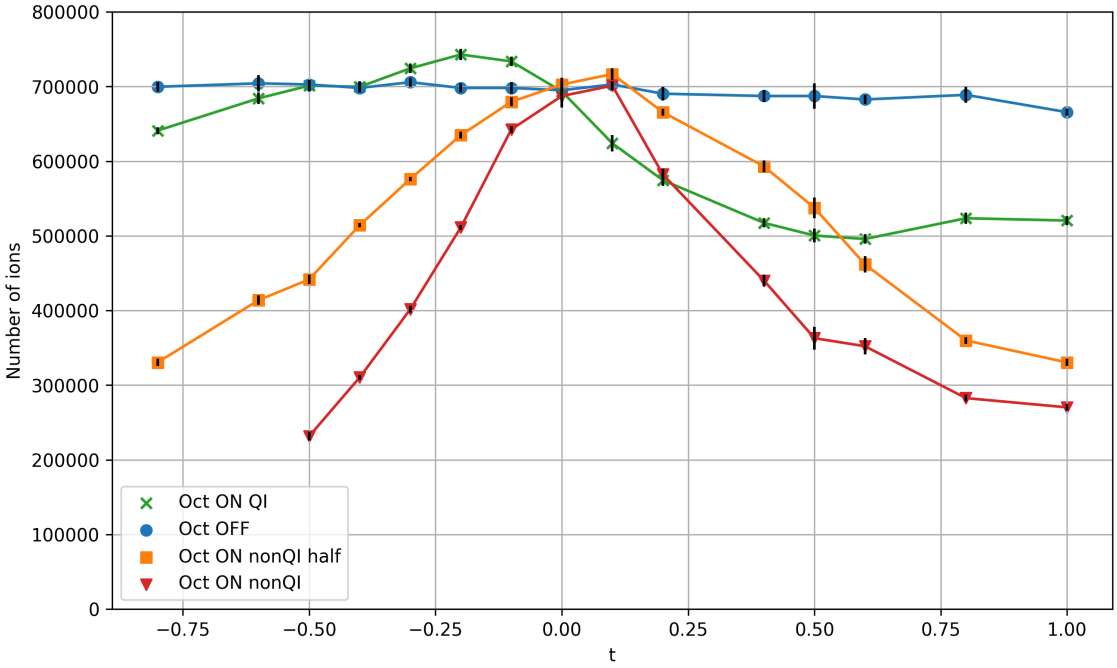

Figure C.1: Number of ions after storing for 2000 two-cell T-insert lattice periods was measured for QI octupoles on (Green, cross), octupoles off (Blue, circle), non-QI octupoles on with half strength (Orange, square) and non-QI octupoles on (Red, triangle). The dimensionless octupole strength parameter t was varied from -0.8 to $+1$.

in Section 3.1.2.1.

From the octupole strength scan in Fig C.1, the negative QI octupole is seen to obtain higher ion survival than both of the non-QI lattices, as was seen throughout Section 6.3.3. However, this was not found to be the case experimentally for all positive octupole strengths. The positive QI octupole was seen to reduce ion survival for positive octupole strengths less than $t = 0.5$ when compared to the non-QI half strength lattice (orange) and for positive octupole strengths of less than $t = 0.25$ when compared to the non-QI lattice (red). At positive octupole strengths of $t > 0.5$, the number of ions surviving the QI lattice seems to plateau, whereas the ion loss for the non-QI lattices continues to decrease with octupole strength. These results could suggest that the positive octupole is causing a positive amplitude-dependent tune shift, causing the ion distribution to coincide with a resonance. However, this surprising result does not agree with simulation and is yet to be understood. Further simulation and experimental work is needed to understand this behaviour.

Bibliography

[1] "High-Luminosity LHC," Accessed: 10.01.2023. [Online]. Available: https://home.cern/science/accelerators/high-luminosity-lhc

[2] "High-Luminosity LHC, Long Shutdown 3 schedule change," Accessed: 10.01.2023. [Online]. Available: https://hilumilhc.web.cern.ch/article/ls3-schedule-change

[3] G. Apollinari, I. Béjar Alonso, O. Brüning, P. Fessia, M. Lamont, L. Rossi, and L. Tavian, *High-Luminosity Large Hadron Collider (HL-LHC): Technical Design Report V. 0.1*, ser. CERN Yellow Reports: Monographs. Geneva: CERN, 2017. [Online]. Available: https://cds.cern.ch/record/2284929

[4] C. M. Beddoes, G. S. Gooris, D. J. Barlow, M. J. Lawrence, R. M. Dalgliesh, M. Malfois, B. Demé, and J. A. Bouwstra, "The importance of ceramide headgroup for lipid localisation in skin lipid models," *Biochimica et Biophysica Acta (BBA) - Biomembranes*, vol. 1864, no. 6, p. 183886, 2022. [Online]. Available: https://www.sciencedirect.com/science/article/pii/S0005273622000281

[5] H. Gong, X. Hu, L. Zhang, K. Fa, M. Liao, H. Liu, G. Fragneto, M. Campana, and J. R. Lu, "How do antimicrobial peptides disrupt the lipopolysaccharide membrane leaflet of gram-negative bacteria?" *Journal of Colloid and Interface Science*, vol. 637, pp. 182–192, 2023. [Online]. Available: https://www.sciencedirect.com/science/article/pii/S0021979723000577

[6] Z. Mileeva, D. Ross, and S. King, "A study of the porosity of nuclear graphite using small-angle neutron scattering," *Carbon*, vol. 64, pp. 20–26, 2013. [Online]. Available: https://www.sciencedirect.com/science/article/pii/S0008622313005393

[7] K. Ninomiya, T. Kudo, P. Strasser, K. Terada, Y. Kawai, M. Tampo, Y. Miyake, A. Shinohara, and K. M. Kubo, "Development of non-destructive isotopic analysis methods using muon beams and their application to the analysis of lead," *Journal of Radioanalytical and Nuclear Chemistry*, vol. 320, no. 3, pp. 801–805, 2019. [Online]. Available: https://doi.org/10.1007/s10967-019-06506-9

[8] "ISIS Neutron and Muon source," https://www.isis.stfc.ac.uk, accessed: 31.01.2022.

[9] "J-PARC," http://j-parc.jp/c/en/index.html, Accessed: 31.01.2022.

[10] "SNS," https://neutrons.ornl.gov/sns, Accessed: 31.01.2022.

[11] J. Thomason, "The ISIS Spallation Neutron and Muon Source—The first thirty-three years," *Nuclear Instruments and Methods in Physics Research Section A: Accelerators, Spectrometers, Detectors and Associated Equipment*, vol. 917, pp. 61–67, 2019. [Online]. Available: https://www.sciencedirect.com/science/article/pii/S0168900218317820

[12] M. Telling, "Drug delivery stays on target ," https://www.isis.stfc.ac.uk/Pages/Drug-delivery-stays-on-target.aspx, Accessed: 31.01.2022.

[13] F. Laake, "Breaking the Barriers to a solar Future," https://www.isis.stfc.ac.uk/Pages/Breaking-the-Barriers-to-a-solar-Future.aspx, Accessed: 31.01.2022.

[14] Nuclear Energy Agency. Organisation for Economic Co-operation and Development, *Accelerator-driven Systems (ADS) and Fast Reactors (FR) in Advanced Nuclear Fuel Cycles: A Comparative Study*. OECD Publishing, Paris, 2002. [Online]. Available: https://www.oecd-nea.org/jcms/pl_33830

[15] "Accelerator-driven Nuclear Energy," https://world-nuclear.org/information-library/current-and-future-generation/accelerator-driven-nuclear-energy.aspx, Accessed: 16.12.2022.

[16] B. Pine, "Space charge induced beam loss on a high intensity proton synchrotron," Ph.D. dissertation, University of Oxford, 2016.

[17] S. van der Meer, "Acromatic Beam Optics for Particle Separator," 1960. [Online]. Available: https://cds.cern.ch/record/278551/files/p1.pdf

[18] E. J. N. Wilson, *An Introduction to Particle Accelerators*. Oxford University Press, 2001. [Online]. Available: https://doi.org/10.1093/acprof:oso/9780198508298.003.0007

[19] F. J. Sacherer, "Transverse Space-Charge Effects in Circular Accelerators," Ph.D. dissertation, University of California, Berkeley, 1968. [Online]. Available: https://www.osti.gov/biblio/877342

[20] I. Hofmann, *Space charge physics for particle accelerators [electronic resource]*, ser. Particle acceleration and detection. Cham, Switzerland: Springer, 2017.

[21] ——, "Stability of anisotropic beams with space charge," *Phys. Rev. E*, vol. 57, pp. 4713–4724, Apr 1998. [Online]. Available: https://link.aps.org/doi/10.1103/PhysRevE.57.4713

[22] R. Baartman, "Betatron resonances with space charge," *AIP Conference Proceedings*, vol. 448, no. 1, pp. 56–72, 1998. [Online]. Available: https://aip.scitation.org/doi/abs/10.1063/1.56781

[23] J. Byrd and D. Sagan, "Measurement of octupole induced decoherence at cesr," in *Conference Record of the 1991 IEEE Particle Accelerator Conference.* IEEE, 1991, pp. 1080–1082.

[24] W. Herr, "Physics of Landau Damping: An introduction (to a mysterious topic)," Accessed: 20.07.2023. [Online]. Available: https://cas.web.cern.ch/sites/default/files/lectures/trondheim-2013/herr1.pdf

[25] ——, "Introduction to Landau Damping," *CERN Yellow Rep. School Proc.*, vol. 3, p. 137, 2017.

[26] E. Forest, H. W. Moshammer, D. Robin, R. Helm, J. Irwin, M. Donald, and A. Zholents, "Sources of amplitude-dependent tune shift in the PEP-II design and their compensation with octupoles," Laurence Berkeley Laboratory, Tech. Rep., 1994.

[27] J. Gareyte, J.-P. Koutchouk, and F. Ruggiero, "Landau damping dynamic aperture and octupole in LHC," CERN, Geneva, Tech. Rep., 1997. [Online]. Available: https://cds.cern.ch/record/321824

[28] X. Buffat, S. Antipov, G. Arduini, R. De Maria, N. Karastathis, S. Kostoglou, A. Koval, E. H. Maclean, N. Mounet, Y. Papaphilippou, T. H. B. Persson, and R. Tomas Garcia, "Strategy for Landau damping of head-tail instabilities at top energy in the HL-LHC," *CERN*, 2020. [Online]. Available: https://cds.cern.ch/record/2745703

[29] V. Danilov and S. Nagaitsev, "Nonlinear accelerator lattices with one and two analytic invariants," *Physical Review Special Topics - Accelerators and Beams*, vol. 13, no. 8, pp. 1–10, 2010.

[30] C. Wayne, "An introduction to KAM theory," *Technical Report*, 2008. [Online]. Available: https://math.bu.edu/people/cew/preprints/introkam.pdf

[31] H. Okamoto and H. Tanaka, "Proposed experiments for the study of beam halo formation," *Nuclear Instruments and Methods in Physics Research Section A: Accelerators, Spectrometers, Detectors and Associated Equipment*, vol. 437, no. 2-3, pp. 178–187, nov 1999. [Online]. Available: http://www.sciencedirect.com/science/article/pii/S0168900299007871

[32] H. Okamoto, Y. Wada, and R. Takai, "Radio-frequency quadrupole trap as a tool for experimental beam physics," *Nuclear Instruments and Methods in Physics Research Section A: Accelerators, Spectrometers, Detectors and Associated Equipment*, vol. 485, no. 3, pp. 244–254, 2002. [Online]. Available: http://www.sciencedirect.com/science/article/pii/S0168900201021398

[33] R. C. Davidson, P. C. Efthimion, R. Majeski, H. Qin, and G. Shvets, "Paul trap experiment to simulate intense nonneutral beam propagation through a periodic focusing field configuration," *Nuclear Instruments and Methods in Physics Research, Section A: Accelerators, Spectrometers, Detectors and Associated Equipment*, vol. 464, pp. 502–511, 2001.

[34] S. L. Sheehy, E. J. Carr, L. K. Martin, K. Budzik, D. J. Kelliher, S. Machida, and C. R. Prior, "Commissioning and first results of the Intense Beam EXperiment (IBEX) linear Paul trap," *Journal of Physics: Conference Series*, vol. 874, no. 1, pp. 4–10, 2017.

[35] S. Antipov, D. Broemmelsiek, D. Bruhwiler, D. Edstrom, E. Harms, V. Lebedev, J. Leibfritz, S. Nagaitsev, C. S. Park, H. Piekarz, P. Piot, E. Prebys, A. Romanov, J. Ruan, T. Sen, G. Stancari, C. Thangaraj, R. Thurman-Keup, A. Valishev, and V. Shiltsev, "IOTA (Integrable Optics Test Accelerator): Facility and experimental beam physics program," *Journal of Instrumentation*, vol. 12, no. 3, 2017.

[36] W. Paul, "Electromagnetic Traps for Charged," *Nobel Lecture*, 1989.

[37] S. Y. Lee, *Accelerator physics*, 4th ed. World Scientific, 2019.

[38] A. Wolski, *Beam dynamics in high energy particle accelerators*, ser. Ebook central. Imperial College Press, 2014.

[39] L. Martin, "Experimental Investigation of Accelerator Beam Dynamics with a Linear Paul Trap," Ph.D. dissertation, University of Oxford, 2020. [Online]. Available: https://ora.ox.ac.uk/objects/uuid:3a42465d-c0e9-4327-b9ff-4de634749d3a/files/d2r36tx54c

[40] G. W. Hill, "On the part of the motion of the lunar perigee which is a function of the mean motions of the sun and moon," *Acta Mathematica*, vol. 8, no. none, pp. 1 – 36, 1900. [Online]. Available: https://doi.org/10.1007/BF02417081

[41] E. D. Courant and H. S. Snyder, "Theory of the alternating-gradient synchrotron," *Annals of Physics*, vol. 281, pp. 360–408, 1958.

[42] R. Weinstock, "On a fallacious proof of earnshaw's theorem," *American Journal of Physics*, vol. 44, no. 4, pp. 392–393, 1976. [Online]. Available: https://doi.org/10.1119/1.10449

[43] D. Leibfried, R. Blatt, C. Monroe, and D. Wineland, "Quantum dynamics of single trapped ions," *Rev. Mod. Phys.*, vol. 75, pp. 281–324, Mar 2003. [Online]. Available: https://link.aps.org/doi/10.1103/RevModPhys.75.281

[44] L. Deniau, H. Grote, G. Roy, and F. Schmidt, "The Mad-X Program (Methodical Accelerator Design): Reference Manual," *CERN*, 2018. [Online]. Available: http://mad.web.cern.ch/mad/releases/5.04.00/madxuguide.pdf

[45] S. White, E. Maclean, and R. Tomás, "Direct amplitude detuning measurement with ac dipole," *Phys. Rev. ST Accel. Beams*, vol. 16, p. 071002, Jul 2013. [Online]. Available: https://link.aps.org/doi/10.1103/PhysRevSTAB.16.071002

[46] F. Chautard, "Particle Accelerator Projects and Upgrades (2020)," https://www.ipac20.org/wp-content/uploads/2020/05/Particle-Accelerator-Projects-and-Upgrades.pdf, Accessed: 07.04.2023.

[47] "Paul Trap Simulator Experiment (PTSX)," https://w3.pppl.gov/ egilson/PTSX/, Accessed: 07.02.2023.

[48] R. C. Davidson, H. Qin, and G. Shvets, "A Paul trap configuration to simulate intense non-neutral beam propagation over large distances through a periodic focusing quadrupole magnetic field," *Physics of Plasmas*, vol. 7, no. 3, pp. 1020–1025, 2000. [Online]. Available: https://doi.org/10.1063/1.873902

[49] E. P. Gilson, R. C. Davidson, P. C. Efthimion, and R. Majeski, "Paul Trap Simulator Experiment to Model Intense-Beam Propagation in Alternating-Gradient Transport Systems," *Phys. Rev. Lett.*, vol. 92, p. 155002, Apr 2004. [Online]. Available: https://link.aps.org/doi/10.1103/PhysRevLett.92.155002

[50] M. Chung, E. P. Gilson, R. C. Davidson, P. C. Efthimion, and R. Majeski, "Use of a linear paul trap to study random noise-induced beam degradation in high-intensity accelerators," *Phys. Rev. Lett.*, vol. 102, p. 145003, Apr 2009. [Online]. Available: https://link.aps.org/doi/10.1103/PhysRevLett.102.145003

[51] E. P. Gilson, R. C. Davidson, M. Dorf, P. C. Efthimion, R. Majeski, M. Chung, M. S. Gutierrez, and A. N. Kabcenell, "Studies of emittance growth and halo particle production in intense charged particle beams using the paul trap simulator experiment," *Physics of Plasmas*, vol. 17, no. 5, p. 056707, 2010. [Online]. Available: https://doi.org/10.1063/1.3354109

[52] E. P. Gilson, R. C. Davidson, P. C. Efthimion, R. Majeski, E. A. Startsev, H. Wang, S. Koppell, and M. Talley, "Excitation of transverse dipole and quadrupole modes in a pure ion plasma in a linear Paul trap to study collective processes in intense beams," *Physics of Plasmas*, vol. 20, no. 5, p. 055706, 2013. [Online]. Available: https://doi.org/10.1063/1.4804408

[53] M. Chung, H. Qin, E. P. Gilson, and R. C. Davidson, "Analysis of continuously rotating quadrupole focusing channels using generalized courant-snyder theory," *Physics of Plasmas*, vol. 20, no. 8, p. 083121, 2013. [Online]. Available: https://doi.org/10.1063/1.4819830

[54] R. Takai, K. Ito, Y. Iwashita, H. Okamoto, S. Taniguchi, and Y. Tomita, "Design and fabrication of a linear paul trap for the study of space-charge-dominated beams," *Nuclear Instruments and Methods in Physics Research Section A: Accelerators, Spectrometers, Detectors and Associated Equipment*, vol. 532, no. 1, pp. 508–512, 2004, international Workshop on Beam Cooling and Related

Topics. [Online]. Available: https://www.sciencedirect.com/science/article/pii/S0168900204013026

[55] D. J. Kelliher, S. Machida, C. Plostinar, C. R. Prior, and S. L. Sheehy, "Plans for a Linear Paul Trap at Rutherford Appleton Laboratory," *6th International Particle Accelerator Conference, IPAC 2015*, pp. 2590–2593, 2015.

[56] K. Izawa, K. Ito, H. Higaki, and H. Okamoto, "Controlled Extraction of Ultracold Ions from a Linear Paul Trap for Nanobeam Production," *Journal of the Physical Society of Japan*, vol. 79, no. 12, p. 124502, 2010. [Online]. Available: https://doi.org/10.1143/JPSJ.79.124502

[57] K. Ito, T. Masuda, H. Higaki, and H. Okamoto, "Accumulating laser-coolable ions in a linear Paul trap for ultrahigh-density beam dynamics experiment," *Journal of Physics: Conference Series*, vol. 1350, no. 1, p. 012126, nov 2019. [Online]. Available: https://dx.doi.org/10.1088/1742-6596/1350/1/012126

[58] K. Ito, M. Matsuba, and H. Okamoto, "Effect of quadrupole focusing-field fluctuation on the transverse stability of intense hadron beams in storage rings," *Progress of Theoretical and Experimental Physics*, vol. 2018, no. 2, 02 2018, 023G01. [Online]. Available: https://doi.org/10.1093/ptep/pty004

[59] H. Takeuchi, K. Fukushima, K. Ito, K. Moriya, H. Okamoto, and H. Sugimoto, "Experimental study of resonance crossing with a Paul trap," *Phys. Rev. ST Accel. Beams*, vol. 15, p. 074201, Jul 2012. [Online]. Available: https://link.aps.org/doi/10.1103/PhysRevSTAB.15.074201

[60] K. Moriya, K. Fukushima, K. Ito, T. Okano, H. Okamoto, S. L. Sheehy, D. J. Kelliher, S. Machida, and C. R. Prior, "Experimental study of integer resonance crossing in a nonscaling fixed field alternating gradient accelerator with a Paul ion trap," *Phys. Rev. ST Accel. Beams*, vol. 18, p. 034001, Mar 2015. [Online]. Available: https://link.aps.org/doi/10.1103/PhysRevSTAB.18.034001

[61] L. K. Martin, S. Machida, D. J. Kelliher, and S. L. Sheehy, "A study of coherent and incoherent resonances in high intensity beams using a linear Paul trap," *New Journal of Physics*, vol. 21, no. 5, pp. 0–16, 2019.

[62] H. Okamoto, K. Kojima, and K. Ito, "A compact Paul ion trap for the study of space-charge effects in drift-tube linear accelerators," *Progress of Theoretical and Experimental Physics*, vol. 2019, no. 9, 09 2019, 093G01. [Online]. Available: https://doi.org/10.1093/ptep/ptz098

[63] M. Goto, C. Ichikawa, K. Ito, K. Kojima, and H. Okamoto, "Stability study of intense hadron bunches in linear accelerators using a Paul ion trap," *Phys. Rev. Accel. Beams*, vol. 25, p. 054201, May 2022. [Online]. Available: https://link.aps.org/doi/10.1103/PhysRevAccelBeams.25.054201

[64] S. Sheehy, D. Kelliher, S. Machida, C. Plostinar, and C. Prior, "Overview of the Design of the IBEX Linear Paul Trap," in *7th International Particle Accelerator Conference*, 2016, p. WEPOY048.

[65] L. K. Martin, D. J. Kelliher, and S. L. Sheehy, "Can a Paul Ion Trap Be Used to Investigate Nonlinear Quasi-Integrable Optics?" *Journal of Physics: Conference Series*, vol. 1350, no. 1, p. 012132, nov 2019. [Online]. Available: https://dx.doi.org/10.1088/1742-6596/1350/1/012132

[66] J. Flowerdew, D. Kelliher, S. Machida, and S. Sheehy, "Exploring Quasi-Integrable Optics with the IBEX Paul Trap," *JACoW*, vol. HB2021, p. THAC3, 2022.

[67] J. A. D. Flowerdew, D. J. Kelliher, S. Machida, and S. L. Sheehy, "Simulating quasi-integrable optics with space charge in the IBEX Paul trap," *Journal of Physics: Conference Series*, vol. 2420, no. 1, p. 012044, jan 2023. [Online]. Available: https://dx.doi.org/10.1088/1742-6596/2420/1/012044

[68] "PA98 operational amplifier," Accessed: 03.01.2023. [Online]. Available: https://www.apexanalog.com/products/pa98.html

[69] Hamamatsu Photonics, "Hamamatsu MCP guide," https://www.triumf.ca/sites, Accessed: 10.02.2023.

[70] Peter Griffin-Hicks, "Internal Report," ISIS Neutron Source, RAL.

[71] C. Prior, "Studies of High Intensity Proton FFAGs at RAL," https://accelconf.web.cern.ch/hb2016/talks, Accessed: 08.04.2023.

[72] P. Mann, *Lagrangian and Hamiltonian Dynamics*. Oxford: Oxford University Press, 2018.

[73] N. Kuklev, "Experimental Studies of Nonlinear Integrable Optics," Ph.D. dissertation, The University of Chicago, 2021. [Online]. Available: https://doi.org/10.6082/uchicago.3361

[74] M. Henon and C. Heiles, "The applicability of the third integral of motion: Some numerical experiments," *The Astronomical Journal*, vol. 69, p. 73, Feb. 1964.

[75] S. D. Webb, D. L. Bruhwiler, D. T. Abell, A. Sishlo, V. Danilov, S. Nagaitsev, A. Valishev, K. Danilov, and J. R. Cary, "Effects of Nonlinear Decoherence on Halo Formation," 2012. [Online]. Available: https://arxiv.org/abs/1205.7083

[76] C. Montag, J. Kewisch, D. Trbojevic, and F. Schmidt, "Overcoming a fast transverse instability by means of octupole-induced tune spread in the relativistic heavy ion collider," *Phys. Rev. ST Accel. Beams*, vol. 5, p. 084401, Aug 2002. [Online]. Available: https://link.aps.org/doi/10.1103/PhysRevSTAB.5.084401

[77] S. Antipov, K. Carlson, R. Castellotti, A. Valishev, and S. Wesseln, "Design of Octupole Channel for Integrable Optics Test Accelerator," in *7th International Particle Accelerator Conference*, 2016. [Online]. Available: https://accelconf.web.cern.ch/ipac2016/papers/tupor030.pdf

[78] G. Darboux, "Sur un probléme de mècanique," *Arch. Néerlandaises Sci.*, vol. 6, p. 371, 1901.

[79] R. G. Smirnov, "The classical bertrand-darboux problem," 2006. [Online]. Available: https://arxiv.org/abs/math-ph/0604038

[80] C. Mitchell, "Complex representation of potentials and fields for the nonlinear magnetic insert of the integrable optics test accelerator," 2019. [Online]. Available: https://arxiv.org/abs/1908.00036

[81] A. Valishev and et al., "First Results of the IOTA Ring Research at Fermilab," *12th Int. Particle Acc. Conf*, 8 2021. [Online]. Available: https://www.osti.gov/biblio/1832847

[82] S. Nagaitsev, A. Valishev, and V. Danilov, "Nonlinear optics as a path to high-intensity circular machines," 2012.

[83] G. Stancari, R. Agustsson, N. Banerjee, C. Boffo, A. Burov, K. Carlson, B. Cathey, Y.-C. Chen, M. Chung, D. Crawford, R. Dhuley, N. Eddy, B. Freemire, C. Hall, Y.-K. Kim, A. Kolehmainen, V. Lebedev, A. Murokh, S. Nagaitsev, C. Park, D. Perini, A. Romanov, J. Ruan, V. Shiltsev, A. Smirnov, E. Stern, and A. Valishev, "Beam physics research with the IOTA electron lens," *Journal of Instrumentation*, vol. 16, no. 05, p. P05002, 2021. [Online]. Available: https://dx.doi.org/10.1088/1748-0221/16/05/P05002

[84] V. Lebedev, J. Jarvis, H. Piekarz, A. Romanov, J. Ruan, and M. Andorf, "The design of Optical Stochastic Cooling for IOTA," *Journal of Instrumentation*, vol. 16, no. 05, p. T05002, 2021. [Online]. Available: https://dx.doi.org/10.1088/1748-0221/16/05/T05002

[85] D. Edstrom, D. Broemmelsiek, K. Carlson, J. P. Carneiro, H. Piekarz, A. Romanov, A. Shemyakin, and A. Valishev, "IOTA Proton Injector Beamline Installation," 2023. [Online]. Available: https://arxiv.org/pdf/2305.09830.pdf

[86] S. D. Webb, D. L. Bruhwiler, A. Valishev, S. N. Nagaitsev, and V. V. Danilov, "Chromatic and Dispersive Effects in Nonlinear Integrable Optics," 2015. [Online]. Available: https://doi.org/10.48550/arXiv.1504.05981

[87] A. Romanov, G. Kafka, S. Nagaitsev, and A. Valishev, "Lattice Correction Modeling for Fermilab IOTA Ring," in *Proc. 5th International Particle Accelerator Conference (IPAC'14), Dresden, Germany, June 15-20, 2014*, ser. International Particle Accelerator Conference, no. 5. Geneva, Switzerland: JACoW, July 2014, paper TUPRO058. [Online]. Available: https://doi.org/10.18429/JACoW-IPAC2014-TUPRO058

[88] A. Romanov, J. Santucci, G. Stancari, A. Valishev, and N. Kuklev, "Experimental 3-dimensional tracking of the dynamics of a single electron in the Fermilab Integrable Optics Test Accelerator (IOTA)," *Journal of Instrumentation*, vol. 16, no. 12, p. P12009, dec 2021. [Online]. Available: https://dx.doi.org/10.1088/1748-0221/16/12/P12009

[89] S. Antipov, S. Nagaitsev, and A. Valishev, "Single-particle dynamics in a nonlinear accelerator lattice: attaining a large tune spread with octupoles in iota," *Journal of Instrumentation*, vol. 12, no. 04, p. P04008, apr 2017. [Online]. Available: https://dx.doi.org/10.1088/1748-0221/12/04/P04008

[90] A. Valishev, N. Kuklev, A. S. Romanov, G. Stancari, and S. Szustkowski, "Nonlinear Integrable Optics (NIO) in IOTA Run 2," in *Fermilab IOTA/FAST Experiment Report*, 2020.

[91] C. E. Mitchell, R. D. Ryne, and K. Hwang, "Bifurcation analysis of nonlinear hamiltonian dynamics in the fermilab integrable optics test accelerator," *Phys. Rev. Accel. Beams*, vol. 23, p. 064002, Jun 2020. [Online]. Available: https://link.aps.org/doi/10.1103/PhysRevAccelBeams.23.064002

[92] S. Baturin, "Hamiltonian preserving nonlinear optics," *Physica D: Nonlinear Phenomena*, vol. 439, p. 133394, 2022. [Online]. Available: https://www.sciencedirect.com/science/article/pii/S0167278922001488

[93] R. Kishek, S. Bernal, Y. Li, M. Reiser, M. Venturini, I. Haber, and T. Godlove, "PIC code simulations of collective effects in the space-charge-dominated beam of the University of Maryland Electron Ring (UMER)," in *Proceedings of the 1999 Particle Accelerator Conference (Cat. No.99CH36366)*, vol. 3, 1999, pp. 1758–1760.

[94] R. A. Kishek, G. Bai, B. Beaudoin, S. Bernal, D. Feldman, R. Feldman, R. Fiorito, T. Godlove, I. Haber, T. Langford, P. O'Shea, B. Quinn, C. Papadopoulos, M. Reiser, D. Stratakis, D. Sutter, K. Tian, J. Thangaraj, M. Walter, and C. Wu, "The University of Maryland Electron Ring (UMER) enters a new regime of high-tune-shift rings," in *2007 IEEE Particle Accelerator Conference (PAC)*, 2007, pp. 820–824.

[95] H. Li, S. Bernal, R. Kishek, T. Godlove, P. O'Shea, and M. Reiser, "Printed-circuit magnets for the University of Maryland Electron Ring (UMER) - new developments," in *PACS2001. Proceedings of the 2001 Particle Accelerator Conference (Cat. No.01CH37268)*, vol. 3, 2001, pp. 1802–1804.

[96] K. Ruisard, "Design of a nonlinear quasi-integrable lattice for resonance suppression at the University of Maryland Electron Ring," Ph.D. dissertation, University of Maryland, College Park, 2018. [Online]. Available: https://arxiv.org/pdf/1808.10020.pdf

[97] K. Ruisard, H. B. Komkov, B. Beaudoin, I. Haber, D. Matthew, and T. Koeth, "Single-invariant nonlinear optics for a small electron recirculator," *Phys. Rev. Accel. Beams*, vol. 22, p. 041601, Apr 2019. [Online]. Available: https://link.aps.org/doi/10.1103/PhysRevAccelBeams.22.041601

[98] L. Dovlatyan, "Study and Mitigation of Transverse Resonances with Space Charge Effects at the University of Maryland Electron Ring," Ph.D. dissertation, University of Maryland, College Park, 2020. [Online]. Available: https://doi.org/10.13016/8pmc-vtcv

[99] K. FUKUSHIMA and H. OKAMOTO, "Design Study of a Multipole Ion Trap for Beam Physics Applications," *Plasma and Fusion Research*, vol. 10, no. 0, pp. 1 401 081–1 401 081, 2015.

[100] C. Prior, "MTD Precision Engineering: Precision Ceramic Components," Accessed: 17.04.2023. [Online]. Available: https://www.mtdltd.co.uk/ceramic-components/

[101] "PA194 operational amplifier," Accessed: 03.01.2023. [Online]. Available: https://www.apexanalog.com/products/pa194.html

[102] A. Devices, "LTspice," https://www.analog.com/en/design-center/design-tools-and-calculators/ltspice-simulator.html, Accessed: 16.05.2023.

[103] J. M. Miller, "Dependence of the input impedance of a three-electrode vacuum tube upon the load in the plate circuit," *Scientific Papers of the Bureau of Standards*, vol. 15, no. 351, pp. 367–385, 1920.

[104] J. Ladislas Wiza, "Microchannel plate detectors," *Nuclear Instruments and Methods*, vol. 162, no. 1, pp. 587–601, 1979. [Online]. Available: https://www.sciencedirect.com/science/article/pii/0029554X79907341

[105] E. H. Eberhardt, "Gain model for microchannel plates," *Appl. Opt.*, vol. 18, no. 9, pp. 1418–1423, May 1979. [Online]. Available: https://opg.optica.org/ao/abstract.cfm?URI=ao-18-9-1418

[106] S. V. Polyakov, "Chapter 3 - photomultiplier tubes," in *Single-Photon Generation and Detection*, ser. Experimental Methods in the Physical Sciences, A. Migdall, S. V. Polyakov, J. Fan, and J. C. Bienfang, Eds. Academic Press, 2013, vol. 45, pp. 69–82. [Online]. Available: https://www.sciencedirect.com/science/article/pii/B9780123876959000032

[107] A. G. Wright, "Secondary emission and gain," in *The Photomultiplier Handbook*. Oxford University Press, 06 2017. [Online]. Available: https://doi.org/10.1093/oso/9780199565092.003.0005

[108] Tabor Electronics, "Multi-Instruments Synchronization with Two WW Tabor AWGs," https://www.taborelec.com/Multi-Instruments-Synchronization-with-Two-WW-Tabor-AWGs, Accessed: 05.06.2023.

[109] ——, "ArbConnection," https://www.taborelec.com/arb-connection, Accessed: 05.06.2023.

[110] ——, "How to Control Tabor AWGs with LabVIEW - Using the IVI driver," https://www.taborelec.com/How-to-Control-Tabor-AWGs-with-LabVIEW-Using-the-IVI-driver, Accessed: 05.06.2023.

[111] "VSim 11.0, Tech-X." https://txcorp.com/vsim/, Accessed: 11.11.2022.

[112] J. A. D. Flowerdew, S. Sheehy, D. J. Kelliher, S. Machida, and S. Rutherford, "Exploring Accelerators for Intense Beans with the IBEX Paul Trap," *Proceedings of IPAC2021*, pp. 1980–1983, 2021. [Online]. Available: https://www.jacow.org/IPAC2021/papers/TUPAB234.pdf

[113] J. A. D. Flowerdew, "Simulating the mitigation of space charge effects with quasi integrable optics using a Paul Trap," https://conference.sns.gov/event/335/contributions/503/, 5th ICFA Mini-Workshop on Space Charge (2022). Accessed: 05.05.2023.

[114] A. Bazzani, G. Servizi, E. Todesco, and G. Turchetti, *A normal form approach to the theory of nonlinear betatronic motion*, ser. CERN Yellow Reports: Monographs. Geneva: CERN, 1994. [Online]. Available: https://cds.cern.ch/record/262179

[115] C. Nieter and J. R. Cary, "Vorpal: a versatile plasma simulation code," *Journal of Computational Physics*, vol. 196, no. 2, pp. 448–473, 2004. [Online]. Available: https://www.sciencedirect.com/science/article/pii/S0021999103006041

[116] Jenkins, Thomas G. and Smithe, David N., "Time-Domain Modeling of RF Antennas and Plasma-Surface Interactions," *EPJ Web Conf.*, vol. 157, p. 03021, 2017. [Online]. Available: https://doi.org/10.1051/epjconf/201715703021

[117] Z. Lécz, A. Andreev, I. Konoplev, A. Seryi, and J. Smith, "Trains of electron micro-bunches in plasma wake-field acceleration," *Plasma Physics and Controlled Fusion*, vol. 60, no. 7, p. 075012, 2018. [Online]. Available: https://dx.doi.org/10.1088/1361-6587/aac064

[118] N. K. Hicks, A. Bowman, and K. Godden, "Particle-in-Cell Simulation of Quasi-Neutral Plasma Trapping by RF Multipole Electric Fields," *Physics*, vol. 1, no. 3, pp. 392–401, 2019. [Online]. Available: https://www.mdpi.com/2624-8174/1/3/28

[119] Tech-X Corporation, "VSim User Guide," https://txcorp.com/, Release 12.0.0 (2022). Accessed: 05.05.2023.

[120] I. M. Kapchinskij and V. V. Vladimirskij, "Limitations Of Proton Beam Current In A Strong Focusing Linear Accelerator Associated With The Beam Space Charge," in *2nd International Conference on High-Energy Accelerators*, 1959, pp. 274–287.

[121] R. Bartolini, A. Bazzani, M. Giovannozzi, W. Scandale, and E. Todesco, "Tune evaluation in simulations and experiments," *Part. Accel.*, vol. 52, no. 3-4, pp. 147–177, 1996. [Online]. Available: https://cds.cern.ch/record/292773

[122] F. Asvesta, N. Karastathis, and P. Zisopoulos, "PyNAFF," https://pypi.org/project/PyNAFF/, Release 1.1.4. Accessed: 05.05.2023.

[123] H. Okamoto and K. Yokoya, "Parametric resonances in intense one-dimensional beams propagating through a periodic focusing channel," *Nuclear Instruments and Methods in Physics Research Section A: Accelerators, Spectrometers, Detectors and Associated Equipment*, vol. 482, no. 1, pp. 51–64, 2002. [Online]. Available: https://www.sciencedirect.com/science/article/pii/S0168900201016849

[124] M. Reiser, *Theory and Design of Charged Particle Beams*. John Wiley & Sons, Ltd, 2008. [Online]. Available: https://onlinelibrary.wiley.com/doi/abs/10.1002/9783527622047.ch6

[125] L. K. Martin, K. Ito, D. J. Kelliher, S. Machida, H. Okamoto, and S. L. Sheehy, "A new method to measure the beta function in a Paul trap," *Journal of Physics: Conference Series*, vol. 1067, no. 6, p. 062016, sep 2018. [Online]. Available: https://dx.doi.org/10.1088/1742-6596/1067/6/062016

[126] D. Breck, *Zeolite Molecular Sieves: Structure, Chemistry, and Use*, ser. A Wiley-Interscience publication. Wiley, 1973. [Online]. Available: https://books.google.co.uk/books?id=aY0vAQAAIAAJ

[127] S. Kunze, R. Groll, B. Besser, and J. Thöming, "Molecular diameters of rarefied gases," *Scientific Reports*, vol. 12, no. 1, p. 2057, 2022. [Online]. Available: https://doi.org/10.1038/s41598-022-05871-y

[128] S. A. Antipov, D. Amorim, N. Biancacci, X. Buffat, E. Métral, N. Mounet, A. Oeftiger, and D. Valuch, "Proof-of-Principle Direct Measurement of Landau Damping Strength at the Large Hadron Collider with an Antidamper," *Phys. Rev. Lett.*, vol. 126, p. 164801, Apr 2021. [Online]. Available: https://link.aps.org/doi/10.1103/PhysRevLett.126.164801

[129] S. Brooks, "Ion trap test stand and laser cooling studies of ultra-low emittance bunches for high luminosity," BNL Internal Proposal, https://stephenbrooks.org/ap/report/, Accessed: 24.07.2023.

[130] S. Brooks, K. Brown, F. Méot, A. Nomerotski, S. Peggs, M. Palmer, T. Roser, T. Shaftan, G. H. Hoffstaetter, S. Nagaitsev, J. Lykken, J. Jarvis, V. Lebedev, G. Stancari, A. Valishev, A. Taylor, A. Hurd, N. Moody, P. Muggli, A. Aslam, S. G. Biedron, T. Bolin, S. S. Guitron, C. Gonzalez-Zacarias, M. Larsson, R. Thomas, B. Huang, T. Robertazzi, J. Cary, B. M. Hegelich, B. B. Blinov, and S. Milton, "Ion Coulomb Crystals in Storage Rings for Quantum Information Science," 2022.